UNIVERSITY OF CALIFORNIA SAN DIEGO

Iron Sources, Sinks, and Cycling in Productive Coastal Seas

A dissertation submitted in partial satisfaction of the
requirements for the degree Doctor of Philosophy

in

Oceanography

by

Kiefer O. Forsch

Committee in charge:

Katherine A. Barbeau, Chair
Lihini Aluwihare
Todd Martz
Joseph O'Connor
Mark D. Ohman
Maria Vernet

2021

The Dissertation of Kiefer O. Forsch is approved, and it is acceptable in quality and form for publication on microfilm and electronically.

University of California San Diego

2021

DEDICATION

This thesis is dedicated to my Family and mentors who supported me over the years. From the opportunities they have provided, this thesis emerged.

EPIGRAPH

"All goes onward and outward, nothing collapses"

Walt Whitman

While the sun and the rain live, these shall be;

Till a last wind's breath upon all these blowing

Roll the sea.

Algernon Sinburne

TABLE OF CONTENTS

LIST OF FIGURES

LIST OF TABLES

ACKNOWLEDGEMENTS

The rest of this thesis is dedicated to the scientific journey I've been on for the last seven years, which is why I want to begin with my personal side of science. I start by thanking my advisor, Kathy Barbeau, who has supported my growth as a scientist. When I chose Kathy as my mentor, seven years ago, I knew I could learn a lot from her and that she would support my enthusiasm. Over the years I was given incredible leeway to explore my interests. From the beginning, Kathy accepted me for who I was and made me feel like I had value. The impact Kathy's mentorship had on me and by extension, others who I have mentored, continues to spread with future generations of scientists.

Next, and importantly, my family (Mom, Dad, Margaux, Garrett, Nick, Kim) who provided the foundational gifts of love and acceptance making it possible for me to be *here*. We are all products of our families, and the values we learn from those we love and respect leave a lasting mark. My parents made science fun, provided me with unconditional love, and showed me that with our talents, we can educate and help others and inspire critical thinking. Thank you, Mom and Dad.

I want to thank my cohort, specifically MCG 2014: Margot, Alyssa, Sara, Matt, and Kenisha. Special thanks to Lauren, my fellow lab mate and closest colleague: I had incredible fun working with her on so many different projects. No matter the challenge, we were able to carry out the science in places like Antarctica, California, and the Great Lakes. Her calming presence and kindness helped me overcome many graduate school hurdles. To Jack, a fellow explorer and scientific dreamer: many of our conversations about science transformed into the questions I find myself exploring now. I also want to thank all the Barbeau Lab students, former (Randie, Shane, Angel, Kayleen) and current (Max, Minerva) for the advice I received and the experiences we shared. Your brilliant minds, incredible talents, and close friendships inspire me to work hard for my dream opportunities, without sacrificing who I am. I am lucky to have them all as my colleagues.

Other important scientists along the way (Rob, Silke, Lihini, Jane, Miriam) who all shared the role of mentor at various stages in my career. Individuals make the academic system *human* by fulfilling various roles.

Finally, I thank my partner, Beverly. There is perhaps no biologist who knows more about my research than she does. She gives much of her time and patience to help others and I get to witness how happy these acts of kindness make her. We have been through a lot together in graduate school and I will forever be thankful for Beverly's encouragement and wisdom.

=====

Chapter 2, in full, is a manuscript of the material as it appears in Forsch, K., Hahn-Woernle, L., Sherrell, R.M., Roccanova, V., Bu, K., Burdige, D., Vernet, M., Barbeau, K.A. (2021) Seasonal dispersal of fjord meltwaters as an important source of iron and manganese to coastal Antarctic phytoplankton, Biogeosciences Discuss., 2021, 1–49, doi:10.5194/bg-2021-79, 2021. The dissertation author was the primary investigator and first author of this paper. Lisa Hahn-Woernle was the main contributor to the physical modeling in this chapter. Rob Sherrell, Kaixan Bu, and Vincent Rocannova at the Rutgers Inorganic Analytical Laboratory helped with mass spectrometry methods. David Burdige provided sediment core analyses. Maria Vernet (FjordEco) and Katherine Barbeau supported this work.

Chapter 3 is being prepared for submission and the dissertation author was the primary investigator and first author of this chapter. Kayleen Fulton and Marley Weiss helped analyze bSi samples. We also thank Mike Stukel for contributing sediment trap data and Katherine Barbeau for supporting this work. The CCE LTER program supported these studies.

Chapter 4 is being prepared for submission and the dissertation author was the primary investigator and first author of this chapter. Lauren Manck is a coauthor on incubation studies and provided syntheses of the transcriptomic data for this chapter. Katherine Barbeau supported this work as well as FjordEco and CCE LTER for the field studies.

VITA

2012	B.A. in Chemistry Oberlin College, Oberlin, OH
2016	M.S. in Oceanography Scripps Institution of Oceanography, University of California San Diego
2014 - 2021	Research Assistant Scripps Institution of Oceanography, University of California San Diego
2021	Ph.D. in Oceanography Scripps Institution of Oceanography, University of California San Diego

PUBLICATIONS

1. **Forsch, K.,** Hahn-Woernle, L., Sherrell, R., Roccanova, J., Bu, K., Burdige, D., Vernet, M. and Barbeau, K. A.: Seasonal dispersal of fjord meltwaters as an important source of iron and manganese to coastal Antarctic phytoplankton, Biogeosciences Discuss., 2021, 1–49, doi:10.5194/bg-2021-79, 2021. (*in press*)

2. Pan, B Jack, Maria Vernet, Lauren Manck, **Kiefer Forsch**, Lindsey Ekern, Martina Mascioni, Katherine A Barbeau, Gastón O Almandoz, and Alexander J Orona. 2020. "Environmental Drivers of Phytoplankton Taxonomic Composition in an Antarctic Fjord." *Progress in Oceanography* 183: 102295. https://doi.org/https://doi.org/10.1016/j.pocean.2020.102295.

3. Sherrell, R.M., Lagerström, M., **Forsch, K.O.**, Stammerjohn, S.E., Yager, P.L. 2015. "Dynamics of dissolved iron and other bioactive trace metals (Mn, Ni, Cu, Zn) in the Amundsen Sea Polynya, Antarctica." *Elementa* 3:71. doi:10.12952/journal.elementa.000071.

FIELDS OF STUDY

Major Field: Oceanography

Studies in Marine Chemistry

Professor Katherine A. Barbeau

ABSTRACT OF THE DISSERTATION

Iron Sources, Sinks, and Cycling in Productive Coastal Seas

by

Kiefer O. Forsch

Doctor of Philosophy in Oceanography

University of California San Diego, 2021

Katherine Barbeau, Chair

The cycling of iron in the ocean is intimately tied to whole ecosystem processes and other biogeochemical cycles. While ocean basin surveys of iron concentration have revealed important sources to the ocean, questions remain regarding the controls on supply of this critical micronutrient to productive planktonic ecosystems. Using a combination of oceanographic-scale observations and mechanistic experiments, work in this thesis seeks to advance our understanding of controls of new and regenerated iron supply to coastal polar and temperate ecosystems and microbially-mediated cycling in such marine environments.

In Chapter 2 we comprehensively characterized the cryospheric inputs of iron to Andvord Bay, a cold glaciomarine fjord located on the west Antarctic Peninsula. Iron content and speciation were measured to characterize inter-seasonal changes in the water column, a subglacial meltwater plume and glacial ice, fjord sediments, including a first assessment of iron-binding organic ligands in a highly productive fjord environment. We utilized multi-elemental analyses to understand the cycling of iron sources. Results from a high-resolution numerical model revealed episodic atmospheric forcing events are important for supplying subglacial meltwater to the surface, and for the export of surface meltwater and associated iron away from the coast. In Chapter 3 we characterize iron supply and cycling in a coastal upwelling filament, a mesoscale feature which commonly occurs during times of intensified along-shore winds in eastern boundary current systems, such as the southern California Current. We used a Lagrangian framework to capture the biogeochemical evolution of a filament, including: the development of iron-limitation of the phytoplankton community, assessment of *in situ* geochemical proxies of iron stress, and impacts of diminishing iron flux on phytoplankton allometric ratios, namely the biogenic silica-to-organic carbon content of diatoms. We have determined filaments are not likely significant sources of dissolved iron to the open ocean, yet their importance for advecting particulate iron remains to be tested. Coincident with the development of iron-limitation of the phytoplankton community we observed greater biogenic silica-to-organic carbon ratios and enhanced export efficiency to depth. In Chapter 4, within microcosm a field experiment, we examined the

production of organic iron-binding ligands during remineralization – an important process supplying iron regenerated from phytoplankton blooms. As a part of this work we developed an improved data processing methods for multiple analytical windows electrochemical iron ligand titration data, enabling more robust detection of distinct pools of iron-binding ligands produced by heterotrophic bacteria and in diverse oceanic waters.

Together, this work examines the processes involved in the flux of new iron to the ocean, and internal transformations affecting its fate within the water column. We hope this work results in an improved understanding of the controls on modern iron supply and ties to the marine biogeochemical cycles of macronutrients.

Chapter 1: Introduction

1.1. Iron in the marine environment

At the base of the food web, microscopic organisms support all life in the ocean. These primary producers flourish in the sunlit surface ocean when nutrients are replete. Dissolved iron (dFe, <0.2 μm) is an essential micronutrient for microbial growth in the marine environment (Morel and Price, 2003). It functions as a metal cofactor present in many enzymes required for life processes and facilitates the transport of electrons during photosynthesis, respiration, and nitrogen fixation (Morel, Milligan and Saito, 2013). Throughout the modern ocean, the demand for dFe surpasses its supply. When this occurs, phytoplankton biomass no longer accumulates and net growth ceases until a new source of dFe is supplied. In vast regions of the world ocean, dFe exists in ultra-low concentrations (sub-nanomolar), but other nutrients (i.e. nitrate, phosphate, silicic acid), supplied to the surface through upwelling, are not completely consumed, and so, accumulate. These regions are classically referred to as high nutrient – low chlorophyll regimes (HNLC's), the largest of which is the entirety of the Southern Ocean.

When the ratio of concentrations of macronutrients to dFe changes, as when upwelled deep water delivers excess nitrate, phosphate, and silicic acid, relative to dFe, to the surface, the phytoplankton community may become dFe limited, since the ability for phytoplankton to uptake nitrate (NO_3^-) is dependent on the iron-rich nitrate reductase enzyme (Price, Andersen and Morel, 1991). It is now established that episodic HNLC conditions occur in Eastern Boundary Currents (EBC), when summer winds upwell deep water and alter the concentration ratios (Hutchins and Bruland 1998; King and Barbeau 2007; Biller and Bruland 2014). Together, chronic and episodic HNLC conditions occur in approximately 40% of the modern ocean. Furthermore, studies have revealed that the supply of dFe in these regions has wide-ranging effects on key biogeochemical processes (Boyd et al. 2004, 2007; de Baar 2005; Moore et al. 2002; Moore and Doney 2007).

Why is there widespread ocean anemia? In oxygenated seawater, Fe^{3+} quickly forms insoluble iron (oxyhydr)oxide precipitates (Liu and Millero, 2002). These minerals sink below the surface where they are unavailable for biological uptake. Due to its reactivity with sinking particles, dFe is further removed from the surface ocean via scavenging. These two processes keep the surface dFe reservoir low and less bioavailable. In high-particulate regions, where adsorption processes dominate the physical size partitioning of dFe and particulate forms of Fe (pFe), it is important to measure total dissolvable Fe (TDFe), which represents the total reactive (bioavailable) pool of Fe. TDFe is defined as >6 month weak acid leach (pH ~1.8) of unfiltered seawater, followed by filtration (0.4 µm filter). This treatment allows for dFe that is adsorbed to the surface of particles to solubilize at weakly acidic pH; such conditions are found within the gut of a zooplankter. Extensive complexation of dFe (>99%), by a heterogenous pool of organic Fe-binding ligands, has been shown to stabilize dFe over long time and spatial scales and can significantly impact the bioavailability and global inventory of dFe in the ocean (Rue and Bruland 1995; van den Berg 1995; Johnson, Gordon, and Coale 1997; Sunda and Huntsman 1997; Tagliabue, Aumont, and Bopp 2014). *Thus, our ability to explain and predict the distribution of primary production in time and space is deepened by our knowledge of the distribution, the sources and sinks, and biogeochemical cycling of dFe and organic Fe-binding ligands.*

The ability to cleanly sample and directly measure the trace elements present in seawater has grown leading to the identification of multiple sources of dFe, including aeolian dust (Jickells, 2005), coastal and shallow sediments (Elrod *et al.*, 2004; Lam and Bishop, 2008), sea ice (Lannuzel *et al.*, 2007), hydrothermal vent fluids (Sander and Koschinsky, 2011; Saito *et al.*, 2013) and enriched deep ocean water masses. Recently, icebergs and glacial meltwater were proposed to constitute an important, yet greatly understudied, source of bioavailable dFe to the high-latitude ocean (Raiswell and Canfield 2012; Bhatia et al. 2013). These external sources supply new dFe to the surface ocean and their significance, in the cryosphere and beyond, including projected changes due to climate change, need to be evaluated. Due to the recognized importance in

controlling the availability of dFe for biota, sources and sinks of natural organic Fe-binding ligands are also now being investigated.

Studies into the organic complexation of dFe have revealed that numerous biotic and abiotic processes produce organic Fe-binding ligands, and that the ligand pool is composed of a continuum of ligand classes, where each class may represent coherent chemical groups. Much uncertainty remains as to the chemical identity of individual ligands present in seawater, however, indirect electrochemical methods, namely Adsorptive Cathodic Stripping Voltammetry (ACSV), allow us to differentiate ligand classes by their affinity for Fe and concentration (van den Berg, 1986). Ligand classes, and their associated binding sites, are distinguishable by their conditional stability constant ($K_{FeLi,\ Fe'}$), and have generally been grouped into strong (L_1) and weaker (L_2) classes (see review by Gledhill and Buck 2012). Water column profiles of ligands have revealed general partitioning of each class, with L_1 detected in the surface layer and close to dFe sources and boundaries, and L_2 ligands at higher concentrations detected throughout the ocean interior (Buck, Sohst and Sedwick, 2015; Buck *et al.*, 2018). Now, with the expanding number of ligand analyses performed in most of the ocean basins, a regional classification is under development to examine the ocean biogeochemical cycle of Fe-binding ligands (Hassler, van den Berg and Boyd, 2017).

The detection of ligands in natural seawater and laboratory experiments has revealed similarity in the $K_{FeLi,\ Fe'}$ of distinct ligand classes with those of cellular exudate (e.g. exopolymeric substances) (Stolpe and Hassellöv, 2010), siderophores (Rue and Bruland, 1995), and humic-like substances (e.g. fulvic acid) (Laglera, Battaglia and van den Berg, 2007; Laglera and van den Berg, 2009). Siderophores are small molecules with high affinities for Fe, and are produced by heterotrophic and autotrophic bacteria to aid in Fe acquisition. It is thought siderophores make up a significant fraction of L_1 ligands, which dominate Fe speciation in the ocean (Mawji *et al.*, 2008). Most studies of Fe-binding ligands have only reported L_1 and L_2 classes, making it difficult to ascertain robust definitions of conditional stability constants. Combined with a Multiple Analytical

Windows (MAWs) approach, which utilizes varying competition strength of a well-characterized added ligand, a wider swath of ligands present in seawater may be examined, and qualitative differences among different sources can be resolved. *Despite these advances, there is a lack of data linking Fe sources and ligand chemistry to the supply of Fe to biologically important regions of the modern ocean.*

Mechanistic bottle incubation experiments can be used to simulate different environmental conditions and key components of the marine Fe biogeochemical cycle can be captured, such as remineralization. Remineralization carried out by heterotrophic bacteria associated with biogenic particles, can contribute recycled Fe and L_2 ligands to the pool of nutrients sustaining life in the ocean through the breakdown of particulate organic matter (POM) (Boyd et al. 2010; Weber et al. 2016; Boyd et al. 2017). This transformation is essential to controlling the depth of the ferricline, the longevity of phytoplankton blooms, and the physicochemical form of Fe (Boyd and Ellwood 2010). With laboratory and bottle incubation experiments pointing towards a bacterial source of L_1 ligands, which dominate dFe speciation and compose a bioavailable dFe pool, remineralization is likely an important process strongly affecting the physicochemical form and residence time of dFe in the ocean. *MAW electrochemical methods applied to incubation experiments is a powerful approach to understanding this key component of the marine Fe biogeochemical cycle.*

1.2. Specialized methods for analysis

The methods used in this thesis to measure Fe and Fe-binding ligands are discussed below.

Measurements of dFe and total dissolvable iron (TDFe) concentrations are conducted in-house using a flow-injection chemiluminometric method (FI-CL) (Figure 1) based on a similar method described in Bowie *et al*. (1998), and a manifold adapted from Lohan *et al*. (2006). The general idea behind the method is that Fe is present in seawater in vanishingly minute amounts (picomolar concentration). Thus, a specially designed column is used to pre-concentrate this analyte. The column is filled with a resin, which has an affinity for Fe and not dissolved salts

present in the seawater matrix. Following an oxidation step converting all Fe^{2+} to Fe^{3+}, Fe is selectively pre-concentrated on the resin (Toyopearl 650 M chelating resin) at pH ~3.5. After the sample has been eluted with hydrochloric acid (0.23 M Q-HCl), the production of radicals by Fe^{3+} catalyzes a three-step oxidation reaction with hydrogen peroxide (0.3 M Q-H_2O_2) and luminol (0.25 mM). The chemiluminescent reaction is detected by a photomultiplier tube (PMT) and controlled using Waterville Analytical software and Labview program and interface. In-house and consensus reference standards are measured each analytical run to ensure long-term accuracy and precision (see **Table 1**).

The organic speciation of iron is measured using a hanging-drop mercury electrode (HDME). The mass balance equation for dFe, regarding its organic speciation, can be expressed as,

$$[Fe_T] = [Fe'] + [FeL_i] \quad (1)$$

where ***Fe'*** is the sum of all inorganic species (assumed to be Fe(III) due to the short half-life of Fe(II) in oxygenated seawater), and FeL_i is the organically-bound fraction. CLE-ASCV is carried out in two phases, the first being the titration of the natural ligand pool with dFe and the addition of a well-characterized organic ligand to compete with the ambient pool, which then allows for the concentration of ambient ligands and the conditional stability constant ($K^{cond}_{Fe(III)L_i,Fe'}$) to be determined. Salicylaldoxime (SA) is the added ligand used to detect electroactive organic Fe complexes, and is shown to coordinate metal ions in a *bis* fashion. A new mass balance is expressed as,

$$[Fe_T] = [Fe'] + [Fe(SA)_2] + [FeL_i] \quad (2)$$

and the following equilibrium expression describes the competition reaction between natural ligands and SA, for Fe^{3+}:

$$\begin{array}{c} Fe' + L' \leftrightarrow Fe(III)L \\ + \\ 2SA' \\ \updownarrow \\ Fe(III)SA_2 \end{array}$$

The mass action expression for complexation of ***Fe′*** by SA is,

$$\beta^{cond}_{2SA/Fe(III)} = [Fe(SA)_2]/([Fe'] * [SA']^2) \qquad (3)$$

and the side reaction coefficient for $Fe(SA)_2$, with respect to ***Fe′*** is, $\alpha'_{Fe(SA)_2} = \frac{[Fe(SA)_2]}{[Fe']} = \beta^{cond}_{2SA/Fe(III)} * [SA']^2$, which was determined such that $\alpha'_{Fe(SA)_2}$was 10-100x the inorganic side reaction coefficient to outcompete [Fe(III)] with [OH^-], but not the natural ligands (Buck and Bruland, 2007). Since [*SA′*]^2 is proportional to $\alpha'_{Fe(SA)_2}$, the amount of SA added defines the analytical window, which most directly describes the likelihood of Fe(III) to form an organic ligand complex with SA, given a competition exists for binding sites of uncomplexed ligands.

The second phase is electrochemical detection of the natural ligands. During the deposition step, an optimal potential is applied (0 V) and the metal-SA complex adsorbs to the surface of a controlled-growth mercury drop electrode (BioAnalytical Systems). The sample is subsequently scanned in differential pulse mode, and the reducing current (at -0.5V) is analyzed by Epsilon 2 software. The current peak intensities, in nA, are plotted versus the added dFe to form a titration curve. The sensitivity (slope) is inversely proportional to the amount of ***Fe′***, thus the concentration of *FeL* can be determined. Using advanced chemical equilibrium software,

multiple linearizations are used to calculate the natural ligand concentration and conditional stability constant for each analytical window (Omanović, Garnier and Pižeta, 2015). Using MAW methods leads to a more complete picture of the ligand pool by estimating its complexation capacity for dFe and determining more robust definitions of stability constants, which describes the effective influence of Fe-binding ligands on Fe speciation.

1.3. Iron in seasonal seas

1.3.1. West Antarctic Fjords

Rapid climate warming along the western Antarctic Peninsula (WAP) has altered the freshwater budget of the region due to increased glacial discharge to the ocean (Meredith *et al.*, 2016). Icebergs and large ice sheets are important sources of dFe nutrition to phytoplankton in the offshore iron-limited surface waters; yet, poor constraints on dFe in glacial meltwater and its dispersal to iron-poor regions hinder our ability to predict regional changes in productivity and climate.

Fjords are deep estuaries originating from the flow of glacial ice from the continent to the ocean. Glacio-marine fjords exist at high-latitudes due to the cold air and ocean temperatures required to sustain marine-terminating glaciers (i.e., tidewater glaciers), which extend into the ocean, thus making them important boundaries between the cryosphere and the ocean. Across this boundary, the chemical gradients are intense. Meltwater discharge and glacial calving processes increase the flux of chemical species on seasonal timescales and sustain highly productive coastal systems. How these fluxes affect WAP fjord ecosystem structure, and their sensitivity to cryosphere-ocean interaction and climate warming remain largely understudied.

Climate controls the rates and mechanisms by which glacial meltwater and ice are delivered to the ocean (reviewed in Meredith, Stefels, and van Leeuwe 2017). The WAP is home to the most extensive system of glacio-marine fjords on the Antarctic continent, and is

experiencing many times the warming rate of the global average (Steig and Orsi, 2013). This will undoubtedly lead to declines in ice volume, increasing the glacial meltwater and ice flux to the coastal ocean. Air temperatures above the WAP have risen steadily over the last few decades, but it is now apparent that intrusions of warmer ocean temperatures at mid-depth are responsible for the acceleration of the retreat of glaciers (Cook *et al.*, 2016; Couto *et al.*, 2017). It is estimated that ninety percent of the 674 glaciers on the WAP are in retreat and calving more ice (Cook *et al.*, 2016). Recent studies have shown a significant freshening of the coastal ocean due to the increase in discharge in the form of meltwater and ice (Meredith *et al.*, 2016). While the impact of warmer temperatures on the freshwater budget of the WAP has been given some attention, the impact of increased glacial melting on Antarctic marine ecosystems is unknown.

Cryospheric inputs are important for sustaining coastal productivity through the delivery of nutrients, such as Fe (Smith et al. 2007; Hodson et al. 2017; Alderkamp et al. 2012; Wehrmann et al. 2014; De Jong et al. 2015). More recently, a study by Meire et al. (2017) demonstrated inputs from buoyant meltwater plumes of marine-terminating glaciers in Arctic fjords entrain and deliver nutrient-rich deep water to the surface. This mechanism would also supply Fe up to the surface, however, high concentrations of particles, observed in the vicinity of glacial outflows, likely promote rapid removal of dFe from solution. In this thesis, cryospheric sources of new Fe, including a subglacial plume, glacial ice, and marine sediment cores were measured. The physical circulation within the fjord was modeled to *constrain the flux of important bioactive elements (Fe and manganese) to the euphotic zone and export to the coastal ocean*.

Due to the effective removal of dFe by estuarine processes (Boyle, Edmond, and Sholkovitz 1977), it is somewhat controversial as to the extent glacial meltwater dFe and pFe could contribute to open ocean primary production (Schroth et al. 2011; Bhatia et al. 2013; Planquette et al. 2013; Schroth et al. 2014; Hodson, Nowak, and Christiansen 2016; Annett et al. 2015; Zhang et al. 2015; Lyons et al. 2015; Hopwood et al. 2016; Markussen et al. 2016; Hodson et al. 2017; Stevenson et al. 2017). Recently, Annett et al. (2016) showed that Fe enrichment on

the open shelf region of the WAP was correlated with elevated proportions of meteoric water. It is clear from these previous studies that the fate of glacial dFe, after mixing into the ocean, is dependent on the mode in which it was delivered (e.g. glacial streams, icebergs, meltwater sediment plumes). One shortcoming of these studies has been little evidence for a mechanism that stabilizes and facilitates long-range transport of dFe, although organic complexation of dFe has been suggested to be one such mechanism (Tagliabue, Aumont and Bopp, 2014; Fitzsimmons *et al.*, 2017). This burgeoning source of dFe to coastal regions could be advected further offshore to iron-limited waters of the Southern Ocean and will depend on the quality and magnitude of the dFe flux across the ice-ocean boundary, in addition to physical forcing.

Excess ligands, defined as [eL] = [L] – [dFe], are a proxy for ligand undersaturation and complexation capacity (Wu and Luther, 1995; Thuróczy *et al.*, 2010). Uncomplexed ligands could mobilize particulate forms of Fe, which are expected to dominate in particle-rich systems, and stabilize sources of new dFe. Excess ligands have been shown to occur with high primary productivity in the surface and could be a result of dFe drawdown (Buck and Bruland 2007; Thuróczy et al. 2012). Grazing pressure on phytoplankton blooms also have been shown to increase eL (Sato, Takeda and Furuya, 2007). Analyses of the composition of the ligand pool present with Fe can be used to understand *how ligands impact the reactivity and ultimate fate of cryospheric Fe*.

As the WAP responds to a changing climate, cryospheric Fe will be released into biogeochemically sensitive regions like the Southern Ocean. We need to better understand the physicochemical form and realm of influence of cryospheric Fe in the Antarctic region. The FjordEco project consisted of two field expeditions (December 2015, April 2016) with the goal of understanding the ecosystem function of Andvord Bay – a productive glacio-marine fjord located on the WAP. The data collected from these expeditions are *poised to advance our knowledge of cryospheric Fe inputs to the ocean*, which are globally increasing in significance.

1.3.2. Towards a more detailed picture of Fe biogeochemistry in the California Current Ecosystem

Gradients in Fe concentrations reveal a *mosaic* of biogeochemical conditions exist in highly dynamic Eastern Boundary Current regimes. A framework for Fe biogeochemistry for these regions has existed since the early 2000's, identifying the importance of sedimentary sources and wind-driven upwelling as the dominant mode of Fe supply to the euphotic zone. In contrast, our understanding of how mesoscale transport mechanisms, such as coastal filaments, connect the nearshore and offshore regions through the delivery of Fe is lacking.

The California Current Ecosystem (CCE) Long-Term Ecological Research (LTER) site is in a coastal upwelling biome. The food web is dependent on seasonal phytoplankton blooms, which occur during the late spring and summer months when along-shore winds intensify and bring nutrient-rich deep water to the surface. As in other eastern margins, upwelling makes these biomes among the most productive ecosystems in the global ocean. No longer in its infancy, the CCE LTER program now seeks to characterize the transient nature of coastal filaments, and their importance for cross-shore fluxes of nutrients, bioactive elements, and biota. How these mesoscale features structure the pelagic ecosystem in time and space, and how these will change in a future climate are the main motivating questions of the program.

Past studies on Fe biogeochemistry in this upwelling region have revealed an important bottom-up control on the phytoplankton community (Johnson, Gordon, and Coale 1997; Hutchins and Bruland 1998; King and Barbeau 2007, 2011). Deckboard and *in situ* bottle amendment experiments show a rapid response of the phytoplankton community to the addition of Fe. To this end, King et al. (2012) highlighted the value of conducting quasi-Lagrangian studies combined with fixed-station observations in a highly heterogeneous and dynamic upwelling region of the California Current System. Incubation experiments conducted in these studies showed that geochemical proxies, such as *Si excess* (Si_{ex} = $[Si(OH)_4]$ – $R_{Si:NO3}[NO_3^-]$), NO_3^-:dFe, and the production of L_1-type ligands can be used to assess the degree of Fe limitation experienced by

the phytoplankton community (King, Buck, and Barbeau 2012). Diatoms uptake silicic acid and nitrate at relatively the same proportion, but when experiencing Fe stress, will preferentially uptake more silicic acid, relative to nitrate (Brzezinski 1985; Hutchins and Bruland 1998). Therefore, a negative Si_{ex} value is a proxy for Fe limitation (King and Barbeau 2011). Since strong Fe-binding ligands (L_1) are important in controlling the availability of dFe, the production of these ligands can serve as an additional indicator of the bacterial and phytoplankton response strategy to access low growth-limiting concentrations of this micronutrient (King, Buck, and Barbeau 2012). However, Bundy et al. (2016) found that bacteria also produce L_1 ligands in Fe replete conditions, which could be a strategy to keep recently supplied Fe in solution, such as from sedimentary sources.

The main source of dFe to this region, during the productive season, is thought to be the continental margins, which accumulate sediments from riverine inputs and enrich the overlying water column in dFe. These iron-rich deposits are rich in organic compounds and have been shown to be a source of dFe and Fe-binding ligands to the overlying water column (Jones, Beckler and Taillefert, 2011; Homoky *et al.*, 2012; Bundy *et al.*, 2014; Boiteau *et al.*, 2019). Having collected fluvial sediments over the Winter season, the pronounced BBL is brought to the surface through strong upwelling close to the coast (several kilometers) and subsequently advected offshore in a coastal filament. Organic ligands from the high-Fe environment could aid in remobilizing and stabilizing BBL dFe, contributing to the bioavailability of this source for the downstream surface phytoplankton community. This general process is episodic and creates a region of Fe replete conditions near the coast, a transition zone from Fe replete to Fe depleted (Fe-limited), and oligotrophic waters further offshore (nitrate-limited).

The filament studies described in this thesis were conducted in June 2017 aboard the *R/V Roger Revelle* (P1706) and in August 2019 aboard the *R/V Atlantis* (P1908). The major goals of these studies were to determine the supply of subsurface BBL Fe, the subsequent lateral transport by a coastal filament, and the response of the phytoplankton community, which have

been the subjects of many, yet separate, studies in this region. *Work in this thesis will provide new insights into Fe biogeochemistry of the California Current through a holistic examination of cycling across a large Lagrangian spatial scale.*

1.4. Mechanistic role of iron-binding ligands

Heterotrophic bacteria associated with particles carry out remineralization of POM in the ocean. Remineralization converts POM back to soluble forms and strongly influences the vertical distribution of dissolved species. In HNLC regions, remineralized or recycled Fe can account for most of the biological supply (Boyd et al. 2010; Tagliabue, Aumont, and Bopp 2014). It was shown in a previous study that L_1 ligands were produced during the initial stages of remineralization of an induced bloom in bottle incubation experiments in the California Current Ecosystem (Hogle et al. 2016). Genomic analysis of the bacterial community revealed that the production of these ligands was correlated with the presence of copiotrophic bacteria, which have been shown to be enriched in their siderophore biosynthesis and organic-Fe uptake capabilities (Hogle *et al.*, 2016; Manck *et al.*, 2020). This suggests ligand production is an active strategy in the ocean for acquiring Fe from POM and that *copiotrophic bacteria play a disproportionate role in the marine biogeochemical cycle of Fe*. The parameterization of Fe remineralization will contribute greatly to Fe biogeochemical modeling efforts, which fail to accurately represent this process in the deep ocean (Völker and Tagliabue, 2015). Examination of the production of Fe-binding ligands in oceanic Fe remineralization and during phytoplankton blooms will elucidate how this process affects the oceanic vertical distribution of Fe and physicochemical forms of surbsurface sources of new dFe.

Bacteria that sense sinking concentrated organic matrices could release strong ligands to mobilize pFe into more labile forms. Fecal pellets are important model marine particles that can, at times, dominate the vertical flux of carbon. Other bioactive and scavenged elements, like Fe, could be removed from the surface by the production of fecal pellets by planktonic grazers, where

it is later remineralized deep in the water column or once sedimented. Concentrated in biomass, fecal pellets are hotspots of Fe and are quickly colonized by copiotrophic bacteria within the water column. To gain energy and essential nutrients for growth, bacteria respire POM and release dissolved species back into the water column (Azam, 1998; Azam and Malfatti, 2007).

Cabanes et al. (2017) conducted dark remineralization experiments on salp fecal pellets and detected elevated concentrations of L_2 ligands through the duration of the incubation. Though it was surprising that strong ligands were not detected, possibly because 0.2 µm filtered seawater was used for the experiment, which may exclude bacteria that might colonize sinking POM. In an analogous experiment, Velasquez et al. (2016) measured siderophores produced during the remineralization phase of phytoplankton biomass, but again, no L_1 ligands were detected electrochemically possibly because the voltammetric analyses did not target strong dFe-binding ligands. Given that no L_1 ligands were detected during remineralization in those studies, more mechanistic experiments, with careful considerations for experimental and analytical design, are needed to ascertain the role of strong dFe-binding ligands. The balance between the removal and remineralization processes sets the vertical distribution of bioactive and particle reactive elements.

Objectives of work in this thesis are to explore the patterns in presence of Fe-binding ligands in productive coastal systems and during a simulated bloom and subsequent remineralization. A link to the bacterial community to production and presence of specific ligand classes will be possible. One impasse is that electrochemical and data processing methods which allow for simultaneous detection of multiple ligand classes within seawater samples require analytical robustness. Therefore, novel methods for improved processing of multiple analytical window (MAW) electrochemical data are developed in this thesis. These MAW methods are then applied to environmental samples and incubation experiment samples to detect multiple classes of dFe-binding ligands. This advance will allow for a more accurate depiction of the dFe-binding ligand pool, and to better pinpoint the presence of the strongest (L_1) class of iron-binding ligands,

ultimately with the goal of interpreting these chemical signatures in the context of *in situ* biogeochemical conditions and cycling.

1.5. Thesis organization

Chapter 2 focuses on identifying important Fe sources to a heavily glaciated Antarctic fjord through an examination of seawater, glacial ice, and sediments. Another focus was to understand the physical drivers of Fe supply to the euphotic zone within the fjord and export downstream. This chapter has been published in *Biogeosciences* in 2021 (Forsch *et al.* 2021).

Chapter 3 examines Fe sources and supply for the first time associated with the cross-shore advection of upwelling coastal filaments in the southern California Current. Impacts on diatom physiology and export flux were also determined in the context of Fe-limitation indicators. This chapter will be submitted to *Limnology and Oceanography* in 2022.

Chapter 4 applies multiple analytical window CLE-ACSV analysis with simultaneous processing of data for the first time to seawater Fe organic speciation, by examining ligands in contrasting productive regions (Antarctic fjord, upwelling filament) and a simulated bloom experiment. This chapter includes multiple publications to be submitted in 2022.

1.6. Figures and Tables

Table 1.1 Analytical figures of merit show long-term precision for the duration of seawater analyses. The detection limit (DL) is calculated as 3 x the standard deviation (SD). In this case, the blank is acidified MilliQ (pH ~1.8). Reference standards are within consensus values (GSP 0.155 ±0.045 nmol Fe l^{-1}, SAFe D1 0.67 ±0.07 nmol Fe l^{-1}, GSC 1.535±0.115 nmol Fe l^{-1}) from Johnson et al. 2007 and latest compilation (geotraces.org).

	Blank	GSP	SAFe D1	GSC
Mean ±SD (nmol Fe l^{-1})	0.10 ±0.02	0.180 ±0.027	0.62 ±0.09	1.449 ±0.115
DL Mean (nmol Fe l^{-1})	0.07	0.08	0.09	0.35
RSD Mean (%)	15	5	14	6

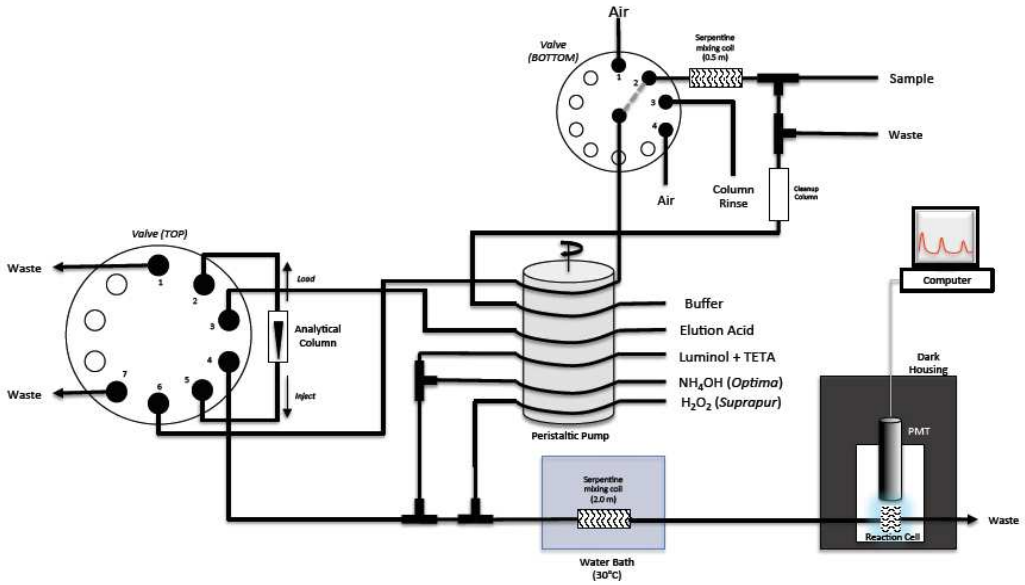

Figure 1.1 Schematic of the FI-CL manifold for the determination of Fe(III) with chemiluminescence.

1.7. References

Alderkamp, A. C., Mills, M. M., van Dijken, G. L., Laan, P., Thuróczy, C. E., Gerringa, L. J. A., de Baar, H. J. W., Payne, C. D., Visser, R. J. W., Buma, A. G. J. and Arrigo, K. R.: Iron from melting glaciers fuels phytoplankton blooms in the Amundsen Sea (Southern Ocean): Phytoplankton characteristics and productivity, Deep. Res. Part II Top. Stud. Oceanogr., 71–76, 32–48, doi:10.1016/j.dsr2.2012.03.005, 2012.

Annett, A. L., Skiba, M., Henley, S. F., Venables, H. J., Meredith, M. P., Statham, P. J. and Ganeshram, R. S.: Comparative roles of upwelling and glacial iron sources in Ryder Bay, coastal western Antarctic Peninsula, Mar. Chem., doi:10.1016/j.marchem.2015.06.017, 2015.

Azam, F.: Microbial control of oceanic carbon flux: The plot thickens, Science (80-.)., 280(5364), 694–696, doi:10.1126/science.280.5364.694, 1998.

Azam, F. and Malfatti, F.: Microbial structuring of marine ecosystems, Nat Rev Micro, 5(10), 782–791, 2007.

de Baar, H. J. W.: Synthesis of iron fertilization experiments: From the Iron Age in the Age of Enlightenment, J. Geophys. Res., 110(C9), C09S16, doi:10.1029/2004JC002601, 2005.

van den Berg, C. M. G.: The determination of trace metals in sea-water using cathodic stripping voltammetry, Sci. Total Environ., 49, 89–99, doi:10.1016/0048-9697(86)90233-0, 1986.

van den Berg, C. M. G.: Evidence for organic complexation of iron in seawater, Mar. Chem., 50(1–4), 139–157, doi:10.1016/0304-4203(95)00032-M, 1995.

Bhatia, M. P., Kujawinski, E. B., Das, S. B., Breier, C. F., Henderson, P. B. and Charette, M. a.: Greenland meltwater as a significant and potentially bioavailable source of iron to the ocean, Nat. Geosci., 6(4), 274–278, doi:10.1038/ngeo1746, 2013.

Biller, D. V. and Bruland, K. W.: The central California Current transition zone: A broad region exhibiting evidence for iron limitation, Prog. Oceanogr., 120, 370–382, doi:10.1016/j.pocean.2013.11.002, 2014.

Boiteau, R. M., Till, C. P., Coale, T. H., Fitzsimmons, J. N., Bruland, K. W. and Repeta, D. J.: Patterns of iron and siderophore distributions across the California Current System, Limnol. Oceanogr., 64(1), 376–389, doi:https://doi.org/10.1002/lno.11046, 2019.

Boyd, P. W. and Ellwood, M. J.: The biogeochemical cycle of iron in the ocean, Nat. Geosci., 3(10), 675–682, doi:10.1038/ngeo964, 2010.

Boyd, P. W., Law, C. S., Wong, C. S., Nojiri, Y., Tsuda, A., Levasseur, M., Takeda, S., Rivkin, R., Harrison, P. J., Strzepek, R., Gower, J., McKay, M., Abraham, E., Arychuk, M., Barwell-Clarke, J., Crawford, W., Crawford, D., Hale, M., Harada, K., Johnson, K., Kiyosawa, H., Kudo, I., Marchetti, A., Miller, W., Needoba, J., Nishioka, J., Ogawa, H., Page, J., Robert, M., Saito, H., Sastri, A., Sherry, N., Soutar, T., Sutherland, N., Taira, Y., Whitney, F., Wong, S.-K. E. and Yoshimura, T.: The decline and fate of an iron-induced subarctic phytoplankton bloom., Nature, 428(6982), 549–553, doi:10.1038/nature02437, 2004.

Boyd, P. W., Jickells, T., Law, C. S., Blain, S., Boyle, E. a, Buesseler, K. O., Coale, K. H., Cullen, J. J., de Baar, H. J. W., Follows, M., Harvey, M., Lancelot, C., Levasseur, M., Owens, N. P. J., Pollard, R., Rivkin, R. B., Sarmiento, J., Schoemann, V., Smetacek, V., Takeda, S., Tsuda, a, Turner, S. and Watson, a J.: Mesoscale iron enrichment experiments 1993-2005: synthesis and future directions., Science, 315(5812), 612–617, doi:10.1126/science.1131669, 2007.

Boyd, P. W., Ibisanmi, E., Sander, S. G., Hunter, K. A. and Jackson, G. A.: Remineralization of upper ocean particles: Implications for iron biogeochemistry, Limnol. Oceanogr., 55(3), 1271–1288, doi:10.4319/lo.2010.55.3.1271, 2010.

Boyd, P. W., Ellwood, M. J., Tagliabue, A. and Twining, B. S.: Biotic and abiotic retention, recycling and remineralization of metals in the ocean, Nat. Geosci., 10(3), 167–173, doi:10.1038/ngeo2876, 2017.

Boyle, E. A., Edmond, J. M. and Sholkovitz, E. R.: The mechanism of iron removal in estuaries, Geochim. Cosmochim. Acta, 41(9), 1313–1324, doi:http://dx.doi.org/10.1016/0016-7037(77)90075-8, 1977.

Brzezinski, M. A.: THE Si:C:N RATIO OF MARINE DIATOMS: INTERSPECIFIC VARIABILITY AND THE EFFECT OF SOME ENVIRONMENTAL VARIABLES1, J. Phycol., 21(3), 347–357, doi:https://doi.org/10.1111/j.0022-3646.1985.00347.x, 1985.

Buck, K. N. and Bruland, K. W.: The physicochemical speciation of dissolved iron in the Bering Sea, Alaska, Limnol. Oceanogr., 52(5), 1800–1808, doi:DOI 10.4319/lo.2007.52.5.1800, 2007.

Buck, K. N., Sohst, B. and Sedwick, P. N.: The organic complexation of dissolved iron along the

U.S. GEOTRACES (GA03) North Atlantic Section, Deep Sea Res. Part II Top. Stud. Oceanogr., 116, 152–165, doi:https://doi.org/10.1016/j.dsr2.2014.11.016, 2015.

Buck, K. N., Sedwick, P. N., Sohst, B. and Carlson, C. A.: Organic complexation of iron in the eastern tropical South Pacific: Results from US GEOTRACES Eastern Pacific Zonal Transect (GEOTRACES cruise GP16), Mar. Chem., 201, 229–241, doi:https://doi.org/10.1016/j.marchem.2017.11.007, 2018.

Bundy, R. M., Biller, D. V, Buck, K. N., Bruland, K. W. and Barbeau, K. A.: Distinct pools of dissolved iron-binding ligands in the surface and benthic boundary layer of the California Current, Limnol. Oceanogr., 59(3), 769–787, doi:10.4319/lo.2014.59.3.0769, 2014.

Cook, A. J., Holland, P. R., Meredith, M. P., Murray, T., Luckman, A. and Vaughan, D. G.: Ocean forcing of glacier retreat in the western Antarctic Peninsula, Science (80-.)., 353(6296), 1261–1273, doi:10.1126/science.aae0017, 2016.

Couto, N., Martinson, D. G., Kohut, J. and Schofield, O.: Distribution of Upper Circumpolar Deep Water on the warming continental shelf of the West Antarctic Peninsula, J. Geophys. Res. Ocean., 122(7), 5306–5315, doi:10.1002/2017JC012840, 2017.

Elrod, V. A., Berelson, W. M., Coale, K. H. and Johnson, K. S.: The flux of iron from continental shelf sediments: A missing source for global budgets, Geophys. Res. Lett., 31(12), doi:https://doi.org/10.1029/2004GL020216, 2004.

Fitzsimmons, J. N., John, S. G., Marsay, C. M., Hoffman, C. L., Nicholas, S. L., Toner, B. M., German, C. R. and Sherrell, R. M.: Iron persistence in a distal hydrothermal plume supported by dissolved-particulate exchange, Nat. Geosci, 10(3), 195–201, 2017.

Gledhill, M. and Buck, K. N.: The organic complexation of iron in the marine environment: a review, Front. Microbiol., 3, 69, doi:10.3389/fmicb.2012.00069, 2012.

Hassler, C. S., van den Berg, C. M. G. and Boyd, P. W.: Toward a Regional Classification to Provide a More Inclusive Examination of the Ocean Biogeochemistry of Iron-Binding Ligands, Front. Mar. Sci., 4, 19, doi:10.3389/fmars.2017.00019, 2017.

Hodson, A., Nowak, A. and Christiansen, H.: Glacial and periglacial floodplain sediments regulate hydrologic transfer of reactive iron to a high arctic fjord, Hydrol. Process., 30(8), 1219–1229, doi:10.1002/hyp.10701, 2016.

Hodson, A., Nowak, A., Sabacka, M., Jungblut, A., Navarro, F., Pearce, D., Ávila-Jiménez, M. L., Convey, P. and Vieira, G.: Climatically sensitive transfer of iron to maritime Antarctic ecosystems by surface runoff, , 8, 14499, 2017.

Hogle, S. L., Bundy, R. M., Blanton, J. M., Allen, E. E. and Barbeau, K. A.: Copiotrophic marine bacteria are associated with strong iron-binding ligand production during phytoplankton blooms, Limnol. Oceanogr. Lett., 1(1), 36–43, doi:https://doi.org/10.1002/lol2.10026, 2016a.

Hogle, S. L., Thrash, J. C., Dupont, C. L. and Barbeau, K. A.: Trace metal acquisition by marine heterotrophic bacterioplankton with contrasting trophic strategies, Appl. Environ. Microbiol., 82(5), 1613–1624, doi:10.1128/aem.03128-15, 2016b.

Homoky, W. B., Severmann, S., McManus, J., Berelson, W. M., Riedel, T. E., Statham, P. J. and Mills, R. A.: Dissolved oxygen and suspended particles regulate the benthic flux of iron from continental margins, Mar. Chem., 134(Supplement C), 59–70, doi:https://doi.org/10.1016/j.marchem.2012.03.003, 2012.

Hopwood, M. J., Connelly, D. P., Arendt, K. E., Juul-Pedersen, T., Stinchcombe, M., Meire, L., Esposito, M. and Krishna, R.: Seasonal changes in Fe along a glaciated Greenlandic fjord. , Front. Earth Sci. , 4(March), 1–13, doi:10.3389/feart.2016.00015, 2016.

Hutchins, D. a and Bruland, K. W.: Iron-limited diatom growth and Si : N uptake ratios in a coastal upwelling regime, Nature, 393(June), 561–564, doi:Doi 10.1038/31203, 1998.

Jickells, T. D.: Global Iron Connections Between Desert Dust, Ocean Biogeochemistry, and Climate, Science (80-.)., 308(5718), 67–71, doi:10.1126/science.1105959, 2005.

Johnson, K. S., Michael Gordon, R. and Coale, K. H.: What controls dissolved iron concentrations in the world ocean?, Mar. Chem., 57(3–4), 137–161, doi:10.1016/S0304-4203(97)00043-1, 1997.

Jones, M. E., Beckler, J. S. and Taillefert, M.: The flux of soluble organic-iron(III) complexes from sediments represents a source of stable iron(III) to estuarine waters and to the continental shelf, Limnol. Oceanogr., 56(5), 1811–1823, doi:10.4319/lo.2011.56.5.1811, 2011.

De Jong, J. T. M., Stammerjohn, S. E., Ackley, S. F., Tison, J.-L., Mattielli, N. and Schoemann, V.: Sources and fluxes of dissolved iron in the Bellingshausen Sea (West Antarctica): The importance of sea ice, icebergs and the continental margin, Mar. Chem., 177, 518–535, doi:https://doi.org/10.1016/j.marchem.2015.08.004, 2015.

King, A. L.: Evidence for phytoplankton iron limitation in the southern California Current System , Mar. Ecol. Prog. Ser., 342, 91–103 [online] Available from: https://www.int-res.com/abstracts/meps/v342/p91-103/, 2007.

King, A. L. and Barbeau, K. A.: Dissolved iron and macronutrient distributions in the southern California Current System, J. Geophys. Res., 116, doi:10.1029/2010jc006324, 2011.

King, A. L., Buck, K. N. and Barbeau, K. A.: Quasi-Lagrangian drifter studies of iron speciation and cycling off Point Conception, California, Mar. Chem., 128, 1–12, doi:10.1016/j.marchem.2011.11.001, 2012.

Laglera, L. M. and van den Berg, C. M. G.: Evidence for geochemical control of iron by humic substances in seawater, Limnol. Oceanogr., 54(2), 610–619, doi:10.4319/lo.2009.54.2.0610, 2009.

Laglera, L. M., Battaglia, G. and van den Berg, C. M. G.: Determination of humic substances in natural waters by cathodic stripping voltammetry of their complexes with iron, Anal. Chim. Acta, 599(1), 58–66, doi:10.1016/j.aca.2007.07.059, 2007.

Lam, P. J. and Bishop, J. K. B.: The continental margin is a key source of iron to the HNLC North Pacific Ocean, Geophys. Res. Lett., 35(7), doi:10.1029/2008GL033294, 2008.

Lannuzel, D., Schoemann, V., de Jong, J., Tison, J. L. and Chou, L.: Distribution and

biogeochemical behaviour of iron in the East Antarctic sea ice, Mar. Chem., 106(1-2 SPEC. ISS.), 18–32, doi:10.1016/j.marchem.2006.06.010, 2007.

Liu, X. and Millero, F. J.: The solubility of iron in seawater, Mar. Chem., 77(1), 43–54, doi:https://doi.org/10.1016/S0304-4203(01)00074-3, 2002.

Lyons, W. B., Dailey, K. R., Welch, K. A., Deuerling, K. M., Welch, S. A. and McKnight, D. M.: Antarctic streams as a potential source of iron for the Southern Ocean, Geology, 43(11), 1003–1006, 2015.

Manck, L. E., Espinoza, J. L., Dupont, C. L. and Barbeau, K. A.: Transcriptomic Study of Substrate-Specific Transport Mechanisms for Iron and Carbon in the Marine Copiotroph Alteromonas macleodii , mSystems, doi:10.1128/msystems.00070-20, 2020.
Markussen, T. N., Elberling, B., Winter, C. and Andersen, T. J.: Flocculated meltwater particles control Arctic land-sea fluxes of labile iron, Sci. Rep., 6, 24033, doi:10.1038/srep24033, 2016.

Mawji, E., Gledhill, M., Milton, J. A., Tarran, G. A., Ussher, S., Thompson, A., Wolff, G. A., Worsfold, P. J. and Achterberg, E. P.: Hydroxamate siderophores: Occurrence and importance in the Atlantic Ocean, Environ. Sci. Technol., 42(23), 8675–8680, doi:10.1021/es801884r, 2008.

Meredith, M. P., Stammerjohn, S. E., Venables, H. J., Ducklow, H. W., Martinson, D. G., Iannuzzi, R. A., Leng, M. J., van Wessem, J. M., Reijmer, C. H. and Barrand, N. E.: Changing distributions of sea ice melt and meteoric water west of the Antarctic Peninsula, Deep Sea Res. Part II Top. Stud. Oceanogr., doi:10.1016/j.dsr2.2016.04.019, 2016.

Meredith, M. P., Stefels, J. and van Leeuwe, M.: Marine studies at the western Antarctic Peninsula: Priorities, progress and prognosis, Deep. Res. Part II Top. Stud. Oceanogr., 139, 1–8, doi:10.1016/j.dsr2.2017.02.002, 2017.

Moore, J. K. and Doney, S. C.: Iron availability limits the ocean nitrogen inventory stabilizing feedbacks between marine denitrification and nitrogen fixation, Global Biogeochem. Cycles, 21(2), doi:10.1029/2006GB002762, 2007.

Moore, J. K., Doney, S. C., Glover, D. M. and Fung, I. Y.: Iron cycling and nutrient-limitation patterns in surface waters of the world ocean, Deep. Res. Part II Top. Stud. Oceanogr., doi:10.1016/S0967-0645(01)00109-6, 2001.

Morel, F. M. M. and Price, N. M.: The biogeochemical cycles of trace metals in the ocean, Science (80-.)., 300(5621), 944–947, doi:10.1126/science.1083545, 2003.

Morel, F. M. M., Milligan, A. J. and Saito, M. A.: Marine Bioinorganic Chemistry: The Role of Trace Metals in the Oceanic Cycles of Major Nutrients, in Treatise on Geochemistry: Second Edition, vol. 8, pp. 123–150., 2013.

Omanović, D., Garnier, C. and Pižeta, I.: ProMCC: An all-in-one tool for trace metal complexation studies, Mar. Chem., 173, 25–39, doi:https://doi.org/10.1016/j.marchem.2014.10.011, 2015.

Planquette, H., Sherrell, R. M., Stammerjohn, S. and Field, M. P.: Particulate iron delivery to the water column of the Amundsen Sea, Antarctica, Mar. Chem., doi:10.1016/j.marchem.2013.04.006, 2013.

Price, N. M., Andersen, L. F. and Morel, F. M. M.: Iron and nitrogen nutrition of equatorial Pacific plankton, Deep Sea Res. Part A. Oceanogr. Res. Pap., 38(11), 1361–1378, doi:10.1016/0198-0149(91)90011-4, 1991.

Raiswell, R. and Canfield, D. E.: The Iron Biogeochemical Cycle Past and Present, Geochemical Perspect., 1(1), 1–220, doi:10.7185/geochempersp.1.1, 2012.

Rue, E. L. and Bruland, K. W.: Complexation of iron(III) by natural organic ligands in the Central North Pacific as determined by a new competitive ligand equilibration/adsorptive cathodic stripping voltammetric method, Mar. Chem., 50(1–4), 117–138, doi:10.1016/0304-4203(95)00031-L, 1995.

Saito, M. A., Noble, A. E., Tagliabue, A., Goepfert, T. J., Lamborg, C. H. and Jenkins, W. J.: Slow-spreading submarine ridges in the South Atlantic as a significant oceanic iron source, Nat. Geosci., 6(9), 775–779, doi:10.1038/ngeo1893, 2013.

Sander, S. G. and Koschinsky, A.: Metal flux from hydrothermal vents increased by organic complexation, Nat. Geosci., 4(3), 145–150, doi:10.1038/ngeo1088, 2011.

Sato, M., Takeda, S. and Furuya, K.: Iron regeneration and organic iron(III)-binding ligand production during in situ zooplankton grazing experiment, Mar. Chem., 106(3), 471–488, doi:http://dx.doi.org/10.1016/j.marchem.2007.05.001, 2007.

Schroth, A. W., Crusius, J., Chever, F., Bostick, B. C. and Rouxel, O. J.: Glacial influence on the geochemistry of riverine iron fluxes to the Gulf of Alaska and effects of deglaciation, Geophys. Res. Lett., 38(16), doi:10.1029/2011GL048367, 2011.

Schroth, A. W., Crusius, J., Hoyer, I. and Campbell, R.: Estuarine removal of glacial iron and implications for iron fluxes to the ocean, Geophys. Res. Lett., 41(11), 3951–3958, doi:10.1002/2014GL060199, 2014.

Smith Jr., K. L., Robison, B. H., Helly, J. J., Kaufmann, R. S., Ruhl, H. A., Shaw, T. J., Twining, B. S., Vernet, M., Smith, K. L., Robison, B. H., Helly, J. J., Kaufmann, R. S., Ruhl, H. A., Shaw, T. J., Twining, B. S. and Vernet, M.: Free-drifting icebergs: hot spots of chemical and biological enrichment in the Weddell Sea., Science, 317(5837), 478–482, doi:10.1126/science.1142834, 2007.

Steig, E. J. and Orsi, A. J.: The heat is on in Antarctica, Nat. Geosci., 6(February), 6–8, doi:10.1038/ngeo1717, 2013.

Stevenson, E. I., Fantle, M. S., Das, S. B., Williams, H. M. and Aciego, S. M.: The iron isotopic composition of subglacial streams draining the Greenland ice sheet, Geochim. Cosmochim. Acta, 213, 237–254, doi:https://doi.org/10.1016/j.gca.2017.06.002, 2017.

Stolpe, B. and Hassellöv, M.: Nanofibrils and other colloidal biopolymers binding trace elements in coastal seawater: Significance for variations in element size distributions, Limnol. Oceanogr., 55(1), 187–202, doi:10.4319/lo.2010.55.1.0187, 2010.

Sunda, W. G. and Huntsman, S. a: Interrelated influence of iron, light and cell size on marine phytoplankton growth, Nature, 390(6658), 389–392, doi:10.1038/37093, 1997.

Tagliabue, A., Aumont, O. and Bopp, L.: The impact of different external sources of iron on the global carbon cycle, Geophys. Res. Lett., 41(3), 920–926, doi:10.1002/2013GL059059, 2014.

Thuróczy, C.-E., Gerringa, L. J. A., Klunder, M. B., Middag, R., Laan, P., Timmermans, K. R. and de Baar, H. J. W.: Speciation of Fe in the Eastern North Atlantic Ocean, Deep Sea Res. Part I Oceanogr. Res. Pap., 57(11), 1444–1453, doi:10.1016/j.dsr.2010.08.004, 2010.

Thuróczy, C. E., Alderkamp, A. C., Laan, P., Gerringa, L. J. A., Mills, M. M., Van Dijken, G. L., De Baar, H. J. W. and Arrigo, K. R.: Key role of organic complexation of iron in sustaining phytoplankton blooms in the Pine Island and Amundsen Polynyas (Southern Ocean), Deep. Res. Part II Top. Stud. Oceanogr., doi:10.1016/j.dsr2.2012.03.009, 2012.

Völker, C. and Tagliabue, A.: Modeling organic iron-binding ligands in a three-dimensional biogeochemical ocean model, Mar. Chem., 173, 67–77, doi:https://doi.org/10.1016/j.marchem.2014.11.008, 2015.

Weber, T., Cram, J. A., Leung, S. W., DeVries, T. and Deutsch, C.: Deep ocean nutrients imply large latitudinal variation in particle transfer efficiency, Proc. Natl. Acad. Sci., 113(31), 8606–8611, doi:10.1073/pnas.1604414113, 2016.

Wehrmann, L. M., Formolo, M. J., Owens, J. D., Raiswell, R., Ferdelman, T. G., Riedinger, N. and Lyons, T. W.: Iron and manganese speciation and cycling in glacially influenced high-latitude fjord sediments (West Spitsbergen, Svalbard): Evidence for a benthic recycling-transport mechanism, Geochim. Cosmochim. Acta, doi:10.1016/j.gca.2014.06.007, 2014.

Wu, J. and Luther, G. W.: Complexation of Fe(III) by natural organic ligands in the Northwest Atlantic Ocean by a competitive ligand equilibration method and a kinetic approach, Mar. Chem., 50(1–4), 159–177, doi:10.1016/0304-4203(95)00033-N, 1995.

Zhang, R., John, S. G., Zhang, J., Ren, J., Wu, Y., Zhu, Z., Liu, S., Zhu, X., Marsay, C. M. and Wenger, F.: Transport and reaction of iron and iron stable isotopes in glacial meltwaters on Svalbard near Kongsfjorden: From rivers to estuary to ocean, Earth Planet. Sci. Lett., 424, 201–211, 2015.

Chapter 2. Seasonal dispersal of fjord meltwaters as an important source of iron and manganese to coastal Antarctic phytoplankton

2.1. Abstract

Glacial meltwater from the western Antarctic Ice Sheet is hypothesized to be an important source of cryospheric iron, fertilizing the Southern Ocean, yet its trace metal composition and factors that control its dispersal remain poorly constrained. Here we characterize meltwater iron sources in a heavily glaciated western Antarctic Peninsula (WAP) fjord. Using dissolved and particulate ratios of manganese-to-iron in meltwaters, porewaters, and seawater, we show that surface glacial melt and subglacial plumes contribute to the seasonal cycle of iron and manganese within a fjord still relatively unaffected by climate change-induced glacial retreat. Organic ligands derived from the phytoplankton bloom and the glaciers bind dissolved iron and facilitate the solubilization of particulate iron downstream. Using a numerical model, we show that buoyant plumes generated by outflow from the subglacial hydrologic system, enriched in labile particulate trace metals derived from a chemically-modified crustal source, can supply iron to the fjord euphotic zone through vertical mixing, and that prolonged katabatic wind events enhance export of meltwater out of the fjord. Thus, we identify an important atmosphere-ice-ocean coupling intimately tied to coastal iron biogeochemistry and primary productivity along the WAP.

2.2. Introduction

Warm atmospheric temperatures are accelerating glacial retreat and increasing meltwater discharge, rapidly changing Earth's cryosphere (Rignot *et al.*, 2013; Mouginot *et al.*, 2019). Ranging from diffuse flows to waterfalls and streams, cryospheric meltwaters deliver dissolved and particulate material, altering coastal ocean biogeochemistry. Glacial meltwater enters the ocean through surface runoff, direct melting of glacial ice (including icebergs), and discharge from liquid water reservoirs beneath glaciers, carrying iron (Fe) and other trace metals weathered from

continental crust. In the surface ocean, the delivery of new Fe is critical for the growth of phytoplankton; and when enhanced, naturally or artificially, primary production increases and potentially carbon export (Boyd *et al.*, 2019). However, direct measurements of Fe in heavily glaciated fjords reveal that up to 90-99% of dissolved Fe (dFe) originating from glaciers is removed upon mixing with seawater due to estuarine-type removal processes, including: precipitation of insoluble oxyhydroxides, adsorption to the surfaces of existing particles, and aggregation of colloids and particles (Boyle, Edmond and Sholkovitz, 1977; Schroth *et al.*, 2014). Together, these processes are known as scavenging and constitute a major control on the distribution of Fe in the ocean by converting soluble forms of Fe into colloidal aggregates and particles (Wu *et al.* 2001). Constraints on the flux of newly delivered glacial Fe that escapes this sink and is transported across continental shelves will enable better predictions of open ocean primary production and carbon sequestration, especially in oceanic regimes where Fe is a limiting nutrient. Given that recent studies revealed a critical role for manganese (Mn) in co-limiting primary production in coastal Antarctica and the core of the ACC (Wu *et al.*, 2019; Browning *et al.*, 2021), an investigation of Mn delivery by glacial meltwaters is also needed (Bown *et al.*, 2018). Currently, very little is known about how glacial meltwaters affect marine Mn cycling.

Evidence for Fe delivery from the cryosphere is historically based on geochemical analysis of endmember glacial discharge (Hawkings *et al.,* 2014; Raiswell and Canfield 2012; Hodson *et al.,* 2017; Hawkings *et al.,* 2020), and discrete sampling of glacial ice (e.g. Hopwood *et al.* 2018) and seawater adjacent to marine-terminating glaciers and ice sheets (Hopwood *et al.,* 2016; Annett *et al.,* 2015; Gerringa *et al.,* 2015; Alderkamp *et al.,* 2012; Sherrell *et al.,* 2018). Trace metal studies at the ice-ocean interface have been conducted previously in fjords experiencing intense seasonal melt, such as in Alaska, Greenland, and Svalbard (Schroth *et al.*, 2014; Zhang *et al.*, 2015; Hopwood *et al.*, 2016; Kanna *et al.*, 2020). These temperate and high Arctic coastal waters are experiencing large freshwater and sediment fluxes as a result of increased glacial discharge, that in turn creates extreme physical and geochemical gradients. Ultimately, such

dramatic changes in turbidity decrease light availability while strong stratification reduces macronutrient supply to local primary producers (Meire *et al.*, 2017; Holding *et al.*, 2019). Even with high particulate and dissolved Fe contents, meltwaters from these fjords do not feed directly into offshore waters without undergoing significant scavenging, mixing and dilution (Hopwood *et al.*, 2015), bringing into question the effectiveness with which glacial meltwater-derived Fe may fertilize the surrounding ocean.

In Antarctica, fjords are less well-studied than their Arctic counterparts, but are also locations of intense seasonal blooms with comparable or higher primary production relative to the adjacent continental shelves, and high sequestration efficiencies of organic carbon (Vernet *et al.*, 2008; Grange and Smith 2013; Taylor *et al.*, 2020). Along the western Antarctic Peninsula (WAP), 674 marine-terminating glaciers drain into the coastal ocean, primarily in fjords (Cook *et al.*, 2016). The vast majority of these marine-terminating glaciers are retreating due to intrusions of warm deep water from the shelf, but many still remain as 'cold-water' glaciers (that is, local ocean temperatures are too cold to melt the glacier terminus), particularly in the northern WAP where Weddell Water from the eastern side advects and mixes into the Bransfield Strait (Pritchard and Vaughan, 2007; Cook *et al.*, 2016). These glaciers are thought to have relatively small subglacial meltwater discharge, with suspended sediment signatures that spread laterally in the coastal ocean (Domack and Ishman, 1993; Domack and Williams, 2011). This makes cold glacio-marine Antarctic fjords unique locations for sampling subglacial discharge with minimal dilution by ambient seawater.

Subglacial environments distinguish themselves from other cryospheric sources of Fe to the oceanic euphotic zone. Within the subglacial cavity, anoxia develops due to enhanced microbial respiration processes, high weathering rates, and limited diffusion of oxygen and exchange with the coastal ocean (Mikucki *et al.*, 2009). The result is increased solubility of iron as Fe(II), and other redox sensitive elements, such as Mn. Meltwater discharge from beneath marine-terminating glaciers enters the ocean in the subsurface but may be mixed into the surface

because of the positive buoyancy of meltwater-seawater mixtures. Enhanced vertical shear occurs episodically in the Antarctic coastal ocean as cooled dense parcels of air accelerate down ice sheets, generating the strongest coastal winds on Earth (>30 m s^{-1}), near the coast. These episodic katabatic wind events could also be important for enhancing the supply of subsurface meltwaters to the surface (Jackson *et al.*, 2014; Lundesgaard *et al.*, 2019). The subglacial meltwater source represents a large uncertainty in the supply of cryospheric Fe to the ocean given the challenge of acquiring samples of this reservoir directly or with minimal alteration, particularly in Arctic environments with intense seasonal melt flows and associated sediment turbidity (Straneo and Cenedese, 2015).

We present trace metal results from two expeditions (December 2015 and April 2016) to Andvord Bay, a cold glacio-marine fjord located mid-latitude along the WAP. This study is part of the FjordEco project which assessed the ecosystem function and seasonality of Andvord Bay (Pan *et al.*, 2019; Pan *et al.*, 2020; Ziegler *et al.*, 2020; Eidam *et al.*, 2019; Lundesgaard *et al.*, 2020, 2019; Hahn-Woernle *et al.*, 2020). The WAP is host to the most extensive collection of glaciomarine fjords on the Antarctic continent, and its shelf waters are subject to ongoing biogeochemical and ecological alteration linked to large-scale changes to the western Antarctic Ice Sheet (Henley *et al.*, 2020). We present a detailed and unprecedented picture of fjord Fe and Mn biogeochemistry and seasonality in the early stages of glacier retreat associated with recent climate change (Pritchard and Vaughan, 2007).

2.3. Methods

2.3.1. Oceanographic setting and sampling

Andvord Bay is a glacio-marine fjord located mid-latitude along the west Antarctic Peninsula (WAP). This site was chosen because it has been identified as a productivity “hotspot” (Grange and Smith, 2013), and because of its proximity to long-standing ecological research programs (Palmer Long Term Ecological Research program). This location is characterized by

converging deep water masses with distinct physical properties (relatively warm modified Upper Circumpolar Deep Water, cold Weddell Water**)**. Bordering Andvord Bay are 11 marine-terminating glaciers (Fig. 2.1) with Moser and Bagshawe glaciers responsible for the majority of the solid ice flux. These glaciers are cold-water (-1 to -0.5 °C) resulting in weak meltwater signatures within the fjord (Lundesgaard *et al.*, 2020). Observations and sampling of Andvord Bay were conducted during two cruises as part of the FjordEco program: LMG15-10 from 27 November to 22 December 2015 (late Spring) on R/V *Laurence M. Gould*, NBP16-03 from 4 April to 26 April (Fall) aboard R/V *Nathaniel B. Palmer*. On December 11, 2015 a strong katabatic wind event, with peak along-fjord velocities of 30 m s^{-1}, was observed and lasted for 5 days. Atmospheric observations by two automatic weather stations (Neko Harbor, Useful Island) recorded episodes of high velocity katabatic winds between field seasons, showing that these are common events in this study region.

A total of 18 stations per season were sampled for Fe geochemical variables using acid-cleaned 12 L GO-Flo bottles (General Oceanics) suspended in series on a clean hydroline (Amsteel) and triggered with acid-cleaned Teflon messengers designed by Ken Bruland (UC Santa Cruz). This sampling effort coincided with concurrent CTD stations. Once on board, GO-Flo bottle tops and bottoms were covered with plastic and placed on a wooden rack located within the trace metal clean shipboard plastic "bubble", which was positively-pressurized with HEPA-filtered air. Samples for dFe analysis were pressure-filtered (N_2 gas, 99.99%) directly from GO-Flo bottles through 0.2 μm Acropak 200 capsule filters (VWR International), into low-density polyethylene bottles (Nalgene) and acidified to pH 1.7 to 1.8 using HCl (Optima grade, Fisher Scientific). Samples for Fe-binding ligands were similarly filtered in-line but collected in fluorinated high-density polyethylene (Nalgene) bottles, unacidified, and frozen at -20ºC until laboratory analysis back on land. In brief, sample bottles were soaked in a soap detergent overnight with heat applied (60ºC), followed by a one-week soak in 3N HNO_3 (trace metal grade) at room temperature, and finally, a one-week soak in a 3N HCl (trace metal grade) bath at room

temperature. Rinsing with ultrapure MilliQ water occurred after each step. This sampling protocol followed established trace-metal clean methods to the standards of the GEOTRACES program to avoid metal contamination. In addition to the filtered samples, unfiltered seawater was sampled directly from the GO-Flo bottles and acidified to pH 1.8 and stored for >6 months (up to 2 years) and vacuum-filtered prior to analysis using acid-cleaned 0.4 μm polycarbonate (PC) filters in a Teflon filtration apparatus to determine total dissolvable Fe (TDFe). Labile particulate Fe (LpFe) is calculated as the difference between TDFe and dFe. Particulate samples were collected on 0.4 μm PC filters and stored at -20°C until complete digestion using an HNO_3/HF mixture. The digestion method employed is described in Planquette and Sherrell (2013) and is widely used in the GEOTRACES program (Cutter and Bruland, 2012; Fitzsimmons *et al.*, 2017) .

Acute attention to cleanliness was applied when sampling icebergs during small boat deployments in the fjord. Floating icebergs were sampled using a clean stainless-steel pickaxe and rust-free stainless-steel screwdriver and plastic mallet for chiseling pieces of ice. Samples were collected by slowly (engine idled) approaching the target piece of floating ice from downwind, limiting the chance of engine exhaust contamination. Each piece of ice was collected above freeboard (sea surface), to reduce the chance the ice was altered by seawater and rinsed with MilliQ prior to placing into acid-cleaned 2 gallon Ziploc polyethylene bags and storing at -4°C until sample processing. Prior to filtration, ice samples were removed from the freezer and left to melt at ambient shipboard temperatures. Once completely melted, a small incision was made on the Ziploc bags using a clean stainless-steel razor and contents poured into the Teflon filtration manifold or directly into sample bottles, thus collecting samples for dissolved, total dissolvable and particulate trace metal fractions.

2.3.2. Trace metal concentrations

Stored acidified filtered seawater samples were analyzed for Fe at Scripps Institution of Oceanography using flow injection with chemiluminescence methods described by Lohan *et al.* (Lohan, Aguilar-Islas and Bruland, 2006). Dissolved Fe in the samples was oxidized to iron(III) for 1 h with 10 mM Q-H_2O_2 (Suprapur grade), buffered in-line with ammonium acetate to pH ~3.5 and pre-concentrated and matrix removed on a chelating column packed with a resin (Toyopearl® AF-Chelate-650M). Dissolved Fe was eluted from the column using 0.14 M HCl (Optima grade, Fisher Scientific) and the chemiluminescence was recorded by a photomultiplier tube (PMT, Hamamatsu Photonics). The manifold was modified based on Lohan *et al*. (2006). Standardization of Fe was carried out with a matrix-matched standard curve (0, 0.4, 0.8, 3.2, 10 nmol kg^{-1} added high purity Fe metal ICP spectrometry standard in 2% HNO_3) using 0.34 nM Pacific surface seawater. Standards were treated identically to samples. Accuracy was assessed by repeated measurements of GEOTRACES coastal and Pacific Ocean reference seawater samples. Our measurements of GSC gave Fe = 1.391±0.115 (*n* = 19, over a three-month period, consensus 1.535±0.115). Our measurements of GSP gave Fe = 0.164±0.024 (*n* = 8, over a one-month period, consensus 0.155±0.045). Consensus values are from the most recent July 2019 compilation (geotraces.org). Precision, determined by replicated analyses of an in-house large-volume reference seawater sample within each analytical session, was typically ±5% or better. For the duration of these analyses, the average limit of detection (defined as 3x the standard deviation of the blank) was 0.036 (*n* = 10).

A subset of the seawater samples and all freshwater samples were run for Fe and Mn at Rutgers University using isotope dilution-inductively coupled plasma mass spectrometry (ICP-MS) methods based on Lagerström *et al.* (2013) and similar to those described in Annett *et al.* (2017). Briefly, 10 mL aliquots of seawater samples were extracted using a commercially available automated SeaFAST pico system (Elemental Scientific, Inc.) after online buffering to pH

approximately 6.5 using ammonium acetate buffer, achieving a 25-fold pre-concentration after column elution in 0.4 mL 1.6 M ultrapure nitric acid (Optima grade, Fisher Scientific)(Lagerström *et al.*, 2013). Isotope dilution was used to standardize Fe, while Mn was standardized using external matrix-matched standard treated identically to samples. The analysis of the concentrate was performed on an Element 2 sector-field ICP-MS (Thermo Fisher Scientific). Accuracy and precision (±3%, 1SD, for Fe and Mn) was assessed by repeated measurements of in-house large-volume reference seawater samples within each analytical session. Blanks averaged 51 pmol kg^{-1} for Fe (n = 59; limit of detection, or LOD = 48 pmol kg^{-1}) and 4 pmol kg^{-1} for Mn (n = 69; LOD = 4 pmol kg^{-1}) for all analytical runs. A comparison of the seawater analysis methods employed here is shown in Fig. A1. In general, there is good agreement (average 11% and 6% difference late Spring and Fall, respectively) between the chemiluminescence and ICP-MS methods, comparable to the uncertainty of GEOTRACES consensus values from the intercalibration of 13 trace metal laboratories (for Fe, RSD 10%, https://www.geotraces.org/standards-and-reference-materials/). Total dissolvable trace metals and particle digests, including freshwater dissolved metals (i.e., glacial melt), were analyzed using direct-injection ICP-MS methods using external standards and added In as a matrix and instrument drift corrector for the quantification of particulate Fe, Mn, aluminum (Al), and titanium (Ti) concentrations (Annett *et al.*, 2017).

2.3.3. Sediment cores and diffusive flux

Cores for this study were collected using a 12-barrel Megacore multi-coring device aboard the R/V *Nathaniel B. Palmer* cruise NBP16-01 in January 2016. Multiple barrels were sampled from a single Megacore deployment. See Taylor *et al.* (2020) for a complete account of coring efforts and Komada *et al.* (2016) for a description of the pore water sampling procedures. Porewater dFe and dMn was determined colorimetrically using the ferrozine and formaldoxime techniques, respectively (Armstrong, Lyons and Gaudette, 1979; Burdige and Komada, 2020). For dFe, hydroxylamine-HCl (0.2% v/v final concentration) was added to the samples before

analysis, to reduce any dissolved Fe(III) in the samples to Fe(II). For dMn, a hydroxylamine solution was added to an acidified (pH ~1-2) sample, and an EDTA solution was added to remove interference from a colored Fe complex. Porewater oxygen concentrations were measured using a polarographic microelectrode (Brendel and Luther 1995; Luther *et al.* 1998, 2008). A sequential extraction technique (Poulton and Canfield, 2005; Goldberg *et al.*, 2012) was used to determine sediment Fe speciation for the following fractions: Fe_{ox} (highly reactive, poorly crystalline iron oxides), Fe_{mag} (magnetite), Fe_{prs} (Fe in poorly reactive sheet silicates), Fe_T (total sediment Fe), Fe_{pyr} (Fe in pyrite), and finally Fe_U (unreactive pool under all treatments = Fe_T – (Fe_{ox} + Fe_{mag} + Fe_{prs} + Fe_{pyr})). All extracts were analyzed for Fe by flame Atomic Absorption Spectrometry (for details see Burdige and Komada 2020).

In this study, we investigate the potential for efflux of dissolved trace metals as a source to the overlying water column. Using equation 1, we can estimate the approximate sediment diffusive flux (J_{sed}) for dissolved porewater species.

$$J_{sed} = -\phi D_{sed} \frac{dC}{dz} \quad (1)$$

In this equation, ϕ is the porosity of the sediments, and was found to be 0.9 on average near the sediment surface. Porewater analyses of dissolved Fe and Mn in the Outer Basin (OB) cores reveal high variability in the top-of-core gradient ($\frac{dC}{dz}$) in porewater Fe and Mn (Fig. A2). An average of two cores gives a gradient of 21.9 μM cm^{-1} dissolved Fe and 3.6 μM cm^{-1} dissolved Mn. Assuming a diffusion coefficient for Fe and Mn in free solution for seawater (D_{SW}) at 0°C to be 3.15×10^{-10} m^2 s^{-1} for Fe(II) and 3.02×10^{-10} m^2 s^{-1} for Mn(II), we can then estimate the diffusion coefficient in the sediments (D_{sed}) by the following relationship (van Duren and Middelburg, 2001; Halbach *et al.*, 2019):

$$D_{sed} = \frac{D_{SW}}{1-2ln\phi} \quad (2)$$

2.3.4. Iron-binding ligands

A subset of seawater samples was analyzed for dFe-binding ligands using single analytical window methods. The methods applied here are described extensively in Buck *et al.* 2018 (Buck *et al.*, 2018). Briefly, natural seawater samples were titrated with dFe (0-35 nM) in order to fully saturate the natural ligands. Following a 2 hour equilibration with the added Fe, a well-characterized ligand (salicylaldoxime, SA) was added to compete with natural dFe-binding ligands. The concentration of SA used in this study to examine ligands was 25.0 μmol L^{-1} ($\alpha_{Fe(SA)_x}$ = 115). After at least 15 minutes of equilibration, the $Fe(SA)_x$ electroactive complex was measured using adsorptive cathodic stripping voltammetry (ACSV) on a hanging mercury drop electrode (BioAnalytical Systems, Incorporated). Peak heights were measured using ECDSOFT and sensitivity was optimized in ProMCC (Omanović, Garnier and Pižeta, 2015). A combination of traditional linearization techniques was used to determine the concentrations and strengths of natural ligands within the seawater sample using ProMCC (Omanović, Garnier, and Pižeta 2015). The uncertainty on modeled complexation parameters was optimized using single or multiple ligand fitting. These methods were applied successfully to the GEOTRACES speciation data sets (Buck *et* al., 2015, 2018).

We calculate the capacity for the free ligand pool to bind Fe at equilibrium (Fitzsimmons *et al.*, 2015), or $\alpha_{FeL'}$, defined as:

$$\alpha_{FeL'} = 1 + ([eL] \times K), \quad (3)$$

where *eL* is the difference between the total ligand concentration (L_t) and the dFe concentration, and *K* is the conditional stability constant.

2.3.5. Numerical model simulations

Based on Hahn-Woernle *et al*. (2020), the ocean in the Andvord Bay region is modeled with the primitive-equation, finite-difference Regional Ocean Model System (ROMS, Haidvogel *et al.,* 2008). The grid has a horizontal resolution of ~350 m and a terrain-following vertical coordinate system with 25 depth layers. Due to the changing terrain, the fixed number of layers, and surface intensified resolution, the maximum thickness for deeper layers is 84.6 m and the minimum thickness for surface layers is 0.5 m (to better resolve e.g. the surface currents). The domain has three open boundaries: the western end of Bismarck Strait, a passage to the continental shelf in the northwest, and along Gerlache Strait to the northeast (Fig. 2.1). Boundary and initial conditions were derived from CTD and ADCP observations. The model is forced with tidal and meteorological data (from TPXO8 Egbert and Erofeeva 2002 [updated] and RACMO van Wessem *et al.,* 2014, respectively) and run from November 2015 for five months. After one month, the transient effects, based on dynamics and thermodynamics, were found to no longer be present, and the system was consistent. Only the final four sea-ice free months were analyzed (December through March). Processes like melting of icebergs and floating sea ice are not modeled directly, therefore such local freshwater sources are represented in a surface intensified meltwater input applied along the glacial fronts (for further details see Hahn-Woernle *et al.* 2020). These new freshwater sources include also surface runoff and local melt of glacial ice, while precipitation and snowfall are represented in the meteorological forcing. To represent the seasonal cycle of temperature-induced melting the volume flux of inflowing meltwater follows a bell-shaped temporal distribution peaking at the end of January.

We use this model to identify the potential supply pathways and estimate the hydrographic export of three Fe-rich sources in Andvord Bay: surface glacial meltwater, subsurface subglacial

plume, and deep water masses located within the inner basin. For this purpose, we designed three model experiments with numerical “dyes” to track potential iron pathways: one, to track the current seasonal input of meltwater from glaciers in Andvord Bay (*surface meltwater dye experiment*) released along the glacial fronts in the inner fjord at 0-50 m depth (Fig. 2.1); and two additional experiments involving subsurface water masses in front of Bagshawe Glacier in Inner Basin A (IBA, 64° 53’ 36’’ S, 62° 34’ 48’’ W) at two different depths (*subsurface* and *deep dye experiments*, respectively). Due to the model geometry, the mean depths the subsurface and deep dyes were released were 107 (94-120 m) and 314 m (290-342 m), respectively. Covering two horizontal grid cells each (with different thickness), the subsurface and deep dyes had initial volumes of 5×10^6 and 11.3×10^6 m^3, respectively. It follows from the experiment setup that the surface meltwater dye has a continuous source while the total amount of the other two dyes is a constant as long as they do not leave through the open boundaries of the model domain.

2.4. Results

2.4.1. Seasonality and hydrography in Andvord Bay

In Andvord Bay (Fig. 2.1), seasonal changes in phytoplankton biomass were documented, as indicated by the proxy Chlorophyll-a, which shows a 10-fold concentration decrease across all taxonomic classes between the late spring and fall cruises (Pan *et al.*, 2020). Associated with these changes in primary production, depletion of the surface macronutrients nitrate (N) and silicic acid (Si) were observed (Ekern, 2017). Increased Si concentrations, with respect to nitrate, within the inner fjord are driven by dissolution of biogenic silica sediments, or weathering of the bedrock by contact with the 11 marine-terminating glaciers feeding into Andvord Bay since Si-to-N ratio is highly correlated with MWf below the surface layer (Hawkings *et al.*, 2018; Ng *et al.*, 2020). Surface stocks of macronutrients were never exhausted (Fig. 2.2). The phytoplankton community was dominated by small size classes, with very few large diatoms (Pan *et al.*, 2020). The

microplankton class, including large diatoms, was sparingly present in the Fall, however, benthic cameras captured a large sedimentation event of marine aggregates indicative of a large diatom bloom in late-January. The export of biogenic particles from the surface also showed a distinct seasonality indicated by increased Chlorophyll-a pigment content in seafloor surface sediments in Fall (Ziegler *et al.*, 2020), as well as higher respiration rates from chamber incubation experiments in the Fall compared to Spring (data not shown), although no indication of sulfate reduction was observed in sediment box and Kasten cores (2.3 m long), suggesting that oxygen, nitrate, and metal oxides were sufficient to oxidize organic matter within the upper sediments (C. Smith pers. comm.).

Derived glacial meltwater fractions (MWf, Fig. 2.2), based on salinity and oxygen isotopes of seawater, ranged from 0.75-2% in late Spring, and from 0.5-2.5% in the Fall (Pan *et al.*, 2019). The fjord also exhibited a gradient in meltwater content, with highest MWf at the glacier terminus. Using a simple mass balance for the surface layer in Andvord Bay, we estimate an approximate meltwater input of 23600 m^3 d^{-1} in order to account for the observed changes in oxygen isotope ratios. This estimate is within the derived estimates of surface meltwater flux generated by warm atmospheric temperatures (1.4×10^4 to 1.2×10^5 m^3 d^{-1}; Lundesgaard *et al.*, 2020). The MWf is strongly correlated with phytoplankton abundance within Andvord Bay; for a detailed discussion see Pan *et al.* (2019). We find that glacial meltwater impacts phytoplankton within the fjord, but the geographical influence of meltwater can extend across the shelf, hundreds of kilometers from the coastal inputs (Dierssen *et al.*, 2002; Meredith *et al.*, 2017).

Physical properties measured in the study region showed the dominant water masses in the fjord were Antarctic Surface Water (cold fresh) and Bransfield Strait water (cold salty) (Lundesgaard *et al.*, 2020). However, during late Spring, greater influence of modified Upper Circumpolar Deep Water was observed outside of the fjord, indicated by its distinctly higher temperature at depth, but this water mass is prevented from entering the fjord due to a shallow sill near the fjord mouth in the Gerlache Strait (Fig. 2.2). Optical measurements recorded a change

in the particle concentration and assemblage between the two cruises. Profiles of beam attenuation coefficient and particulate backscattering coefficient showed strong seasonality (see Fig. 2.4 and discussion in Pan *et al.,* 2019). Pan *et al*. interpreted these optical signatures in the upper water column as a change from a surface biogenic-dominated signal in late Spring to a subsurface lithogenic-dominated signal in the Fall, composed of fine suspended particles contained within plumes. An important feature observed within the fjord was a subsurface neutrally-buoyant plume (~100 m) characterized by a point source of relatively cold and particle-laden water emanating from the terminus of Bagshawe Glacier and extending several kilometers over the inner basin (Fig. A3).

Strong buoyant plumes can drive circulation in fjords via the “meltwater pump”, but small amounts of basal and subglacial melt have a negligible effect on circulation in Andvord Bay. While this process is described in-depth for Arctic glaciers, Andvord Bay differs in that ocean temperatures are approximately -1 °C at depth, too cold to ablate the glacier terminus, and neutral buoyancy is reached below the surface layer (indicated by subsurface sediment plumes, Domack and Ishman 1993). However, cold-water glaciers must have some mass loss even at seawater temperatures below the glacial ice melting point. Two important consequences of these plumes are a flux of suspended particulate matter within subsurface “layers” as indicated by high beam attenuation coefficient and optical backscatter (Fig. S3 in Pan *et al.*, 2019), and general mid-water cooling found in the inner fjord (Figure 8 in Lundesgaard *et al.*, 2020). Downstream mixing mechanisms, such as flow over topographic features or wind induced upwelling, can displace plume water closer to the euphotic zone.

2.4.2. Water column trace metals

Dissolved Fe concentrations in the surface, defined as the upper ~20 m based on similar mixed layer depths (MLD) for both seasons (Lundesgaard *et al.*, 2020), changed seasonally with an overall increase in dFe concentration in the Fall (Fig. 2.3). The average surface concentration

during late Spring was 2.47±0.92 nM (*n* = 21), while in Fall it was 6.67±1.41 nM (*n* = 19). Water column trace metals are presented in Table S1. These concentrations are within the ranges of dFe determined in prior studies (1-31 nM) in the northern WAP region but indicate that large temporal variability exists in surface waters in this region (Bown *et al.* 2018; Hatta *et al.* 2013; Sanudo-Wilhelmy *et al.* 2002; Ardelan *et al.* 2010; Martin *et al.* 1990). The smaller range of surface concentrations during late Spring suggests that dFe was more tightly controlled by phytoplankton uptake, whereas in the Fall, patchiness among stations arises due to varying proximity to Fe sources and the effects of circulation and mixing. Vertical profiles of dFe showed a steep increase to values greater than 10 nM at the deepest depths sampled during late Spring, especially at stations located within the inner fjord and basins (Fig. 2.2, 2.4). In the subsurface (50-150 m), an enriched dFe source was present with average concentrations 3.68±1.52 nM in late Spring and 7.38±2.49 nM in the Fall. Deep water masses greater than 150 m deep had the highest average concentrations of dFe and similar mean concentrations were observed for both seasons (8.79±4.75 nM in late Spring, 6.37±2.38 nM in Fall). The greatest concentrations of dFe were found in the inner fjord and basin stations, with the exception of one station located at the mouth of the fjord near Aguirre Channel (station AC in Fig. 2.1). Water column concentrations were lower in the Gerlache Strait and fjord mouth. The general shapes of the profiles in late Spring are characteristic of a stratified water column, with dramatic ferriclines below the surface.

In the Fall, surface dMn was more than double that observed in the late Spring, but surface dFe showed a greater seasonal increase, such that the dissolved Mn:Fe ratio decreased overall and was more variable than in late Spring, when concentrations of dMn remained below 4.5 nM, even at depth. Labile particulate Mn (LpMn = TDMn – dMn) showed strong co-variation with LpFe and beam attenuation coefficient c(660). The comparatively high surface dissolved Mn:Fe ratios in late Spring were presumably due to intense biological drawdown of Fe during the vernal bloom, evidenced from low concentrations of dFe where phytoplankton biomass (as Chl-a) was highest

(Fig. 2.5a). In the late Spring, dFe is anti-correlated with MWf (Fig. 2.5c), whereas there was no significant trend between dFe, biomass and MWf variables in the Fall (Fig. 2.5b,d). The correlation between dMn and dFe was stronger in the Fall, however, compared to the late Spring (Fig. 2.5e,f). Labile particulate iron (LpFe = TDFe - dFe) concentrations were elevated in the inner basins in the late Spring and Fall, and strongly correlated with suspended particle concentrations, indicated by optical beam attenuation coefficient c(660) m^{-1} (Fig. 2.5.2n, 6). Average TDFe and LpFe concentrations in the surface were comparable to surface waters in Ryder Bay (southern Antarctic Peninsula), where TDFe varied temporally from 57 to 237 nM (Annett *et al.*, 2015). This comparison between LpFe and TDFe is valid since TDFe is much greater than dFe in these two coastal locations, hence it is a good approximation of LpFe. The LpFe maxima were associated with high turbidity in the inner basins, reaching as high as 900 nM at 300 m depth in the Fall (Fig. 2.6). Dissolved Fe and LpFe were correlated (r^2 = 0.48 late Spring *n* = 19; 0.77 Fall *n* = 28) (Fig. 2.5g,h). On average, dFe made up 3.1% (late Spring) and 4.6% (Fall) of the total dissolvable pool. The LpMn concentrations displayed similar seasonality to LpFe and similar association with total particles, but were more strongly correlated in the Fall (Fig. 2.5l). Dissolved Mn and LpMn were highly correlated (r^2 = 0.70 late Spring *n* = 19; 0.79 Fall *n* = 28; Fig. 2.5i,j). On average, dMn composed 52% (late Spring) and 57% (Fall) of the total dissolvable pool.

2.4.3. Glacial ice and plume trace metals

Glacial ice and plume samples were analyzed for Fe, Mn, Al, and Ti concentrations, which are presented in Table 2.1. Three glacial ice samples were analyzed for dFe (72±121 nM) and dMn (49±83 nM). Visual inspection of Glacial Ice 3 and 4 showed these pieces contained low particle loads, while Glacial Ice 1 and 2 had a comparatively high content of dark colored coarse-grained particles. Hence, these and the “clean” glacial ice samples are indicative of the variability of trace metal concentrations in icebergs found in Andvord Bay. Labile particulate trace metal

concentrations were two orders of magnitude higher than the dissolved fraction based on two ice samples (41±86 μM LpFe, 3.6±5.1 μM LpMn). We did not determine labile particulate trace metals for Glacial Ice 3 and 4, thus these average labile particulate concentrations are skewed toward a high value. Total particulate trace metals showed similar concentration variability to the dissolved fraction (95±181 μM TpFe, 2.7±5.1 μM TpMn). For Glacial Ice 3 and 4, the concentration of dMn was greater than TpMn. The ratios of labile and total particulate Mn:Fe were 0.061±0.002 mol:mol and 0.028±0.004 mol:mol, respectively.

Dissolved Al and Ti were not analyzed for these ice samples, but total dissolvable and total particulate samples were analyzed for Glacial Ice 1 and 2, and 1-4, respectively. We defined the refractory particulate trace metal concentration as the difference between the total particulate and total dissolvable fractions (RpTM = TpTM - TDTM). Total dissolvable Al and Ti average concentrations were skewed due to the heavy particle load present within Glacial Ice 1 and 2 (603±716 μM TDAl, 20.8±27.1 μM TDTi). Total particulate Al and Ti had similar variability to the total dissolvable fraction and included all four glacial ice samples with averages of 428±790 μM TpAl and 13.4±25.7 μM TpTi, therefore the average total particulate concentrations were lower than the average determined for total dissolvable Al and Ti in Glacial Ice 1 and 2. We found the labile particulate concentration to be a valid comparison to total dissolvable since dFe concentration was on average 1.8±1.5% of TpFe concentration. Thus, the particulate fraction dominated trace metal speciation of total Fe, Mn, Al, and Ti in glacial ice.

Four seawater samples were collected from 100-110 m depth, corresponding to the core of the subsurface turbidity plume within IBA. Average concentrations of dissolved metals were 8.75±2.25 nM dFe and 5.52±0.62 nM dMn. LpFe (351±148 nM) and LpMn (8.23±2.68 nM) were indistinguishable from the total particulate fractions (416±93 nM TpFe, 9.52±2.05 nM TpMn) within measurement error, including filter splitting and sample distribution uncertainties. The average ratio of labile particulate Mn:Fe was 0.024±0.003 mol:mol. Particles collected from the plume had

high concentrations of Al and Ti, but with distinctly different lability from that of Mn and Fe. The TDAl was 894±68 nM while TpAl was 1734±369 nM. Similarly, TDTi was 14.1±0.45 nM and TpTi was 45.1±10.7 nM. The total dissolvable Al:Ti ratio was 64±6 mol mol^{-1} and the total particulate Al:Ti ratio was 39±1 mol mol^{-1}. The Al:Ti ratio is elevated above the crustal ratio (35 mol mol^{-1}) in the total dissolvable fraction, suggesting a larger adsorbed fraction for Al than for Ti.

2.4.4. Glacial sediments

Solid phase Fe speciation of one sediment core from the outer basin station (OB, 64° 46' 46'' S, 62° 43' 57'' W, ~500 m, collected in January 2016), showed an enrichment of authigenic Fe oxides at the surface. Chemical treatments of the sediments with HCl dissolves poorly crystalline Fe oxy(hydr)oxides (ferrihydrite and lepidocrocite), which are found to be 10% of the total particulate Fe of the surface sediments in this location, compared to an average of 2% below 1.5 cm (Fig. A4). In the surficial sediments, a larger portion of the Fe is associated with poorly labile sheet silicates (e.g. structural Fe(III) in clays, 36%), and a comparable fraction is refractory and is not liberated by any of the solution treatments (31%). Other fractions of particulate Fe are associated with more crystalline Fe oxides (goethite, hematite) and the minerals magnetite and pyrite. Porewater analyses were performed on two OB cores using colorimetric methods, revealing high concentrations of dFe and dMn. Below the well-oxygenated layer (upper ~0.5 cm), but within the upper 10 cm, dFe reaches its peak concentration of 80 μM, while maximum dMn is 6 μM. Down-core from the peak, concentrations tend to decrease for both trace metals, but there is considerable variability between 15 and 25 cm, including several deeper local maxima. The average porewater concentration of dFe in the top 2.5 cm is 26 μM (Fig. A2). There is considerable difference in the porewater concentrations of the two OB cores indicating bioturbation of the sediments resulting in large variability on small scales. Points excluded from the oxygen profiles

were below the detection limit, while several samples were lost from the porewater profiles, represented as gaps in the vertical traces of dFe and dMn.

2.4.5. Fe-binding organic ligands

To gain insight into the speciation of dFe within the fjord, we analyzed seawater samples for Fe-binding ligands and to identify comparative strengths of organic Fe complexes (See *Methods*). Analysis of the ligands within Andvord Bay shows a down-fjord gradient in both quantity and quality (all ligand data presented in Table 2.2). In the late Spring, strong ligands ($LogK^{cond}_{FeL,Fe'} \geq 12.0$) were detected in the surface at stations located within the fjord at concentration levels ranging from 4.06±1.74 nM at Inner Basin A (IBA) to 7.27±1.97 nM at Sill 3 (S3), while only weak ligands ($LogK^{cond}_{FeL,Fe'} < 12.0$) were detected in the Gerlache Strait (GS; 5.72±2.21 nM). An excess of strong ligands, relative to dFe, was detected in the inner basins. A gradient in concentration of undersaturated ligands (eL in Table 2.2) is observed towards the GS, with increasing eL. Within the fjord, weak ligands were detected at Inner Basin B (IBB), closest to Moser Glacier. In the Fall, total ligand concentrations (L_t) were elevated everywhere within the fjord, but the surface ligands were somewhat weaker compared to the late Spring. The greatest concentrations of ligands were found closest to the glaciers (range 11.18 – 15.42 nM) and in the GS (12.00±2.94 nM). For both seasons, weak ligands were detected in the subsurface, but a greater concentration in the Fall suggested that these ligands have a local source within the fjord. Compared to other stations in the Fall, we found the plume to contain a small excess of weak ligands (IBA, 110 m). Interestingly, the highest concentration of strong ligands (17.44±1.12 nM) among all sites was in deep water of Station IBA, at 280 m. This is the deepest depth sampled for Fe-binding ligands and the IBA bottom depth was 382 m. We found a down-fjord gradient in ligand strength at the surface, decreasing with distance from the inner basins ($LogK^{cond}_{FeL,Fe'}$ = 11.95 at IBA, 11.03 at GS).

We determined the free (uncomplexed) Fe concentration (Fe' in Table 2.2) within samples analyzed for Fe-binding ligands. In the surface, a greater mean concentration of Fe' was found in the Fall (8.74±6.43 pM, *n* = 7) compared to the late Spring (2.44±2.18 pM, *n* = 7). Water below the surface showed similar concentrations for each season (5.8±0.21 pM late Spring, 4.61±2.22 pM Fall). The greatest concentrations of Fe' were observed mid-fjord at the surface (18.7 pM Fe' at MB, 15.67 pM Fe' at S3) in the Fall.

2.4.6. Dye experiments

To study the transport pathways for dFe, we use numerical passive dyes in the Hahn-Woernle *et al.* (2020) regional model of Andvord Bay (see Fig. 1 in Hahn-Woernle *et al.,* 2020) to track three potential sources of dFe: surface glacial meltwater (0-50 m) from Bagshawe and Moser Glacier termini, neutrally-buoyant subsurface plume (100 m), and deep water located in IBA (300 m; as in *Methods*). Due to numerous inputs and complex biogeochemical processes which result in observed dFe distributions in time and space, we simplify the problem by assuming no removal over the duration of simulated dye experiments. We use this approach to illustrate the multiple transport pathways for dFe supply to the fjord and surrounding ocean from December through March (St-Laurent *et al.*, 2017). The results are presented first for the surface meltwater experiment, followed by two fixed-volume experiments, referred to as subsurface and deep dye experiments.

Most of the surface glacial meltwater dye remains in the upper 100 m throughout the model run, and due to its proximity to the surface, it is quickly dispersed over a large region by relatively rapid surface currents. It takes about 10-15 days for the surface meltwater to exit the fjord mouth, where most ends up in the central and northern Gerlache Strait after 120 days (Fig. A5a).

The subsurface dye (100 m) is spread more rapidly than the deep dye (300 m). After 8 days, the subsurface dye reaches the fjord mouth, which is 4 days before the deep dye, implying it has a shorter residence time within the fjord compared to the deep dye. We loosely define

residence time as the model timestamp at which a fixed fraction of dye remains within the fjord domain. After 22 days, 25% of the subsurface dye has left the fjord, while it takes the deep dye almost twice as long (43 days). At the end of the 120 days long model run, less than 18% of the subsurface dye and over 30% of the deep dye remain in the fjord domain (Fig. A6a). Looking at the whole model domain in Fig. 2.1, which includes Andvord Bay and Gerlache Strait, only 59% of the subsurface dye and 75% of the deep dye are still present after 120 days. The missing 41% (25%) has mainly left the model domain through the Gerlache Strait to the north, where these waters mix with Bransfield Strait water and subsequently with the southern Antarctic Circumpolar Front waters.

We analyzed the vertical distribution of the subsurface and deep dyes along the fjord mouth and horizontally over different depth layers. Within the first day, the subsurface dye spreads over the depth range of 20 to 125 m and the deep dye over 125 to 500 m (>1% of dye per depth layer). The subsurface dye leaves the fjord mainly within the upper 200 m. After 8 days, as the subsurface dye reaches the fjord mouth (Fig. A5b), the maximum concentration is still found close to its release depth at 100-125 m. Over the next few days, surface layer concentrations (<20 m) increase, but the highest concentration is soon found below 125 m (after 2 weeks) (Fig. A6a).

The deep dye remains mainly below 200 m as it passes the fjord mouth (maximum water depth at the fjord mouth is 360 m). After 12 days, as the deep dye reaches the fjord mouth, the maximum concentration is found below 300 m depth. In contrast to the subsurface dye, the deep dye remains longer in the proximity of the fjord mouth and on several occasions, re-enters the fjord leading to a longer residence time within the fjord (Fig. A5c). The majority of the deep dye leaves the fjord at depths below 100 m and along the southwestern coastline. Both dyes, subsurface and deep, have low concentrations in the upper 100 m of the northeastern flank of the fjord mouth. This is due to the inflow of external water from the GS along the northeastern coastline. Throughout the run, the deep dye is confined to the inner basins of the fjord. In all

cases, the dyes remain at higher concentrations and for longer periods in the subsurface fjord waters than in the surface layer, which shows faster transport out of the fjord.

2.5. Discussion

2.5.1. Iron sources in a heavily glaciated fjord

Due to the proximity to glaciers and influence of ice within Andvord, we hypothesized meltwaters to be an important source of Fe. We focus on quantifying dissolved, total dissolvable and particulate Fe and Mn, as well as total dissolvable and particulate Al and Ti. Ratios of these elements are treated as proxies for contributions of various endmembers. Candidate endmembers include reducing sediments, weathered crustal material, and biogenic particles (Taylor and McLennan 1995; Twining *et al.*, 2004). Where possible, we estimate fluxes of dFe. We begin by examining the relationship between glacial meltwater and dFe.

2.5.2. Role of surface glacial meltwater

Glacial meltwater at the surface has the potential to be a significant source of Fe to phytoplankton. There exists a weakly negative correlation between derived MWf and dFe at the start of the melt season (late Spring: $r^2 = 0.29$, n = 30; early-Fall: $r^2 = 0.05$, n = 13; Fig. 2.5c,d). One possible explanation is that increased meltwater at the surface leads to greater stratification and limits upwelling of Fe-rich deep water, with the effect augmented by removal processes, such as biological drawdown and scavenging of dFe onto sinking particles. Indeed, higher rates of primary production are associated with greater fractions of meltwater in Andvord Bay (Pan *et al.*, 2020). While we observe high concentrations of dissolved and particulate trace metals within glacial ice, we note that the icebergs within Andvord were predominantly “clean” ice, with little sediment embedded in the ice, indicated by relatively low dFe and TpFe (for instance, Glacial Ice 3 and 4 in Table 2.1). Based on Fe:Al ratios in particles and average values for continental crust

(Taylor and McLennan 1995), we estimate 87±22% (*n* = 4) of the particulate Fe contained within Andvord icebergs is terrigenous in origin. This is consistent with mechanical weathering of continental crust followed by inclusion of the particles into the ice (freeze-in, Raiswell *et al.*, 2018). Low Fe:Ti and Al:Ti ratios also reflect a continental crust source, but it is worth noting that Glacial Ice 2 had significantly more Mn and Al, relative to continental Fe and Ti. Further, Mn and Al solid speciation suggests there are high concentrations of Mn- and Al-oxides, which may be formed when crustal material is altered (Raiswell *et al.*, 2018). It is also possible that fjord sediments were the source of particulate matter within Glacial Ice 2, which would correspondingly have higher Mn content (and higher Mn:Fe) than what is found in basal ice interacting with the subglacial environment (Hawkings *et al.*, 2020). Continental crust material delivered to the ocean would contain a relatively low Mn content compared to Fe (Fe is 4% w/w in crustal material, while Mn is 0.08% w/w, Rudnick and Gao 2013). Since glacial meltwater is restricted to the surface, it constitutes a significant input of Fe to the surface throughout the growth season.

Visual inspection suggests that the majority of the ice within Andvord has relatively low concentrations of particles, whereas basal ice, with dark layers of sediment (Glacial Ice 1 in Table 2.1), will likely skew the average towards high values (Hopwood *et al.*, 2019). A compilation of TDFe in icebergs in Antarctica estimated an average concentration of 24 μM (Hopwood *et al.*, 2019). Our two measurements of LpFe in glacial ice are different (mean for this study is 61±70 μM LpFe, *n* = 2) but are within the range of concentrations determined in the previous study. Thus, we use our mean concentration (Table 2.1) as indicative of the glacial ice composition in Andvord to compute the following meltwater fluxes. It is important to note that the mean and median values in glacial ice are likely different, with median values closer to Glacial ice 1 and 2 concentrations. Using a range of estimated surface glacial meltwater volume inputs (2.4×10^4 m^3 d^{-1} for this study based on oxygen stable-isotope mass balance; 1.8×10^4 to 1.2×10^5 m^3 d^{-1} Lundesgaard *et al.*, 2020; 1.1×10^6 m^3 d^{-1} Hahn-Woernle *et al.*, 2020 including other freshwater sources that are not precipitation) and assuming the input of meltwater is distributed evenly over

the fjord surface layer, we calculate fluxes on the order of 15 to 704 nmol m^{-2} d^{-1} for dFe and 10 to 487 nmol m^{-2} d^{-1} for dMn. Based on modeling work in this paper, it will become evident that meltwater released to Andvord does not stay within the fjord. Additionally, significant metal loss results from scavenging processes, transferring Fe to depth on sinking particle surfaces, rendering it inaccessible for phytoplankton uptake. Still, the availability of excess macronutrients within Andvord Bay (Fig. 2.2) means that substantial increases in the supply of trace metals from glacial meltwater would stimulate growth in the euphotic zone if light were not limiting (Pan *et al.*, 2020).

2.5.3. The nature of Fe in subglacial plumes

The inner basins consistently show higher beam attenuation and particle backscattering coefficients than mid-fjord and shelf stations (see Figure 3 in Supplementary Information in Pan *et al.* 2019). These signals are attributed to ultra-fine suspended sediments (<0.8 μm). The high particle backscattering coefficient in the surface at all stations in late Spring is due to the high concentrations of biogenic particles associated with the vernal bloom. Inner basins also show local maxima in beam attenuation coefficients at 70-150 m, as well as approaching the benthic boundary layer (Fig. 2.6). Buoyant turbulent plumes that spread laterally are consistent with the presence of glacial meltwater plumes, or “cold tongues”, which originate at the glacier grounding line (described in Domack and Williams 2011), entrain deep water masses, and resuspend sediments (Straneo and Cenedese, 2015). Since ocean temperatures remained below 0°C in Andvord (see Fig. 2.2), there is little to suggest basal melting of the ice, as is observed further south along the WAP. It appears reasonable on the basis of the evidence given above, that the subsurface plume signature is subglacial in origin.

Total digestion and subsequent analyses of marine particles collected within the plume revealed high concentrations of weathered crustal sediments (82-86% of TpFe, 61-64% of TpMn),

and also ingrowth of authigenic particles most likely consisting of precipitated Fe- and Mn-oxide phases (16-18% TpFe, 36-39% TpMn). These results suggest that the origin of plume particles is a chemically-altered crustal source (see *Supplemental Methods*). Labile particulate Fe is 82-100% of TpFe (Table 2.1). The Fe:Al and Fe:Ti in plume particles (0.24±0.01 mol mol^{-1} and 9.25±0.24 mol mol^{-1}, respectively) were elevated above the average crustal ratios (0.2 mol mol^{-1} Fe:Al, 7 mol mol^{-1} Fe:Ti), which implies these samples are enriched in Fe relative to both crustal Al and Ti. In agreement with these results, particulate Al:Ti (39±1 mol mol^{-1}) was elevated above crustal ratios (35 mol mol^{-1}), indicating a large oxide fraction is associated with this particulate matter, since the total dissolvable fraction, more enriched in Al than the total particulate fraction, forms when Al is heavily scavenged on to oxy(hydr)oxides at oceanic pH levels (Kryc *et al.*, 2003). This substantiates our claim that most of the Fe found in the plume is weakly adsorbed to particles and recently precipitated, since dilute HCl leaches liberate the most labile forms of Fe, most likely oxy(hydr)oxides (e.g. ferrihydrite) in addition to some Fe from clays. This could include oxides directly precipitated from the anoxic subglacial source, as well as a potential fraction of oxides derived from fjord sediments and porewaters entrained at the grounding line.

Cold-water glaciers are locations where the subglacial environment flows directly into the fjord with minimal mixing with seawater. We find elevated concentrations of dMn (~15 nM, Fig. 2.2) emanating from the inner fjord, indicative of the reducing conditions beneath Moser and Bagshawe glaciers, consistent with other studies of subglacial environments (Henkel *et al.*, 2018; Zhang *et al.*, 2015). Compared to subglacial fluids in contact with bedrock, we report relatively low concentrations of dFe within the plume (8.75±2.25 nM) <1 km away from the glacier terminus. If we assume a MWf of 0.01 for the plume, and assuming a deep fjord seawater concentration of zero, the subglacial meltwater endmember would have a dFe concentration of 875±231 nM, which is higher than the mean value for TDFe measured within the plume (347±160 nM) suggesting settling loss through flocculation is likely occurring even within 1 km of the grounding line. The subglacial endmember dFe is lower than the range used to parameterize subglacial inputs from

ice shelves to the SO (3 – 30 μM in Death *et al.*, 2014). The long residence time and enhanced chemical weathering beneath large glaciers in west Antarctica (PIG, Thwaites Glacier) could result in large accumulations of dissolved trace metals in subglacial outflow. However, subglacial discharge occurs at some distance from the open continental shelf waters because of the broad floating horizontal ice shelves, which make up about 45% of the Antarctic coastline (Schodlok *et al.*, 2016). Advective transport under ice shelves reduces the flux of dFe upwelled into the euphotic zone 10s – 100s km away from the point source of meltwater discharge (Krisch *et al.*, 2021). Our results suggest that assumptions of high export efficiency to the coastal ocean (i.e., using endmember dFe concentrations from glacial runoff and groundwaters as in Death *et al.*, 2014) potentially overestimates dFe supply from anoxic subglacial environments because significant dFe boundary scavenging occurs during lateral transport. It is therefore important, albeit difficult, to parameterize scavenging and removal at the ice-ocean interface as all studies suggest intense removal of dFe on short time and length scales.

2.5.4. Role of sediments

Analyses of Andvord Bay sediments reveal they are compositionally distinct from temperate fjords consisting of poorly sorted fine silt and clay, many dropstones, suspension deposits and ice-rafted debris (Eidam *et al.*, 2019). Sediment accumulation rates are spatially variable, but a weak along-fjord gradient is present. These deposits suggest sluggish circulation, allowing for the deposition of sediments close to their source, likely through flocculation processes (Cowan and Powell, 1990).

Profiles of beam attenuation coefficient show highest concentration of particles in the inner basins compared to other station locations (see Figure 4 in Pan *et al.,* 2019). There is little evidence for mechanical resuspension through gravity flows (i.e., turbidites) along the steep basin walls, yet such processes could be responsible for the near-bottom elevation in water column particles (Eidam *et al.*, 2019). The presence of elevated particles in the inner basins is

accompanied by the greatest concentrations of dissolved and labile particulate Fe and Mn (Fig. 2.6), demonstrating the potential of resuspended fjord sediments as a source of dissolved trace metals.

Based on the core top porewater profiles, we estimate the sedimentary efflux to be 43.7 μmol m^{-2} d^{-1} for dFe and 7.2 μmol m^{-2} d^{-1} for dMn, due to diffusion alone (Fig. A2). This magnitude of flux was also observed in the shelf sediments in the vicinity of South Georgia Island in the SO (Schlosser *et al.*, 2018). Abundant epibenthic fauna were observed within Andvord Bay, which mix the sediments through bioturbation while consuming labile organic matter. Taylor *et al.* (2020) used ^{234}Th as a proxy to investigate the effect of bioturbation on short timescales and found Andvord Bay sediments possess a high mixing coefficient down to 5 cm (D_b = 36 cm^2 yr^{-1}) consistent with greater deposition and subsequent utilization of organic carbon in the sediments compared to data from the adjacent continental shelf. We believe this accurately reflects the conditions in this fjord: bioturbation by dense aggregations of epibenthic fauna within the basins.

These results are not surprising when compared to a global compilation of *in situ* measurements of sedimentary efflux of dFe, which is on average ~12 μmol m^{-2} d^{-1} for water masses located on continental margins and with O_2 concentrations greater than 63 μmol L^{-1} (Dale *et al.*, 2015). The bottom water oxygen concentration in Andvord Bay always exceeded 230 μmol L^{-1}. The bottom water O_2 concentration for OB at the time sediments were cored, was 270 μmol L^{-1}. Abundant epibenthic fauna found within Andvord (Ziegler *et al.* 2017, 2020) would introduce oxygen to the upper few centimeters of the sediments through bioturbation and could decrease the efflux of reduced metals (Severmann *et al.*, 2010). Taylor *et al*. (2020) found Andvord Bay sediments possessed high inventories of ^{210}Pb relative to open shelf and Palmer Deep stations indicating a high mixing coefficient for sediments between 7 and 22 cm depth on timescales of 100 years (Taylor *et al.*, 2020). The effect of this process is mixing of oxide- and organic carbon-rich surficial sediments further down in the core on short- to long-timescales. These dFe flux

estimates, together with solid phase speciation results, highlight the importance of rapid oxidation and precipitation occurring at the seawater interface, which effectively retain most Fe as oxy-hydroxides within the sediments (Burdige and Komada, 2020; Laufer-Meiser *et al.*, 2021). The Fe oxides are enriched within the penetration depth of oxygen (~0.5 cm, Fig. A2 inset) and once bioturbated downward, could be a source of dFe following microbial cycling. Multiple local maxima of porewater dFe were observed deeper in the cores. While dissimilatory iron reduction would be a source for Fe, oxidation of Fe with bottom water O_2 and Mn(IV) are important sinks and exert a control on the dFe concentration of deep water masses. The deep inner basin water column samples had high dFe concentrations concomitant with high LpFe concentrations (Fig. 2.2, 2.6), suggesting some loss of porewater dFe to the water column and rapid formation of authigenic Fe mineral particles. Therefore, the fluxes calculated from porewater profiles are upper limit estimates because they do not account for oxidative losses at the sediment-water interface (e.g., Burdige and Komada 2020). In the Ross Sea, Marsay *et al*. (2014) estimated spatially variable efflux spanning 0.028-8.2 μmol m^{-2} d^{-1} based on water column dFe profiles, which might better illustrate the net effect of rapid oxidation of reduced Fe, for which large uncertainties remain (Marsay *et al.*, 2014).

Due to weak midwater circulation, low tidal energy, and stratification of the surface, a disconnect between deep water masses enriched in dFe and the surface of Andvord Bay persists during prolonged quiescent periods. For these reasons, we believe most sedimentary-sourced Fe is restricted to deep water masses and therefore plays a minor role in dFe concentrations within the upper water column. There is potential, however, for resuspension and entrainment of surface sediments where subglacial meltwater discharges at the grounding line. Due to the low inferred volume of discharge and lack of strong tides in Andvord Bay, it is unclear if resuspended sediments contribute to the total particulate mass within the plume.

The Mn:Fe ratio is a useful signature of the source of dissolved and particulate trace metals in Antarctica and has been applied to the PAL LTER data set (Annett *et al.*, 2017). Applying

this same framework to our study, we find that water column dissolved trace metals are heavily influenced by surface glacial ice melt and subglacial meltwater, and to a lesser extent, sediment sources within the fjord, irrespective of season, depth, and meteoric water input (Fig. 2.7). Due to the shorter residence time of dFe relative to dMn (i.e., inorganic oxidation of Mn(II) is 10^7 times slower than Fe(II), Sherrell *et al.*, 2018), we would expect the porewater dissolved Mn:Fe ratio to tend towards higher values once exposed to the seawater oxidative front. We therefore cannot rule out porewaters as a source of dMn to the water column. A similar process occurs within the plume, where the elevated dissolved Mn:Fe (0.65 mol mol^{-1}) relative to labile particulate Mn:Fe (0.024 mol mol^{-1}) shows the effect of rapid conversion of Fe to authigenic mineral particles. Although we do not have comparable measurements for sedimentary labile particulate Mn, based on labile particulate Mn:Fe, we find that the water column labile particulate Mn:Fe ratio is precisely the same ratio as particles found within the subglacial plume, again irrespective of when and where the sample was taken (Fig. 2.8), suggesting plume particles remain suspended throughout the fjord water column.

2.5.5. Organic speciation of dissolved Fe

It has been hypothesized that excess ligands (eL = $[L_t]$ – [dFe]) increase the solubility of particulate Fe phases (Thuróczy *et al.*, 2011; Gledhill and Buck, 2012; Wagener *et al.*, 2012; Tagliabue *et al.*, 2019). The persistence of exchangeable pools of dFe would therefore be controlled primarily by particle assemblage and organic ligand complements, where pFe dominates total Fe speciation. We observe remarkable consistency between late Spring and Fall in the relative contribution of dFe to total Fe (4% to 5% of TDFe, respectively), implying dFe is controlled by scaling closely to LpFe (Fig. 2.5g,h) since both pools have large interseason differences. An increase in eL between seasons is observed (average 2.1±1.3 nM late Spring n = 9, 6.0±3.2 nM Fall n = 12). The ligands are likely produced during microbial high-affinity uptake or remineralization processes following the termination of a bloom (Gledhill and Buck, 2012; Hogle

et al., 2016). The only subsurface sample to contain strong Fe-binding ligands is the deep inner basin adjacent to Bagshawe Glacier (IBA), possibly indicating these ligands have a sedimentary source. It appears, based on these results, ligands in Andvord Bay have the capacity to complex additional Fe input, as well as prevent significant loss due to scavenging (Thuróczy *et al.*, 2012). The nature of these ligands, taken together with the low concentration of dFe and abundance of LpFe within the plume, leads us to speculate that Fe minerals are the target for ligand-mediated mineral dissolution and perhaps microbial uptake, previously hypothesized to occur in deep-sea hydrothermal vent plumes (Li *et al.*, 2014). In the Fall, despite a greater eL, a lower average conditional stability constant of the ligand pool results in lower complexation capacity and inferred ability to compete with particle binding sites (Ardiningsih *et al.*, 2020). However, the fraction of dFe and TDFe does not reflect a greater enrichment of particles.

While we observe a seasonal increase in the excess ligand concentration, there is no significant change in the ratio of L_t:dFe (late Spring 1.8±0.5, Fall 2.0±0.7). In the Amundsen sector, Thuróczy *et al.* (2012) found waters heavily influenced by the Pine Island Glacier to have L_t:dFe ratios <2.5 throughout the water column, with relatively weaker ligands compared with those found in the highly productive surface waters of the polynya. We too identify weaker Fe-binding ligands associated with the glaciers, and only at MB and Sill 3 did we observe elevated L_t:dFe (3.13, and 2.99 respectively, in the Fall). It is possible that sea ice released strong Fe-binding ligands in Andvord that remained in the surface until sampling in the late-Spring (Lannuzel *et al.*, 2015). The presence of excess strong Fe-binding ligands at IBA and S3 during the bloom onset also correspond to elevated NO_3^-:dFe (data not shown) above the threshold for potential Fe-limitation of coastal diatoms in the California Current region (10-12 μmol $nmol^{-1}$ King and Barbeau 2011). The presence of strong Fe-binding ligands might suggest an active microbial strategy in this coastal region to sequester additional Fe from particulate phases during the bloom initiation.

The intense seasonality in primary production and the presence of an undersaturated ligand pool could further increase the bioavailability of particles for downstream communities,

where particles within the water column are rare. We calculated the capacity for the free Fe-binding ligands to bind Fe ($\alpha_{FeL'}$ = 1 + (eL • K)). Calculations of $\alpha_{FeL'}$ are included for each sample in Table 2.2 as well as the inter-seasonal percent change in Fe' for reoccupied stations ($R_{Fe'}$). We find the $\alpha_{FeL'}$ increased between late Spring and Fall at IBA and Sill 4, while a decrease was found at IBB, Sill 3, and Gerlache Strait stations. While all reoccupied stations show an increase in the Fe' concentration ($R_{Fe'}$), the percent change is greatest where $\alpha_{FeL'}$ decreased in the Fall. Thus, the seasonal increase in Fe' reflects the increase in dFe concentrations as well as lower complexation coefficient of weaker Fe-ligand complexes, which contribute most to dFe speciation in the Fall and are associated with surface waters adjacent to glaciers.

These first results of organic speciation of dFe in an Antarctic fjord highlight the importance of seasonal ligand sources in establishing the solubility of new Fe entering the coastal ocean. Accurate ligand pools are not currently represented within SO biogeochemical models (Death *et al.*, 2014; Oliver *et al.*, 2019; Person *et al.*, 2019; St-Laurent *et al.*, 2019). During the bloom initiation, overall ligand strengths are higher than in the Fall, however, concentrations of ligands increase following the bloom. Concurrently, dFe concentrations increase and do not saturate the ligands to the same extent as in late-Spring. This is due to the lower complexation capacity of the ligand pool resulting from considerably weaker ligands present. Therefore, the dFe pool in the Fall may be more subject to boundary scavenging as free Fe. Ligand-mediated complexation has the potential to greatly expand the spatial extent over which solubilization of particulate Fe occurs and could be critical for sustaining productivity over a larger geographical region (Lippiatt, Lohan and Bruland, 2010; Ardiningsih *et al.*, 2020). Thus, the size, sinking rate, and composition of particles is critical to their lateral transport and reactivity over time with excess ligands. Our understanding of how cryospheric Fe is transformed after entering the coastal ocean is an important step towards understanding its impact on marine productivity and global biogeochemical cycles of the macronutrients. For the marine Fe cycle, these geochemical

transformations control the bioavailability of Fe, while vertical advection and mixing supply this critical micronutrient to the surface ocean and the euphotic zone.

2.5.6. Using dye experiments to explore Fe sources and export

Rapid communication between the surface and subsurface water masses occurs during katabatic wind events. The large magnitude of vertical shear initializes an upwelling cell close to the inner basins of the fjord. Using an idealized model of a fjord, Lundesgaard *et al.* (2018) found that katabatic winds can export the surface layer, depending on wind velocity, elapsed time of the event, and whether the wind is along-fjord versus off-axis. Within this idealized model of the fjord, the forcing event leads to outcropping of deeper isohalines (up to 0.3 PSU greater) at the surface along the northern flank of the fjord, corresponding to upwelling (see Figure 11 in Lundesgaard *et al.,* 2019). Wind-induced overturning circulation, along with deepening of the mixed layer by up to 25 m, would increase surface dFe concentrations**.** These general model results showed that wind forcing caused water at depths of 50-150 m to upwell rapidly (within 24 hours) near the glacier termini. This is an important consequence explored further in the highly-resolved model representation of the study region by Hahn-Woernle *et al.* (2020).

The results of the dye experiments allow for the determination of fluxes, either prescribed (in the case of glacial meltwater) or as a result of wind forcing. St. Laurent *et al.* applied similar methods in the Amundsen Sea with explicit coupling of sea ice – ice sheet – ocean interactions (St-Laurent *et al.*, 2017). In a more rigorous biogeochemical model, which included ocean interactions with both sea ice and ice shelves, as well as parameterized Fe reactions, the productive waters in the Amundsen Sea Polynya were supplied by an advected source of dFe from the “meltwater pump” and coastal currents, but this model lacked explicit contributions of subglacial Fe (St-Laurent *et al.*, 2019). These prior modeling results highlight the importance of lateral exchange of surface water masses, providing the impetus to investigate the export of the surface water out of the fjord mouth as explored in the following section.

2.5.6.1. Surface meltwater Fe sources and export

Given that the MWf varied from 1-2.5% within Andvord Bay during the time of sampling, it is expected that the input of glacial meltwater throughout the melt season would supply some dFe to the surface. We extracted vertical profiles of MWf from the model at both stations and found that glacial meltwater originating from Bagshawe and Moser glaciers reaches maximum concentration during the summer bloom (late-January 2016) at Sill 3, relatively constrained to the upper 25 m (Fig. A7b). In early February, when the bloom was terminated, glacial meltwater concentrations in the fjord decreased due to a weakening meltwater input and lateral dispersal. The weakening input is designed to reflect the seasonal cycle of ice melting. Ocean circulation dispersed the meltwater into the Gerlache Strait, as shown by a progressive increase in meltwater in the upper water column throughout the melt season (Fig. A7a). If the volume flux of meltwater input is indeed correlated to the seasonal air temperature cycle, as it is parameterized in the model, the results in Fig. 2.3 would reaffirm that meltwater is an important control on the accumulation of phytoplankton biomass within Andvord Bay (Pan *et al.*, 2020).

The effect of the wind in driving vertical fluxes will vary with wind direction and location within the fjord. The vertical velocity is analyzed for the observation site at Sill 3 and in front of Bagshawe Glacier (IBA). The latter site is an example location for which katabatic winds are expected to lead to intensified upwelling and is also the location of the subsurface and deep dye experiments. Figure 2.9 (a) and (b) depict the relationship between the katabatic wind events and vertical velocities at 20 m: landward-blowing wind generally leads to downwelling, while seaward-blowing katabatic wind leads to upwelling. Based on observations of dFe from the late Spring prior to a wind event that started on December 11 ([dFe] at 20 m: 1.97 nM at S3, 2.01 nM at IBA), and the modeled maximum vertical velocities during the wind event (2.09×10^{-5} m s^{-1} at S3, 5.08×10^{-5} m s^{-1} at IBA), we computed the upwelling flux of dFe into the surface (20 m) at Sill 3 and IBA to be 3.54 μmol m^{-2} d^{-1} and 8.81 μmol m^{-2} d^{-1}, respectively. These results shed light on the

spatial heterogeneity of upwelling conditions within the fjord. Model results for Sill 3 are supported by late Spring observations of elevated dFe and low meltwater fraction at this station (Fig. 2.3). We argue that these punctuated periods of upwelling could be a substantial source of dFe to surface waters in Andvord Bay. Further, this supply, together with the flux of glacial meltwater, provides dFe to fuel phytoplankton community growth.

The efficiency with which wind events export the fjord surface water is explored in the glacial meltwater dye experiment. To account for the changing amount of meltwater in the fjord, export across the fjord mouth in Fig. 2.9c is given as the percentage of the total amount of dye present within the fjord to resolve the effect of katabatic winds on dispersal dynamics of Fe-rich sources. The meltwater dye experiences up to a 28-fold increased export into the Gerlache Strait during periods of strong along-fjord wind, primarily through the surface. To analyze the correlation between along-fjord wind velocity and the relative meltwater export, we first apply a 24-hr Gaussian filter to the relative export of glacial meltwater (Fig. 2.9), to exclude tidal signals. Applying the same filter to the wind time series, we find the wind and export data are positively correlated ($r = 0.628$). The correlation between export and along-fjord winds supports the results by Lundesgaard et al. (2019) who found that katabatic winds control the export of fjord water. This has important implications for the dispersal of Fe-rich waters downstream, which eventually mix with Fe-poor waters located on the continental shelf (Annett *et al.*, 2017).

2.5.6.2. Subsurface and deep sources supplying Fe to export

In addition to upwelling at the glacier terminus, periods of vertical mixing due to overturning circulation and mixed layer deepening are shown to occur during katabatic wind events (Lundesgaard *et al.*, 2019, 2020). This could be an important mechanism for supplying additional dFe to the fjord surface from the subglacial plume. Prior to the wind event on December 11, the subsurface dye increases gradually in the upper 20 m (Fig. A6b). With the onset of the wind event, the vertical transport of the subsurface dye into the upper 20 m intensifies and reaches a

maximum of 32.7 x 10^3 m^3 d^{-1}. In comparison, the deep dye does not enter the upper 20 m prior to the wind event and its maximum vertical transport is only 4.2 x 10^3 m^3 d^{-1}. It follows that katabatic wind events increase mixing in front of Bagshawe Glacier and have a particularly strong effect on water masses at intermediate depth. Assuming a mean concentration of 8.75 nM dFe for the subsurface plume (Table 2.1) and 8.68 nM dFe for deep (~300 m) IBA waters in the late Spring, these periods of vertical mixing correspond to dFe fluxes of up to 2.81 nmol dFe m^{-2} d^{-1} and 0.36 nmol m^{-2} d^{-1} (3.17 nmol m^{-2} d^{-1} combined) based on the subsurface dye and deep dye, respectively. Following the katabatic wind event, which lasted approximately 11 days, model results show that 36% of the subsurface dye has shoaled above 75 m, with 10% of dye found within the surface layer (<20 m, Fig. A6b). Of the deep water dye, less than 1% is found within the surface layer. The behavior of the deep water masses suggests an insignificant contribution of deep water masses to the surface hydrography and thus, to surface dFe inventory. The vertical fluxes estimated in this section are interpreted as a lower-bound for the contribution of the subsurface plume, since the modeled subglacial plume is a fixed volume, when in reality, subglacial meltwater might be supplied continually throughout the melt season. Compared to the flux of surface glacial meltwater input, and the flux due to subsurface and deep water mixing, the upwelling flux generated by wind events is the largest by an order of magnitude.

The quicker export of the subsurface dye, and therefore the low surface dye concentration, is mainly due to its proximity to the ocean surface (Fig. A5b). The upper water column is controlled by katabatic winds, which exports the surface layer out of the fjord mouth. In contrast, the deep dye is exported more slowly and is more continuously released to Gerlache Strait (Fig. A5c). These modeling results provide evidence for the flushing of fjord water to the Gerlache Strait which coincides with periods of intensified winds. Thus, katabatic winds are important both for replenishing the surface Fe concentrations from the subglacial plume as well as exporting Fe-rich surface waters. It is reasonable to assume that in the absence of a strengthened buoyancy-driven

overturning circulation, sources from fjord sediments are negligible in supplying the surface with dFe in Andvord Bay.

2.4.7. Wind driven meltwater export from WAP fjords

Given that the west Antarctic Peninsula hosts the greatest number of glaciomarine fjords on the continent, and multiple katabatic wind events occur throughout the year, wind events can play a crucial role for the export of Fe and Mn to the larger shelf water region. The modeled export of meltwater integrated over the week after the wind event on December 11 is 38×10^7 m^3, which is about 43% of the meltwater input during the same time. For comparison, during the following week, with relatively calm wind conditions, only 20% of the meltwater input is exported. We estimate the Fe export to be 272 mol dFe $week^{-1}$ and 245 mol dMn $week^{-1}$ for this event. However, the warming climate may lessen the likelihood for pulsed export of meltwater-derived Fe by intensifying coastal currents due to declines in sea ice (Moffat *et al.*, 2008), and reduced surface cooling, decreasing the velocity and frequency of katabatic winds over the west Antarctic Ice Sheet (Bintanja *et al.*, 2014).

The large variability in inferred dFe content of glacial meltwaters along the WAP (Annett *et al.*, 2017) means that supply likely depends on fjord-specific processes and future changes in ice volume. Advected sources of dFe remain the largest contribution (~50%) to the inventory on the productive continental shelves (De Jong *et al.*, 2015), while reducing marine sediments are thought to be the main source of dMn (Annett *et al.*, 2015; Sherrell *et al.*, 2015, 2018). Therefore, we believe that a latitudinal assessment of WAP fjords could begin to address variable responses to ocean and atmospheric forcing in these productive ecosystems. Indeed, less than 160 km south of Andvord Bay, observations of warm modified UCDW intrusions and an invigorated “meltwater pump” present an alternative mechanism for sustaining local primary production in Barilari Bay, a glaciomarine fjord (Cape *et al.*, 2019).

The scope of our results should be highlighted. If we assume Andvord Bay is representative of a typical cold-water fjord, and similarly, Barilari Bay is representative of a warm-water fjord (6% MWf at surface, Cape *et al.*, 2019) then we can estimate the glacial meltwater export resulting from a single wind event for the entire western coast of the WAP (see *Supplemental Methods*). A total of 3.6 x 10^{10} m^3 (36 km^3) of surface glacial meltwater is exported seaward, which corresponds to 2.0 x 10^6 mol dFe and 1.8 x 10^6 mol dMn. Thus, katabatic winds are highly efficient at delivering surface meltwater produced near the coast to the continental shelves and ACC, where Fe and Mn limit and co-limit primary production (Browning *et al.*, 2021). However, this volume of surface meltwater exported per year from WAP fjords is small compared to the total basal meltwater production rate due to warm ocean temperatures for the largest ice shelves in Antarctica. Using highly accurate remote sensing topographic measurements Adusumilli *et al.* (2020) found that the major Antarctic ice sheets have a steady-state meltwater production value of 1100±60 km^3 yr^{-1}. In a different modeling study, it was estimated 300 – 800 km^3 yr^{-1} meltwater enters the SO accounting for observed trends in SO sea surface temperature, sea ice expansion, and sea surface height (Rye *et al.,* 2020). It should be noted that the WAP feeds most directly into the Antarctic Circumpolar Current (ACC), which advects modified coastal waters downstream to the productive Scotia Sea region, potentially magnifying the ecological impact of WAP fjord meltwater production.

2.6. Conclusion: Andvord Bay as a source of Fe and Mn to shelf waters of the western Antarctic Peninsula

We have argued that, for glaciers terminating in cold-water fjords with a resultant absence of buoyancy-driven upwelling, the interaction of the ice sheet, atmosphere, and surface ocean is important for resupplying the surface waters with Fe throughout the summer season. Using a high-resolution ROMS model of the study region, we showed katabatic wind events result in pulsed export of the surface layer to the adjacent shelf water, while upwelling and vertical mixing

entrains subglacial plume water in the inner fjord. Observed surface concentrations of dFe in Fall lend support to these modeled dynamics since elevated concentrations of dFe and meltwater are found within the inner fjord and at Sill 3 (see Fig. 2.3). At both fjord locations, upwelling of subsurface water masses occurs, potentially entraining subglacial plume water. We summarize the findings of this study in a conceptual diagram showing important seasonal sources of Fe during the growth and melt season (Fig. 2.10). We highlight important processes in the diagram using circled number notation. We found ocean temperatures are cold ① and do not melt the fronts of glaciers, but warm summer atmospheric temperatures contribute to the surface melting of glacial ice ②. Variability in dissolved and particulate Fe concentrations in glacial ice imposes large uncertainties in the calculated Fe flux associated with melting. Iron occurs in glacial ice predominantly in the form of refractory Fe-bearing mineral particles ③. Only a small fraction of these particles may be stabilized by excess organic ligands. Another Fe source is fjord sediments ④, though there is considerable uncertainty shown in the magnitude of this flux because evidence indicates that a significant fraction of porewater Fe rapidly precipitates at the oxidative front, forming a rich surface layer of Fe oxyhydroxides at the sediment surface ⑤. Intense bioturbation of fjord sediments mixes the surface sediments downwards fueling redox processes in deeper sediment layers. The dFe that escapes this sink enriches deep waters within the fjord basins. Small amounts of subglacial meltwater discharge enter the ocean and form turbid buoyant subsurface plumes ⑥. Within the plumes, speciation is dominated by high concentrations of labile authigenic Fe-bearing particles that can be solubilized by Fe-binding organic ligands ⑦. Seaward-blowing katabatic winds ⑧ occur episodically and cause upwelling and vertical mixing supplying additional Fe to the surface phytoplankton assemblage. These intense energetic periods facilitate the dispersion and export of surface Fe, Mn, and meltwater away from the fjord where it is advected downstream in the Gerlache Strait and into the Bransfield Strait ⑨.

In Andvord Bay, primary production will be sensitive to future changes in subglacial discharge as Antarctic glaciers continue to melt in response to oceanic and atmospheric warming

(Smith *et al.*, 2020). As part of a natural tidewater glacier cycle, increased meltwater discharge will generate a greater flux of sediment to the fjord (Brinkerhoff, Truffer and Aschwanden, 2017), reducing light availability for primary producers, while stratifying the upper water column and preventing nutrient replenishment (Hopwood *et al.* 2018). A key question outside the scope of this research is how the quantity and quality of Fe-binding ligands will change in the future. To a first approximation, decreases in the magnitude of local phytoplankton blooms and associated ligand sources is expected to reduce efficacy of solubilization of particulate Fe and natural fertilization downstream resulting from this fjord. This climatic trend is not yet realized within Andvord Bay (Eidam *et al.*, 2019), but is expected to decrease dFe export through increased scavenging and sedimentation, further resembling high-Arctic and temperate fjords (Hopwood *et al.*, 2016).

2.7. Acknowledgements

The authors would like to thank all participating principal investigators and their affiliates during the NSF FjordEco project (PLR -1443705). Dr. Lauren Manck (University of Montana) assisted with sampling efforts during *NBP1603*. We would like to thank the captain and crew of R/V Laurence M. Gould and RVIB Nathaniel B. Palmer and United States Antarctic Program contractors. We also thank Dr. Brian Powell (University of Hawai`i, Manoa) for helpful comments and for providing resources for the modeling effort.

2.8. Figures and Tables

Table 2.1. Glacial ice and seawater samples analyzed for dissolved, labile, and total particulate trace metals. Crustal averages from Taylor and McClellen (1995): Mn:Fe (0.017 mol:mol), Fe:Al (0.2), and Al:Ti (35).

Sample Type	Cruise	Location		dFe [nmol kg-1]	TDFe [nmol kg-1]	TpFe [nmol L-1]	dMn [nmol kg-1]	TDMn [nmol kg-1]	TpMn [nmol L-1]	dFe:LpFe	dFe:TpFe	LpMn:LpFe [mol:mol]	TpMn:TpFe [mol:mol]	Description
												(0.017)	(0.017)	Crustal averages
Glacial Ice 1	LMG1510	Inner Basin A		211.59	122228	366332	144.85	7359	10187	0.17%	0.1%	0.059	0.028	floating
Glacial Ice 2	LMG1510	Inner Basin A		n.a.	994	13036	n.a.	61.55	435	n.a.	n.a.	0.062	0.033	floating
Glacial Ice 3	NBP1603	Neko Harbor		1.43	n.a.	56.36	1.62	n.a.	1.41	n.a.	2.5%	n.a.	0.025	floating
Glacial Ice 4	NBP1603	Neko Harbor		1.52	n.a.	52.75	1.81	n.a.	1.26	n.a.	2.9%	n.a.	0.024	floating
			AVG	71.52	61611	94869	49.43	3710	2656	0.17%	1.8%	0.061	0.028	
			STDEV	121.31	69994	181078	82.64	5160	5025		1.5%	0.002	0.004	
Plume 19_100m	NBP1603	Inner Basin A		11.64	419.89	402.26	5.82	15.73	9.169	2.9%	2.9%	0.024	0.023	seawater
Plume 20_100m	NBP1603	Inner Basin A		9.40	538.34	514.90	6.22	17.29	11.73	1.8%	1.8%	0.021	0.023	seawater
Plume 26_110m	NBP1603	Inner Basin A		7.26	227.24	330.37	5.28	11.63	7.665	2.7%	2.2%	0.024	0.023	seawater
Plume 27_110m	NBP1603	Inner Basin A		6.72	202.35	n.a.	4.79	10.36	n.a.	3.4%	n.a.	0.028	n.a.	seawater
			AVG	8.75	346.95	415.84	5.52	13.75	9.52	2.7%	2.3%	0.024	0.023	
			STDEV	2.25	160.40	93.01	0.62	3.29	2.05	0.7%	0.5%	0.003	0.0002	

Sample Type	Cruise	Location		TDAl [nmol kg-1]	TpAl [nmol kg-1]	TDTi [nmol kg-1]	TpTi [nmol kg-1]	TpFe:TpAl [mol:mol]	RpFe:RpAl [mol:mol]	TpFe:TpTi [mol:mol]	LpFe:TDAl [mol:mol]	TDAl:TDTi [mol:mol]	TpAl:TpTi [mol:mol]	Description
								(0.2)	(0.2)	(7)	(0.2)	(35)	(35)	Crustal averages
Glacial Ice 1	LMG1510	Inner Basin A		1109261	1611691	39878	51906	0.23	0.49	7.06	0.11	28	31	floating
Glacial Ice 2	LMG1510	Inner Basin A		97132	100239	1614.4	1709.0	0.13	3.88	7.63	0.01	60	59	floating
Glacial Ice 3	NBP1603	Neko Harbor		n.a.	259.19	n.a.	6.56	0.22	n.a.	8.59	n.a.	n.a.	40	floating
Glacial Ice 4	NBP1603	Neko Harbor		n.a.	262.50	n.a.	6.58	0.20	n.a.	8.02	n.a.	n.a.	40	floating
			AVG	603197	428113	20747	13407	0.19	2.18	7.82	0.06	44	42	
			STDEV	715684	790458	27057	25679	0.04	2.40	0.40	0.07	23	12	
Plume 19_100m	NBP1603	Inner Basin A		887.79	1719.1	14.57	44.45	0.23	-0.01	9.05	0.46	61	39	seawater
Plume 20_100m	NBP1603	Inner Basin A		965.50	2110.5	13.74	56.07	0.24	-0.01	9.18	0.55	70	38	seawater
Plume 26_110m	NBP1603	Inner Basin A		828.98	1373.4	13.85	34.72	0.24	0.11	9.52	0.33	60	40	seawater
Plume 27_110m	NBP1603	Inner Basin A		n.a.	n.a.	n.a.	n.a.	n.a.	n.a.	n.a.	n.a.	n.a.	n.a.	seawater
			AVG	894.09	1734.3	14.06	45.08	0.24	0.03	9.25	0.44	64	39	
			STDEV	68.48	368.79	0.45	10.69	0.01	0.07	0.24	0.11	6	1	

Table 2.2. Ligand concentrations and equilibrium constants detected in seawater samples. Fe' is the free (unbound) iron concentration. L_t is the total ligand concentration. logK is the conditional stability constant. eL is the excess ligand concentration (eL = L_t – [dFe]). log$\alpha_{FeL'}$ is the complexation capacity. $R_{Fe'}$ is the ratio of Fe' of reoccupied stations, expressed as a percentage.

	Station	Depth [m]	dFe [nM]	Fe' [pM]	L_t [nM]	±	logK	±	eL [nM]	L_t:dFe	log$\alpha_{FeL'}$	$R_{Fe'}$
December 2015 (LMG1510)	IBA	6	1.85	0.62	4.06	1.74	12.13	0.69	2.21	2.2	12.5	
	IBA	160	5.84	5.66	8.18	0.57	11.63	0.20	2.34	1.4	12.0	
	IBB	6	3.36	1.19	6.22	0.52	11.99	0.14	2.86	1.9	12.4	
	MBA	8	2.12	4.70	2.82	0.37	11.58	0.20	0.69	1.3	11.4	
	S3	11	3.41	0.79	7.27	1.97	12.05	0.44	3.85	2.1	12.6	
	S4	7	2.01	2.39	5.00	1.22	11.44	0.33	2.99	2.5	11.9	
	S4	175	4.76	5.95	5.05	1.06	10.90	0.28	0.29	1.1	10.4	
	GS	6	1.53	6.20	2.26	0.33	11.00	0.14	0.73	1.5	10.9	
	OBB	6	2.50	1.16	5.72	2.21	11.82	0.44	3.22	2.3	12.3	
April 2016 (NBP1603)	IBA	25	7.80	1.15	15.42	2.82	11.95	0.26	7.62	2.0	12.8	85%
	IBA	110	6.72	7.18	8.54	0.88	11.69	0.35	1.82	1.3	12.0	
	IBA	280	14.45	1.82	17.44	1.12	12.42	0.37	2.99	1.2	12.8	
	IBA	80	8.51	3.86	17.62	3.57	11.38	0.27	9.11	2.1	12.3	
	IBB	20	6.89	4.16	11.18	1.39	11.58	0.26	4.29	1.6	12.2	249%
	IBB	75	5.94	3.64	14.03	1.57	11.30	0.13	8.09	2.4	12.2	
	MBA	20	4.25	18.70	13.32	4.08	10.37	0.25	9.07	3.1	11.3	297%
	S3	15	5.41	15.67	15.33	2.18	11.54	0.14	9.92	3.0	12.5	1883%
	S4	25	6.93	4.63	15.40	3.11	11.20	0.24	8.47	2.2	12.1	94%
	Fjord Mouth	15	4.69	10.05	6.29	1.29	11.43	0.55	1.60	1.3	11.6	
	Fjord Mouth	120	5.37	6.56	7.34	1.87	11.60	0.68	1.97	1.4	11.9	
	GS	15	5.14	6.82	12.00	2.94	11.03	0.32	6.86	2.3	11.9	10%

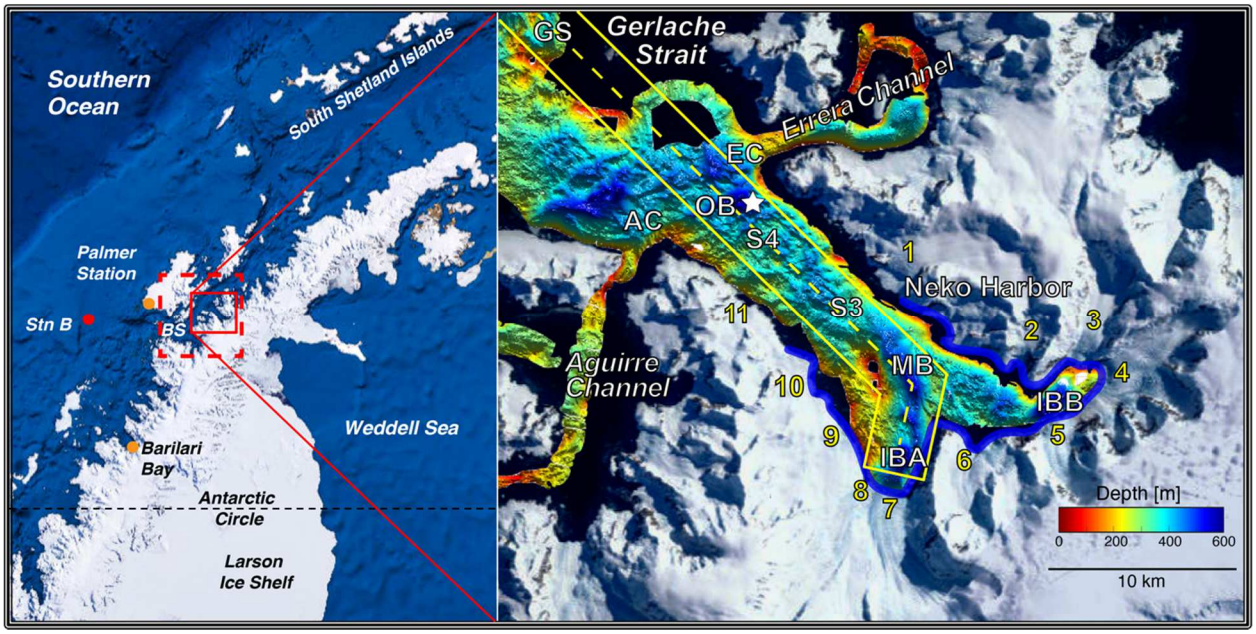

Figure 2.1. Regional map of study region (red box, inset right) and model domain (dashed red box) with nearby Palmer Station, shelf station (Stn B), and Bismarck Strait (BS). Bathymetric map of Andvord Bay with important stations labeled (GS = Gerlache Strait, AC = Aguirre Channel, EC = Errera Channel, OB = Outer Basin, S4 = Sill 4, S3 = Sill 3, MB = Middle Basin, IBA = Inner Basin A, IBB = Inner Basin B) and the surrounding tidewater glaciers numbered (4 = Moser Glacier, 7 = Bagshawe Glacier). The locations for sediment cores collected in January 2016 and included in this study are indicated by the star. The dashed yellow line indicates the transect along which vertical sections are plotted. Blue outline (inset right) shows glacial fronts where meltwater is introduced in the model.

Figure 2.2. Seasonal phytoplankton, macro-, micronutrient, temperature, and meltwater distributions plotted as sections extending from the inner basin (IB, left) towards Gerlache Strait (GS, right). Plots were made with Ocean Data View visualization software (Schlitzer, 2002, Ocean Data View, last access: 1 February 2021).

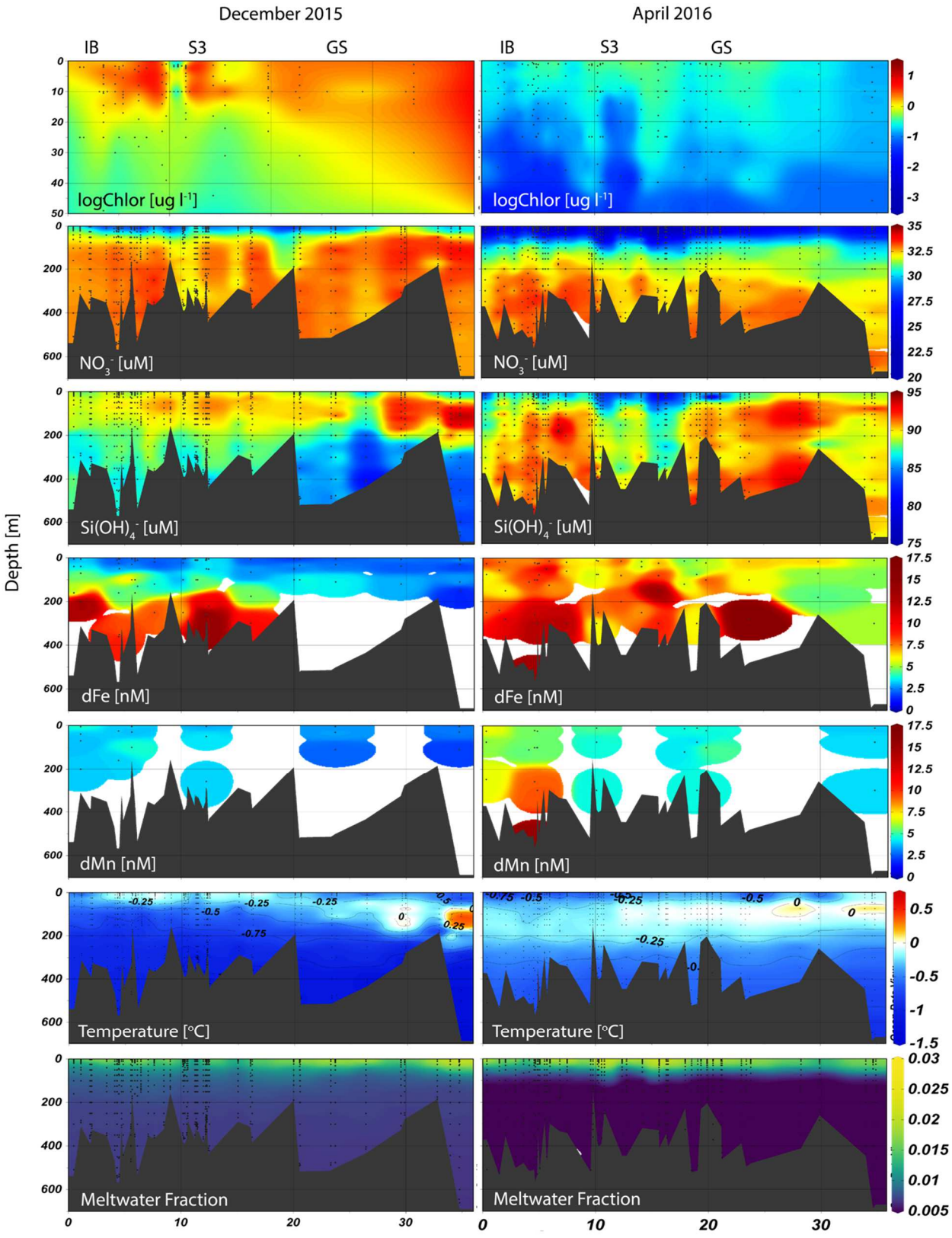
December 2015
April 2016
IB
S3
GS
logChlor [ug l-1]
NO3- [uM]
Si(OH)4- [uM]
dFe [nM]
dMn [nM]
Temperature [°C]
Meltwater Fraction
Depth [m]
Distance from Bagshawe Glacier [km]

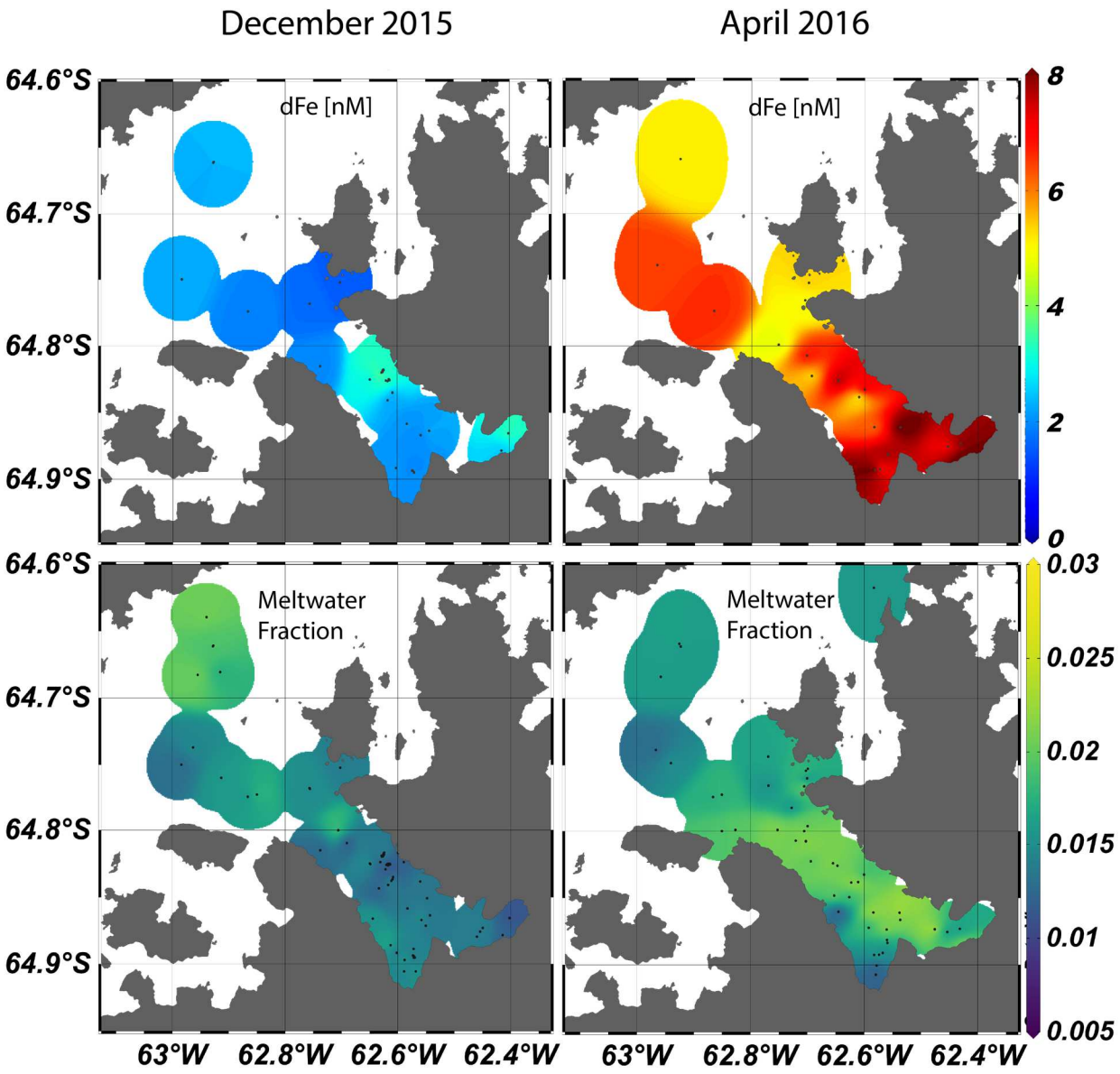

Figure 2.3. Surface (<20m) dissolved Fe (top) and meltwater fraction (bottom) for late Spring (left two panels) and Fall (right two panels). Plots were made with Ocean Data View visualization software (Schlitzer, 2002, Ocean Data View, last access: 1 February 2021).

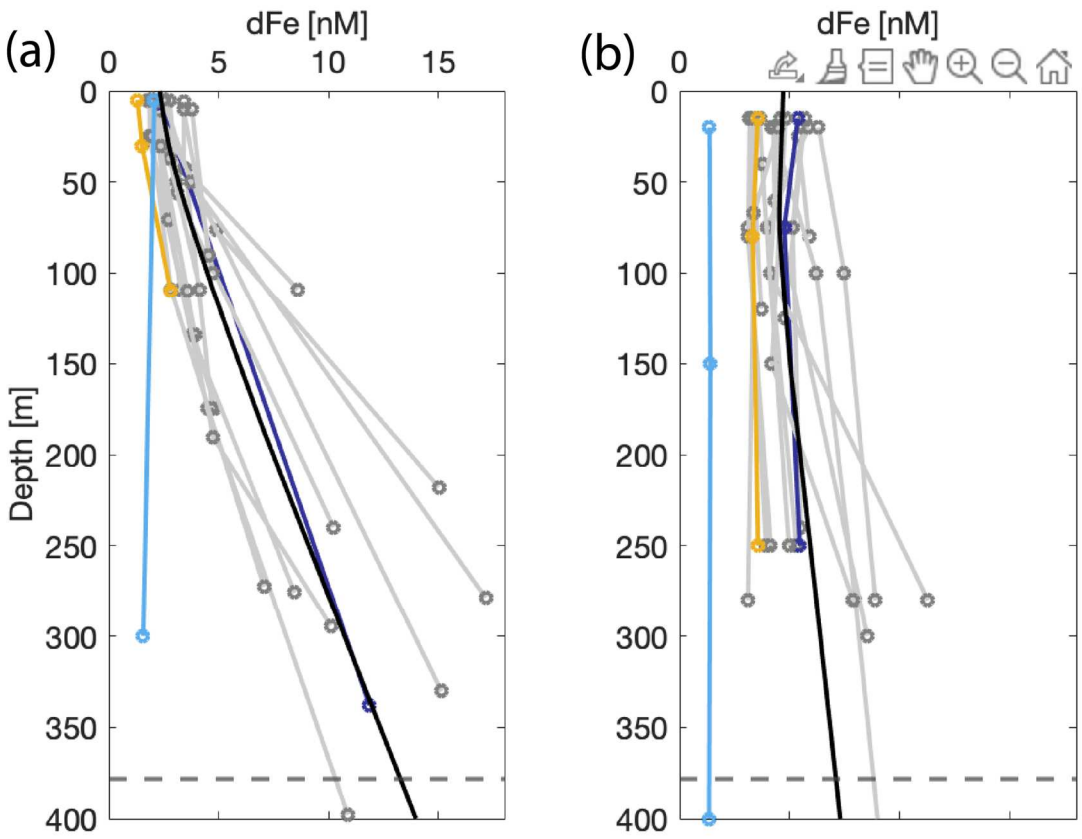

Figure 2.4. Depth profiles of dissolved Fe [nM] sampled in the Andvord Bay region for December 2015 (A) and April 2016 (B). The colored lines indicate highlighted profiles: the geometric mean of the linearly interpolated data points within Andvord Bay (black), Station B on the continental shelf (light blue, see Fig. 1), Station GS (Gerlache Strait, yellow) and Station S3 (dark blue). Other Andvord Bay stations are shown in grey. The dashed line is the average bottom depth within the fjord.

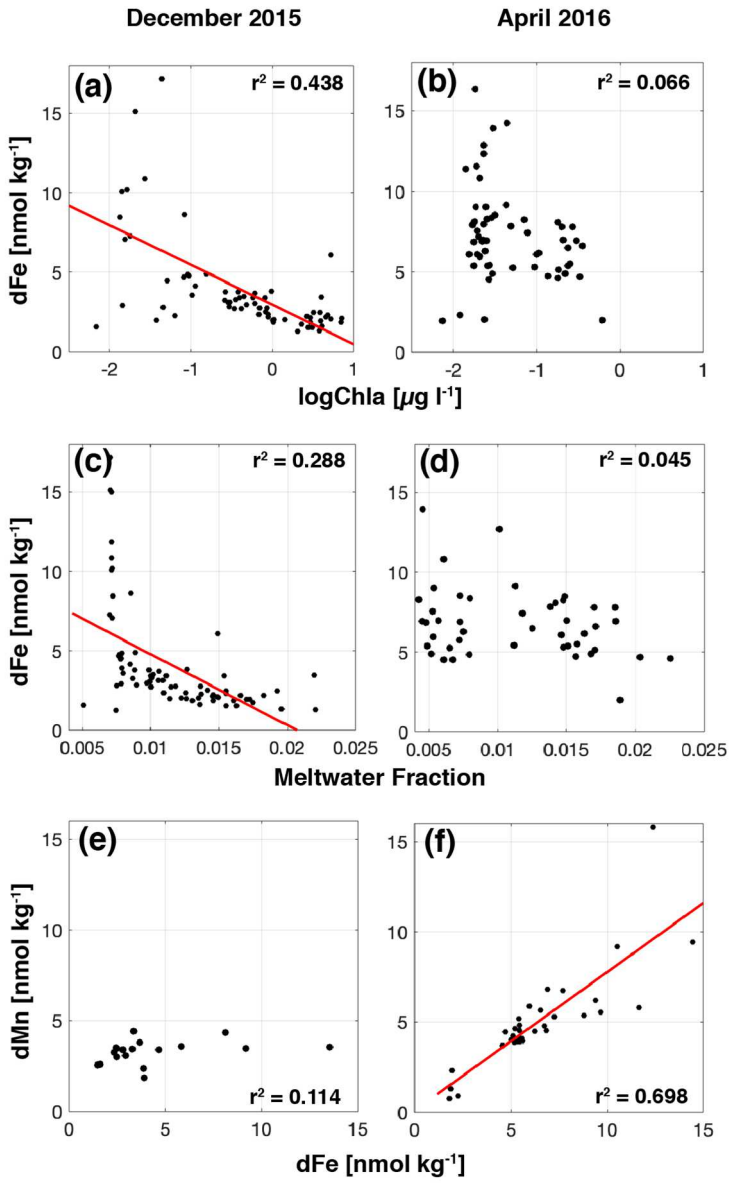

Figure 2.5.1 Dissolved trace metals plotted against observed and derived variables for December 2015 (a, c, e) and April 2016 (b, d, f). Dissolved Fe (a-b) versus logChlorophyll-a concentrations. Dissolved Fe (c-d) versus meltwater fraction. Dissolved Mn (e-f) versus dissolved Fe. Least-squares regression lines are shown where they are statistically significant ($p < 0.005$).

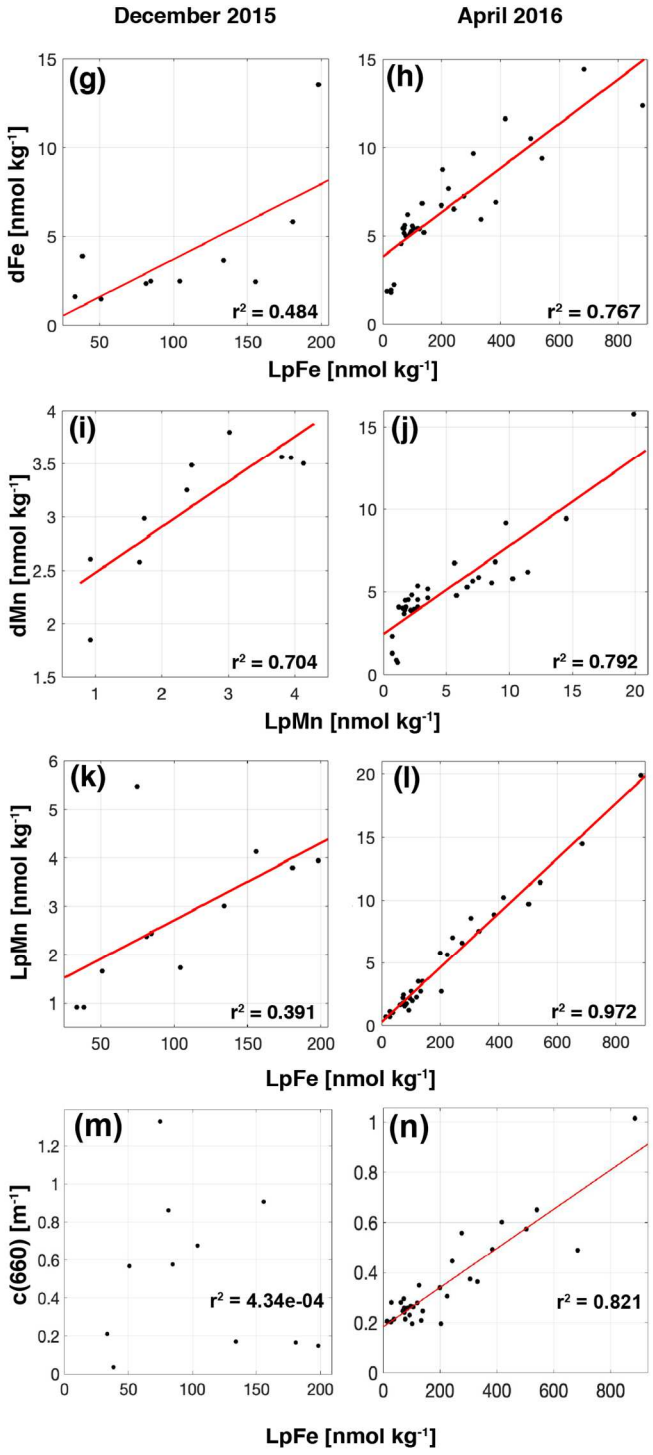

Figure 2.5.2 Dissolved Fe and Mn concentrations versus labile particulate Fe and Mn for each season. Dissolved Fe (g-h), labile particulate Mn (k-l), and beam attenuation coefficient (m-n) versus labile particulate Fe. Dissolved Mn (i-j) versus labile particulate Mn. Least-squares regression lines are shown where they are statistically significant ($p < 0.005$).

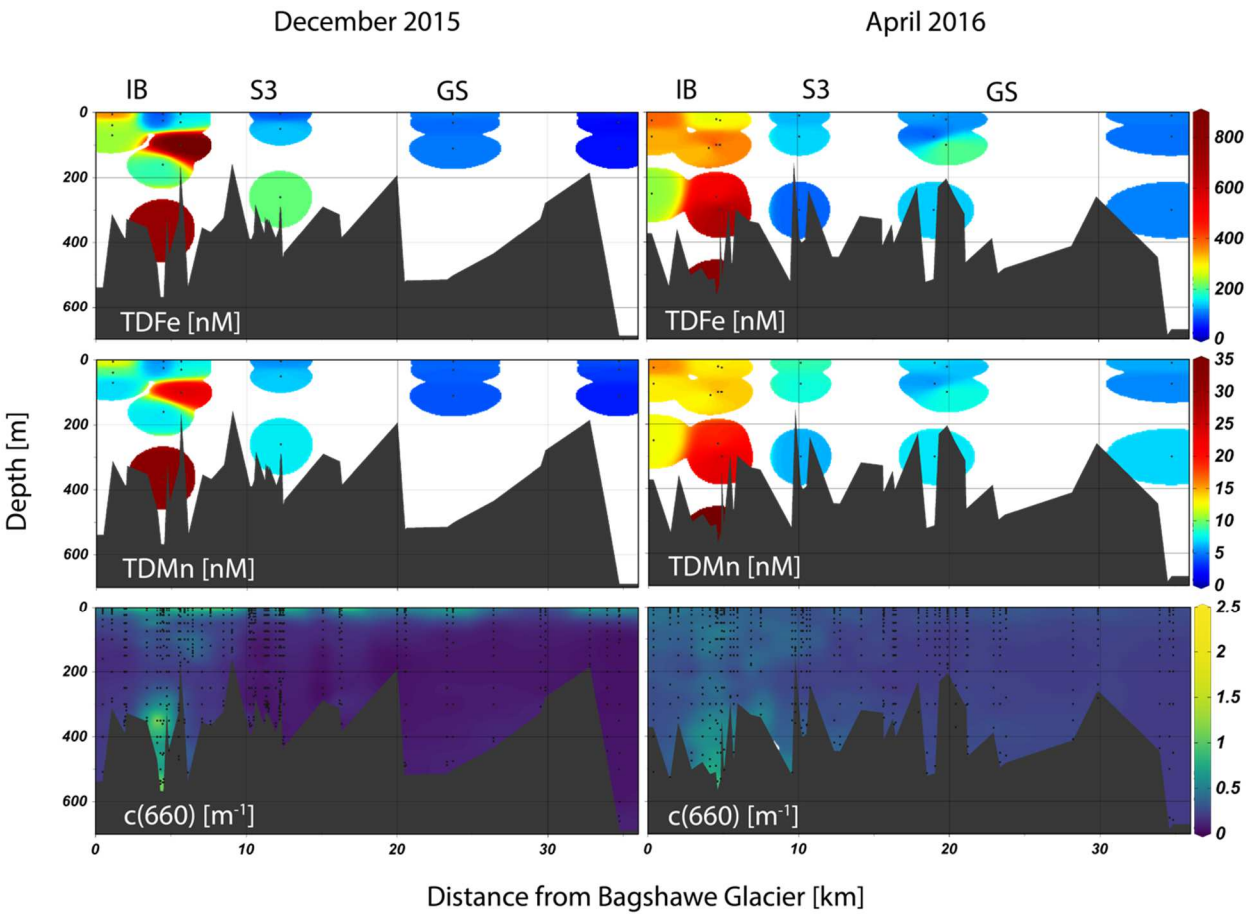

Figure 2.6. Total dissolvable trace metals and beam attenuation coefficient c(660) for both seasons. The transects are plotted as distance from the Bagshawe Glacier terminus. Plots were made with Ocean Data View visualization software (Schlitzer, 2002, Ocean Data View, last access: 1 February 2021).

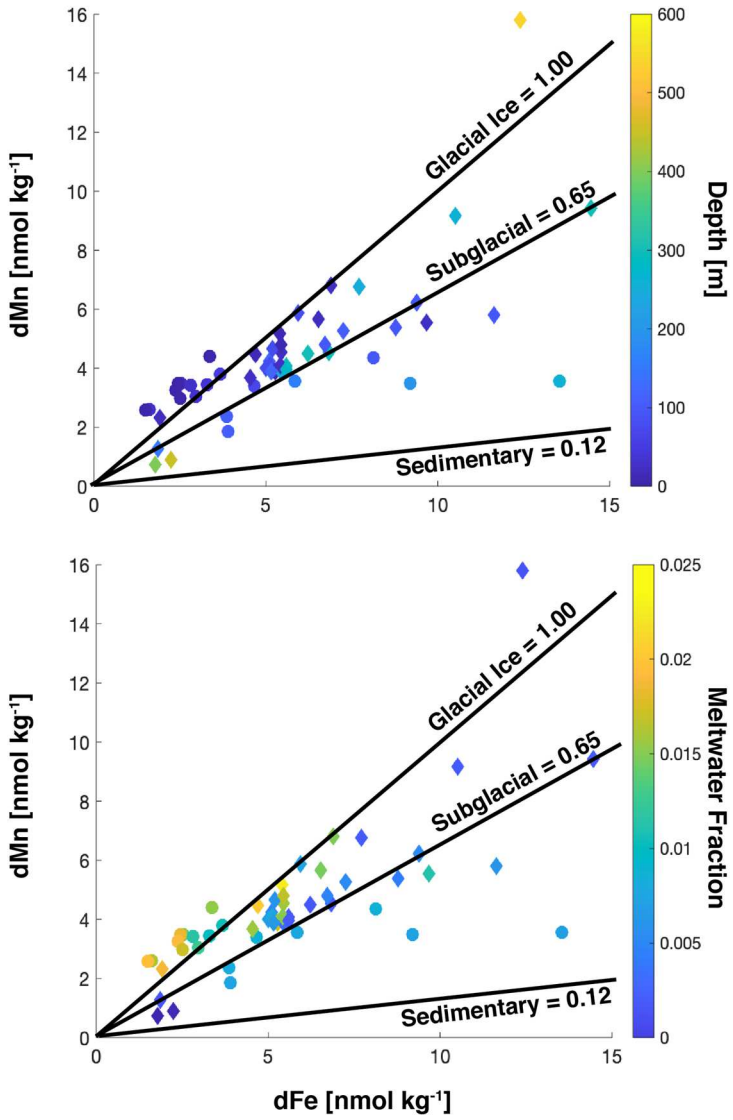

Figure 2.7. Dissolved Fe and Mn plotted for water column samples. The colorbar shows depth (top panel) or meltwater fraction (bottom panel). For both panels, December 2015 cruise is indicated by filled circles and the April 2016 cruise is indicated by filled diamonds. The lines indicate the average Mn:Fe ratio for each candidate source.

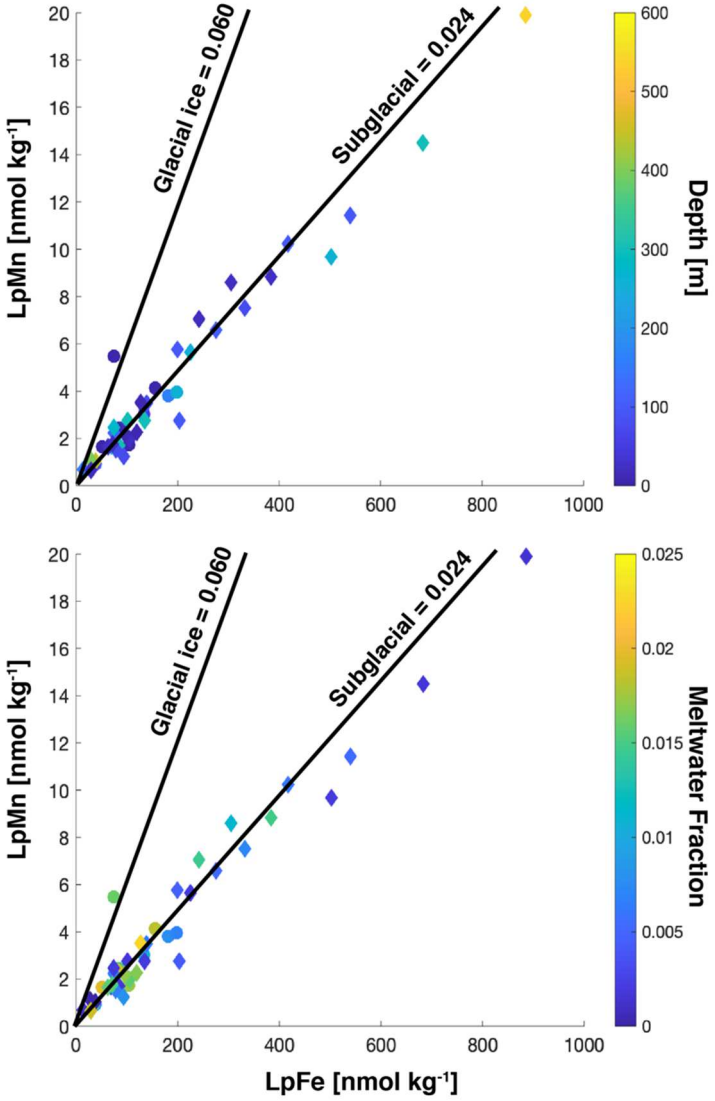

Figure 2.8. Labile particulate Fe and Mn plotted for water column samples. The colorbar shows the influence of depth (top panel) or meltwater fraction (bottom panel). For both panels, December 2015 cruise is indicated by filled circles and the April 2016 cruise is indicated by filled diamonds. The lines indicate the average ratio of Mn:Fe determined from candidate sources.

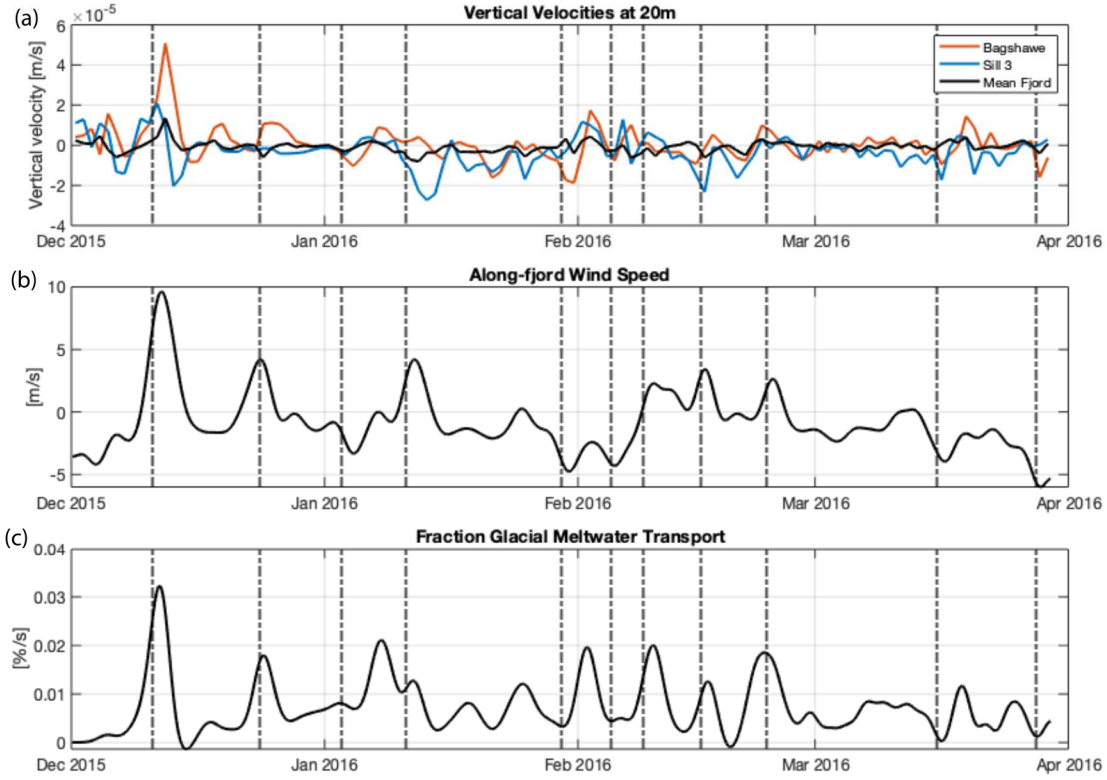

Figure 2.9. (a) Modeled vertical velocities at 20 m for the following locations: Bagshawe Glacier (IBA), Sill 3 and the fjord region average. 24 hr gaussian filter applied to time series of along-fjord wind velocity (b) and relative meltwater export out of the fjord (c). Wind events exceeding an absolute velocity of 8 m s^{-1} are indicated by vertical dashed lines. Wind speed data is based on bias-corrected RACMO model output for the center of the fjord, used to force the ROMS model. The transport of meltwater dye is shown relative to the total amount of meltwater dye within Andvord Bay to focus on the physical dynamics and not the changes in volume of dye present in the fjord.

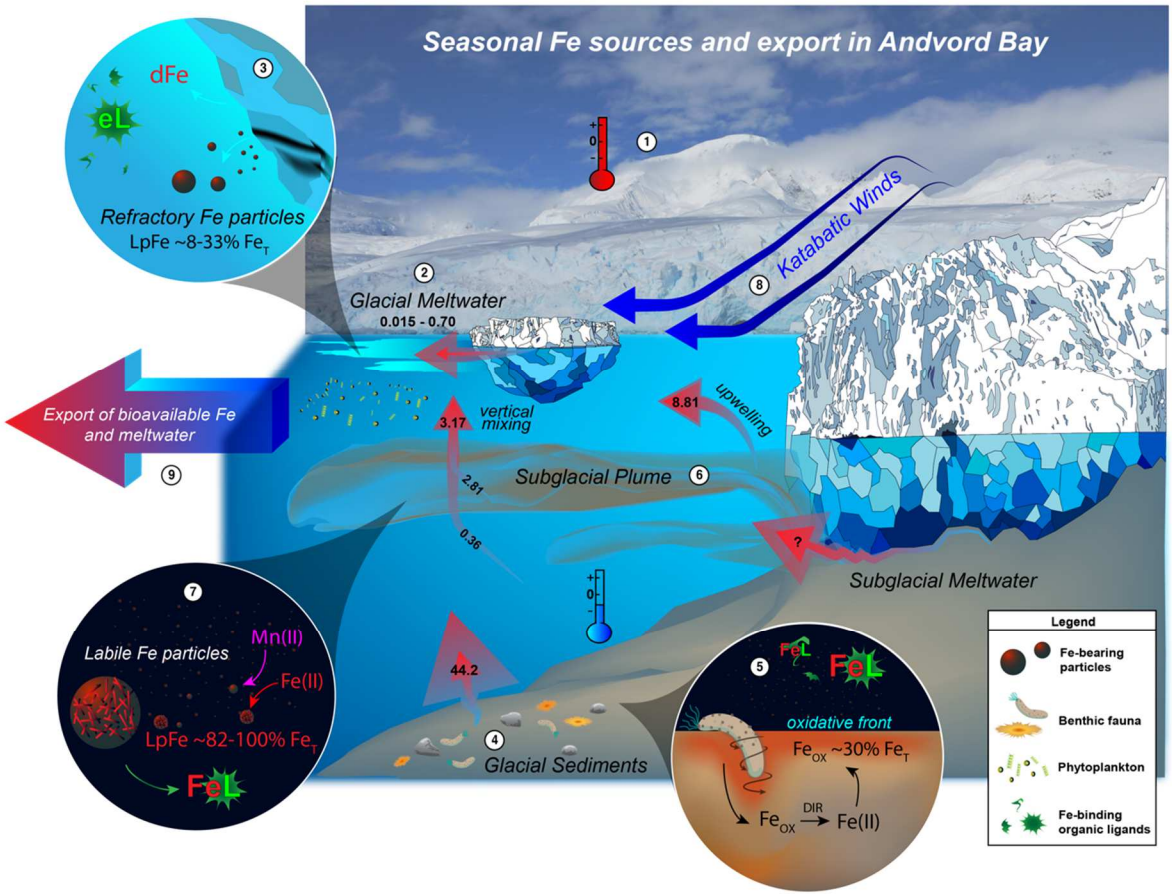

Figure 2.10. Conceptual diagram showing the important seasonal sources of new Fe during the growth and melt season. The red arrows indicate the major fluxes (in [μM m^{-2} d^{-1}]), with the size ranges showing the uncertainty in the measurement – some fluxes are difficult to quantify. These fluxes also vary from season to season and from location to location and may even be going through long-term changes due to human influences, such as climate change, though this is not shown here. The small arrows show internal transformations of Fe, which play an important role in the supply of Fe to phytoplankton. See text for a description of important processes highlighted by circled numbers.

2.9. References

Alderkamp, A. C., Mills, M. M., van Dijken, G. L., Laan, P., Thuróczy, C. E., Gerringa, L. J. A., de Baar, H. J. W., Payne, C. D., Visser, R. J. W., Buma, A. G. J. and Arrigo, K. R.: Iron from melting glaciers fuels phytoplankton blooms in the Amundsen Sea (Southern Ocean): Phytoplankton characteristics and productivity, Deep. Res. Part II Top. Stud. Oceanogr., 71–76, 32–48, doi:10.1016/j.dsr2.2012.03.005, 2012.

Annett, A. L., Skiba, M., Henley, S. F., Venables, H. J., Meredith, M. P., Statham, P. J. and Ganeshram, R. S.: Comparative roles of upwelling and glacial iron sources in Ryder Bay, coastal western Antarctic Peninsula, Mar. Chem., doi:10.1016/j.marchem.2015.06.017, 2015.

Annett, A. L., Fitzsimmons, J. N., Séguret, M. J. M., Lagerström, M., Meredith, M. P., Schofield, O. and Sherrell, R. M.: Controls on dissolved and particulate iron distributions in surface waters of the Western Antarctic Peninsula shelf, Mar. Chem., doi:10.1016/j.marchem.2017.06.004, 2017.

Ardiningsih, I., Krisch, S., Lodeiro, P., Reichart, G.-J., Achterberg, E. P., Gledhill, M., Middag, R. and Gerringa, L. J. A.: Natural Fe-binding organic ligands in Fram Strait and over the northeast Greenland shelf, Mar. Chem., 224, 103815, doi:https://doi.org/10.1016/j.marchem.2020.103815, 2020a.

Ardiningsih, I., Seyitmuhammedov, K., Sander, S. G., Stirling, C. H., Reichart, G.-J., Arrigo, K. R., Gerringa, L. J. A. and Middag, R.: Sources of Fe-binding organic ligands in surface waters of the western Antarctic Peninsula, Biogeosciences Discuss., 2020, 1–25, doi:10.5194/bg-2020-357, 2020b.

Armstrong, P. B., Lyons, W. B. and Gaudette, H. E.: Application of Formaldoxime Colorimetric Method for the Determination of Manganese in the Pore Water of Anoxic Estuarine Sediments, Estuaries, 2(3), 198–201, doi:10.2307/1351736, 1979.

Bintanja, R., Severijns, C., Haarsma, R. and Hazeleger, W.: The future of Antarctica's surface winds simulated by a high-resolution global climate model: 1. Model description and validation, J. Geophys. Res. Atmos., 119(12), 7136–7159, doi:10.1002/2013JD020847, 2014.

Boudreau, B. P.: The diffusive tortuosity of fine-grained unlithified sediments, Geochim. Cosmochim. Acta, 60(16), 3139–3142, doi:https://doi.org/10.1016/0016-7037(96)00158-5, 1996.

Bown, J., van Haren, H., Meredith, M. P., Venables, H. J., Laan, P., Brearley, J. A. and de Baar, H. J. W.: Evidences of strong sources of DFe and DMn in Ryder Bay, Western Antarctic Peninsula, Philos. Trans. A. Math. Phys. Eng. Sci., 376(2122), 20170172, doi:10.1098/rsta.2017.0172, 2018.

Boyd, P. W., Claustre, H., Levy, M., Siegel, D. A. and Weber, T.: Multi-faceted particle pumps drive carbon sequestration in the ocean, Nature, 568(7752), 327–335, doi:10.1038/s41586-019-1098-2, 2019.

Boyle, E. A., Edmond, J. M. and Sholkovitz, E. R.: The mechanism of iron removal in estuaries, Geochim. Cosmochim. Acta, 41(9), 1313–1324, doi:http://dx.doi.org/10.1016/0016-7037(77)90075-8, 1977.

Brendel, P. J. and Luther, G. W.: Development of a Gold Amalgam Voltammetric Microelectrode for the Determination of Dissolved Fe, Mn, O2, and S(-II) in Porewaters of Marine and Freshwater Sediments, Environ. Sci. Technol., doi:10.1021/es00003a024, 1995.

Brinkerhoff, D., Truffer, M. and Aschwanden, A.: Sediment transport drives tidewater glacier periodicity, Nat. Commun., 8(1), 90, doi:10.1038/s41467-017-00095-5, 2017.

Browning, T. J., Achterberg, E. P., Engel, A. and Mawji, E.: Manganese co-limitation of phytoplankton growth and major nutrient drawdown in the Southern Ocean, Nat. Commun., 12(1), 884, doi:10.1038/s41467-021-21122-6, 2021.

Buck, K. N., Sohst, B. and Sedwick, P. N.: The organic complexation of dissolved iron along the U.S. GEOTRACES (GA03) North Atlantic Section, Deep Sea Res. Part II Top. Stud. Oceanogr., 116, 152–165, doi:https://doi.org/10.1016/j.dsr2.2014.11.016, 2015.

Buck, K. N., Sedwick, P. N., Sohst, B. and Carlson, C. A.: Organic complexation of iron in the eastern tropical South Pacific: Results from US GEOTRACES Eastern Pacific Zonal Transect (GEOTRACES cruise GP16), Mar. Chem., 201, 229–241, doi:https://doi.org/10.1016/j.marchem.2017.11.007, 2018.

Burdige, D. J. and Komada, T.: Iron redox cycling, sediment resuspension and the role of sediments in low oxygen environments as sources of iron to the water column, Mar. Chem., doi:10.1016/j.marchem.2020.103793, 2020.

Cape, M. R., Vernet, M., Pettit, E. C., Wellner, J., Truffer, M., Akie, G., Domack, E., Leventer, A., Smith, C. R. and Huber, B. A.: Circumpolar Deep Water Impacts Glacial Meltwater Export and Coastal Biogeochemical Cycling Along the West Antarctic Peninsula , Front. Mar. Sci. , 6, 144, 2019.

Cook, A. J., Holland, P. R., Meredith, M. P., Murray, T., Luckman, A. and Vaughan, D. G.: Ocean forcing of glacier retreat in the western Antarctic Peninsula, Science (80-.)., 353(6296), 283 LP – 286, doi:10.1126/science.aae0017, 2016.

Cowan, E. A. and Powell, R. D.: Suspended sediment transport and deposition of cyclically interlaminated sediment in a temperate glacial fjord, Alaska, U.S.A., Geol. Soc. London, Spec. Publ., 53(1), 75 LP – 89, doi:10.1144/GSL.SP.1990.053.01.04, 1990.

Cutter, G. A. and Bruland, K. W.: Rapid and noncontaminating sampling system for trace elements in global ocean surveys, Limnol. Oceanogr. Methods, 10(6), 425–436, doi:https://doi.org/10.4319/lom.2012.10.425, 2012.

Dale, A. W., Nickelsen, L., Scholz, F., Hensen, C., Oschlies, A. and Wallmann, K.: A revised global estimate of dissolved iron fluxes from marine sediments, Global Biogeochem. Cycles, 29(5), 691–707, doi:10.1002/2014GB005017, 2015.

Death, R., Wadham, J. L., Monteiro, F., Le Brocq, A. M., Tranter, M., Ridgwell, A., Dutkiewicz, S. and Raiswell, R.: Antarctic ice sheet fertilises the Southern Ocean, Biogeosciences, doi:10.5194/bg-11-2635-2014, 2014.

Dierssen, H. M., Smith, R. C. and Vernet, M.: Glacial meltwater dynamics in coastal waters west of the Antarctic peninsula, Proc. Natl. Acad. Sci. U. S. A., doi:10.1073/pnas.032206999, 2002.

Domack, E. W. and Ishman, S.: Oceanographic and physiographic controls on modern sedimentation within Antarctic fjords, Geol. Soc. Am. Bull., doi:10.1130/0016-7606(1993)105<1175:OAPCOM>2.3.CO;2, 1993.

Domack, E. W. and Williams, C. R.: Fine structure and suspended sediment transport in three Antarctic fjords., 2011.

Egbert, G. D. and Erofeeva, S. Y.: Efficient Inverse Modeling of Barotropic Ocean Tides, J. Atmos. Ocean. Technol., 19(2), 183–204, doi:10.1175/1520-0426(2002)019<0183:EIMOBO>2.0.CO;2, 2002.

Eidam, E. F., Nittrouer, C. A., Lundesgaard, Homolka, K. K. and Smith, C. R.: Variability of Sediment Accumulation Rates in an Antarctic Fjord, Geophys. Res. Lett., doi:10.1029/2019GL084499, 2019.

Ekern, L.: Assessing Primary Production via nutrient deficits in Andvord Bay, Antarctica 2015–2016, University of California, San Diego., 2017.

Fitzsimmons, J. N., Bundy, R. M., Al-Subiai, S. N., Barbeau, K. A. and Boyle, E. A.: The composition of dissolved iron in the dusty surface ocean: An exploration using size-fractionated iron-binding ligands, Mar. Chem., doi:10.1016/j.marchem.2014.09.002, 2015.

Fitzsimmons, J. N., John, S. G., Marsay, C. M., Hoffman, C. L., Nicholas, S. L., Toner, B. M., German, C. R. and Sherrell, R. M.: Iron persistence in a distal hydrothermal plume supported by dissolved–particulate exchange, Nat. Geosci., 10(3), 195–201, doi:10.1038/ngeo2900, 2017.

Gerringa, L. J. A., Laan, P., van Dijken, G. L., van Haren, H., De Baar, H. J. W., Arrigo, K. R. and Alderkamp, A. C.: Sources of iron in the Ross Sea polynya in early summer, Mar. Chem., 2015.

Gerringa, L. J. A., Gledhill, M., Ardiningsih, I., Muntjewerf, N. and Laglera, L. M.: Comparing CLE-AdCSV applications using SA and TAC to determine the Fe-binding characteristics of model ligands in seawater, Biogeosciences, 18(19), 5265–5289, doi:10.5194/bg-18-5265-2021, 2021.

Gledhill, M. and Buck, K. N.: The organic complexation of iron in the marine environment: a review, Front. Microbiol., 3, 69, doi:10.3389/fmicb.2012.00069, 2012.

Goldberg, T., Archer, C., Vance, D., Thamdrup, B., McAnena, A. and Poulton, S. W.: Controls on Mo isotope fractionations in a Mn-rich anoxic marine sediment, Gullmar Fjord, Sweden, Chem. Geol., doi:10.1016/j.chemgeo.2011.12.020, 2012.

Grange, L. J. and Smith, C. R.: Megafaunal communities in rapidly warming fjords along the West Antarctic Peninsula: Hotspots of abundance and beta diversity, PLoS One, doi:10.1371/journal.pone.0077917, 2013.

Hahn-Woernle, L., Powell, B., Lundesgaard, Ø. and van Wessem, M.: Sensitivity of the summer upper ocean heat content in a Western Antarctic Peninsula fjord, Prog. Oceanogr., 183, 102287, doi:https://doi.org/10.1016/j.pocean.2020.102287, 2020.

Haidvogel, D. B., Arango, H., Budgell, W. P., Cornuelle, B. D., Curchitser, E., Di Lorenzo, E., Fennel, K., Geyer, W. R., Hermann, A. J., Lanerolle, L., Levin, J., McWilliams, J. C., Miller, A. J., Moore, A. M., Powell, T. M., Shchepetkin, A. F., Sherwood, C. R., Signell, R. P., Warner, J. C. and Wilkin, J.: Ocean forecasting in terrain-following coordinates: Formulation and skill assessment of the Regional Ocean Modeling System, J. Comput. Phys., 227(7), 3595–3624, doi:https://doi.org/10.1016/j.jcp.2007.06.016, 2008.

Halbach, L., Vihtakari, M., Duarte, P., Everett, A., Granskog, M. A., Hop, H., Kauko, H. M., Kristiansen, S., Myhre, P. I., Pavlov, A. K., Pramanik, A., Tatarek, A., Torsvik, T., Wiktor, J. M., Wold, A., Wulff, A., Steen, H. and Assmy, P.: Tidewater Glaciers and Bedrock Characteristics Control the Phytoplankton Growth Environment in a Fjord in the Arctic , Front. Mar. Sci. , 6, 254 [online] Available from: https://www.frontiersin.org/article/10.3389/fmars.2019.00254, 2019.

Hawkings, J. R., Wadham, J. L., Tranter, M., Raiswell, R., Benning, L. G., Statham, P. J., Tedstone, A., Nienow, P., Lee, K. and Telling, J.: Ice sheets as a significant source of highly reactive nanoparticulate iron to the oceans., Nat. Commun., 5(May), 3929, doi:10.1038/ncomms4929, 2014.

Hawkings, J. R., Hatton, J. E., Hendry, K. R., de Souza, G. F., Wadham, J. L., Ivanovic, R., Kohler, T. J., Stibal, M., Beaton, A., Lamarche-Gagnon, G., Tedstone, A., Hain, M. P., Bagshaw, E., Pike, J. and Tranter, M.: The silicon cycle impacted by past ice sheets, Nat. Commun., 9(1), 3210, doi:10.1038/s41467-018-05689-1, 2018.

Hawkings, J. R., Skidmore, M. L., Wadham, J. L., Priscu, J. C., Morton, P. L., Hatton, J. E., Gardner, C. B., Kohler, T. J., Stibal, M., Bagshaw, E. A., Steigmeyer, A., Barker, J., Dore, J. E., Lyons, W. B., Tranter, M. and Spencer, R. G. M.: Enhanced trace element mobilization by Earth's ice sheets, Proc. Natl. Acad. Sci., 117(50), 31648 LP – 31659, doi:10.1073/pnas.2014378117, 2020.

Henley, S. F., Cavan, E. L., Fawcett, S. E., Kerr, R., Monteiro, T., Sherrell, R. M., Bowie, A. R., Boyd, P. W., Barnes, D. K. A., Schloss, I. R., Marshall, T., Flynn, R. and Smith, S.: Changing Biogeochemistry of the Southern Ocean and Its Ecosystem Implications , Front. Mar. Sci. , 7, 581 [online] Available from: https://www.frontiersin.org/article/10.3389/fmars.2020.00581, 2020.

Hodson, A., Nowak, A., Sabacka, M., Jungblut, A., Navarro, F., Pearce, D., Ávila-Jiménez, M. L., Convey, P. and Vieira, G.: Climatically sensitive transfer of iron to maritime Antarctic ecosystems by surface runoff, , 8, 14499, 2017.

Hogle, S. L., Bundy, R. M., Blanton, J. M., Allen, E. E. and Barbeau, K. A.: Copiotrophic marine bacteria are associated with strong iron-binding ligand production during phytoplankton blooms, Limnol. Oceanogr. Lett., 1(1), 36–43, doi:https://doi.org/10.1002/lol2.10026, 2016.

Holding, J. M., Markager, S., Juul-Pedersen, T., Paulsen, M. L., Møller, E. F., Meire, L. and Sejr, M. K.: Seasonal and spatial patterns of primary production in a high-latitude fjord affected by Greenland Ice Sheet run-off, Biogeosciences, 16(19), 3777–3792, doi:10.5194/bg-16-3777-2019, 2019.

Hopwood, M. J., Bacon, S., Arendt, K., Connelly, D. P. and Statham, P. J.: Glacial meltwater from Greenland is not likely to be an important source of Fe to the North Atlantic, Biogeochemistry, 124(1), 1–11, doi:10.1007/s10533-015-0091-6, 2015.

Hopwood, M. J., Connelly, D. P., Arendt, K. E., Juul-Pedersen, T., Stinchcombe, M., Meire, L., Esposito, M. and Krishna, R.: Seasonal changes in Fe along a glaciated Greenlandic fjord. , Front. Earth Sci. , 4(March), 1–13, doi:10.3389/feart.2016.00015, 2016.

Hopwood, M. J., Carroll, D., Höfer, J., Achterberg, E. P., Meire, L., Le Moigne, F. A. C., Bach, L. T., Eich, C., Sutherland, D. A. and González, H. E.: Highly variable iron content modulates iceberg-ocean fertilisation and potential carbon export, Nat. Commun., 10(1), 5261, doi:10.1038/s41467-019-13231-0, 2019.

Hopwood, M. J., Carroll, D., Dunse, T., Hodson, A., Holding, J. M., Iriarte, J. L., Ribeiro, S., Achterberg, E. P., Cantoni, C., Carlson, D. F., Chierici, M., Clarke, J. S., Cozzi, S., Fransson, A., Juul-Pedersen, T., Winding, M. H. S. and Meire, L.: Review article: How does glacier discharge affect marine biogeochemistry and primary production in the Arctic?, Cryosph., 14(4), 1347–1383, doi:10.5194/tc-14-1347-2020, 2020.

Hudson, R. J. M., Rue, E. L. and Bruland, K. W.: Modeling Complexometric Titrations of Natural Water Samples, Environ. Sci. Technol., 37(8), 1553–1562, doi:10.1021/es025751a, 2003.
Jack Pan, B., Vernet, M., Reynolds, R. A. and Greg Mitchell, B.: The optical and biological properties of glacial meltwater in an Antarctic fjord, PLoS One, doi:10.1371/journal.pone.0211107, 2019.

Jackson, R. H., Straneo, F. and Sutherland, D. A.: Externally forced fluctuations in ocean temperature at Greenland glaciers in non-summer months, Nat. Geosci., 7(7), 503–508, doi:10.1038/ngeo2186, 2014.

De Jong, J. T. M., Stammerjohn, S. E., Ackley, S. F., Tison, J.-L., Mattielli, N. and Schoemann, V.: Sources and fluxes of dissolved iron in the Bellingshausen Sea (West Antarctica): The importance of sea ice, icebergs and the continental margin, Mar. Chem., 177, 518–535, doi:https://doi.org/10.1016/j.marchem.2015.08.004, 2015.

Kanna, N., Sugiyama, S., Fukamachi, Y., Nomura, D. and Nishioka, J.: Iron Supply by Subglacial Discharge Into a Fjord Near the Front of a Marine-Terminating Glacier in Northwestern Greenland, Global Biogeochem. Cycles, 34(10), e2020GB006567, doi:https://doi.org/10.1029/2020GB006567, 2020.

King, A. L. and Barbeau, K. A.: Dissolved iron and macronutrient distributions in the southern California Current System, J. Geophys. Res. Ocean., 116(C3), doi:10.1029/2010JC006324, 2011.

Krisch, S., Hopwood, M. J., Schaffer, J., Al-Hashem, A., Höfer, J., Rutgers van der Loeff, M. M., Conway, T. M., Summers, B. A., Lodeiro, P., Ardiningsih, I., Steffens, T. and Achterberg, E. P.: The 79°N Glacier cavity modulates subglacial iron export to the NE Greenland Shelf, Nat. Commun., 12(1), 3030, doi:10.1038/s41467-021-23093-0, 2021.

Kryc, K. A., Murray, R. W. and Murray, D. W.: Al-to-oxide and Ti-to-organic linkages in biogenic sediment: relationships to paleo-export production and bulk Al/Ti, Earth Planet. Sci. Lett., 211(1), 125–141, doi:https://doi.org/10.1016/S0012-821X(03)00136-5, 2003.

Lagerström, M. E., Field, M. P., Séguret, M., Fischer, L., Hann, S. and Sherrell, R. M.: Automated on-line flow-injection ICP-MS determination of trace metals (Mn, Fe, Co, Ni, Cu and Zn) in open ocean seawater: Application to the GEOTRACES program, Mar. Chem., 155, 71–

80, doi:https://doi.org/10.1016/j.marchem.2013.06.001, 2013.

Lannuzel, D., Grotti, M., Abelmoschi, M. L. and van der Merwe, P.: Organic ligands control the concentrations of dissolved iron in Antarctic sea ice, Mar. Chem., 174, 120–130, doi:https://doi.org/10.1016/j.marchem.2015.05.005, 2015.

Laufer-Meiser, K., Michaud, A. B., Maisch, M., Byrne, J. M., Kappler, A., Patterson, M. O., Røy, H. and Jørgensen, B. B.: Potentially bioavailable iron produced through benthic cycling in glaciated Arctic fjords of Svalbard, Nat. Commun., 12(1), 1349, doi:10.1038/s41467-021-21558-w, 2021.

Li, M., Toner, B. M., Baker, B. J., Breier, J. A., Sheik, C. S. and Dick, G. J.: Microbial iron uptake as a mechanism for dispersing iron from deep-sea hydrothermal vents, Nat. Commun., 5(1), 3192, doi:10.1038/ncomms4192, 2014.

Lippiatt, S. M., Lohan, M. C. and Bruland, K. W.: The distribution of reactive iron in northern Gulf of Alaska coastal waters, Mar. Chem., doi:10.1016/j.marchem.2010.04.007, 2010.

Lohan, M. C., Aguilar-Islas, A. M. and Bruland, K. W.: Direct determination of iron in acidified (pH 1.7) seawater samples by flow injection analysis with catalytic spectrophotometric detection: Application and intercomparison, Limnol. Oceanogr. Methods, 4(6), 164–171, doi:10.4319/lom.2006.4.164, 2006.

Lundesgaard, Ø., Powell, B., Merrifield, M., Hahn-Woernle, L. and Winsor, P.: Response of an antarctic Peninsula fjord to summer Katabatic wind events, J. Phys. Oceanogr., doi:10.1175/JPO-D-18-0119.1, 2019.

Lundesgaard, Ø., Winsor, P., Truffer, M., Merrifield, M., Powell, B., Statscewich, H., Eidam, E. and Smith, C. R.: Hydrography and energetics of a cold subpolar fjord: Andvord Bay, western Antarctic Peninsula, Prog. Oceanogr., doi:10.1016/j.pocean.2019.102224, 2020.

Luther, G. W., Glazer, B. T., Ma, S., Trouwborst, R. E., Moore, T. S., Metzger, E., Kraiya, C., Waite, T. J., Druschel, G., Sundby, B., Taillefert, M., Nuzzio, D. B., Shank, T. M., Lewis, B. L. and Brendel, P. J.: Use of voltammetric solid-state (micro)electrodes for studying biogeochemical processes: Laboratory measurements to real time measurements with an in situ electrochemical analyzer (ISEA), Mar. Chem., 108(3), 221–235, doi:https://doi.org/10.1016/j.marchem.2007.03.002, 2008.

Luther III, G. W., Brendel, P. J., Lewis, B. L., Sundby, B., Lefrançois, L., Silverberg, N. and Nuzzio, D. B.: Simultaneous measurement of O2, Mn, Fe, I−, and S(—II) in marine pore waters with a solid-state voltammetric microelectrode, Limnol. Oceanogr., 43(2), 325–333, doi:https://doi.org/10.4319/lo.1998.43.2.0325, 1998.

Marsay, C. M., Sedwick, P. N., Dinniman, M. S., Barrett, P. M., Mack, S. L. and McGillicuddy, D. J.: Estimating the benthic efflux of dissolved iron on the Ross Sea continental shelf, Geophys. Res. Lett., doi:10.1002/2014GL061684, 2014.

Meire, L., Mortensen, J., Meire, P., Juul-Pedersen, T., Sejr, M. K., Rysgaard, S., Nygaard, R., Huybrechts, P. and Meysman, F. J. R.: Marine-terminating glaciers sustain high productivity in Greenland fjords, Glob. Chang. Biol., 23(12), 5344–5357, doi:10.1111/gcb.13801, 2017.

Meredith, M. P., Stammerjohn, S. E., Venables, H. J., Ducklow, H. W., Martinson, D. G., Iannuzzi, R. A., Leng, M. J., van Wessem, J. M., Reijmer, C. H. and Barrand, N. E.: Changing distributions of sea ice melt and meteoric water west of the Antarctic Peninsula, Deep Sea Res. Part II Top. Stud. Oceanogr., 139, 40–57, doi:https://doi.org/10.1016/j.dsr2.2016.04.019, 2017.

Mikucki, J. A., Pearson, A., Johnston, D. T., Turchyn, A. V, Farquhar, J., Schrag, D. P., Anbar, A. D., Priscu, J. C. and Lee, P. A.: A Contemporary Microbially Maintained Subglacial Ferrous "Ocean", Science (80-.)., 324(5925), 397 LP – 400, doi:10.1126/science.1167350, 2009.

Moffat, C., Beardsley, R. C., Owens, B. and van Lipzig, N.: A first description of the Antarctic Peninsula Coastal Current, Deep Sea Res. Part II Top. Stud. Oceanogr., 55(3), 277–293, doi:https://doi.org/10.1016/j.dsr2.2007.10.003, 2008.

Mouginot, J., Rignot, E., Bjørk, A. A., van den Broeke, M., Millan, R., Morlighem, M., Noël, B., Scheuchl, B. and Wood, M.: Forty-six years of Greenland Ice Sheet mass balance from 1972 to 2018, Proc. Natl. Acad. Sci., 116(19), 9239 LP – 9244, doi:10.1073/pnas.1904242116, 2019.

Ng, H. C., Cassarino, L., Pickering, R. A., Woodward, E. M. S., Hammond, S. J. and Hendry, K. R.: Sediment efflux of silicon on the Greenland margin and implications for the marine silicon cycle, Earth Planet. Sci. Lett., 529, 115877, doi:https://doi.org/10.1016/j.epsl.2019.115877, 2020.

Oliver, H., St-Laurent, P., Sherrell, R. M. and Yager, P. L.: Modeling Iron and Light Controls on the Summer Phaeocystis antarctica Bloom in the Amundsen Sea Polynya, Global Biogeochem. Cycles, 33(5), 570–596, doi:10.1029/2018GB006168, 2019.

Omanović, D., Garnier, C. and Pižeta, I.: ProMCC: An all-in-one tool for trace metal complexation studies, Mar. Chem., 173, 25–39, doi:https://doi.org/10.1016/j.marchem.2014.10.011, 2015.

Pan, B. J., Vernet, M., Manck, L., Forsch, K., Ekern, L., Mascioni, M., Barbeau, K. A., Almandoz, G. O. and Orona, A. J.: Environmental drivers of phytoplankton taxonomic composition in an Antarctic fjord, Prog. Oceanogr., doi:10.1016/j.pocean.2020.102295, 2020.

Person, R., Aumont, O., Madec, G., Vancoppenolle, M., Bopp, L. and Merino, N.: Sensitivity of ocean biogeochemistry to the iron supply from the Antarctic Ice Sheet explored with a biogeochemical model, Biogeosciences, doi:10.5194/bg-16-3583-2019, 2019.

Poulton, S. W. and Canfield, D. E.: Development of a sequential extraction procedure for iron: implications for iron partitioning in continentally derived particulates, Chem. Geol., 214(3), 209–221, doi:https://doi.org/10.1016/j.chemgeo.2004.09.003, 2005.

Pritchard, H. D. and Vaughan, D. G.: Widespread acceleration of tidewater glaciers on the Antarctic Peninsula, J. Geophys. Res. Earth Surf., 112(F3), doi:10.1029/2006JF000597, 2007.
Raiswell, R. and Canfield, D. E.: The Iron Biogeochemical Cycle Past and Present, Geochemical Perspect., 1(1), 1–220, doi:10.7185/geochempersp.1.1, 2012.

Raiswell, R., Hawkings, J., Elsenousy, A., Death, R., Tranter, M. and Wadham, J.: Iron in Glacial Systems: Speciation, Reactivity, Freezing Behavior, and Alteration During Transport, Front. Earth Sci., doi:10.3389/feart.2018.00222, 2018.

Rignot, E., Jacobs, S., Mouginot, J. and Scheuchl, B.: Ice-Shelf Melting Around Antarctica, Science (80-.)., 341(6143), 266 LP – 270, doi:10.1126/science.1235798, 2013.

Rudnick, R. L. and Gao, S.: Composition of the Continental Crust, in Treatise on Geochemistry: Second Edition., 2013.

Schlosser, C., Schmidt, K., Aquilina, A., Homoky, W. B., Castrillejo, M., Mills, R. A., Patey, M. D., Fielding, S., Atkinson, A. and Achterberg, E. P.: Mechanisms of dissolved and labile particulate iron supply to shelf waters and phytoplankton blooms off South Georgia, Southern Ocean, Biogeosciences, 15(16), 4973–4993, doi:10.5194/bg-15-4973-2018, 2018.

Schodlok, M. P., Menemenlis, D. and Rignot, E. J.: Ice shelf basal melt rates around Antarctica from simulations and observations, J. Geophys. Res. Ocean., doi:10.1002/2015JC011117, 2016.

Schroth, A. W., Crusius, J., Hoyer, I. and Campbell, R.: Estuarine removal of glacial iron and implications for iron fluxes to the ocean, Geophys. Res. Lett., 41(11), 3951–3958, doi:10.1002/2014GL060199, 2014.

Severmann, S., McManus, J., Berelson, W. M. and Hammond, D. E.: The continental shelf benthic iron flux and its isotope composition, Geochim. Cosmochim. Acta, 74(14), 3984–4004, doi:https://doi.org/10.1016/j.gca.2010.04.022, 2010.

Sherrell, R. M., Lagerström, M. E., Forsch, K. O., Stammerjohn, S. E. and Yager, P. L.: Dynamics of dissolved iron and other bioactive trace metals (Mn, Ni, Cu, Zn) in the Amundsen Sea Polynya, Antarctica, Elem. Sci. Anthr., 3, 000071, doi:10.12952/journal.elementa.000071, 2015.

Sherrell, R. M., Annett, A. L., Fitzsimmons, J. N., Roccanova, V. J. and Meredith, M. P.: A “shallow bathtub ring” of local sedimentary iron input maintains the Palmer Deep biological hotspot on the West Antarctic Peninsula shelf, Philos. Trans. R. Soc. A Math. Phys. Eng. Sci., doi:10.1098/rsta.2017.0171, 2018.

Smith, B., Fricker, H. A., Gardner, A. S., Medley, B., Nilsson, J., Paolo, F. S., Holschuh, N., Adusumilli, S., Brunt, K., Csatho, B., Harbeck, K., Markus, T., Neumann, T., Siegfried, M. R. and Zwally, H. J.: Pervasive ice sheet mass loss reflects competing ocean and atmosphere processes, Science (80-.)., eaaz5845, doi:10.1126/science.aaz5845, 2020.

St-Laurent, P., Yager, P. L., Sherrell, R. M., Stammerjohn, S. E. and Dinniman, M. S.: Pathways and supply of dissolved iron in the Amundsen Sea (Antarctica), J. Geophys. Res. Ocean., 122(9), 7135–7162, doi:10.1002/2017JC013162, 2017.

St-Laurent, P., Yager, P. L., Sherrell, R. M., Oliver, H., Dinniman, M. S. and Stammerjohn, S. E.: Modeling the Seasonal Cycle of Iron and Carbon Fluxes in the Amundsen Sea Polynya, Antarctica, J. Geophys. Res. Ocean., doi:10.1029/2018JC014773, 2019.

Straneo, F. and Cenedese, C.: The Dynamics of Greenland’s Glacial Fjords and Their Role in Climate, Ann. Rev. Mar. Sci., doi:10.1146/annurev-marine-010213-135133, 2015.

Tagliabue, A., Bowie, A. R., DeVries, T., Ellwood, M. J., Landing, W. M., Milne, A., Ohnemus, D.

C., Twining, B. S. and Boyd, P. W.: The interplay between regeneration and scavenging fluxes drives ocean iron cycling, Nat. Commun., 10(1), 4960, doi:10.1038/s41467-019-12775-5, 2019.

Taylor, R. S., DeMaster, D. J. and Burdige, D. J.: Assessing the distribution of labile organic carbon from diverse depositional environments on the West Antarctic Peninsula shelf, Deep Sea Res. Part I Oceanogr. Res. Pap., 156, 103166, doi:https://doi.org/10.1016/j.dsr.2019.103166, 2020.

Taylor, S. R. and McLennan, S. M.: The geochemical evolution of the continental crust, Rev. Geophys., 33(2), 241–265, doi:10.1029/95RG00262, 1995.

Thuróczy, C.-E., Gerringa, L. J. A., Klunder, M., Laan, P., Le Guitton, M. and de Baar, H. J. W.: Distinct trends in the speciation of iron between the shallow shelf seas and the deep basins of the Arctic Ocean, J. Geophys. Res. Ocean., 116(C10), doi:10.1029/2010JC006835, 2011.

Thuróczy, C. E., Alderkamp, A. C., Laan, P., Gerringa, L. J. A., Mills, M. M., Van Dijken, G. L., De Baar, H. J. W. and Arrigo, K. R.: Key role of organic complexation of iron in sustaining phytoplankton blooms in the Pine Island and Amundsen Polynyas (Southern Ocean), Deep. Res. Part II Top. Stud. Oceanogr., doi:10.1016/j.dsr2.2012.03.009, 2012.

Twining, B. S., Baines, S. B., Fisher, N. S. and Landry, M. R.: Cellular iron contents of plankton during the Southern Ocean Iron Experiment (SOFeX), Deep. Res. Part I Oceanogr. Res. Pap., doi:10.1016/j.dsr.2004.08.007, 2004.

Vernet, M., Martinson, D., Iannuzzi, R., Stammerjohn, S., Kozlowski, W., Sines, K., Smith, R. and Garibotti, I.: Primary production within the sea-ice zone west of the Antarctic Peninsula: I-Sea ice, summer mixed layer, and irradiance, Deep. Res. Part II Top. Stud. Oceanogr., doi:10.1016/j.dsr2.2008.05.021, 2008.

Wagener, P., Schwenke, A. and Barcikowski, S.: How Citrate Ligands Affect Nanoparticle Adsorption to Microparticle Supports, Langmuir, 28(14), 6132–6140, doi:10.1021/la204839m, 2012.

van Wessem, J. M., Reijmer, C. H., Lenaerts, J. T. M., van de Berg, W. J., van den Broeke, M. R. and van Meijgaard, E.: Updated cloud physics in a regional atmospheric climate model improves the modelled surface energy balance of Antarctica, Cryosph., 8(1), 125–135, doi:10.5194/tc-8-125-2014, 2014.

Wu, J., Boyle, E., Sunda, W. and Wen, L.-S.: Soluble and colloidal iron in the oligotrophic North Atlantic and North Pacific, Science (80-.)., 293(5531), 847–849, 2001.

Wu, M., McCain, J. S. P., Rowland, E., Middag, R., Sandgren, M., Allen, A. E. and Bertrand, E. M.: Manganese and iron deficiency in Southern Ocean Phaeocystis antarctica populations revealed through taxon-specific protein indicators, Nat. Commun., 10(1), 3582, doi:10.1038/s41467-019-11426-z, 2019.

Zhang, R., John, S. G., Zhang, J., Ren, J., Wu, Y., Zhu, Z., Liu, S., Zhu, X., Marsay, C. M. and Wenger, F.: Transport and reaction of iron and iron stable isotopes in glacial meltwaters on Svalbard near Kongsfjorden: From rivers to estuary to ocean, Earth Planet. Sci. Lett., 424, 201–211, 2015.

Ziegler A.F., Smith, C. R., Edwards, K.F., and Maria, V.: Glacial dropstones: islands enhancing seafloor species richness of benthic megafauna in West Antarctic Peninsula fjords, Mar. Ecol. Prog. Ser., 583, 1–14 [online] Available from: https://www.int-res.com/abstracts/meps/v583/p1-14/, 2017.

Ziegler, A. F., Cape, M., Lundesgaard, Ø. and Smith, C. R.: Intense deposition and rapid processing of seafloor phytodetritus in a glaciomarine fjord, Andvord Bay (Antarctica), Prog. Oceanogr., 187, 102413, doi:https://doi.org/10.1016/j.pocean.2020.102413, 2020.

2.10. Appendix

2.10.1 Supplemental Methods: Estimating particulate matter crustal and authigenic fractions

To estimate the fractional contribution of crustal, biogenic, and authigenic particulate matter in our samples using equation 4, we first identify the geochemical composition of the weathered source bedrock surrounding Andvord Bay. It is known that there is widespread volcanism and metamorphism (Jordan, Riley and Siddoway, 2020), and thus, ratios (Me:Al, where Me is either Fe or Mn) should reflect basaltic and andesitic crusts. However, uncertainty of the source of weathered particulate matter leads us to use average upper continental crust values (Table 1), although any contribution of a volcanic source would lead to some enrichment of TpFe and TpMn relative to TpAl and a greater estimate of the crustal contribution. Equation 4 allows for the calculation of the crustal contribution:

$$\%crustal = ([TpAl]_{sample} * Me{:}\,Al_{crustal})/[TpMe]_{sample} \quad (4)$$

After accounting for a biological contribution based on Me:P quotas for Fe-replete diatom cultures (0% for all samples, data not shown), we then assume the remaining particulate fraction to be authigenic.

2.10.2 Supplemental Methods: Limitations of surface meltwater dye experiment

When we examine the time series derived from the model, we find the model consistently underestimates the contribution of meltwater to the surface (Fig. S8). The MWf does not exceed 0.0013 at either S3 or GS stations, and its seasonal maximum of 0.0046 is found at IBB in early February. Since processes like melting of drifting icebergs and sea ice cannot be captured in the model, the applied meltwater flux is based on a simplified representation of all new freshwater sources except for precipitation in Andvord Bay. These sources include, for example, surface runoff and local melt of glacial ice exposed to the atmosphere. The flux which best recreates observed salinity and temperature profiles in Andvord Bay was achieved by a meltwater input of 0.15 GT over 4 months (Hahn-Woernle *et al.*, 2020).

The overall low modeled meltwater fraction is likely a consequence of multiple factors of which we discuss three. First, the meltwater was tracked only for the field season. The generally low salinity in the upper layer at the beginning of the season and the presence of meltwater dye at the end of the summer season (fjord average of 0.0003 MWf in upper 20m) suggested that meltwater can reside for multiple years in the fjord and cannot be fully captured by our meltwater dye. Second, local melt of glacial ice, e.g. floating icebergs, caused by a summertime surface heat flux, can have a strong impact on the MWf in the surface layer and is likely to be underestimated and not well-represented with the parameterization of the modeled meltwater input. Third, only meltwater from the inner Andvord Bay is tracked and other sources are neglected. Based on other modeled meltwater dyes that track sources just outside Andvord Bay, the impact of the external sources is minor (maximum of 0.0003 MWf in early February) compared to the local sources, but they still contribute to the seasonal increase in MWf.

2.10.2 Supplemental Methods: Estimating total surface meltwater export from WAP fjords

To estimate the meltwater export resulting from a single katabatic wind event along the WAP, we first identify two fjord types: 1) fjords where waters are below the freezing temperature (cold-water); and 2) fjords where intrusions of modified UCDW reach the glacier terminus (warm-

water). This distinction leads to different MWf production rates. We use data collected from Andvord Bay as a basis for export occurring in cold-water fjords. In this instance, a maximum MWf of 0.025 was observed, which corresponded to an export of $38x10^7$ m^3 glacial meltwater and is based on the glacial meltwater dye export across the mouth of Andvord Bay integrated over the duration of a week-long katabatic wind event.

Meltwater runoff from glaciers due to warm atmospheric temperatures is parameterized as a function of number of days above a temperature threshold. The area of the glacier in contact with the atmosphere predicts how much meltwater is generated. We use this simple relationship with surface area and relate it to the MWf we observe, allowing us to estimate the fractional contribution from each glacier in Andvord Bay. As an example, Bagshawe Glacier has an area of 250 km^2, which is 48% of the total glacier area for this fjord, and so would be responsible for producing 48% of the surface glacial meltwater (~18.4×10^7 m^3). By dividing the total surface glacial meltwater export for a single katabatic wind event by the total area of glaciers in Andvord Bay, we calculate the export rate of meltwater in Andvord Bay glaciers to be 7.4×10^5 m^3 km^{-2} assuming glaciers have an equal rate of meltwater production per unit area. We use this rate as representative for cold-water type glaciers.

Since warm atmospheric temperatures in contact with the glacier surface cause production of meltwater, which enters the ocean as surface runoff, this seems a reasonable assumption. Additionally, intrusions of modified UCDW can reach the glacier terminus, causing slightly higher fractions of meltwater at the surface (~0.06 in Barilari Bay). Our general model results showed exchange with water outside of the fjord occurred during katabatic wind events, including inflow of water masses at depth located from outside of the fjord. Thus, these events are likely to enhance delivery of modified UCDW to the glacier terminus (Jackson, Straneo and Sutherland, 2014). We scale the meltwater export to the meltwater fraction since both Barilari and Andvord Bays had similar mixed layer depths. Also, ~40% export of meltwater during katabatic wind events in our model is reasonable compared to estimates for Arctic fjords (10-50%, Jackson

et al., 2014). Based on the area of glaciers in Barilari, we calculate an export rate of meltwater for representative warm-water glaciers to be 10.2 x 10^5 m^3 km^{-2}. We extrapolate these rough estimates for all glaciers on the western coast of the WAP identified by Cook et al. (2016). All glaciers to the south of Andvord Bay are considered warm-water, while those to the north are cold-water (Fig. S9). The area of each of the glaciers used here is published in Cook *et al.* (2016).

Summing the entire volume export of surface glacial meltwater, we find that if all surface waters along the western coast of the WAP experienced a single katabatic wind event, reminiscent of the one recorded in Andvord Bay, a total of 3.6 x 10^{10} m^3 (36 km^3) of surface glacial meltwater is exported towards the continental shelf (5 km^3 from cold-water glaciers; 31 km^3 from warm-water glaciers). This latitudinal difference is consistent with greater meltwater fractions found on the continental shelf in the southern lines of the PAL LTER grid (Annett *et al.*, 2017). Based on a recent compilation of TDFe content in icebergs from Antarctica (Hopwood *et al.*, 2019), and including two measurements from our study, we use a median concentration of 544 nM (n = 57). We then assume a rough estimate for 10% of TDFe as the dissolved phase, which yields a dFe content of glacial meltwater to be 54.4 nM. This is close to our average dFe measured for three glacial ice pieces in this study (71±121 nM). To our knowledge, there are no other measurements of dMn in glacial ice, so we use our mean for three glacial ice pieces from this study (49±82 nM). We estimate a single wind event lasting one week on the western coast of the WAP corresponds to an export of 2.0 x 10^6 mol dFe and 1.8 x 10^6 mol dMn.

We realize this analysis does not take in to account the impact of shallow sills in fjords that might be important for restricting UCDW from entering the fjord mouth and interacting with glaciers. Invigorated upwelling due to buoyant plumes originating at the glacier face is expected to have a positive feedback on the melting of the glacier terminus by increasing the delivery of modified UCDW to glaciers and enhancing melt (Cape *et al.*, 2019). This may be driven by warm ocean temperatures, directly melting the face of the glaciers, or atmospheric warming could increase drainage of surface melt to the base of the glacier, resulting in subglacial discharge and

buoyant plumes driving circulation. Directionality of the katabatic winds is an important parameter for wind forcing in fjords surrounded by steep topographic features (Lundesgaard *et al.*, 2019). We have explored the possibility when one katabatic wind event per year occurs in the along-fjord direction (seaward) for the entire western coast of the WAP. These mechanisms are fjord specific and deserve further attention due to the complex interactions between the ice, ocean, and atmosphere. We also concede that areal extent of glaciers may not be the most representative measure for meltwater production, when in fact glacier flow velocities might better correlate with meltwater production rates, and thus, meltwater export rates. However, the interplay between surface melt and the subglacial hydrological system, and thus flow rates could mean this is a sufficient, albeit rough assumption. Finally, large uncertainties exist for the average glacial ice content of dFe and the degree to which TDFe may be solubilized and made bioavailable. This analysis does not take into account the large quantities of solid ice (i.e., icebergs) exported via this mechanism.

2.10.4 Figures and Tables

Table A1. Seawater samples: Fe, Mn determined for the dissolved (dTM, 0.2 μm) and the total dissolvable (TDTM) determined by FIA and ICPMS methods, and collected during LMG1510 and NBP1604. Additional information covers sampling date, location (station), and latitude and longitude.

Date Sampled	Station Name	Latitude [deg N]	Longitude [deg E]	Depth [m]	FIA [nM] dFe	ICPMS [nM] dFe	dMn	TDFe	TDMn
11/27/15	SIII 5	-64.7498	-62.9844	8	2.29				
				35	1.97				
				134	2.93				
11/28/15	MBA	-64.8582	-62.5832	8	2.12				
				25	1.88				
				134	3.77				
				276	8.44				
11/29/15	SIII 3	-64.8407	-62.6176	5	2.08				
				25	1.97				
				109	2.83				
				273	7.06				
11/30/15	IBA	-64.8635	-62.5434	6	2.32				
				15	2.14				
				109	3.26				
				174	4.83				
12/1/15	SIII 4	-64.8149	-62.7378	7	2.01				
				71	2.70				
				191	4.76				
				294	10.09				
12/2/15	IBA	-64.8937	-62.5724	5	1.85			154.91	7.48
				27	1.87	2.52	3.49	170.70	8.33
				174	4.47	5.84	3.56	992.57	22.70
				398	10.87			355.82	12.02
12/3/15	IBB	-64.8783	-62.4146	5	2.51			239.87	9.38
				43	3.48			230.98	6.88
				174	4.69				
12/3/15	SIII 3	-64.8180	-62.6261	11	2.49				
				338	11.86				
12/4/15	SIII 3	-64.8180	-62.6261	11	6.05				
12/4/15	SIII 3	-64.8180	-62.6261	11	3.82				
12/4/15	SIII 3	-64.8180	-62.6261	11	2.25				
				330	15.13				
12/5/15	IBA	-64.8915	-62.6025	5	2.18	2.46	3.50		
				33	2.71	2.81	3.42		
				109	8.60	8.14	4.36		
12/6/15	IBB	-64.8654	-62.4024	6	3.41	3.36	4.40		
				43	3.40	3.29	3.45		
				76	4.88	4.67	3.39		
				218	15.01	9.19	3.49		
12/7/15	MBB	-64.8252	-62.6492	5	2.78				
				56	3.12				
				240	10.22				
12/8/15	SIII 3	-64.8175	-62.6251	4	2.49	2.37	3.25	83.61	5.63
				50	3.72	3.66	3.80	137.58	6.81
				279	17.14	13.55	3.56	211.86	7.51
12/9/15	OBA	-64.7680	-62.7565	5	1.73			104.42	4.62
				37	2.74			90.99	4.42
				109	4.16			102.24	4.16
12/9/15	Gerlache Strait	-64.6607	-62.9274	11	3.44				
				121	1.25				
12/10/15	MBA	-64.8669	-62.5585	4	1.96				
				134	3.92				
12/11/15	IBA	-64.8950	-62.5704	5	2.19				
12/11/15	Gerlache Strait	-64.6613	-62.9283	5	1.31	1.49	2.58	52.27	4.24
				30	1.51	1.61	2.60	35.17	3.53
				110	2.81	3.91	1.85	42.25	2.77
12/12/15	OBB	-64.7738	-62.8663	5	1.95	2.50	2.98		
				30	2.33	2.96	3.06		
				110	3.58	3.87	2.37		
12/12/15	SIII 3	-64.8257	-62.6204	10	3.40				
				100	4.76				
12/13/15	SIII 3	-64.8255	-62.6141	10	3.12				
12/13/15	SIII 3	-64.8248	-62.6155	10	3.29				
12/13/15	SIII 3	-64.8261	-62.6176	10	3.78				
				90	4.53				
12/14/15	Errera Strait	-64.7520	-62.7026	5	1.53				
				35	2.36				
				100	2.98				
12/16/15	IBA	-64.8936	-62.5737	5	2.01				
				50	3.05				
				344	7.28				
12/17/15	SIII 3	-64.8348	-62.6089	4	1.61				
12/18/15	SIII 4	-64.8095	-62.6908	5	5.52				
12/20/15	Station B	-64.7732	-65.3177	5	2.07				
				300	1.57				
4/6/16	SIII 4	-64.8072	-62.7027	25	6.93				
				80	8.35				
				150	13.93				
				300	9.03				
4/7/16	IBA	-64.8812	-62.5598	25	7.80				
				80	8.51				
4/8/16	Andvord Front	-64.7990	-62.7525	15	4.69	4.69	4.46		
				120	5.37	5.10	4.24		
4/9/16	Errera Strait	-64.7525	-62.6993	25	5.49	5.45	4.54	108.95	6.37
				100	-	8.78	5.37	207.99	7.98
4/10/16	MBA	-64.8606	-62.5837	20	6.16				
				60	6.27				
				300	12.35				
4/11/16	IBB	-64.8752	-62.4044	20	8.48	6.89	6.81	383.25	15.34
				75	5.76	5.94	5.87	330.75	13.11
				250	7.68	7.70	6.76	227.84	12.17
4/11/16	SIII 3	-64.8380	-62.6106	15	4.61	5.41	5.17	131.97	8.69
				75	4.53	5.20	4.65	141.41	7.97
				250	5.69	6.22	4.49	89.42	6.09
4/11/16	OBA	-64.7657	-62.7057	15	4.89	5.44	4.80	122.35	6.94
				80	4.51	4.99	4.01	81.36	5.44
				250	6.00	6.82	4.54	138.19	7.14
4/11/16	Gerlache Strait	-64.6590	-62.9255	15	5.14	5.27	3.90	101.84	6.07
				80	4.83	5.12	4.09	96.21	5.21
				250	5.16	5.59	4.07	104.76	6.70
4/12/16	Andvord Front	-64.8224	-62.6941	15	5.29				
				40	5.43				
				250	7.20				
4/13/16	SIII 1.5	-64.8608	-62.5378	15	8.23				
				125	6.92				
4/14/16	MBB	-64.8258	-62.6472	15	7.83				
				80	6.96				
				200	8.12				
4/14/16	MBA	-64.8734	-62.5605	60	12.69				
4/16/16	SIII 3	-64.8323	-62.6004	15	7.78				
				75	6.90				
				250	7.91				
4/16/16	IBA	-64.8925	-62.5825	20	9.15	9.67	5.54	308.83	13.84
				100	10.84	11.64	5.82	419.88	15.73
				280	12.88	14.45	9.43	683.63	23.46
4/17/16	IBA	-64.8922	-62.5738	20	6.08	6.54	5.67	248.94	12.72
				100	9.01	9.40	6.22	538.33	17.28
				280	11.56	10.51	9.18	502.70	18.48
				500	14.25	12.41	15.79	879.48	34.96
4/18/16	IBB	-64.8728	-62.4315	20	8.09				
				75	7.43				
				240	7.97				
4/19/16	OBB	-64.7736	-62.8663	15	6.61				
				100	5.96				
				280	16.34				
4/20/16	SIII 1	-64.8752	-62.4538	15	6.98				
				150	6.07				
				280	11.41				
4/21/16	SIII 5.5	-64.7385	-62.9666	20	6.50				
				67	4.90				
				280	4.51				
4/22/16	IBA	-64.9003	-62.5780	110	7.54	7.26	5.28	277.24	11.63
4/22/16	IBA	-64.8834	-62.5590	110	6.87	6.72	4.79	202.34	10.36
4/26/16	Station B	-64.8167	-65.3537	20	1.97	1.91	2.32	30.51	2.99
4/26/16				150	2.04	1.85	1.27	15.40	1.93
4/26/16				400	1.94	1.79	0.73	28.75	1.82

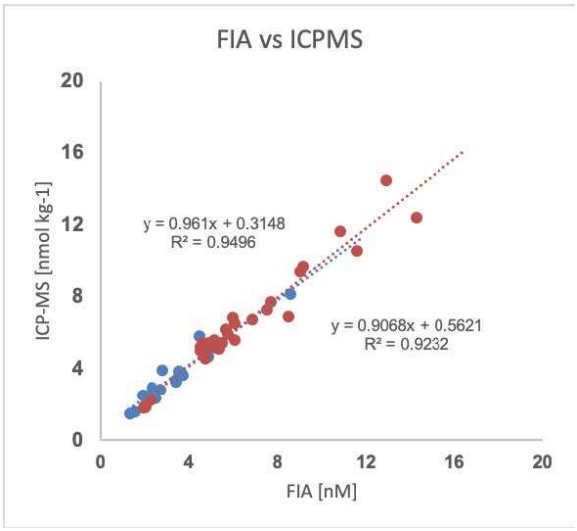

Figure A1. Comparison of analytical detection methods used for the determination of dissolved Fe (FIA versus ICP-MS). The red line denotes the 1:1.

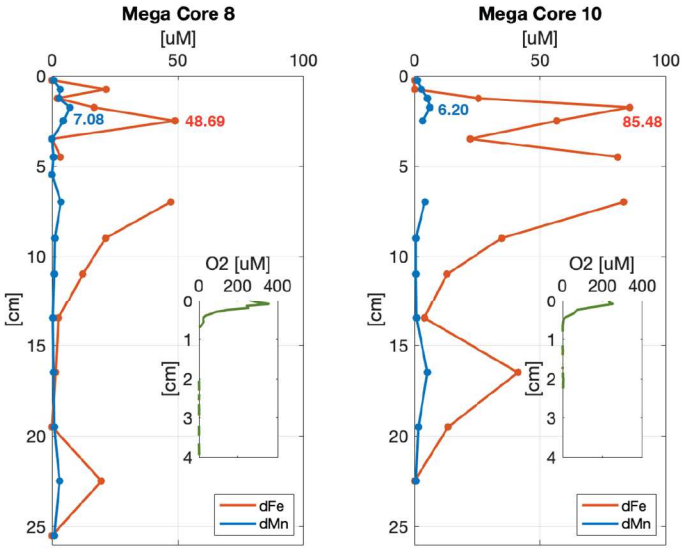

Figure A2. Porewater dissolved metal concentrations for Fe (red), manganese (blue), and oxygen (green) for Mega Core 8 (left) and 10 (right), at the coring station near OB (see Fig. 1).

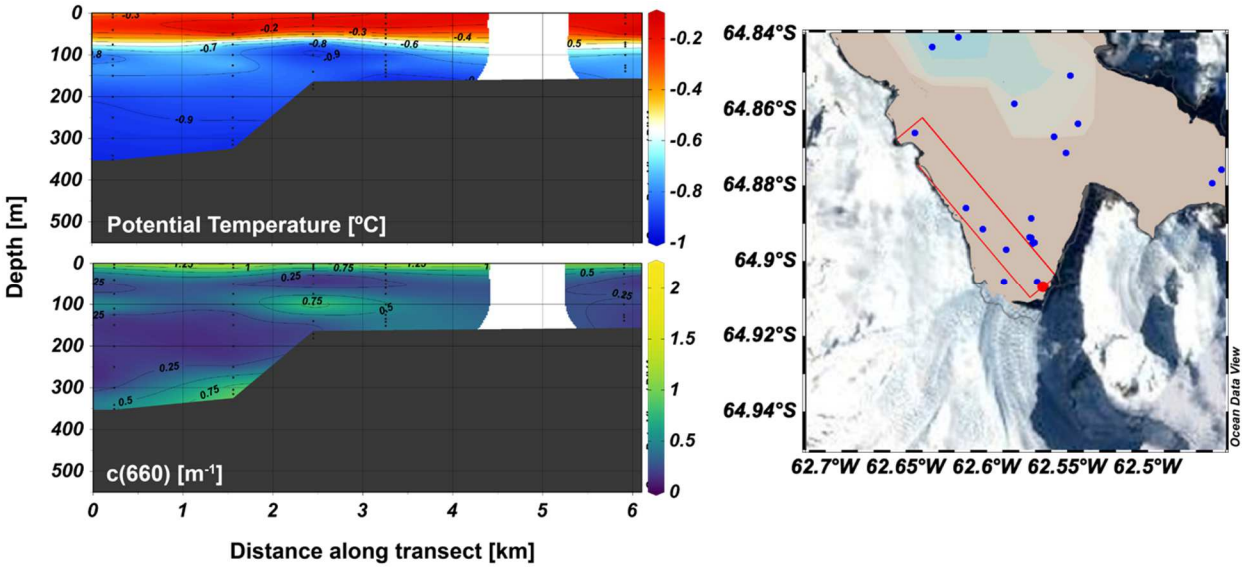

Figure A3. Bagshawe Glacier CTD transect during LMG1510 (late Spring) showing temperature (top panel) and beam attenuation coefficient at 660 nm (bottom panel). Section plots are oriented as if facing the coast. The transect is highlighted by a red box on the map. (Plots were made with Ocean Data View visualization software (Schlitzer, 2002, Ocean Data View, last access: 1 February 2021).

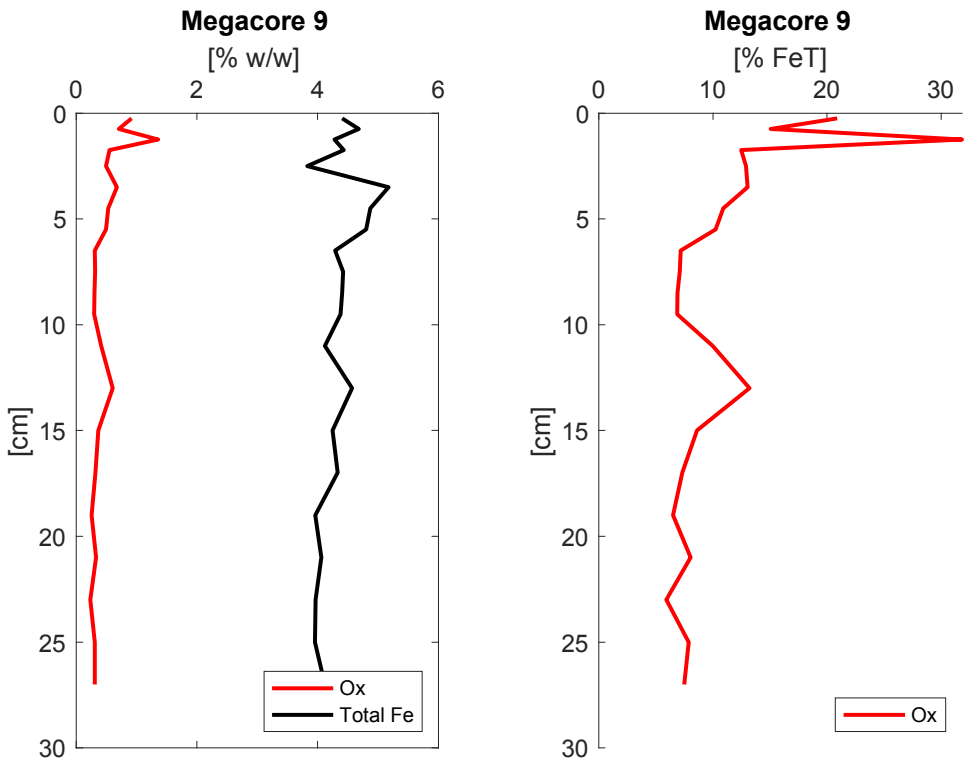

Figure A4. Speciation of Andvord Bay sediments as percent dry sediment weight (left) and percent total Fe (right) for defined fractions based on chemical lability, as in Burdige *et al.* (2020). Ox = oxides.

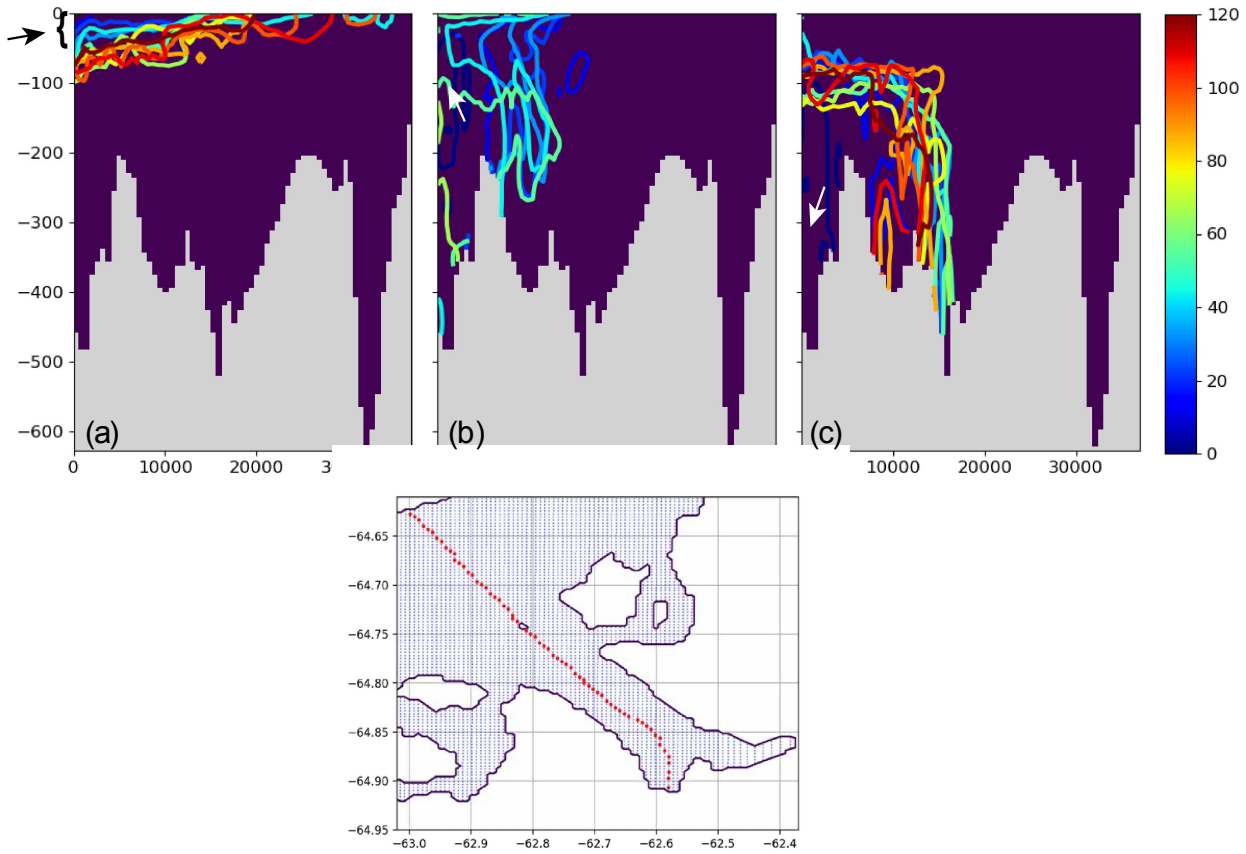

Figure A5. Modeled fate of numerical dyes representing three possible Fe sources. Contours show the 0.1% extent for the (a) meltwater dye and the 0.01% extent of the (b) subsurface, and (c) deep dyes according to the day in the model run (colorbar). Approximate dye release depth and location are highlighted by the arrows. The plots are oriented from the inner basins (0 m) to the Gerlache Strait (~35000 m) as distance from Bagshawe Glacier ([m]).

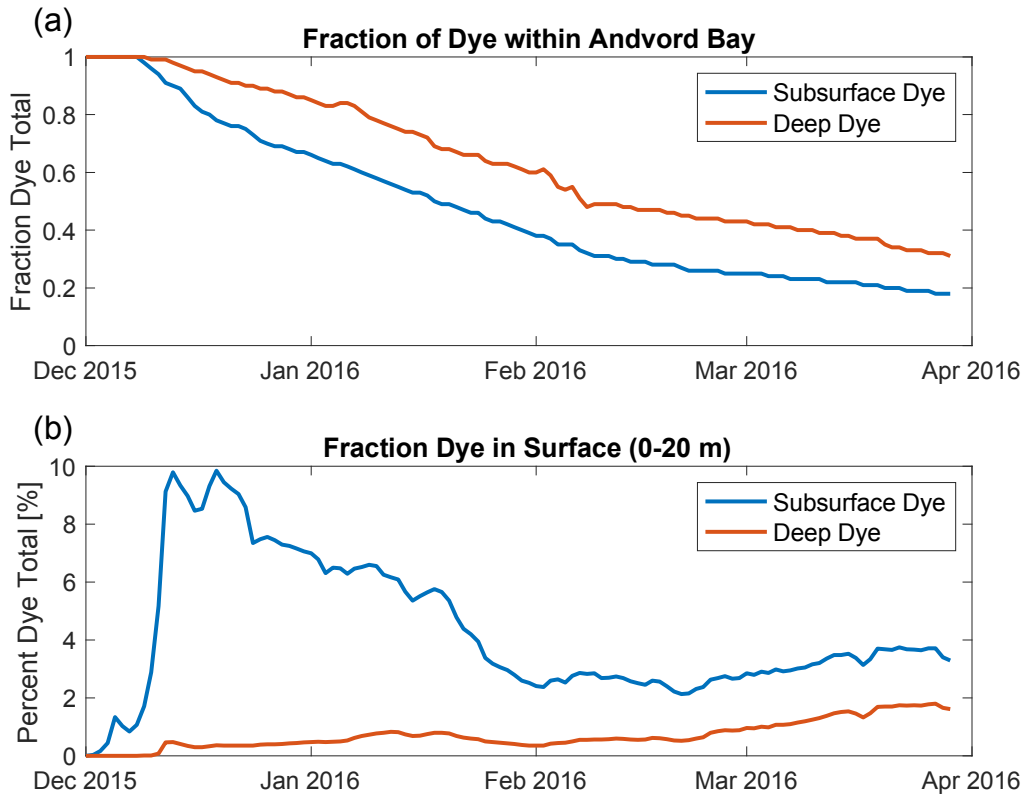

Figure A6. (a) Fraction of initial subsurface (blue) and deep (orange) numerical dye within the fjord domain over the 120-day model run. (b) Percentage of subsurface and deep dye within the surface layer (0-20m) over the 120-day model run.

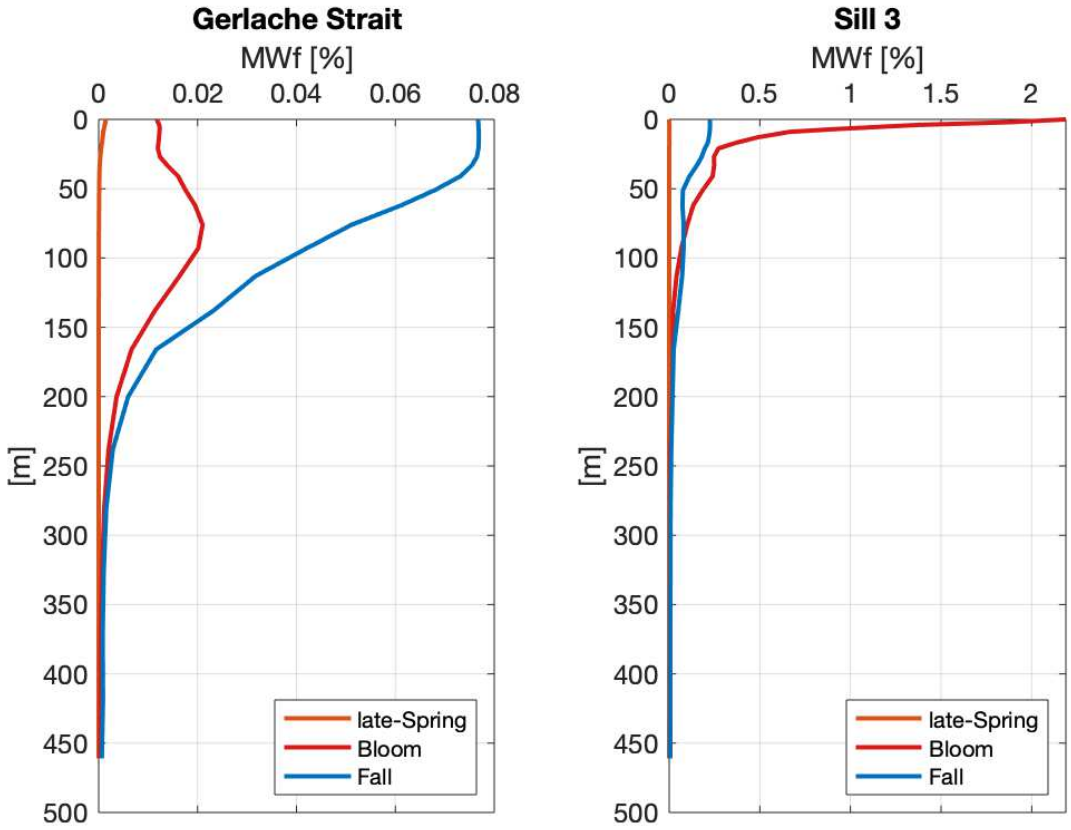

Figure A7. Modeled meltwater dye profiles as a percent of water volume in the (left) Gerlache Strait and (right) Sill 3. Each profile corresponds to a different timepoint: late Spring (December 11, 2015 Gerlache, December 3, 2015 Sill 3), peak bloom period (January 27, 2016), and simulation end (March 29, 2016). Note the different x-scales.

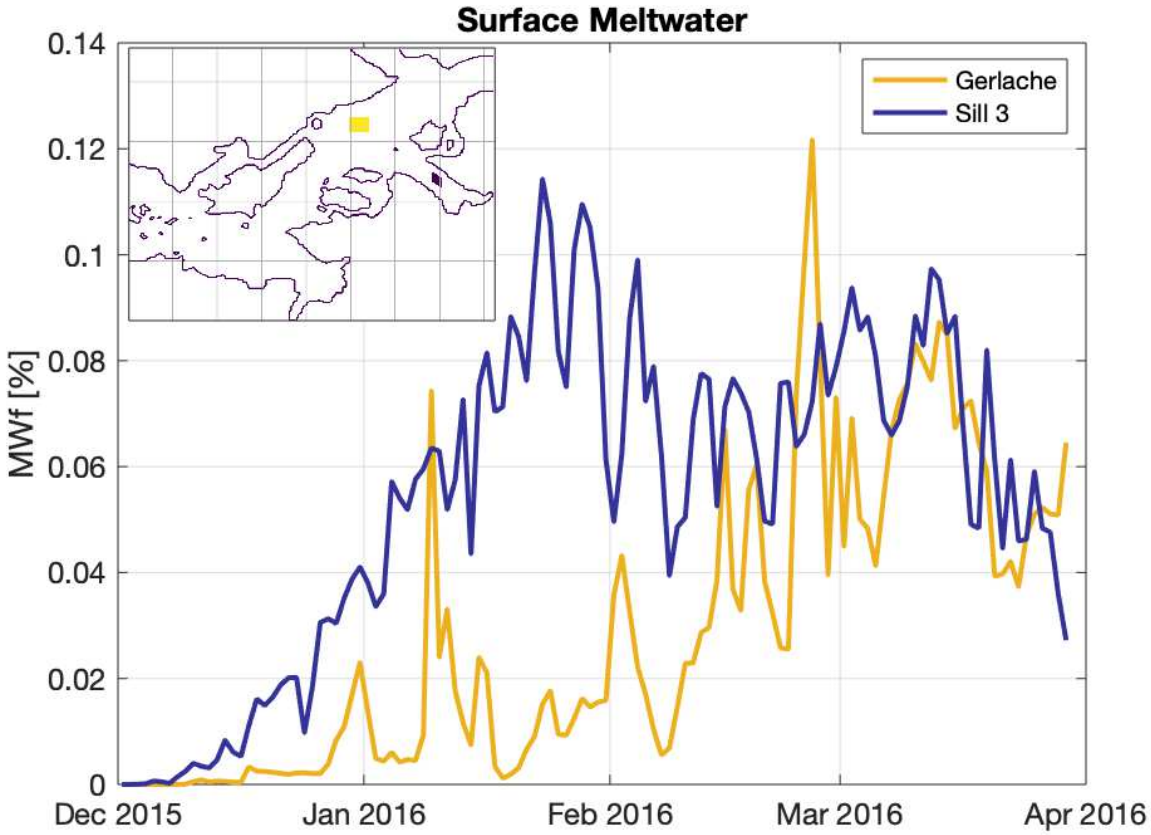

Figure A8. Modeled surface (0-20m) meltwater fraction for Gerlache Strait and Sill 3 (map inset), over the course of the 2015-16 summer season.

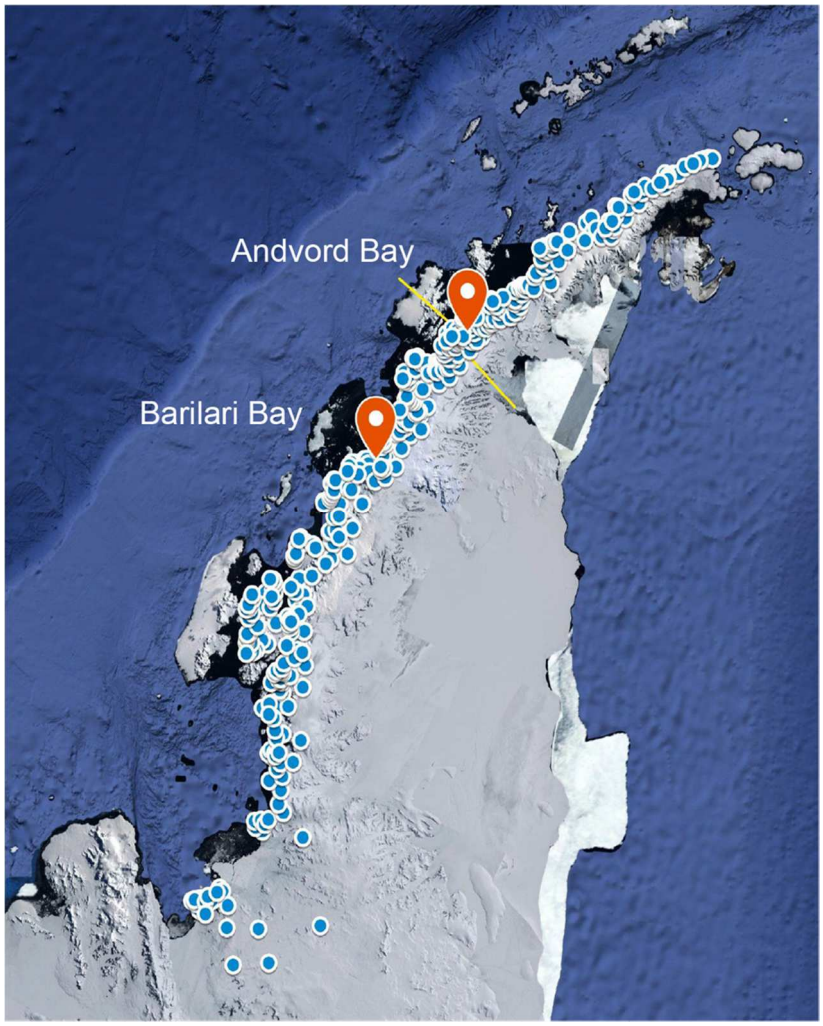

Figure A9. Map showing all 432 glaciers (blue dots) located on the western coast of the WAP (from Cook *et al.,* 2016). The yellow line indicates the region of convergence of two intermediate water masses; cold Weddell Water to the north and warm modified UCDW to the south. Image was produced using © *Google Maps*, 10 January 2021.

2.10.5 References

Annett, A. L. *et al.* (2017) 'Controls on dissolved and particulate iron distributions in surface waters of the Western Antarctic Peninsula shelf', *Marine Chemistry*. doi: 10.1016/j.marchem.2017.06.004.

Cape, M. R. *et al.* (2019) 'Circumpolar Deep Water Impacts Glacial Meltwater Export and Coastal Biogeochemical Cycling Along the West Antarctic Peninsula ', *Frontiers in Marine Science* , p. 144.

Hahn-Woernle, L. *et al.* (2020) 'Sensitivity of the summer upper ocean heat content in a Western Antarctic Peninsula fjord', *Progress in Oceanography*, 183, p. 102287. doi: https://doi.org/10.1016/j.pocean.2020.102287.

Hopwood, M. J. *et al.* (2019) 'Highly variable iron content modulates iceberg-ocean fertilisation and potential carbon export', *Nature Communications*, 10(1), p. 5261. doi: 10.1038/s41467-019-13231-0.

Jackson, R. H., Straneo, F. and Sutherland, D. A. (2014) 'Externally forced fluctuations in ocean temperature at Greenland glaciers in non-summer months', *Nature Geoscience*, 7(7), pp. 503–508. doi: 10.1038/ngeo2186.

Jordan, T. A., Riley, T. R. and Siddoway, C. S. (2020) 'The geological history and evolution of West Antarctica', *Nature Reviews Earth & Environment*, 1(2), pp. 117–133. doi: 10.1038/s43017-019-0013-6.

Lundesgaard, *Ø*. *et al.* (2019) 'Response of an antarctic Peninsula fjord to summer Katabatic wind events', *Journal of Physical Oceanography*. doi: 10.1175/JPO-D-18-0119.1.

Chapter 2, in full, is a manuscript of the material as it appears in Forsch, K., Hahn-Woernle, L., Sherrell, R.M., Roccanova, V., Bu, K., Burdige, D., Vernet, M., Barbeau, K.A. (2021) Seasonal dispersal of fjord meltwaters as an important source of iron and manganese to coastal Antarctic phytoplankton, Biogeosciences Discuss., 2021, 1–49, doi:10.5194/bg-2021-79, 2021. The dissertation author was the primary investigator and first author of this paper.

Rob Sherrell, Kaixan Bu, and Vincent Rocannova at the Rutgers Inorganic Analytical Laboratory helped with mass spectrometry methods. David Burdige provided sediment core analyses. Maria Vernet (FjordEco) and Katherine Barbeau supported this work.

Chapter 3. The 'Morro Bay' and 'Pt. Sur' coastal upwelling filaments: Examinations of iron cycling during lateral advection in the southern California Current

"*Flesh is grass*." Walt Whitman

"*Fish is diatoms*." Henry Bigelow

"*Diatoms are nitrogen and iron*." Ken Bruland

3.1. Abstract

In the spring and summer, high rates of primary production occur in the California Current System (CCS) when nutrients are supplied to the euphotic zone. During periods of intense coastal upwelling, a flux of the micronutrient iron comes from nearshore sedimentary sources. In this upwelling region, mesoscale filament features distribute iron laterally, leading to distinct iron-influenced ecological zones. The studies here are the first to focus on the biogeochemical links between iron, the macronutrients, and carbon in coastal upwelling filaments. Broad spatial patterns of iron and biogenic silica concentrations, and proxies of iron-stress of diatoms, support results from microcosm amendment studies conducted during CCE LTER (California Current Ecosystem Long Term Ecological Research) process cruises in the summers of 2017 and 2019. We found that the benthic boundary layer source and the shoreward filament endmember supply dissolved and total dissolvable iron, but rapid conversion to sinking biogenic particles depletes the surface. In turn, diatom blooms formed in recently upwelled water masses become iron limited, affecting the ratios of surface macronutrient reservoirs and biogeochemical length scales and lateral fluxes. The development of Fe-limitation during lateral advection may lead to efficient carbon export of downstream, offshore primary producers in a biologically productive and globally significant ecosystem.

3.2. Introduction

The California Current is the eastern limb of the large, clockwise circulation of the North Pacific Ocean subtropical gyre. The California Current System (CCS) of central and southern California consists of a broad, eddy-rich, southward flowing section of the California Current, a seasonally variable surface northward flowing Inshore Countercurrent, a persistent but variable subsurface California Undercurrent (CUC) centered on the continental slope, carrying water from the tropics poleward, and an energetic and seasonally dynamic zone of frontogenesis and mixing near the continental shelf. This nearshore zone alternates between a wind-driven equatorward flow, driving periods of intense coastal upwelling in spring and summer, to a poleward flow in the fall and winter (Hickey, 1998).

Upwelling of cold, dense, nutrient-rich water occurs when equatorward winds strengthen during the summer through the process of Ekman transport. When this occurs in the California Current System, which is a characteristic Eastern Boundary Upwelling System (EBUS), high rates of primary production may be observed in these upwelled waters (Carr and Kearns, 2003; Checkley and Barth, 2009). Despite the small spatial area that EBUSs occupy in the ocean (<1%), they host nearly 20% of global fisheries yield because of the intense spring-summer blooms (Chavez et al., 2009; Carr, 2001).

Macronutrient (e.g., nitrate NO_3^-, silicic acid $Si(OH)_4$, phosphate PO_4^{3-}) replete conditions in upwelling waters in the California Current region, which typically have ~20% more silicic acid $Si(OH)_4$ than nitrate NO_3^- (Zentara and Kamykowski, 1977) generally result in blooms of diatoms (Van Oostende et al., 2015). Diatoms are an abundant type of phytoplankton whose prominent siliceous shells (frustules), relatively large size, and fast growth rates make them critical components of oceanic primary production; fixing as much carbon as all terrestrial rain forests and account for up to 40% of all marine carbon export (Nelson *et al.*, 1995; Field *et al.*, 1998; Marchetti and Cassar, 2009). Dense silica (Si) frustules offer some protection from zooplankton grazers (Wilken et al., 2011; Zhang et al., 2017). Frustules also play a role in mineral ballasting

of organic material, making it more likely for biogenic particulate matter to sink from the mixed layer. A portion of this carbon sediments on the seafloor and becomes sequestered, balancing the input of Si to the ocean from the world's rivers. For these reasons, diatoms are major exporters of both Si and organic carbon (Smetacek, 1999; Timmermans et al., 2004). Factors that affect diatoms' nutrient uptake, growth, sinking rates, and remineralization rates can have major impacts on macro- and micronutrient cycling, coupling of pelagic and benthic communities, and carbon sequestration. Understanding how the biogeochemical landscape affects diatoms will enable models to predict future ocean primary productivity more accurately.

Iron (Fe) supply in upwelling regions is now recognized as an important bottom-up control on the diatom community (Bruland et al., 2005; Hogle et al., 2018; Hutchins and Bruland, 1998; King, 2007; King and Barbeau, 2011). All studies indicate that new dissolved iron (dFe) sources to the ocean are rapidly removed from the water column (Boyle et al., 1977), which means that for diatom blooms, with high cellular Fe quotas (Twining et al., 2021), diatom community dFe demand increases while supply decreases. Fe-limitation has been observed in high production, coastally upwelled water masses in EBUSs (Biller et al., 2013; Bruland et al., 2001; Firme et al., 2003; Hutchins and Bruland, 1998; Johnson et al., 1999; Till et al., 2019). Deckboard and *in situ* bottle amendment experiments in many cases show a rapid response of the diatom community to the addition of dFe, indicating Fe-limitation.

Links between Fe and Si biogeochemistry are particularly important in areas of natural Fe-limitation. Low-latitude nutrient-replete marine diatoms use dissolved NO_3^- and $Si(OH)_4$, on average, in approximately equimolar ratios (1:1) (Brzezinski, 1985). Under Fe-limitation, this uptake ratio is significantly affected (Hutchins and Bruland, 1998; Takeda, 1998), increasing to 4-6 (Franck et al., 2003), and these uptake ratios can increase cellular Si content (Bucciarelli et al., 2004; Rocha et al., 2000). This has been documented in areas of natural Fe fertilization and in bottle manipulation experiments (Brzezinski et al., 2015; Hoffmann et al., 2007; Price, 2005; Takeda, 1998; Twining et al., 2004). Under Fe limiting conditions, the surface reservoir of

macronutrients is preferentially depleted of $Si(OH)_4$, relative to nitrate and is correlated with the occurrence of negative Si_{ex} ($Si_{ex} = [Si(OH)_4] - R_{Si(OH)4:NO3-} \times [NO_3^-]$) values in the water column, where $R_{Si(OH)4:NO3-}$ is the ratio of $Si(OH)_4$:NO_3^- found in subthermocline waters on the shelf ($R_{Si(OH)4:NO3-}$ ~1). Indeed, negative Si_{ex} values are co-located with direct evidence of Fe-limitation occurring at subsurface Chla maxima in the CCS (Hogle et al., 2018).

Previous studies have demonstrated changes in diatom nutrient uptake ratios in response to Fe-limitation, and correlations between export efficiency and diatom Fe-limitation are now being examined in the California Current Ecosystem (CCE) (Brzezinski et al., 2015; Krause et al., 2015). Episodic mesoscale features, such as eddies and filaments, can move upwelling-related Fe fertilization events offshore. As upwelling waters flow over the continental shelf, they become enriched in resuspended Fe-rich sediments (Bruland et al., 2001) and Fe-binding ligands accumulated from riverine input (Biller et al., 2013; Bundy et al., 2014; Homoky et al., 2012). These turbid layers overlying continental shelves are thought to be the primary source of new Fe (mainly as mineral Fe forms) for upwelling- associated blooms (Chase et al., 2005; Elrod et al., 2004; Johnson et al., 1999). Fluvial inputs accumulate in the benthic boundary layer (BBL) over the winter season and are transported to the surface with strong spring and summer upwelling. As upwelling water masses age and move offshore, there is a tendency for Fe limiting conditions to develop (King, 2007; Till et al., 2019).

The data presented here are unique in that they attempt to follow the progression of two upwelling filaments from recently upwelled and nutrient-replete to aged and Fe-limited conditions to gain insight into the changing dynamics of Fe and biogenic silica (bSi) as this evolution occurs. Filaments are characteristic of most eastern boundary currents (e.g., Rossi *et al.*, 2013; Sangrà *et al.*, 2015; Chabert *et al.*, 2021) and usually contain a long core of cold water that originates from subsurface water upwelled near the coast. They have cross filament scales of 10 - 50 km, and along-filament scales of 50 - 200 km (Zaba et al., 2021). The offshore flows make filaments efficient vehicles for transporting biogeochemical tracers from zones of upwelling to offshore

waters, with nutrient-rich conditions enabling the formation of phytoplankton blooms and fast-moving cores advecting particulate matter offshore (Mohrholz et al., 2014; Muller et al., 2013; Nagai et al., 2015). Mesoscale features such as filaments can contain a predictable primary producer population gradient driven by processes of mixing, nutrient drawdown, and phytoplankton community evolution. Thus, they are excellent natural laboratories for studying processes of ecosystem connectivity and ecological transitions. Although filaments as physical phenomena and Fe-limitation as a biogeochemical condition have both been studied in the CCS for decades, no published work has yet examined these concepts simultaneously.

The study locations were chosen because of their characteristic seasonal filaments. The coastline in the Point Conception region abruptly bends to the east to form the Santa Barbara Channel and the Southern California Bight (SCB). In this region, cool pools often form (Sverdrup 1938) and upwelled waters to the north meet northward flowing coastal currents (Barth and Brink, 1987; Winant et al., 1999, 2003). Where these currents meet, a cold filament can form and propagate 10s of km offshore where it can be tracked for hundreds of km (Centurioni et al., 2008; Kim et al., 2011). Further north, strong upwelling is observed off Pt. Sur and is a region with historical importance to the field of Fe biogeochemistry in the California Current System. We hypothesized that filaments would likely be particularly susceptible to the development of Fe-limitation as upwelling water picks up Fe from the BBL but is then rapidly transported offshore and away from the Fe sources as phytoplankton take up Fe and Fe is lost from the system. The framework we build upon is that as coastal filaments are drawn offshore, diatom communities become Fe limited, leading to preferential removal of Si as sinking biogenic material (Figure 3.1). We argue that changes in diatom physiology and community driven by the availability of dFe in coastal upwelling filaments may lead to enhanced carbon export and pelagic-deep ocean coupling in the CCS.

This chapter addresses important aspects of Fe biogeochemistry in the California Current System, with an emphasis on eastern boundary coastal upwelling filaments. We address the

following questions: What is the source of iron to filaments? Are there distinct iron-influenced ecological regimes? What are the consequences of iron-limitation on the biogeochemistry of the macronutrients, biogenic silica, and carbon?

3.3. Materials and Methods

3.3.1. Study sites and Lagrangian approach

An initial hydrographic survey was conducted using a towed SeaSoar and a ship-mounted Acoustic Doppler Current Profiler (ADCP). In June of 2017, a cold, chlorophyll-rich, and offshore-moving water parcel was detected in Morro Bay (Figure 3.2). Over the span of two weeks (June 9 – June 25), the 'Morro Bay' Filament (P1706) was tracked aboard the *R/V Roger Revelle*. On the next process cruise in August 2019, another upwelled water parcel was identified just south of Pt. Sur (Figure 3.2). The 'Pt. Sur' Filament (P1908) was tracked aboard the *R/V Atlantis*. In the fashion of previous CCS process studies (Landry et al., 2009), four Lagrangian studies of each filament (termed cycles) followed the upwelled water parcel by deploying low-profile floating drift arrays and sediment traps, each equipped with a holey sock drogue centered at 15 m depth to follow mixed layer surface currents. Drifters were deployed at the beginning of each cycle, initiating a study period of 2 – 5 days per cycle. Locations for the beginning of each cycle were chosen based on *Spray* glider, remote sensing (Chla), and Moving Vessel Profiler (Ohman et al. 2012) survey data.

Cross-filament surveys were achieved by sampling in a line perpendicular to the mean current of the filament ('Transects'), capturing the structure and bounds of the filament over a 24 hr period. This sampling strategy allowed for quasi-synoptic portraits of the filament structure, important for the quantification of lateral biogeochemical fluxes. A BBL survey was conducted of the shoreward filament endmember at Morro Bay (35.35ºN, -120.93ºE) and Pt. Sur (36.23ºN, -121.83ºE) located on the inner-continental shelf. Additional sampling of long-term BBL transect sites and the Santa Barbara Basin (SBB) were conducted following the last filament cycle as part of an ongoing time series in the Barbeau Lab.

3.3.2 *In situ* samples

During cycles and transects, profiles for bSi, macronutrients, Chla and POC were collected as whole seawater from Niskin bottles once per day at 11 a.m. (local). Trace metal clean samples for dFe and TDFe were sampled from Teflon-coated X-Niskin bottles on a powder-coated rosette, deployed on a coated hydrowire. Fe samples were handled in a Class 100 trace metal clean van and filtered in-line using acid-washed Teflon tubing and acid-washed 0.2 µm Acropak-200 capsule filters pressurized by filtered air. Filtered samples were acidified to pH 1.8 with hydrochloric acid and stored in 250 acid-clean low-density polyethylene (LDPE) bottles for on-shore analysis (King and Barbeau, 2007). The trace metal methods described here are to the standards of the GEOTRACES program (Cutter and Bruland, 2012). Briefly, the cleaning procedure for plastic sample bottles and filters involved a series of bath soaks: acidic detergent with heating (60ºC), one week leach in 3N HNO_3 (trace metal grade), followed by a one-week leach in 3N HCl (trace metal grade). In between each soak step, sample and incubation bottles were rinsed thoroughly 3x with 18.2 MΩ cm^{-1} MilliQ water (total organic carbon ≈ 28 ppb). Filters were rinsed with methanol prior to soaking in 3N HCl at room temperature, followed by a MilliQ rinse and storage in pH~1.8 MilliQ.

3.3.3. Benthic boundary layer sampling

Trace metal clean samples from the BBL were collected using Teflon-coated 10 liter GO-Flo bottles (General Oceanics) suspended on a Kevlar line and triggered with Teflon messengers. Hydrographic data was collected using the ship's rosette system, which contained a conductivity, temperature and depth (CTD) sensor as well as a Chl-*a* fluorometer, dissolved oxygen sensor and beam transmissometer. The BBL sampling locations were determined based on the local maximum in beam attenuation within 10 meters of the ocean bottom obtained from a CTD cast immediately preceding the GO-Flo cast. An attempt was made to obtain the GO-Flo sample

approximately 5 meters off the bottom within the BBL. A total of 9 stations were sampled during the 'Morro Bay' filament. Three 'Pt. Sur' filament BBL stations were sampled near the shoreward filament endmember within 5 km of the coast. An additional 9 stations were sampled during the 2019 BBL transect, reoccupying stations sampled in 2017.

3.3.4. Fe addition grow-out incubations

The biochemical response of the phytoplankton community to the addition of Fe was tested in incubation studies. These were initialized during the Lagrangian cycles at various stages of each cruise. Seawater from the trace metal clean rosette was collected from the depth of maximum Chlorophyll-a (Chla) fluorescence and placed into acid-cleaned 2.7 L polycarbonate (PC) bottles with unamended controls and +Fe (5 nmol L-1 FeCl3 in pH 1.8 MilliQ water) treatment. Each treatment was done in triplicate. On-deck incubations were conducted in flow-through incubators (sea surface temperature, SST) screened to 30% surface irradiance using nickel grading for 3-4 days. On-deck incubation studies were sampled every day for Chla and macronutrient (NO_3^- and $Si(OH)_4$). At the final timepoint (t_f), bSi, POC and community composition were sampled. The water sampled for these experiments was analyzed for dFe. For the 'Morro Bay' filament, the phytoplankton community composition was assessed by 18S v9 genomic sampling of the water column (P1706, Rivera et al. *in prep*). For P1908, the community composition was assessed by 18S genomic sampling on the initial sample (t_0) (P1908, Lampe et al. *in prep*). During the 'Pt. Sur' filament cruise, an additional two treatments (+N and +N/+Fe) were used in the Cycle 4 incubation experiment to test for NO_3^- and dFe co-limitation at the subsurface chlorophyll maximum. NO_3^- was added in this experiment so that the bottle had a final concentration of 10 µM NO_3^-.

3.3.5. Sediment traps

Eight to twelve VERTEX-style particle interceptor traps (PITs) were placed on a sediment trap array at three nominal depths: 150 m, 100 m, and the base of the euphotic zone (40 – 60 m). PITs were 70 mm in diameter, with an 8:1 height to diameter aspect ratio, and a baffle on top consisting of 13 acrylic tubes with a similar 8:1 aspect ratio and tapered ends. Tubes contained a solution made from 0.1 μm filtered seawater amended with 60 g L^{-1} NaCl and 0.4% (v/v, final concentration) formaldehyde. Sediment traps were deployed at the beginning of a cycle, collected on the last day of the cycle and vertical flux was averaged over the deployment period (Knauer et al., 1979; Morrow et al., 2018).

3.3.6. Macronutrient and Chlorophyll-a analysis

Macronutrient samples were collected and filtered from *in situ* water column and Fe-addition incubations and immediately frozen at -20°C for on-shore autoanalyzer analysis. Water column nutrient samples in most instances were filtered through a 0.2-μm capsule filter before being frozen. Chla samples in dark bottles were filtered onto 25 mm glass fiber filters (GF/F) and analyzed on-board the ship, following an extraction step for 24 hr in 90% acetone at -20°C. Chla concentrations were calibrated using a standard curve quantified by a Turner Designs 10-AU Fluorometer, fitted with a red-sensitive photomultiplier tube (PMT).

3.3.7. Biogenic silica (bSi) analysis

In situ bSi samples were transferred to 1 L PC bottles and filtered onto 47 mm 0.8 μm polycarbonate filters, placed into cryovials, which were then dried in the oven (with the vial cap loosened) at 60˚C for 24 hours and stored for on-shore analysis. Incubation bSi samples used 400-900 mL seawater, depending on availability, and were filtered and dried similarly. Samples were digested in 4 mL 0.2 N NaOH in HF-clean teflon tubes at 95˚C for 40 minutes and then cooled in an ice bath and neutralized with 1 mL 1 N HCl. After centrifuging 10 min at 1100 x g, 4 mL were withdrawn, diluted, and measured at 810 nm for reactive silicate via the colorimetric

ammonium molybdate method (Brzezinski and Nelson, 1995; Strickland and Parsons, 1972), where a 10 mL sample was added to a 4 mL molybdate solution and allowed to stand 10 minutes before being reduced for 2 hours. A total of 262 and 284 water column and incubation samples were processed for P1706 and P1908, respectively. BSi export flux data was collected at nominal depths of 50 m (base of euphotic zone), 100, and 150 m for all cycles by deploying drifting sediment traps at the start and end of each Lagrangian cycle.

3.3.8. Particulate organic carbon (POC) analysis

0.5-2 liters of seawater was filtered through pre-combusted 25 mm Whatman GF/F filters under low vacuum pressure. The filter was subsequently wrapped in precombusted aluminum foil, flash-frozen in liquid nitrogen and stored at -80˚C until processing. Samples were then placed on combusted petri plates and acidified in a desiccator with HCl fumes to remove particulate inorganic carbon, then dried for 48 hr at 60°C. The samples were cut in half, weighed, placed in tin capsules, and measured on a CHN elemental analyzer at the Scripps Institution of Oceanography Analytical Facility. More information on this method can be found at https://cce.lternet.edu/data/methods-manual/. POC export flux data was collected at nominal depths of 50 m (base of euphotic zone), 100, and 150 m for all cycles by deploying drifting sediment traps at the start and end of each Lagrangian cycle.

3.3.9. Dissolved iron (dFe) and total dissolvable iron (TDFe) analysis

Stored acidified filtered seawater samples were analyzed for dFe using flow injection with chemiluminescence methods described by Lohan et al. (2006)(Lohan et al., 2006). DFe in the resulting samples was oxidized to iron(III) for 1 hr with 10 mM Q-H_2O_2, buffered in-line with ammonium acetate to pH ~3.5 and selectively pre-concentrated on a chelating column packed with a resin (Toyopearl® AF-Chelate-650M). DFe was eluted from the column using 0.14 M HCl (Optima grade, Fisher Scientific) and the chemiluminescence recorded by a PMT (Hamamatsu

Photonics). The methods used were described by King and Barbeau 2007, 2011, and a manifold adapted from Lohan *et al.* (2006). The standardization of Fe used was a matrix-matched standard curve (0, 0.4, 0.8, 3.2, 10 nmol kg^{-1}) using low-Fe surface Pacific seawater (0.4 nM). Standards were treated identically to samples. Accuracy was assessed by repeated measurements of GEOTRACES coastal and open Pacific Ocean reference seawater samples. Our measurements of GSC gave Fe = 1.506±0.148 nM (n = 23, consensus 1.535±0.115). Our measurements of GSP gave Fe = 0.195±0.029 nM (n = 20, consensus 0.155±0.045 nM). Consensus values are from the most recent July 2019 compilation (https://www.geotraces.org/wp-content/uploads/2020/03/2019_Consensus_Values_2009_samples.pdf). Precision, determined by replicated analyses of an in-house large volume surface Pacific (0.40 nM) and GEOTRACES reference seawater within each analytical session, was typically ±5% or better. For the duration of these analyses, the average limit of detection (defined as 3x the standard deviation of the blank) was 0.036 nM (n = 43). All dFe station data is available at https://oceaninformatics.ucsd.edu/datazoo/catalogs/ccelter/datasets.

Total dissolvable Fe (TDFe) samples were analyzed using the same analytical methods as for dFe samples. These unfiltered samples were acidified to pH 1.8 (HCl, optima grade) and stored for 22-24 months. Immediately prior to analysis, the samples were syringe-filtered using acid-cleaned syringes and filters (Supor, 0.2 µm). The process blank from the syringe-filtration was assessed to be an average 0.058 nM, which is at most a 6% correction to the overall measurement of TDFe. Due to the calibration range of the standards, it was necessary to dilute many of the samples, especially nearshore. Therefore, offshore filtered surface Pacific seawater (0.22 nM) was used to dilute samples by a factor of 10 prior to analysis.

A subset of BBL samples were analyzed for dissolved and total dissolvable iron and manganese using sector field inductively coupled plasma mass spectrometry (ICP-MS) methods at Rutgers University in October 2018. Standardization for Fe was accomplished by isotope dilution methods while Mn (with only one stable isotope) was calibrated using a standard curve.

Internal drift was monitored by an addition of Indium spike (1 ppb) with each sample. The methods employed are described in Forsch et al., 2021.

3.3.10. Estimating cross-shore advective flux

Cross-filament transects were used to estimate the lateral and vertical structure of the filament, and then using ADCP data from the Cycles, to estimate current velocities over specific depth intervals. The high-resolution data acquired by ship-based ADCP can be used to estimate the zonal flux (J_u) of dFe and bSi in the off-shore flowing filaments. The horizontal current determined by ADCP from a moving ship can be prone to masking by tidal currents, turbulence, and other small-scale flows (Foreman and Freeland, 1991). To analyze flow patterns of the filament, it is necessary to remove these interference signals. Since we are in a Lagrangian framework, our approach was to time-average (25 hr) the ADCP data for each Cycle, in which a single water mass was monitored for 3 – 5 days. We then spatially average ADCP profiles over 0.01 degrees of latitude and longitude around a transect profile located within the filament core.

The depth-average horizontal velocity measurements were binned as <25 m, 25 – 50 m, and 50 – 150 m. We estimated geometric means of Fe and bSi concentration data for these depth bins and multiplied them by the average zonal velocity measurements for each Cycle to estimate J_u and J_v within the filament core (Table 3.1). Before the velocity vector u and concentration data were multiplied to estimate J_u, we necessarily defined the boundaries of the filament. We used Ocean Data View (ODV) graphing software to plot sections of interpolated potential temperature, Chla, and derived buoyancy frequency, which is a measure of the stability of the water column or degree of stratification. We assumed the filament was a productive surface feature and contained a signature of its upwelled water mass source, namely its relatively cold temperature. This analysis was applied to ‘Morro Bay’ filament Transects 1 and 2, and ‘Pt. Sur’ filament Transects 1, 2, and 3. ‘Morro Bay’ filament Transect 3 was excluded since the filament water parcel properties were considered heavily modified by CC water entrainment.

3.4. Results

3.4.1. Spatial orientation

3.4.1.1. The 'Morro Bay' Filament (P1706)

Remotely sensed sea surface temperature (SST) and Chla, and MVP profiling transects informed the location for the first Lagrangian cycle. The water parcel was relatively low temperature (10-12ºC), high salinity (33.75), and high in Chla located on the shelf near Morro Bay. The water parcel was determined to have a fast-moving southwestward flow. Cycle 2 began off the shelf and within the filament, 71 km southwest from the start-point of Cycle 1, just above the Santa Lucia Escarpment. At the end of Cycle 2, a sediment trap drift array (Cycle 2.5) was deployed and left for five days while Cycle 3 was completed, 135 km southwest of the start-point of Cycle 2 (Figure 3.2). Cycle 4 sampling was conducted in the northeastward flow, the most time-evolved signature of the 'Morro Bay' filament. A Temperature versus Salinity (T-S) plot (Figure 3.3) shows that the signatures of the water masses in Cycles 1, 2 and 4 have similar water mass origins while Cycle 3 is heavily modified and did not resemble the filament. Besides the first day, Cycle 3 was conducted in a relatively fresher water mass, more characteristic of CC water.

3.4.1.2. The 'Pt. Sur' Filament (P1908)

The 'Pt. Sur' Filament process study was initiated toward the end of summer 2019 and the upwelling season (August 18 - September 2). A pool of cold and salty upwelled water formed just south of Pt. Sur and was quickly advected ~75 km offshore directly west (Cycles 1 and 2), before warming significantly and moving 25 km south (Cycle 3, Figure 3.2). Cycle 4 was started in a westward propagating water mass characterized by well stratified, relatively warm, and fresh CC surface water ~200 km offshore (Figure 3.3).

3.4.2. *In situ* biogeochemical conditions

3.4.2.1. Macronutrients and dissolved iron

Nitrate (NO_3^-) and silicic acid ($Si(OH)_4$) were elevated in recently upwelled Chla-rich water masses (Figure 3.4). The 'Morro Bay' filament had an initial surface concentration of ~10 μM NO_3^- and ~9 μM $Si(OH)_4$. Similarly elevated concentrations of macronutrients were found in the 'Pt. Sur' filament shoreward endmember, with initial surface concentrations of ~10 μM NO3- and ~13 μM $Si(OH)_4$. Given similar initial concentrations, the 'Pt. Sur' filament showed greater decrease of the macronutrient concentrations relative to the 'Morro Bay' filament during lateral advection. By the end of the filament studies, surface waters were heavily depleted of $Si(OH)_4$ (<1 μM) but contained some remaining NO_3^- (3.5 μM and 1 μM for the 'Morro Bay' and 'Pt. Sur' filaments, respectively).

The 'Morro Bay' filament BBL endmember had an elevated concentration of 14.77 nM dFe at 57 m depth. Nearshore surface waters, where Cycle 1 was initialized, had a concentration of ~1.2 nM dFe. Over all cycles, concentrations of dFe decreased in the surface (Figure 3.5), and quickly reached levels less than 0.2 nM dFe in Cycle 2, where concentrations remained low in the offshore cycles. An elevated dFe plume was observed ~50 km offshore at a depths of 50 to 75 m. A subsurface dFe maximum of 2-3 nM was found occurring at 75 to 150 m depth approximately 140 km along the filament track at Cycle 2 Day 4 profile.

The 'Pt. Sur' filament BBL endmember had a concentration of 8.49 nM at 34 m depth, and this dFe rich plume was found extending only 35 km along the filament track, at a depth of ~40 m. Profiles from Cycle 1 showed a thick (50 – 250 m depth) ~3 nM dFe signature close to the continental slope (Figure 3.5). Like the 'Morro Bay' filament, dFe concentrations in the surface decrease along the filament track although concentrations approaching 0.2 nM are not found until Cycle 3. Cycle 2 had surface (<25 m) concentrations around 0.4 to 0.6 nM dFe. Similar to the 'Morro Bay' filament, a deep maximum in dFe (1.5 nM) is found ~100 km along the 'Pt. Sur' filament track at the Cycle 2 Day 4 profile.

3.4.2.2. Labile particulate iron, biogenic silica, and particulate matter

Cycle 1 vertical profiles of labile particulate Fe (LpFe = TDFe – dFe) are shown in Figure 3.6. The 'Pt. Sur' filament had subsurface maxima in LpFe for the first two days of the cycle (days 1 and 2). The 'Pt. Sur' filament day 4 profile, which is furthest from the continental margin, had similar concentrations to the 'Morro Bay' day 1 profile. At this station a maximum in the surface of ~8 nM LpFe decreases with depth. Water column bSi and POC measurements were highest in Cycles 1 and 2 for both cruises (Figure 3.7). While bSi and POC maxima are restricted to the euphotic zone (<50 m), LpFe and beam attenuation coefficient (beam c) show surface and subsurface maxima. Beam c has highest absolute values in the euphotic zone, where biogenic particles associated with the phytoplankton bloom are present. Close to the continental margin, elevated beam c and LpFe co-occur indicating potential resuspension of shelf sediments. This was most clearly observed for the 'Morro Bay' filament. A prominent turbid plume was not detected during the 'Pt. Sur' filament, however, elevated LpFe concentrations coincided with higher dFe in profiles adjacent to the margin sediments.

The trends in bSi and POC for the 'Morro Bay' filament were previously documented (Fulton, 2019). These prior results showed that bSi and POC generally increased through Cycle 1, and then decreased in Cycle 2 (Figure 3.7) indicating the dynamic nature of biogenic particles during a bloom cycle in upwelled waters. These changes were accompanied by a deepening of the Chla maximum as the filament moved offshore. Offshore cycles had significant reductions in bSi and POC concentrations within the euphotic zone. During the 'Pt. Sur' filament cruise, concentrations of bSi were greatly elevated in surface waters in Cycle 1 (range 3.1 – 11.4 μM), but quickly decreased by Cycle 2 (0.38 – 1.36 μM). A nearly undetectable level of bSi (<0.1 μM) was found in the surface throughout Cycle 3. Trends in POC are more dynamic than bSi, where nearshore concentrations decrease during Cycle 1, followed by an increase to the highest measured concentrations in Cycle 2. Finally, Cycle 3 had low concentrations of POC at the surface.

3.4.3. Benthic boundary layer transects

We conducted repeat surveys of BBLs at 9 stations located on the continental shelf extending from Cambria to just south of Pt. Conception (Figure 3.8). In summer 2017, we measured dFe, TDFe, dissolved manganese (dMn), and total dissolvable Mn (TDMn) and the results are shown in Figure 3.9. In 2017, the concentrations of dFe ranged from 2.4 (station 1) to 15 nM (station 4) with an average of 8.77±4.41 nM. TDFe concentrations ranged from 140 (station 1) to 719 nM (station 4) with an average of 424±227 nM. We observed a similar pattern with dMn, where station 4 had elevated levels compared to adjacent stations, however, the highest concentrations of dMn were observed at stations 7 and 9 (5.41 and 5.81 nM, respectively). The highest concentration of TDMn was found at station 7 (13.0 nM), followed by stations 3 (12.2 nM) and 4 (11.6 nM).

Results for dFe and TDFe for the summer 2019 transect are shown in Figure 3.10. Similar to the summer 2017 transect, concentrations of dFe and TDFe were highest at station 4 (27.0 nM dFe, 1175 nM TDFe). Compared to the 2017 transect, the average concentrations of dFe (11.4±8.10 nM) and TDFe (546±284 nM) were higher and with greater variability in dFe between stations. At the shoreward Pt. Sur region of upwelling, 3 BBL stations were sampled (Figure 3.11). Station 2 was considered as the 'Pt. Sur' filament shoreward endmember, located within the zone of upwelling. The Pt. Sur region BBL stations had an order of magnitude lower TDFe concentrations (33.4 – 58.3 nM) than 2017 and 2019 BBL transects, but similar dFe concentrations.

3.4.4. Incubations

Direct evidence of Fe stress was revealed by significant increases in biomass, by proxy of Chla concentrations, and macronutrient uptake in incubation bottles amended with +Fe and +Fe/+N. For the 'Morro Bay' filament, significant differences in the uptake of NO_3^- and increases

in Chla (i.e., Fe-limitation) were found in 4 of 5 incubations (Figure 3.12). Cycle 1 Day 1 was the only location which did not show a significant response to +Fe treatment, and therefore was considered Fe replete. Rapid response in Chla and uptake of NO_3^- occurred at Cycle 2 incubations, with ~8 μM NO_3^- taken up by the +Fe treatment within 24 hours of Cycle 2 Day 1 incubation. A similar response occurred in Cycle 2 Day 4 and Cycle 3 Day 1 incubations, although NO_3^- concentrations remained nonzero up to 48 hours following +Fe. Following exhaustion of NO_3^- concentrations, Chla declined. The Cycle 4 Day 2 incubation only showed evidence of Fe stress after 3 days. No significant differences in the uptake of $Si(OH)_4$ was observed in any of the treatments and incubations.

Fe-limitation of the phytoplankton community was tested during the 'Pt. Sur' filament and was observed in three of the four +Fe amendment studies. Like the 'Morro Bay' filament, Fe replete conditions were found to occur at Cycle 1 Day 2, close to shore (Figure 3.13). Cycle 2 Day 2 and Cycle 2 Day 3 incubations are characterized by Fe-limitation, where +Fe treatments draw down NO_3^- and accumulate Chla faster than the control. However, the results are less obvious for Cycle 2 Day 3, which was initialized with surface water containing already little NO_3^- (1.5 μM). Cycle 3 Day 2 +Fe treatment showed a strong response but was not significantly different from the control until 24 hours. Unlike all other incubations where Fe limitation was observed, a significant increase in the uptake rate of $Si(OH)_4$ was found in the +Fe treatments of Cycle 2 Day 2 and Cycle 3 Day 2 incubations.

Co-limitation of Fe and NO_3^- was observed in the far offshore Cycle 4 incubation of subsurface chlorophyll maximum (SCM, ~70 m) water (Figure 3.14). Following 48 hours of incubation, no growth was observed in the control, but greater Chla concentrations were observed in the +Fe, +N, and +Fe/N treatments, in order of increasing growth response.

In all instances where the addition of Fe stimulated additional Chla production, there was a corresponding increase in the POC concentration, but no difference between treatments in the bSi concentration (Incubations 2 – 5 'Morro Bay' filament, 2 – 4 'Pt. Sur' filament). Additional POC

within the +Fe treatments in these incubations resulted in a significantly lower bSi:POC ratio (Figure 3.15), however the difference in bSi:POC ratio between the +Fe and control in the 'Pt. Sur' filament were smaller than in the 'Morro Bay' filament.

3.4.5. Offshore Transport: dFe and bSi advective flux

In the 'Morro Bay' filament Transect 1, outcropping of the 12.5°C isotherm and elevated concentrations of Chla indicate stations within the loosely defined filament. A relatively cold-core feature is still present at Transect 2, indicated by outcropping of the 13.5°C isotherm. The filament is expected to warm as it is advected offshore due to insolation at the sea surface. A broader and more cohesive filament is indicated by elevated concentrations of Chla (>3 µg L-1). The horizontal structure of the 'Pt. Sur' filament was less distinct. Transect 1 contained elevated Chla concentrations across all stations, however, it was slightly higher within a core of 12ºC water. In Transect 2, a broad core of Chla was contained within a core of 14 – 15ºC surface water. Lastly, Chla and temperature were broadly even over the entire Transect 3. We interpret a maximum in the Brunt-Vaisala frequency (N) as the lower boundary of the filament, where resistance to vertical displacement is at a maximum. Nmax occurs at 45 - 50 m across the 'Morro Bay' filament cycles, whereas it varies from 25 - 40 m across the 'Pt. Sur' filament cycles.

In the 'Morro Bay' filament, the within-filament zonal flux (J_u) of bSi increased between the transects 1 and 2 due to increases in both the off-shore velocity of the filament and inventory of bSi. At the surface (<25 m) and in the subsurface (50 – 150 m), dFe J_u increased between transects, but a decrease was found at 25 – 50 m (Table 3.1). A similar trend was found for bSi. Overall advective fluxes in the 'Pt. Sur' filament are higher than the 'Morro Bay' filament. The dFe J_u is the same for all depth bins in Transect 1, due to high concentrations of dFe at the surface and at depth. The highest bSi J_u is found <25 m in Transect 1 (1191 µmol m-2 s-1 westward) and a decrease of two orders of magnitude in Transect 2 (16 µmol m-2 s-1 westward). The greatest

flux is also found at the surface in Transect 1, and a decrease with depth due to lower bSi concentrations. In Transect 3, there is a small bSi flux in the onshore direction in all depth bins.

3.4.6. Export

For the 'Pt. Sur' filament, an additional deep trap was deployed at Cycles 2, 3, and 4 at a nominal depth of 450 m. The flux data are per day averages over the duration of the cycle and shown in Figure 16. For the 'Morro Bay' filament, bSi export was highest at the base of the euphotic zone and in Cycle 1 (16 mmol Si m^{-2} d^{-1}), followed by Cycle 4 (11 mmol Si m^{-2} d^{-1}), while the lowest export was found at Cycle 3 outside of the filament (3.5 mmol Si m^{-2} d^{-1}). POC export for the 'Morro Bay' filament was highest at the base of the euphotic zone in Cycles 2 (44 mmol C m^{-2} d^{-1}), Cycle 3 (47 mmol C m^{-2} d^{-1}), and Cycle 2.5 (46 mmol C m^{-2} d^{-1}), however flux strongly attenuated with depth. The POC flux in the deepest trap in Cycle 4 (26 mmol C m^{-2} d^{-1} at 56 m) attenuated 28% from the flux at base of the euphotic zone (36 mmol C m^{-2} d^{-1}). Higher POC export was measured in the 'Pt. Sur' filament compared to the 'Morro Bay' filament. The highest POC export was found to occur at Cycle 3 at the base of the euphotic zone (53 mmol C m^{-2} d^{-1}). The 'Pt. Sur' filament followed a similar trend towards higher POC export values during offshore cycles. However, there is much lower bSi export occurring during all cycles when compared to the 'Morro Bay' filament (0.26 – 7.1 mmol Si m^{-2} d^{-1}). Generally, the bSi and POC export track each other during the 'Pt. Sur' filament.

3.5. Discussion

3.5.1 Fe limiting conditions and macronutrient ratios in upwelling filaments

From the standpoint of Fe biogeochemistry in the CCS, the 'Pt. Sur' location is of particular interest, because the Big Sur upwelling region was one the of the areas characterized as chronically Fe limited in the seminal work of Ken Bruland, Dave Hutchins, and co-workers in this area. For example, the well-known "iron mosaic" paper published in 1998, which Hutchins *et al.*

contrasted the Big Sur upwelling and filament region with the Mendocino shelf region further north, to make the case that spatial variation in the mud belt shelf width and riverine input along the CCS region is a key factor in determining the Fe-limitation status of upwelling waters (Hutchins et al., 1998). With narrow shelf widths and low riverine input, the Morro Bay and Pt. Sur regions are likely candidates for potential Fe-limitation, especially given that Fe-limitation has been shown even with moderate shelf widths in upwelling areas (Till et al., 2019). Whether or not the parcel of water is beyond the shelf break is an additional indicator for upwelled waters to become Fe limited. These results highlight the need to further examine the link between sampling location and time with respect to Fe-limitation. Despite the number of previous studies in this region, the Lagrangian approach in CCE LTER studies has not generally been applied.

Biomass limitation by Fe (Liebig limitation) can be approximated using the NO_3^-:dFe ratio because coastal diatoms have an optimal uptake ratio required for their cellular components. Ratios with values > 10-12 μM:nM are indicative of a nutrient regime that is likely to become Fe-limited because diatoms lack sufficient Fe to draw the surface NO_3^- completely (King and Barbeau, 2007). Additionally, Fe limited diatoms preferentially deplete the water of $Si(OH)_4$ over NO_3^- (Brzezinski et al., 2015; Firme et al., 2003; Franck et al., 2003; Hogle et al., 2018; Hutchins and Bruland, 1998; Krause et al., 2015; M. Franck et al., 2000; Takeda, 1998), decreasing *in situ* Si_{ex} and leaving a compounding signature of Fe-limitation. By utilizing both the *in situ* NO_3^-:dFe ratio as well as Si_{ex}, we can gain insight into where and importantly, when, coastal upwelling filaments exhibit evidence for Fe-limitation.

The phytoplankton community composition for the 'Morro Bay' filament was investigated in a previous study based on 18S and microscopy data (Fulton, 2019). This work showed the 'Morro Bay' filament to be diatom-dominated community, contributing most to biomass and Chla. Mixed layer Si_{ex} values decreased significantly in Cycle 2, compared to Cycle 1, and remained low in Cycle 4 (Figure 3.17). These changing uptake rates of macronutrients suggest that dFe was rapidly consumed between Cycles 1 and 2, resulting in an Fe-limited diatom community,

which preferentially depleted the surface of $Si(OH)_4$ relative to NO_3^- (low Si_{ex}). This was also reflected in the NO_3^-:dFe which reached values >100 μM:nM, indicating the potential for strong Fe limitation (Figure 3.17). These high values have only been observed in chronically Fe-limited regions of the ocean, such as the Gulf of Alaska and the Southern Ocean (Hopwood et al., 2020). The onset of significant Fe-limitation of the bloom was captured in the Cycle 2 Day 1 incubation (Figure 3.12), where complete exhaustion of the NO_3^- pool occurred within 24 hr of Fe addition. Rapid accumulation of Chla and consumption of NO_3^- was also observed for the Fe addition treatments in Cycle 2 Day 4 and Cycle 3 Day 1 incubation experiments. These were conducted using surface water from off the shelf break (Figure 3.2). In the Cycle 4 Day 2 incubation, growth was slower, and Fe-limitation was not observed to be significant until the third day of growth (Figure 3.12) likely due to the degree of senescence occurring within the bloom. These results confirm the hypothesis put forth by Chavez et al. (1991), that waters advected offshore with their phytoplankton populations will become Fe limited.

The high concentrations of bSi within the 'Pt. Sur' filament suggests that in Cycle 1 and for the first few days of Cycle 2, the phytoplankton community was dominated by diatoms. However, surface NO_3^-:dFe ratios decrease in Cycle 2 and 3 (Figure 3.17), driven by decreasing concentrations of NO_3^- at the surface (Figure 3.5). This suggests a weakly Fe-limited community, as incubations from these cycles do show some evidence of Fe-limitation of the phytoplankton community at Cycles 2 and 3 (Figure 3.13). It could be the case that the +Fe treatment in these incubations selected for highly silicifying diatoms, while the control phytoplankton community had overall lower Fe and $Si(OH)_4$ requirements.

Metagenomic assessments of the eukaryotic communities showed that phytoplankton communities of inshore Cycles (1 and 2) from both cruises were dominated by high relative abundance of pennate (*Pseudo-nitzschia*) and large centric diatom (*Chaetoceros, Thalassiosira*) sequences. A shift to smaller flagellate phytoplankton (*Pelagomonas*) occurred in offshore cycles as the Chla maximum deepened (Rivera et al. *in prep*, Lampe et al. *in prep*). These two datasets

are not directly comparable due to the different sequencing methods used (operational taxonomic units, Rivera et al. *in prep*, amplicon sequence variances in Lampe et al. *in prep*), but broad generalizations within each are discussed. Compared to the 'Pt. Sur' filament, the 'Morro Bay' filament contained much greater relative proportions of *Pseudo-nitzschia*, a pennate diatom, which are able to acquire additional dFe as luxury Fe and store it intracellularly as ferritin (Marchetti et al., 2006). Further, pennate diatoms are able to maintain Fe quotas 10 times higher than centric diatoms due to this enhanced ability for storage (Twining et al., 2021). Together with intense scavenging onto particles, these community compositions could explain the rapid depletion observed in surface dFe concentrations between Cycles 1 and 2 in the 'Morro Bay' filament, but a quantitative assessment of pennate versus centric diatom contributions to the phytoplankton community Fe demand is outside the scope of this paper. The 'Morro Bay' and 'Pt. Sur' filaments had different relative proportions of pennate and centric diatoms in Cycle 1 and 2, which may suggest that a different NO_3^-:dFe ratio might be more appropriate threshold indicator for potential Fe-limitation of 'Pt. Sur' phytoplankton communities. In both filaments, the formation of SCMs at Cycles 3 and 4 led to shifts in diatom communities towards picoeukaryotes known to inhabit deep nitraclines in the CCS (Hogle et al., 2018). These SCM communities located at the top of the nitracline exhibit Fe and NO_3^- co-limitation (Figure 3.14) and could be a widespread biochemical condition for eukaryotic and prokaryotic primary producers over vast regions of the oligotrophic ocean where SCMs are ubiquitous.

The geochemical indicators of Fe stress (NO_3^-:dFe, Si_{ex}) agree with direct evidence of Fe stress from incubation samples which point towards diatom growth being Fe limited off of the shelf break, consistent with the hypothesis of the upwelling filament transitioning from nutrient replete to Fe limiting for diatom growth as it moves offshore (Figure 3.1).

3.5.2 Sources of Fe to upwelling filaments

3.5.2.1 Sediments within the Benthic Boundary Layer

The continental shelf is a well-studied dFe and TDFe-rich source (Elrod et al., 2004) and relationships between the shelf width, winter storms, riverine deposition of lithogenics and Fe concentrations within the BBL are established (Chase et al., 2005, 2007). These historical insights of Fe content of upwelled waters are considered first-order controls on phytoplankton biomass, describing Fe concentrations in a predictable spatial context. Recently, the assemblage of Fe-binding organic ligands was shown to be distinct within the BBL compared to surface and offshore waters (Bundy et al., 2014), adding nuance to our simplified perspective of Fe supply from margin sediments. Adding to this complexity, we speculate on the effect of additional controls, including particle concentration and dissolved oxygen (DO), by leveraging the BBL dataset from the 'Morro Bay' filament cruise in summer 2017.

The dFe and TDFe content of 'Morro Bay' filament cruise BBL stations 3, 4, 7, and 9 were elevated relative to other stations (Figure 3.9). Since TDFe and total dissolvable manganese (TDMn) may be related to the suspended particulate mass, we plotted profiles beam transmission and found that stations 3, 4, and to a lesser extent station 7, had thick bottom suspensions of particles at the time of sampling (Figure A1). Beam attenuation coefficient is correlated with dFe (r^2 = 0.35, n = 21) and TDFe (r^2 = 0.60, n = 21) when considering all BBL data collected in summers 2017 and 2019, indicating the expected first-order control of sediment resuspension on Fe concentrations. The relationship between dFe and suspensions of particles is, however, less straightforward, since adsorption sites compete with organic Fe-binding ligands to scavenge dFe (Ardiningsih et al., 2020). Such high concentrations of dFe in BBL waters could be explained by the excess of organic material available in sediments to bind and stabilize dFe from returning to particulate form and is resuspended during times of upwelling (Bundy et al., 2014). Therefore, the nature of this dFe is most likely a mixture of Fe mineral colloid and soluble organic Fe-ligand complexes.

Dissolved oxygen in the CUC is declining (Ren et al., 2018), and the areal extent of sediments in contact with low oxygen water masses may increase (Dussin et al., 2019). Bottom

water DO may be an additional control, adjusting the relative proportions of soluble Fe flux from sediments (as reduced Fe(II)) and co-occurring Fe-oxy(hyr)oxide colloids (Burdige and Komada, 2020; Dale et al., 2015). Fluxes of reduced Fe from sediments rapidly oxidize at the sediment-seawater interface. To investigate this point further, we plotted DO profiles for the 9 stations from the 2017 BBL survey (Figure A1). Manganese (Mn), similar to Fe, undergoes dissimilatory reductive cycling in marine sediments, however, its oxidative half-life is ~10^6 times that of Fe(II) and is therefore a good tracer for recent sedimentary input (Sherrell et al., 2018). A comparison of dFe and dMn concentrations at the summer 2017 BBL stations 3 and 4 with station 7 illustrates the importance of bottom water DO on the sensitive redox behavior of dFe. Stations 3 and 4 have bottom water DO of ~72 μmol kg^{-1}, relatively high dMn concentrations, and the highest dFe concentrations measured (~15 nM, Figure 3.9). At station 7, bottom water DO is ~112 μmol kg^{-1} (Figure A1), dMn concentration is similar to BBL stations 3 and 4, yet dFe concentrations are greatly reduced (4 nM, Figure 3.9). This indicates bottom water DO could be an important control on dFe supply from the BBL, since dFe is rapidly oxidized and converted to insoluble particles once in the water column, if equilibration with strong Fe-binding ligands is absent.

The summer 2019 BBL transect overall had a greater range in dFe and TDFe concentrations compared to the 2017 transect, despite having overall higher DO concentrations (126 to 183 μmol kg^{-1}). This suggests that the conditions were not similar between the two cruises at the time of sampling (Figure A1). We do not have corresponding measurements of Mn for the 2019 survey, but future work might utilize differences in redox kinetics of Fe and Mn through trace metal ratios. Within the BBL, depth sampled was found to strongly correlate with dFe and TDFe, which we interpret as the ability to sample close to the sediments depending on shipboard personnel, sampling configuration, and ocean state. In summer 2019, our samples were taken closer to the sediments and had correspondingly higher dFe concentrations, although accurate detection of the bottom depth depends on shipboard instrumentation performance. The Pt. Sur BBL stations had much an order of magnitude lower TDFe concentrations compared to the

transect further south (Figures 3.10, 3.11). This is consistent with observations of Fe-limitation in this region, which were attributed to a zone of poor sedimentary Fe accumulation because of the extremely narrow shelf and lack of fluvial inputs. We also note that the Santa Maria and Santa Ynez rivers discharge closest to BBL stations 4 – 7, but these stations do not consistently contain the highest concentrations of dFe, suggesting considerable deviation from trends found in the northern CCS (Chase et al., 2005). Therefore, local factors must be considered. Inner shelf dynamics are important for the formation of BBLs, but the longevity of these turbid layers has not been investigated and has important implications dFe scavenging and timing with upwelling and coastal filament formation. More statistical approaches and continued monitoring of these stations are required to understand the relative strengths of upwelling currents, winter riverine discharge, local circulation, topography, Fe-binding organic ligands, and DO on setting the Fe content of these waters.

3.5.2.2 California Undercurrent

In the 'Morro Bay' filament cruise, the California Undercurrent (CUC) was the primary water mass composing crosshore advected waters (Zaba et al., 2021). Low-oxygen CUC water can impinge on the shelf during times of upwelling. The degree to which the CUC contributes to the upwelled Fe source has thus far been overlooked as a significant source of Fe in the CCS. The 'Pt. Sur' filament showed much higher subsurface concentrations of dFe and TDFe (2 – 3 nM and 30 – 60 nM, respectively) adjacent to the shelf slope, compared to the 'Morro Bay' filament (0.5 – 1 nM dFe)(Figures 3.5,3.6). In the 'Morro Bay' filament, a dFe maximum was found ~100 km offshore at 75 – 150 m depth, which could be an offshore signature of the CUC, although it is expected to be found closer to the coast during the summer months (Kurczyn et al., 2019; Rudnick et al., 2017).

Summertime climatological maps of the CCS indicate that the CUC is located close to the shelf slope (centered 50 km offshore) off Pt. Conception (Rudnick et al., 2017). Further north,

near Monterey Bay, the CUC core is found 75-100 km offshore, but can be found in the subsurface up to 150 km from the coast. The elevated concentrations of dFe (~2-3 nM) in the 'Morro Bay' filament subsurface offshore waters match those found in the inshore profiles during the 'Pt. Sur' filament, with similarly elevated salinity (33.75 to 34) but lower DO (50 to 100 μmol kg^{-1}, Figure A2). Generalizing water mass climatologies for the Morro Bay and Pt. Sur regions and the biogeochemical signatures, the observed dFe subsurface signatures in ocean transects (Figure 3.5) may be derived from the poleward flowing CUC.

How can we explain the offshore CUC signature in the 'Morro Bay' filament transect? Isopycnals are domed within this feature (Figure A2) indicating this may be a subsurface anticyclonic eddy, or *puddy* (poleward undercurrent subsurface eddy, Frenger et al., 2018). These features have been described previously as low DO and high nutrient extreme events in the CCS that propagate westward along the 26.7 kg m^{-3} isopycnal, but biogeochemical measurements within *puddies* are sparse. *Puddies* can travel several thousand kilometers, isolating a parcel of CUC water and advecting it offshore (Lukas and Santiago-Mandujano, 2001). Therefore, in addition to surface filaments, *puddies* are important for the leakage of CUC water towards the subtropical gyre. We speculate that during the 'Morro Bay' filament, the presence of a *puddy* with elevated dFe, derived from the CUC, removed an dFe enriched portion of CUC water from being upwelled. Thus, it is possible that this physical and biogeochemical feature contributed to the intensity of Fe-limitation observed in 2017 by removing dFe from being upwelled. Determination of the geostrophic currents in these transects will help to ascertain the location of the CUC.

Northward geostrophic currents are intensified near the continental margin during the summer and into the Fall. We hypothesize that the CUC, during its northward transit, may entrain additional dFe and TDFe from resuspended margin sediments and that this is enhanced near prominent headlands during times of wind driven upwelling. Additional local considerations, such as seasonality in internal waves breaking on shelf slopes (Lam et al., 2018) may be important additional mechanisms for suspending Fe-bearing sediments and increasing LpFe in subsurface

water masses near the coast. New results suggest that the CUC may be the most biologically-active water mass in the CCS since it provides upwelling water with remineralized sources of macronutrients (Zaba et al., 2021). Now, we suggest such high rates of primary production associated with upwelled CUC waters may be, in part, explained by its relatively high concentrations of dFe. The relative contribution of dFe from the CUC and the BBL to upwelled waters should be explored further to accurately predict changes in the primary production potential of upwelled waters in the CCS.

3.5.3 Fe-limitation and diatom community elemental stoichiometry

Phytoplankton Fe stress affects light harvesting, carbon acquisition, and NO_3^- assimilation because these are Fe-intensive processes (Hutchins and Bruland, 1998; Morel, 2008). Diatoms, when Fe stressed, may prefer to remain in cell cycle stages that facilitate slower growth, increasing silicification (Rocha et al., 2000; Smith et al., 2016). When $Si(OH)_4$ is not limiting, cellular Si (as bSi) content can increase, but even so, reductions in NO_3^- assimilation and carbon fixation increase Si:N and Si:C uptake ratios. This results in increases in the bSi:POC ratio (Marchetti and Harrison, 2007). Such cellular reconfigurations can affect the efficiency of carbon export and sequestration, through changing sinking speeds and predation pressure (Assmy et al., 2013; Brzezinski et al., 2015; Hutchins and Bruland, 1998).

Concentrations of bSi, POC, and bSi:POC ratio in deckboard incubation experiments conducted during the 'Morro Bay' filament were previously documented (Fulton, 2019). The increasing trend in bSi:POC between Cycles 1 and 2 suggests that diatoms entrained into the filament underwent a physiological change with the development of Fe-limitation (Figure 3.7). Both bSi and POC measurements include detrital material and contributions from other planktonic organisms, besides diatoms, and differences in the remineralization of POC and bSi in incubations could also contribute to these spatial and temporal trends. A decline in the bSi:POC ratio, was found to occur in Cycles 3 and 4 suggesting a decline of the diatom bloom. The higher

bSi:POC diatom communities are likely to sink faster due to their increased ballast, which could contribute to the observed declines (Brzezinski et al., 2015). These studies provide useful correlations between *in situ* nutrient data and bSi:POC ratios in this region. The results of amendment experiments (Figure 3.15) are strong evidence in support of a mechanistic link between the Fe biogeochemical condition and increasing bSi:POC ratios of diatom blooms. In particular, our results point towards Fe-limitation of photosynthesis as a likely driver for bSi:POC ratios, since greater POC concentrations and lower bSi:POC ratios resulted when Fe-limitation was alleviated. Silicification rates, on the other hand, remained unchanged by the addition of Fe in any of the experiments. While we attributed bSi:POC ratios to physiological changes of diatom communities, a shift in community composition towards more lightly silicified small diatoms would also decrease bSi:POC (Quéguiner, 2013; Tréguer et al., 2018). Other planktonic organisms could affect the observed patterns in bSi:POC, but a quantitative assessment is currently lacking. Caveats with interpreting *in situ* ratios will be discussed later (see section 3.5.4).

Fe addition grow-out incubations were generally carried out for 3 days, as has been typical in Fe-limitation studies of surface phytoplankton communities. In previous studies in the California Current, as well as the Ross Sea, the Humboldt current and the Peru Upwelling (Hutchins et al., 1998, 2002; Hutchins and Bruland, 1998; King, 2007; Sedwick et al., 2000), a 3-4 day incubation timeline captured macronutrient depletion and Chla increases following Fe addition fairly evenly. However, in the 'Morro Bay' filament incubation studies, macronutrients in Fe limited Cycles were quickly depleted compared to these previous studies (Figure 3.12). This observed decoupling of nutrient uptake has been observed in and is consistent with previous Fe incubation studies (Hutchins and Bruland, 1998; Till et al., 2019). The Fe acquisition strategies likely differ between the phytoplankton communities, where 'Morro Bay' diatoms might have higher affinity uptake of Fe, and are able to divert these few atoms per cell towards assimilating available nitrate as was discussed in section 3.5.1.

3.5.4 Length scales, advective flux, export efficiency, and oceanic budgets

Macronutrient and dFe concentrations decrease exponentially with distance the upwelled water parcel has traveled along the core of the filament. Since phytoplankton are present in surface waters, the distribution of dFe in the upper 10-25 m is a function of both uptake by phytoplankton and conversion to other particulate pools because of scavenging. The concentrations (*C*) of dFe, $Si(OH)_4$, and NO_3^- are fit exponentially to the equation

$$\boldsymbol{C(x) = C_0 e^{-x/D}}$$

where C_0 is the concentration of the upwelled water at the surface, *x* is the distance traveled along the core of the filament during Lagrangian cycles (km), and *D* is the scale length (km), defined as the distance where $C(x) = 0.37C_0$ (i.e., the concentration has decreased to 37% of the initial concentration). During the 'Morro Bay' filament, for dFe at 10-25 m, we find $[dFe] = 2.673e^{-x/43}$ ($r^2 = 0.89$, $n = 12$, $D = 43 \pm 15$ km, Figure 3.18). The 'Pt. Sur' filament had a significantly longer length scale, where $[dFe] = 0.687e^{-x/250}$ ($r^2 = 0.53$, $n = 22$, $D = 250 \pm 150$ km, Figure 3.18).

The degree of Fe-limitation was found to be more extreme in the 'Morro Bay' filament, whereas more efficient consumption of the macronutrients occurred during the 'Pt. Sur' filament, suggesting, in part, sufficient concentrations of bioavailable Fe remained within the filament for longer, or the phytoplankton community shifted towards small phytoplankton with lower Fe cellular quotas. This is reflected in the length scale parameters for NO_3^- and $Si(OH)_4$ during the 'Pt. Sur' filament, which are 85 ± 18 km and 79 ± 18 km, respectively, compared to 399 ± 173 and 155 ± 45 km in the 'Morro Bay' filament (Table 3.2). An important implication of these observations is that Fe-limitation modulates the ability for upwelled nutrients to be advected offshore to the oligotrophic ocean (Chabert et al., 2021).

The efficiency with which bSi and POC are exported from the filament depends on the remineralization efficiency and time spent within the water column, the latter of which is strongly

related to sinking speed. Sinking speed in this sense is related to the density of the particle (Stokesian settling rate), but also the energetics of currents and turbulence. As the filaments accelerate offshore, particles, even large ones, can remain suspended until the current slows and lacks sufficient energy to maintain a particulate suspension. Additional biological processes can greatly affect sinking speeds, such as packaging of diatom cells into quick sinking aggregates and fecal pellets produced by micro- and mesozooplankton grazers (Longhurst and Glen Harrison, 1989). Given that particulate matter with high bSi:POC ratios sink quicker, it might be surprising we do not observe greater bSi:POC in sediment traps (Figure 3.16) compared to suspended particles in the overlying water column, except for at Cycle 1 in the 'Pt. Sur' filament (Figure 3.7).

There are several caveats with interpreting *in situ* and sediment trap bSi:POC ratios. First, while diatom community changes were observed, we do not necessarily know the Si content of each species present. Furthermore, we lack a quantification of each species' contribution to the overall bSi and POC inventories. Second, even though incubation results suggest a mechanistic link between Fe-limitation and bSi:POC ratios of diatom communities, *in situ* ratios include a detrital fraction not accounted for in our incubations. The fraction of detrital particulate matter to the total is unknown. Finally, micro- and mesozooplankton have been shown to preferentially graze on lightly-silicified diatoms, which are typically smaller diatoms (Zhang et al., 2017). Zooplankton grazing has also been shown to promote the remineralization of bSi and POC within the water column (Schultes et al., 2010). Therefore, diatom community composition, contributions of detrital bSi, and preferential predation and remineralization may also be responsible for controlling *in situ* bSi:POC ratios, in addition to Fe-limitation.

Stukel and Barbeau (2020) compiled sediment trap export flux data for all CCE LTER process studies, including the 'Morro Bay' filament (P1706) and found that patterns in the nutrient landscape of the CCS region are better predictors of the flux of sinking particles than measurements of net primary production (Stukel and Barbeau, 2020). Carbon export was found

to be enhanced during high-nutrient and Fe-stressed conditions. We investigated the efficiency with which particulate matter is exported from the euphotic zone with relation to the Fe-limitation status of the phytoplankton community. In the 'Morro Bay' filament, Cycle 4 showed the highest export of POC relative to all other cycles, despite having the lowest biomass. The same is true for bSi, except for at Cycle 1 in the ~100 and 150 m traps, which is likely a result of the production of anchovy fecal pellets (Figure 3.16). Bourne *et al.* (2021) found these pellets in Cycle 1 were full of diatom frustules and fragments (Bourne et al., 2021). We found that ~9% of the bSi inventory at Cycle 1 is exported to 150 m, whereas ~24% is exported at Cycle 4. POC export efficiency shows similar trends with 1.5% and 4.9% of the inventory exported per day for Cycles 1 and 4, respectively.

The 'Pt. Sur' filament showed similar export efficiency of POC within the top 50 m in Cycles 1 and 2 (3.8% per day and 4.0% per day, respectively). However, Cycle 3 reached as high as 11% of the POC inventory exported per day to 50 m. This cycle had the highest values of POC flux measured over both cruises (Figure 3.16). Far offshore, 3.2% of the POC inventory reached 120 m per day. The bSi export efficiency to 150 m depth was similar between Cycles 1 and 2 (3.3% per day and 4.2% per day, respectively). An increase to ~27% bSi inventory per day was estimated at Cycle 3, which is similar to the export in the offshore cycle in the 'Morro Bay' filament. The oligotrophic Cycle 4 had the lowest export efficiency (2.8% bSi inventory per day). Cycles 1 and 2 had the highest bSi flux in the 'Pt. Sur' filament, however, these stations also had the highest bSi concentrations measured. It is likely that the high concentrations of bSi accumulated in early stages of the filament remained suspended until Cycle 3, where incubation results showed the greatest degree of Fe-limitation (Figure 3.13).

It appears that within regimes of Fe-limitation, export of biomass is more efficient. These results support the hypothesis put forward by Stukel and Barbeau (2020) and finding of increased diatom-mediated POC export in Fe-limited CCS upwelled waters (Brzezinski et al., 2015). Coastal upwelling filaments are mechanisms by which coastally upwelled waters are advected offshore,

resulting in decoupling of net primary production and export (Chabert et al., 2021; Kelly et al., 2018). This decoupling within mesoscale features of the CCS has been described previously and was attributed to lateral transport of high-biomass stages of phytoplankton blooms (Landry et al., 2009; Plattner et al., 2005). We argue that increased ballasting due to Fe-limitation of diatom aggregates and fecal pellets may be an additional control of *when* and *where* export occurs. These findings may help better resolve and explain the spatial and temporal observations of Fe-limitation in the CCS, with implications for global models of primary productivity and export.

3.6. Conclusions

Coastal filaments are seasonally transient features of high productivity in global Eastern Boundary Upwelling Systems, connecting the coastal pelagic to the deep open ocean. The 'Morro Bay' and 'Pt. Sur' coastal upwelling filaments allowed for *in situ* observation of developing Fe-limitation of diatom blooms carried offshore from areas of cool, nutrient-rich, upwelling waters. These are the first studies to follow coastal upwelling filaments in the California Current from upwelling to offshore, in a Lagrangian fashion, with a focus on Fe biogeochemistry and Fe-limitation. Two filaments were successfully identified, followed in Lagrangian sampling scheme, and defined by cross-sectional quasi-synoptic transects.

We found that the extent to which additional NO_3^- stimulated primary production in filaments depends on the availability of Fe. The BBL source of dFe is important, especially in the heavily Fe-limited 'Morro Bay' filament. CUC is an additional new source of dFe and TDFe, which likely depends on the topography (headlands), latitude, and breaks in its flow due to subsurface eddies. Trends in this current suggest decreasing dissolved O_2 content (Ren et al. 2018), which could result in greater dFe concentrations in BBL waters as soluble Fe (as Fe^{2+}) in places which lack extensive continental shelves or riverine input. Ongoing climate change is expected to intensify regional droughts and ocean hypoxia which will have important consequences for Fe biogeochemistry in the CCS. We do not reject our hypothesis, Fe-limitation occurs in upwelling

filaments and this condition is reflected in macronutrients, upholding the use of geochemical proxies in the CCS. The development of Fe-limitation led to elevated *in situ* NO_3^-:dFe ratios and decreasing Si_{ex} signatures. Deckboard incubation studies showed varying degrees of growth and uptake of NO_3^- and $Si(OH)_4$ in response to Fe-fertilization in cycles located offshore form the continental shelf. Changes in the uptake ratios of the macronutrients and the effects of Fe-limitation on photosynthesis were linked to bSi:POC ratios of the phytoplankton communities. At Fe-limited stations, enhanced bSi:POC ratios are attributed to decreased POC content, rather than changes in bSi.

Changes in diatom elemental stoichiometry makes them denser and more probable to sediment in the deep ocean. We also presented evidence in support of enhanced organic carbon export efficiency offshore coincident with these biogeochemical spatial and temporal observations. In offshore evolutions of the filaments, we found enhanced export of carbon, which is a consequence of lateral transport of biogenic particles and enhanced ballasting of diatoms due to increased bSi:POC ratios under Fe-limitation. This is an important step towards understanding how nutrients in mesoscale features in eastern boundary upwelling systems support high rates of primary production and facilitate carbon sequestration in the ocean. The length scales of macronutrients are related to incomplete utilization, which is modulated by Fe-limitation. This has important implications for oceanic gyre budgets of the macronutrients. Filaments are important for lateral advection of elements derived from the continental crust, as well as biogenic particulate matter, but dFe appears to be controlled by diatom community growth in the surface and sub-mesoscale features and sediment plumes in the subsurface. We expect that a similar fate is shared for other bioactive or heavily scavenged metals. The Lagrangian approach reveals that the *iron limitation mosaic* in the California Current System is more temporal than spatial.

3.7. Acknowledgements

We thank CCE LTER and captains and crews of the *R/Vs Revelle and Atlantis* for facilitating sample collection. We thank Chief Scientist Mark D. Ohman, who selected the two filaments for study, the Cycle locations, and sampling schema for quasi-synoptic transects and the Seasoar. We also would like to thank Robert Sherrell, Vincent Roccanova, and Kaixan Bu for assistance with analyzing BBL samples for multiple trace elements and the Department of Marine and Coastal Sciences at Rutgers University. Data sets presented here were supported in part by CCE-LTER funding (NSF grant OCE-1026607). K.O.F. was supported by an NSF GRF (NSF 15-597). Sample analyses at Rutgers University were supported by an Edna Bailey Sussman Trust Special Merit Award in 2018.

3.8. Data Availability

All data produced by the CCE LTER program are available at http://oceaninformatics.ucsd.edu/datazoo/catalogs/CCSlter/datasets.

3.9. Figures and Tables

Table 3.1. DFe (units nM) and bSi (units μM) concentrations are averaged over the indicated depth interval. Average zonal (J_u) and meridional (J_v) advective flux estimates with uncertainties associated with spatial and temporal averaging. Units for dFe J_u and J_v are in nmol m^{-2} s^{-1} and bSi J_u and J_v are units μmol m^{-2} s^{-1}.

Cruise	Transect	Depth Interval	[dFe] AVG	±	[bSi] AVG	±	dFe J_u	±	dFe J_v	±	bSi J_u	±	bSi J_v	±
P1706	1	<25m	0.36	0.25	1.50	0.80	-3	17	-15	22	-14	72	-63	85
P1706	1	25 - 50m	0.38	0.04	1.99	0.56	-63	45	-12	16	-333	254	-63	87
P1706	1	50 - 150m	0.40	0.15	0.50	0.43	0	15	-14	15	0.6	19	-18	24
P1706	2	<25m	0.27	0.02	1.36	0.75	-43	18	8	3	-214	148	40	27
P1706	2	25 - 50m	1.13	0.17	0.30	0.09	-23	16	-3	35	-6	5	-1	9
P1706	2	50 - 150m	0.81	0.24	0.72	0.61	-132	53	45	36	-118	104	40	45
P1908	1	<25m	1.95	1.58	10.03	2.69	-232	307	-32	161	-1191	1287	-164	55
P1908	1	25 - 50m	2.70	2.09	0.92	0.48	-293	313	81	141	-100	91	28	46
P1908	1	50 - 150m	3.39	1.66	0.81	0.36	-313	190	150	209	-75	43	36	49
P1908	2	<25m	1.14	0.64	0.70	0.26	-26	29	-67	62	-16	17	-41	57
P1908	2	25 - 50m			0.66	0.31					-18	10	-19	15
P1908	2	50 - 150m			0.30	0.33					-9	13	-7	10
P1908	3	<25m	0.45		0.11		25	3	6	35	6	0.7	2	0.3
P1908	3	25 - 50m			0.19						8	0.9	3	12
P1908	3	50 - 150m			0.13						0.6	2	-0.3	4

Table 3.2. Length scale parameters for nitrate, silicic acid, and dFe for the 'Morro Bay' and 'Pt. Sur' filaments surface waters (P1706, P1908, respectively). PXXXX refer to the cruise identification, P for 'process', XXXX for 'year year month'.

Cruise	Nutrient	r^2	*D* [km]	*n*
P1706	nitrate	0.20	399±173	103
P1706	silicic acid	0.41	155±45	103
P1706	dissolved Fe	0.89	43±15	12
P1908	nitrate	0.44	85±18	112
P1908	silicic acid	0.45	79±18	89
P1908	dissolved Fe	0.53	250±150	22

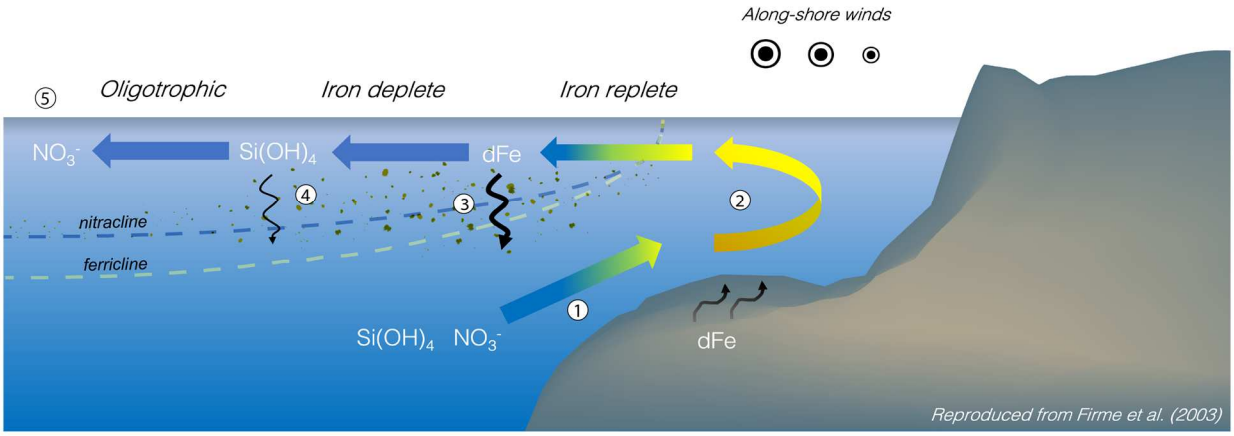

Figure 3.1. Framework for the biogeochemical evolution of a coastal upwelling filament in the CCS. During prolonged periods of intense along-shore winds, water masses on the continental slope, enriched in remineralized macronutrients ($Si(OH)_4$ and NO_3^-), are upwelled to the surface, replacing offshore-transported surface water near the coast ①. During episodes of wind-driven upwelling, deep water masses impinge on the shelf and interact with muddy continental shelf sediments. Resuspended Fe-bearing sediments from these muds form a turbid benthic boundary layer, which is entrained into the euphotic zone creating iron replete conditions for primary producers ②. This pulse of macro- and micronutrients selects for quickly-growing diatoms. The cold, nutrient-rich water parcel can be detected by autonomous and ship-towed instrumentation, as well as by space-borne detectors. The water parcel is only partially mixed with the surrounding ocean, and is advected offshore forming a filament. High rates of primary production within the filament can lead to the formation of a diatom bloom. When this occurs, Fe is preferentially removed from the surface layer (relative to $Si(OH)_4$ and NO_3^-) as sinking biogenic and mineral particles, leading to decoupling of the ferricline and nitracline ③. Once off the shelf, concentrations of Fe are heavily depleted and an excess of macronutrients (high NO_3^-:dFe ratio) results in Fe limitation of the diatom community. A lack of Fe inhibits key diatom metabolic processes, such as NO_3^- assimilation and carbon fixation, but not precipitation of biogenic silica (bSi) frustrules. Fe-limited diatoms preferentially deplete the surface $Si(OH)_4$ reservoir (relative to NO_3^-) and begin to sink ④. With the $Si(OH)_4$ reservoir depleted, the phytoplankton community shifts towards non-silicifying phytoplankton capable of surviving at subsurface Chla maxima at the edge of the oligotrophic subtropical gyre, the furthest detectable trace of the filament ⑤. This figure is reproduced from Firme *et al.* (2003).

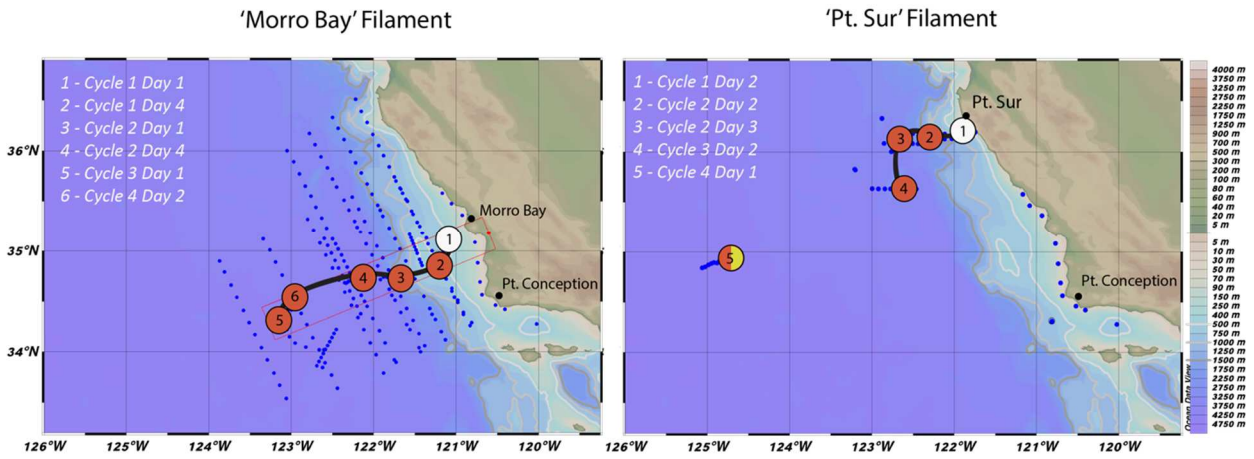

Figure 3.2. On-deck experiment locations during the 'Morro Bay' (left) and 'Pt. Sur' (right) filaments. Red circles indicate Fe-limited sites (as indicated by Chla and nitrate drawdown response in deck-board incubations). Split red-yellow symbol indicates Fe-NO_3^- co-limitation. White symbol indicates no micronutrient limitation detected. Black line roughly indicates the filament track for the Lagrangian cycles. Gray isopleths indicate the 500, 1000, and 1500 m isobath. Red box and black line indicates direction for transect section plots.

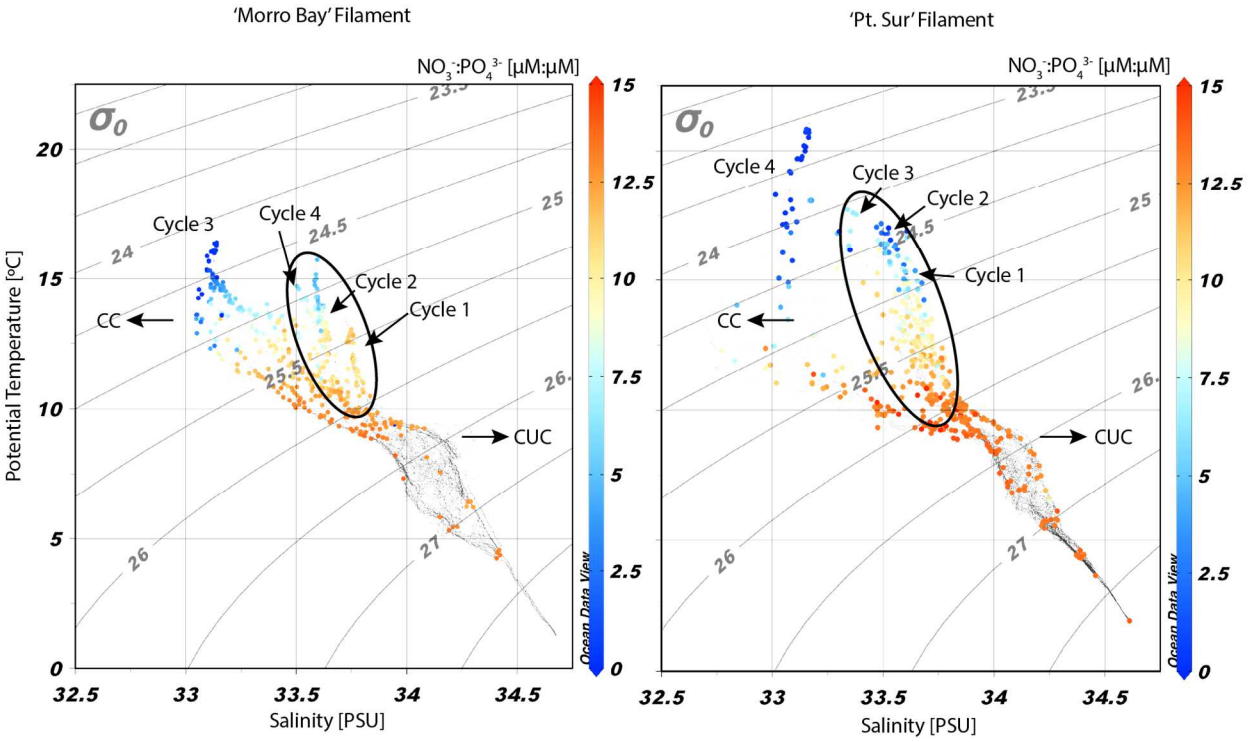

Figure 3.3. θ-S diagram of the 'Morro Bay' (left) and 'Pt. Sur' (right) filaments. The color bar is nitrate:phosphate ratio. The ellipse outlines the stations located within the surface filament core, distinguished by its relatively high salinity signature from upwelled California Undercurrent (CUC) water sources, compared to the relatively fresh and offshore California Current (CC) surface water (Zaba et al., 2021). Contours of constant potential (σ_θ) density are overlaid. Based on the location of the CUC along CalCOFI line 93.30 according to Bograd et al. (2019), the NO_3^-:PO_4^{3-} ratio at σ_θ = 25.8 kg m^{-3} is 11.73 and 12.20, in 2017 and 2019 respectively. The NO_3^-:PO_4^{3-} ratio at σ_θ = 26.5 kg m^{-3} is 11.06 and 11.51, in 2017 and 2019 respectively.

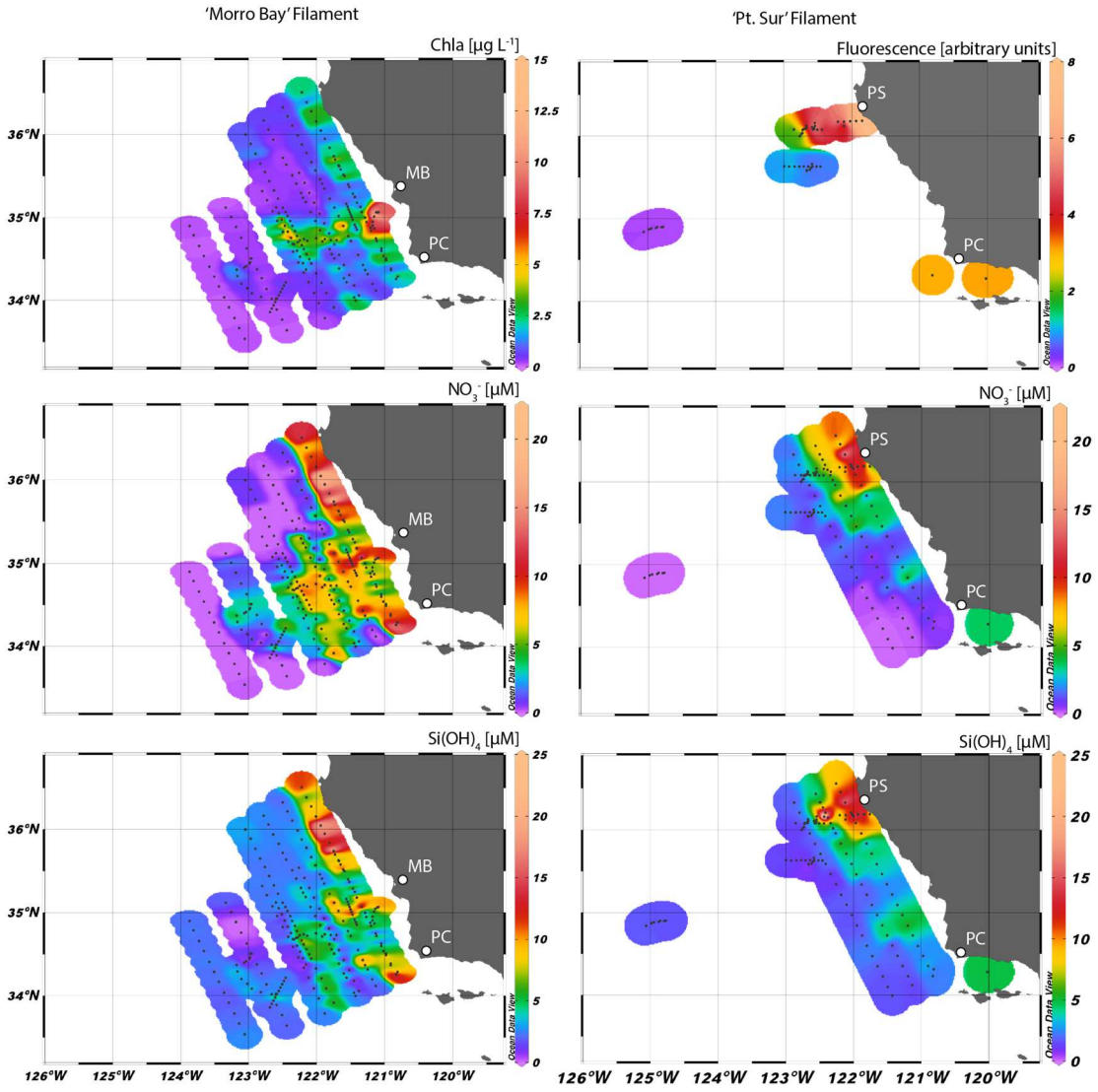

Figure 3.4. Surface plots of Chla fluorescence (top-left) and Chla *in vivo* fluorescence (top-right), nitrate (middle row), and silicic acid concentrations (bottom). Important locations on the California coast are indicated in the top maps: Morro Bay (MB), Pt. Conception (PC), and Pt. Sur (PS).

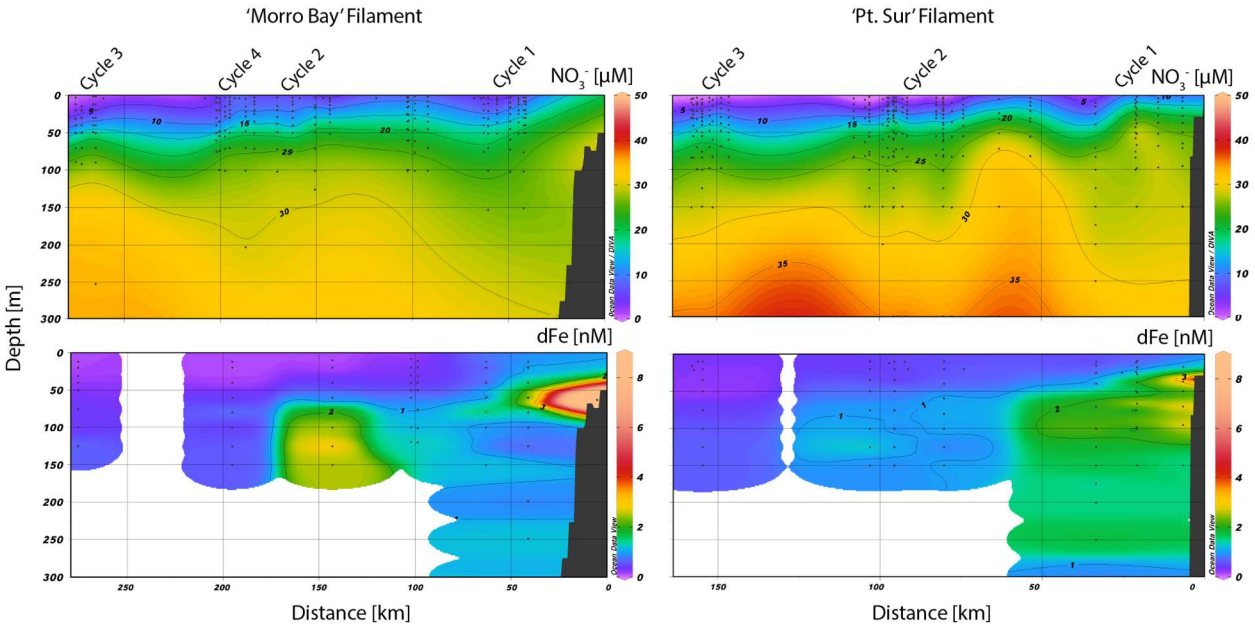

Figure 3.5. Concentrations of NO_3^- (top) and dFe (bottom). These variables are plotted as sections, generally as a function of distance transported (according to **Figure 3.2**) within the 'Morro Bay' (left) and 'Pt. Sur' (right) filaments.

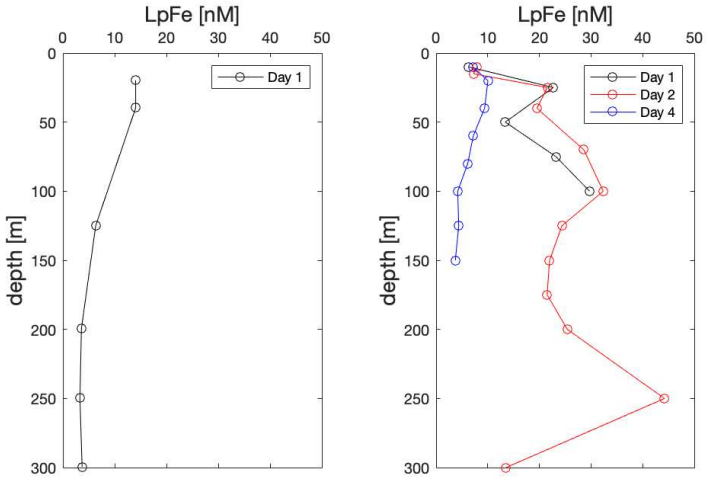

Figure 3.6. Profiles of labile particulate Fe (LpFe = TDFe – dFe) for Cycle 1 for both the 'Morro Bay' (left) and 'Pt. Sur' filament (right).

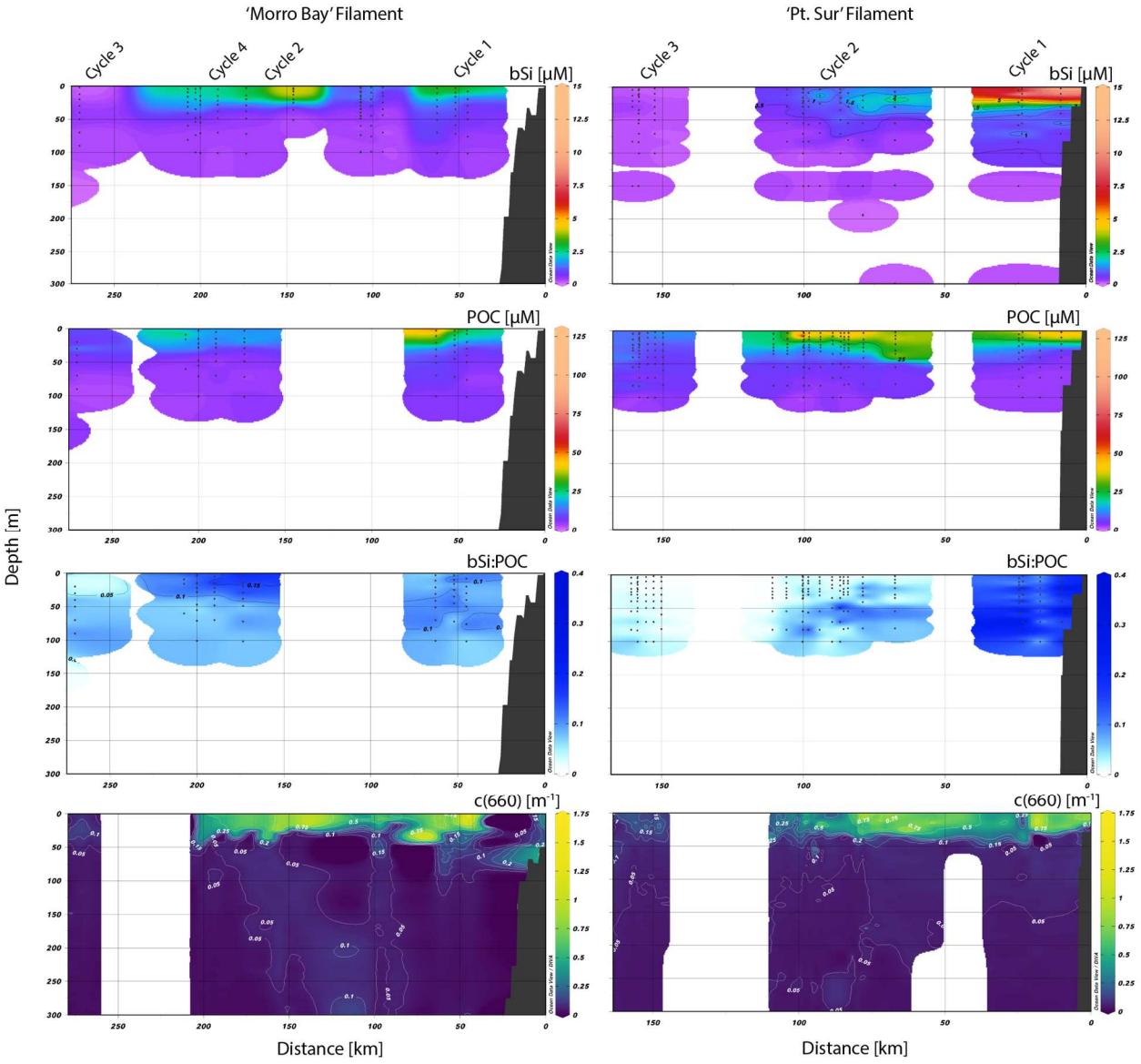

Figure 3.7. Concentrations of bSi (top) and POC, as well as bSi:POC are plotted with beam attenuation coefficient at 660 nm (bottom). These variables are plotted as sections, generally as a function of distance transported (according to Figure 3.2) within the 'Morro Bay' (left) and 'Pt. Sur' (right) filaments.

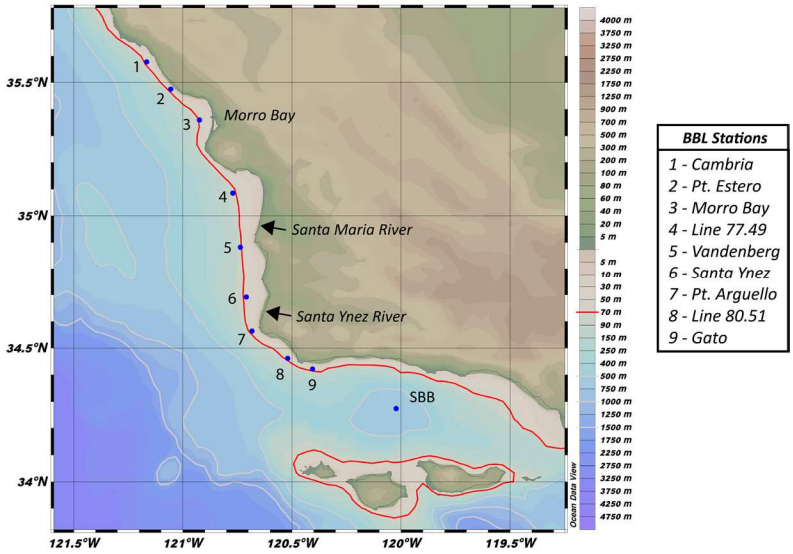

Figure 3.8. Map showing stations for the BBL Transect, a series of stations sampled along the Californian coast. Stations are labeled by numbers according to the map legend. The red contour denotes the 70 m isobath. The gray contours denote the 500, 1000, and 1500 m isobaths. SBB is the Santa Barbara Basin station.

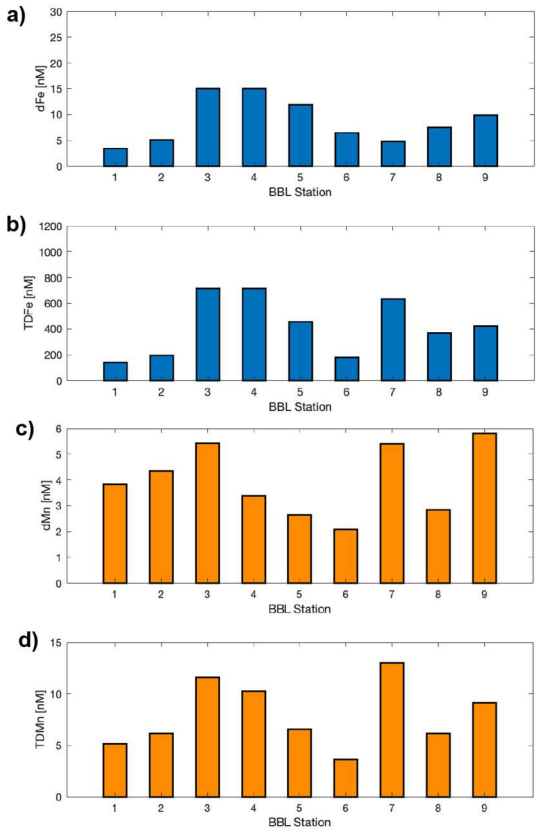

Figure 3.9. Dissolved Fe (a), dissolved Mn (dMn, c), total dissolvable iron (TDFe, b) and manganese (TDMn, d) trace metal concentrations found within the benthic boundary layer stations in summer 2017. Numbers are station labels and mapped in Figure 7 (1 – *Cambria,* 2 – *Pt. Estero,* 3 – *Morro Bay,* 4 – *Line 77.49,* 5 – *Vandenberg,* 6 – *Santa Ynez,* 7 – *Pt. Aguello,* 8 – *Line 80.51,* 9 – *Gato*).

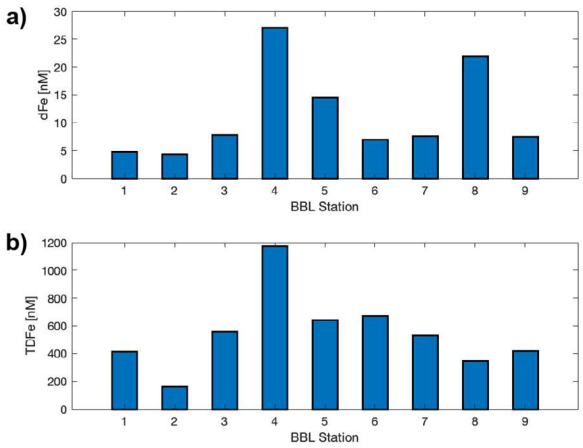

Figure 3.10. Dissolved Fe (a) and total dissolvable iron (TDFe, b) trace metal concentrations found within the benthic boundary layer stations in summer 2019. Numbers are station labels and mapped in Figure 7 (1 – *Cambria,* 2 – *Pt. Estero,* 3 – *Morro Bay,* 4 – *Line 77.49,* 5 – *Vandenberg,* 6 – *Santa Ynez,* 7 – *Pt. Aguello,* 8 – *Line 80.51,* 9 – *Gato*).

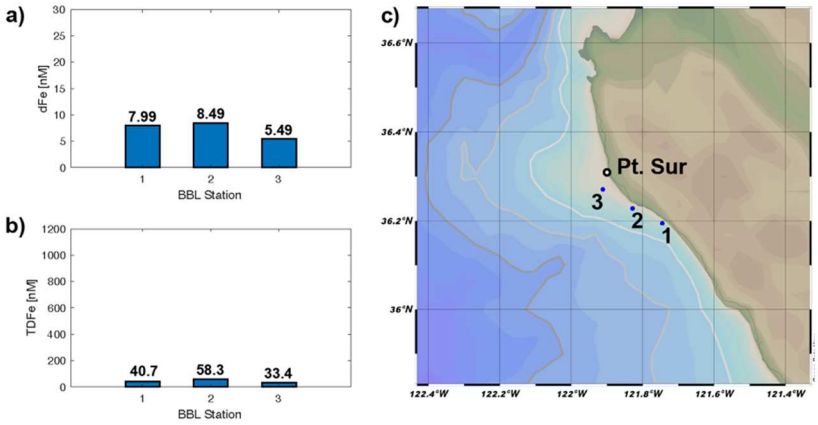

Figure 3.11. Dissolved Fe (a) and total dissolvable iron (TDFe, b) trace metal concentrations found within three benthic boundary layer stations located along the shelf near Pt. Sur (map, c). Pt. Sur is labeled on the map, and the grey contours indicate the 500 m, 1000 m, and 1500 m isobaths.

Figure 3.12. Growth and nutrient uptake monitored during deckboard incubation experiments during the 'Morro Bay' filament cruise (P1706). The cycle and day for experiment initiation (day = 0) is indicated for each row. The left column is NO_3^- concentration, middle column is $Si(OH)_4$ concentration, and the right column is Chla concentration as a proxy for phytoplankton biomass. These experiments correspond to the number labels in Figure 2. Note the different y-axes, '+Fe' refers to the Fe addition treatment and 'Control' is unamended.

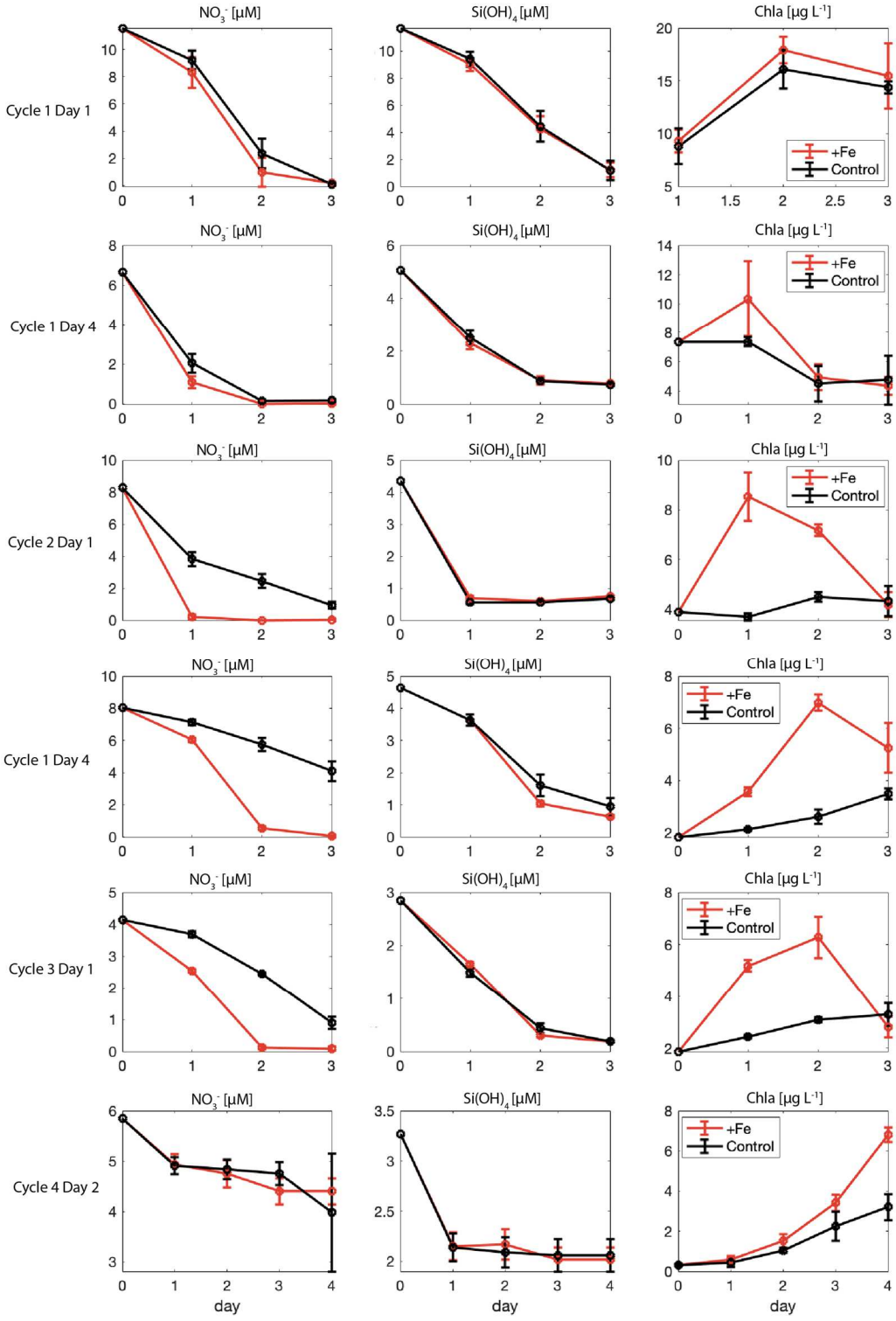
NO3- [µM]
Si(OH)4 [µM]
Chla [µg L-1]
Cycle 1 Day 1
Cycle 1 Day 4
Cycle 2 Day 1
Cycle 1 Day 4
Cycle 3 Day 1
Cycle 4 Day 2
+Fe
Control
day

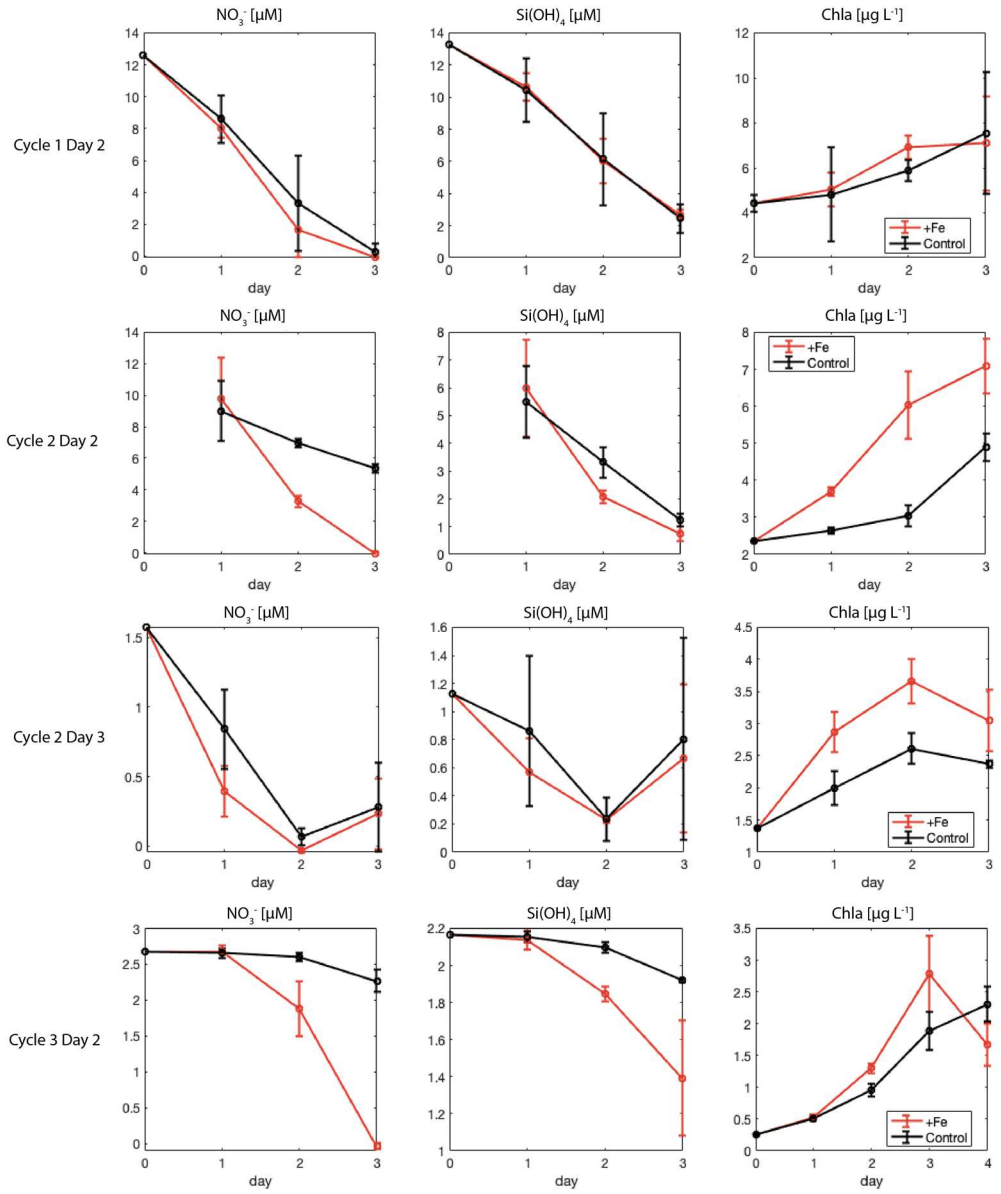

Figure 3.13. Growth and nutrient uptake monitored during deckboard incubation experiments during the 'Pt. Sur' filament cruise (P1908). The cycle and day for experiment initiation (day = 0) is indicated for each row. The left column is NO_3^- concentration, middle column is $Si(OH)_4$ concentration, and the right column is Chla concentration as a proxy for phytoplankton biomass. Experiment names correspond to the number labels in Figure 2 (except for 'Pt. Sur' filament Cycle 4 experiment which is labelled as 5). Note the different y-axes, '+Fe' refers to the Fe addition treatment and 'Control' is unamended.

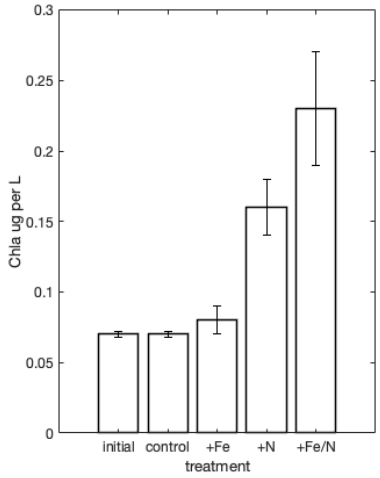

Figure 3.14. Growth monitored during deckboard incubation experiment at Cycle 4 during the 'Pt. Sur' filament (**Figure 2**). All Chla values are presented for the final timepoint (after 2 days) except for 'initial' which is the starting concentration of Chla. The x-axis label denotes the treatment.

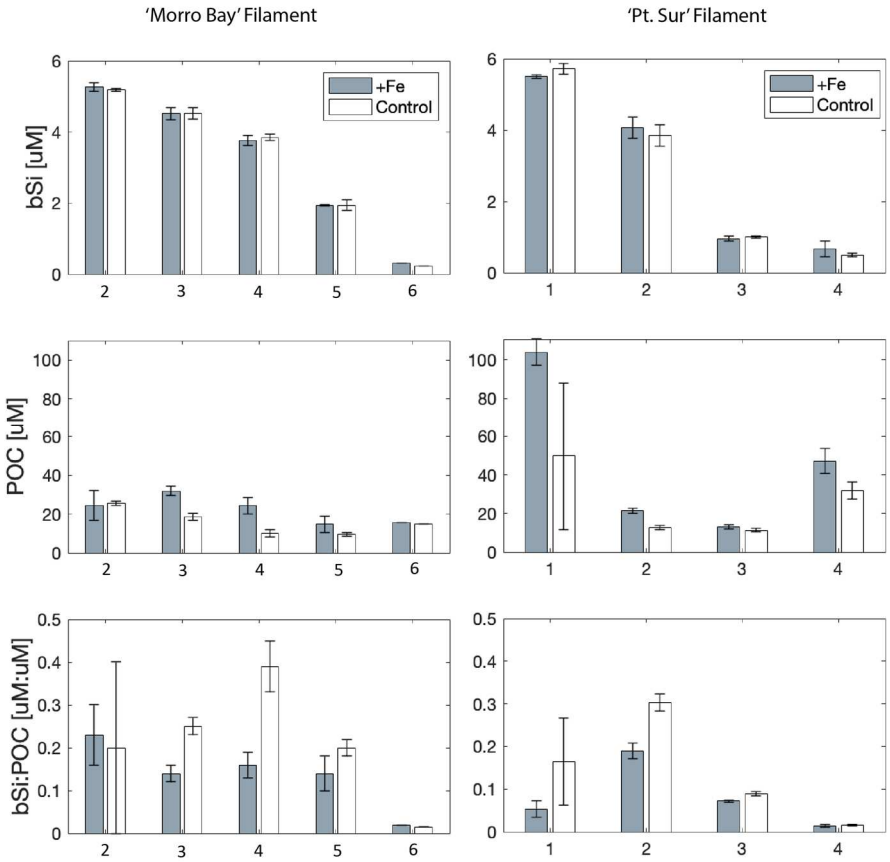

Figure 3.15. Final timepoint measurements of bSi (top), POC (middle row), and bSi:POC ratios (bottom) for deckboard incubations according to number labels in Figure 3.2.

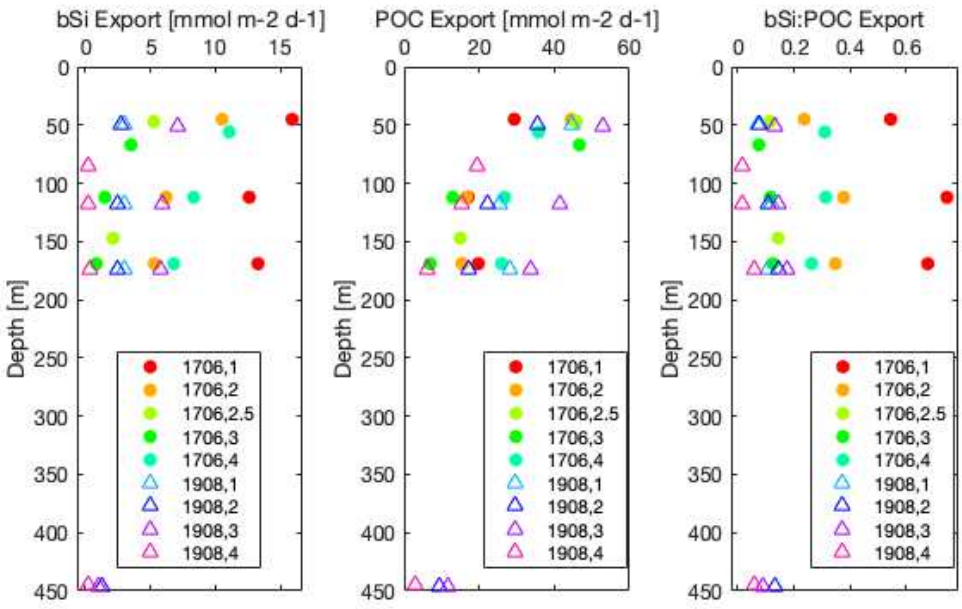

Figure 3.16. Measured sediment trap export flux of biogenic silica (bSi), particulate organic carbon (POC), and the bSi:POC ratio for the 'Morro Bay' (circle symbols) and 'Pt. Sur' Filaments (triangle symbols). Units for bSi and POC export flux are in mmol m^{-2} d^{-1}. Colors of symbols correspond to the 'Cruise' and 'Cycle' numbers indicated by the legend. Cycle 2.5 corresponded to a sediment trap which remained in the Cycle 2 Day 4 water mass.

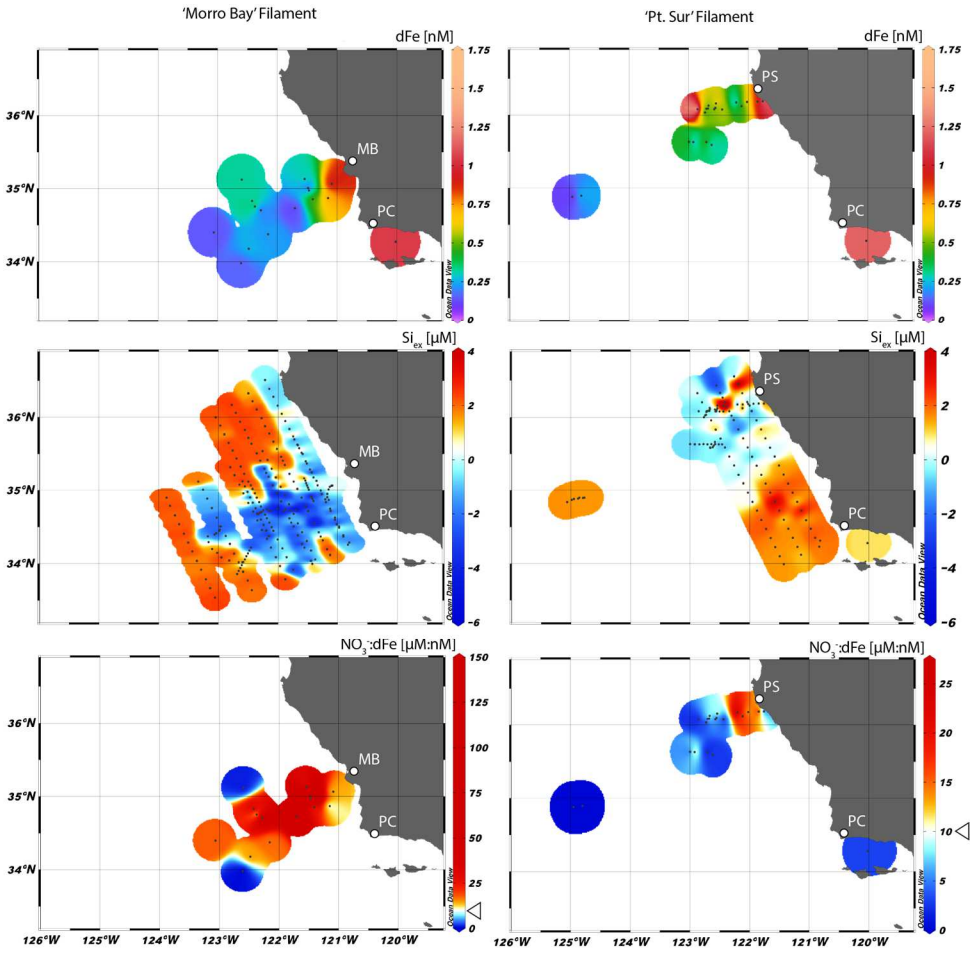

Figure 3.17. Surface plots of dFe (top), Si_{ex} (middle row), and NO_3^-:dFe ratio (bottom). Important locations on the California coast are indicated: MB (Morro Bay), PC (Pt. Conception), and PS (Pt. Sur). Color scale NO_3^-:dFe ratio is set to white at 10 µM:nM, which is an indicator threshold of possible Fe limitation of diatom communities in incubation experiments (King et al., 2007).

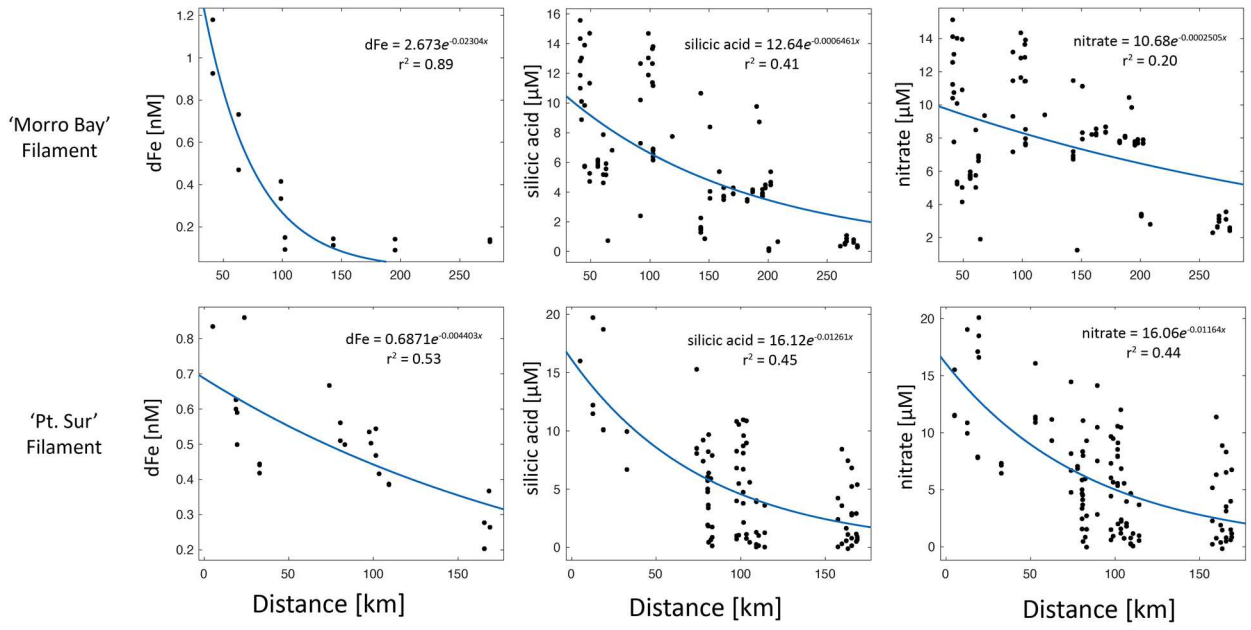

Figure 3.18. Concentrations of dFe (left), silicic acid (middle), and nitrate (right) at 10-25 m for all stations contained within the 'Morro Bay' filament (top) and 'Pt. Sur' filament (bottom) core. The blue line represents the exponential fit of the data. In the displayed equations, the variable *x* is Distance in kilometers.

3.10. Appendix

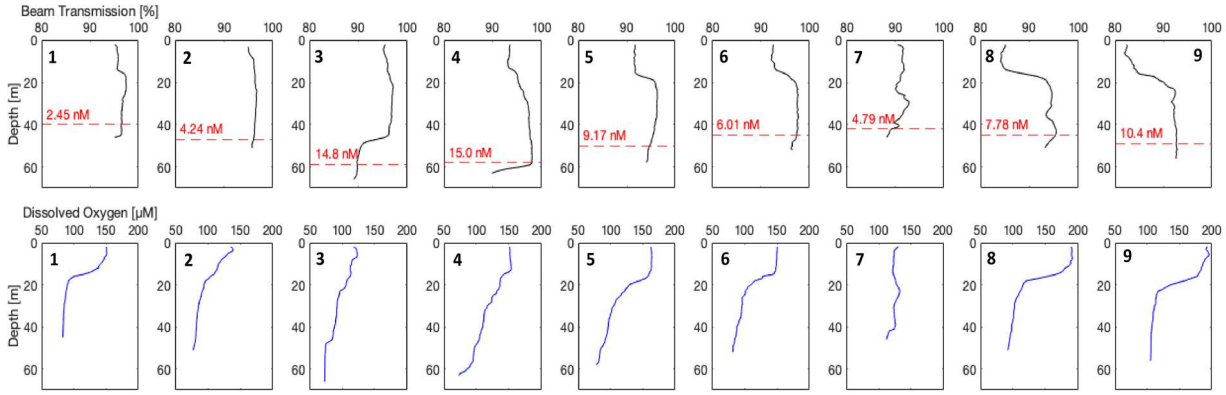

Figure A1. Water column profiles of beam transmission [%] (top), dissolved oxygen [µM] (middle row), and density [kg m^{-3}] (bottom) for numbered P1706 BBL stations (1 – 9). Trace metal GO-Flo sampling depth is indicated by a horizontal dashed line with the dFe concentration [nM] written above the line.

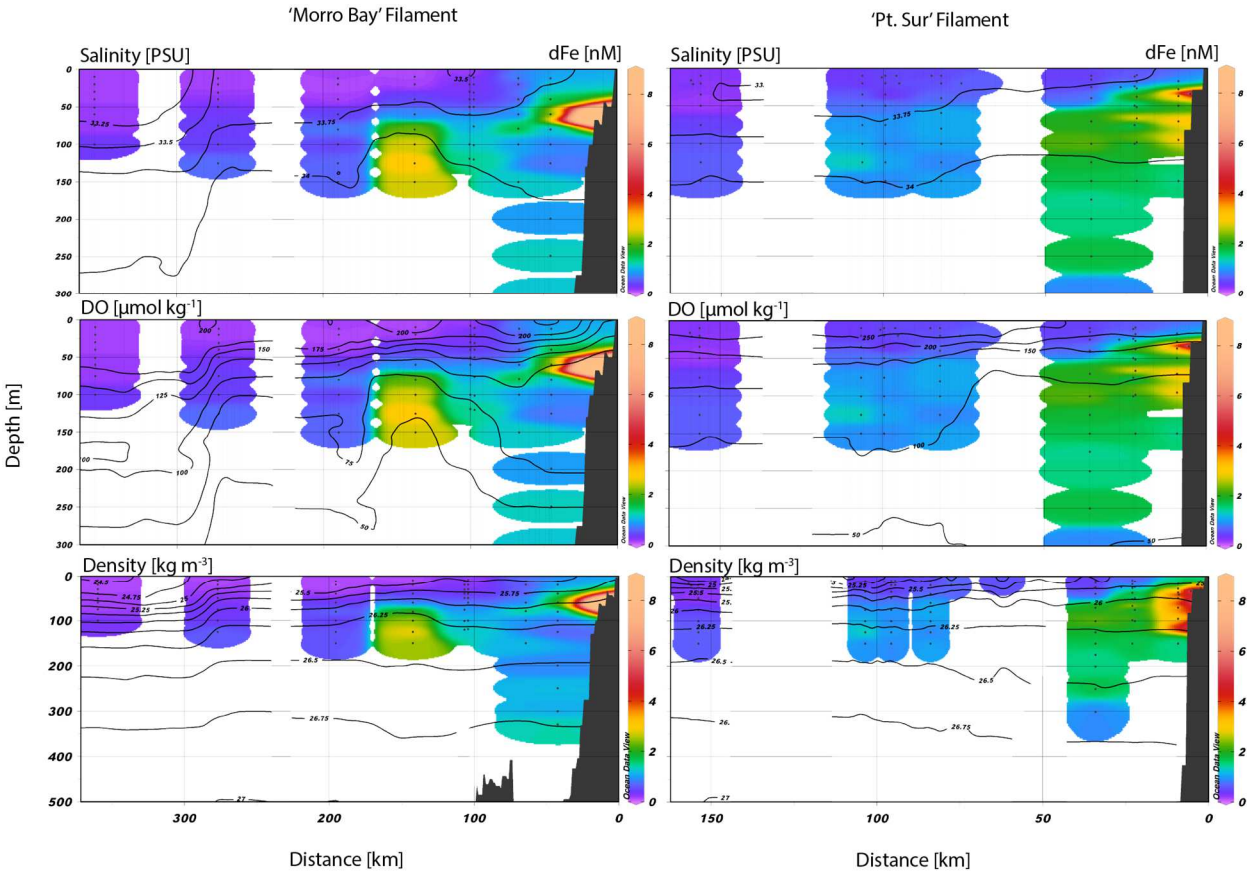

Figure A2. Section plots of dFe (colorbar) with overlays of salinity (top), dissolved oxygen (DO, middle row), and density (bottom) contours for the 'Morro Bay' (left) and 'Pt. Sur' (right) filaments. Contours are based on shipboard CTD profile data.

3.11. References

A., L., Bucciarelli, E., Claquin, P., Dugdale, R. C., Martin-Jézéquel, V., Pondaven, P. and Ragueneau, O.: Effect of iron deficiency on diatom cell size and silicic acid uptake kinetics, Limnol. Oceanogr., 49(4), 1134–1143, doi:https://doi.org/10.4319/lo.2004.49.4.1134, 2004.

Ardiningsih, I., Krisch, S., Lodeiro, P., Reichart, G.-J., Achterberg, E. P., Gledhill, M., Middag, R. and Gerringa, L. J. A.: Natural Fe-binding organic ligands in Fram Strait and over the northeast Greenland shelf, Mar. Chem., 224, 103815, doi:https://doi.org/10.1016/j.marchem.2020.103815, 2020.

Assmy, P., Smetacek, V., Montresor, M., Klaas, C., Henjes, J., Strass, V. H., Arrieta, J. M., Bathmann, U., Berg, G. M., Breitbarth, E., Cisewski, B., Friedrichs, L., Fuchs, N., Herndl, G. J., Jansen, S., Krägefsky, S., Latasa, M., Peeken, I., Röttgers, R., Scharek, R., Schüller, S. E., Steigenberger, S., Webb, A. and Wolf-Gladrow, D.: Thick-shelled, grazer-protected diatoms decouple ocean carbon and silicon cycles in the iron-limited Antarctic Circumpolar Current, Proc. Natl. Acad. Sci., 110(51), 20633 LP – 20638, doi:10.1073/pnas.1309345110, 2013.

B., F. C., J., B. M., T., R. J. and Paul, F.: Primary Production of the Biosphere: Integrating Terrestrial and Oceanic Components, Science (80-.)., 281(5374), 237–240, doi:10.1126/science.281.5374.237, 1998.

Barth, J. A. and Brink, K. H.: Shipboard acoustic Doppler profiler velocity observations near Point Conception: Spring 1983, J. Geophys. Res. Ocean., 92(C4), 3925–3943, doi:https://doi.org/10.1029/JC092iC04p03925, 1987.

Biller, D. V, Coale, T. H., Till, R. C., Smith, G. J. and Bruland, K. W.: Coastal iron and nitrate distributions during the spring and summer upwelling season in the central California Current upwelling regime, Cont. Shelf Res., 66, 58–72, doi:https://doi.org/10.1016/j.csr.2013.07.003, 2013.

Bourne, H. L., Bishop, J. K. B., Connors, E. J. and Wood, T. J.: Carbon export and fate beneath a dynamic upwelled filament off the California coast, Biogeosciences, 18(10), 3053–3086, doi:10.5194/bg-18-3053-2021, 2021.

Boyle, E. A., Edmond, J. M. and Sholkovitz, E. R.: The mechanism of iron removal in estuaries, Geochim. Cosmochim. Acta, 41(9), 1313–1324, doi:http://dx.doi.org/10.1016/0016-7037(77)90075-8, 1977.

Bruland, K. W., Rue, E. L. and Smith, G. J.: Iron and macronutrients in California coastal upwelling regimes: Implications for diatom blooms, Limnol. Oceanogr., 46(7), 1661–1674, doi:https://doi.org/10.4319/lo.2001.46.7.1661, 2001.

Bruland, K. W., Rue, E. L., Smith, G. J. and DiTullio, G. R.: Iron, macronutrients and diatom blooms in the Peru upwelling regime: brown and blue waters of Peru, Mar. Chem., 93(2), 81–103, doi:https://doi.org/10.1016/j.marchem.2004.06.011, 2005.

Brzezinski, M. A.: THE Si:C:N RATIO OF MARINE DIATOMS: INTERSPECIFIC VARIABILITY AND THE EFFECT OF SOME ENVIRONMENTAL VARIABLES1, J. Phycol., 21(3), 347–357, doi:https://doi.org/10.1111/j.0022-3646.1985.00347.x, 1985.

Brzezinski, M. A. and Nelson, D. M.: The annual silica cycle in the Sargasso Sea near Bermuda, Deep Sea Res. Part I Oceanogr. Res. Pap., 42(7), 1215–1237, doi:https://doi.org/10.1016/0967-0637(95)93592-3, 1995.

Brzezinski, M. A., Krause, J. W., Bundy, R. M., Barbeau, K. A., Franks, P., Goericke, R., Landry, M. R. and Stukel, M. R.: Enhanced silica ballasting from iron stress sustains carbon export in a frontal zone within the California Current, J. Geophys. Res. Ocean., 120(7), 4654–4669, doi:https://doi.org/10.1002/2015JC010829, 2015.

Bundy, R. M., Biller, D. V, Buck, K. N., Bruland, K. W. and Barbeau, K. A.: Distinct pools of dissolved iron-binding ligands in the surface and benthic boundary layer of the California Current, Limnol. Oceanogr., 59(3), 769–787, doi:10.4319/lo.2014.59.3.0769, 2014.

Burdige, D. J. and Komada, T.: Iron redox cycling, sediment resuspension and the role of sediments in low oxygen environments as sources of iron to the water column, Mar. Chem., doi:10.1016/j.marchem.2020.103793, 2020.

Carr, M.-E.: Estimation of potential productivity in Eastern Boundary Currents using remote sensing, Deep Sea Res. Part II Top. Stud. Oceanogr., 49(1), 59–80, doi:https://doi.org/10.1016/S0967-0645(01)00094-7, 2001.

Carr, M.-E. and Kearns, E. J.: Production regimes in four Eastern Boundary Current systems, Deep Sea Res. Part II Top. Stud. Oceanogr., 50(22), 3199–3221, doi:https://doi.org/10.1016/j.dsr2.2003.07.015, 2003.

Centurioni, L. R., Ohlmann, J. C. and Niiler, P. P.: Permanent Meanders in the California Current System, J. Phys. Oceanogr., 38(8), 1690–1710, doi:10.1175/2008JPO3746.1, 2008.

Chabert, P., d'Ovidio, F., Echevin, V., Stukel, M. R. and Ohman, M. D.: Cross-Shore Flow and Implications for Carbon Export in the California Current Ecosystem: A Lagrangian Analysis, J. Geophys. Res. Ocean., 126(2), e2020JC016611, doi:https://doi.org/10.1029/2020JC016611, 2021.

Chase, Z., Hales, B., Cowles, T., Schwartz, R. and van Geen, A.: Distribution and variability of iron input to Oregon coastal waters during the upwelling season, J. Geophys. Res. Ocean., 110(C10), doi:https://doi.org/10.1029/2004JC002590, 2005.

Chase, Z., Strutton, P. G. and Hales, B.: Iron links river runoff and shelf width to phytoplankton biomass along the U.S. West Coast, Geophys. Res. Lett., 34(4), doi:https://doi.org/10.1029/2006GL028069, 2007.

Checkley, D. M. and Barth, J. A.: Patterns and processes in the California Current System, Prog. Oceanogr., 83(1), 49–64, doi:https://doi.org/10.1016/j.pocean.2009.07.028, 2009.
Cutter, G. A. and Bruland, K. W.: Rapid and noncontaminating sampling system for trace elements in global ocean surveys, Limnol. Oceanogr. Methods, 10(6), 425–436, doi:https://doi.org/10.4319/lom.2012.10.425, 2012.

Dale, A. W., Nickelsen, L., Scholz, F., Hensen, C., Oschlies, A. and Wallmann, K.: A revised global estimate of dissolved iron fluxes from marine sediments, Global Biogeochem. Cycles, 29(5), 691–707, doi:10.1002/2014GB005017, 2015.

Dussin, R., Curchitser, E. N., Stock, C. A. and Van Oostende, N.: Biogeochemical drivers of changing hypoxia in the California Current Ecosystem, Deep Sea Res. Part II Top. Stud. Oceanogr., 169–170, 104590, doi:https://doi.org/10.1016/j.dsr2.2019.05.013, 2019.

Elrod, V. A., Berelson, W. M., Coale, K. H. and Johnson, K. S.: The flux of iron from continental shelf sediments: A missing source for global budgets, Geophys. Res. Lett., 31(12), doi:https://doi.org/10.1029/2004GL020216, 2004.

Firme, G. F., Rue, E. L., Weeks, D. A., Bruland, K. W. and Hutchins, D. A.: Spatial and temporal variability in phytoplankton iron limitation along the California coast and consequences for Si, N, and C biogeochemistry, Global Biogeochem. Cycles, 17(1), doi:https://doi.org/10.1029/2001GB001824, 2003.

Foreman, M. G. G. and Freeland, H. J.: A comparison of techniques for tide removal from ship-mounted acoustic Doppler measurements along the southwest coast of Vancouver Island, J. Geophys. Res. Ocean., 96(C9), 17007–17021, doi:https://doi.org/10.1029/91JC01314, 1991.

Forsch, K., Hahn-Woernle, L., Sherrell, R., Roccanova, J., Bu, K., Burdige, D., Vernet, M. and Barbeau, K. A.: Seasonal dispersal of fjord meltwaters as an important source of iron to coastal Antarctic phytoplankton, Biogeosciences Discuss., 2021, 1–49, doi:10.5194/bg-2021-79, 2021.

Franck, V. M., Bruland, K. W. and Hutchins, D. A.: Iron and zinc effects on silicic acid and nitrate uptake kinetics in three high-nutrient, low-chlorophyll (HNLC) regions , Mar. Ecol. Prog. Ser., 252, 15–33 [online] Available from: https://www.int-res.com/abstracts/meps/v252/p15-33/, 2003.

Frenger, I., Bianchi, D., StühRenberg, C., Oschlies, A., Dunne, J., Deutsch, C., Galbraith, E. and Schütte, F.: Biogeochemical Role of Subsurface Coherent Eddies in the Ocean: Tracer Cannonballs, Hypoxic Storms, and Microbial Stewpots?, Global Biogeochem. Cycles, 32(2), 226–249, doi:https://doi.org/10.1002/2017GB005743, 2018.

Fulton, Kayleen. "Dynamics of Biogenic Silica in a Coastal Upwelling Filament in the California Current." (2019).

Hoffmann, L. J., Peeken, I. and Lochte, K.: Effects of iron on the elemental stoichiometry during EIFEX and in the diatoms Fragilariopsis kerguelensis and Chaetoceros dichaeta, Biogeosciences, 4(4), 569–579, doi:10.5194/bg-4-569-2007, 2007.

Hogle, S. L., Dupont, C. L., Hopkinson, B. M., King, A. L., Buck, K. N., Roe, K. L., Stuart, R. K., Allen, A. E., Mann, E. L., Johnson, Z. I. and Barbeau, K. A.: Pervasive iron limitation at subsurface chlorophyll maxima of the California Current, Proc. Natl. Acad. Sci., 115(52), 13300 LP – 13305, doi:10.1073/pnas.1813192115, 2018.

Homoky, W. B., Severmann, S., McManus, J., Berelson, W. M., Riedel, T. E., Statham, P. J. and Mills, R. A.: Dissolved oxygen and suspended particles regulate the benthic flux of iron from continental margins, Mar. Chem., 134(Supplement C), 59–70, doi:https://doi.org/10.1016/j.marchem.2012.03.003, 2012.

Hopwood, M. J., Carroll, D., Dunse, T., Hodson, A., Holding, J. M., Iriarte, J. L., Ribeiro, S., Achterberg, E. P., Cantoni, C., Carlson, D. F., Chierici, M., Clarke, J. S., Cozzi, S., Fransson, A., Juul-Pedersen, T., Winding, M. H. S. and Meire, L.: Review article: How does glacier discharge affect marine biogeochemistry and primary production in the Arctic?, Cryosph., 14(4), 1347–

1383, doi:10.5194/tc-14-1347-2020, 2020.

Hutchins, D. A. and Bruland, K. W.: Iron-limited diatom growth and Si:N uptake ratios in a coastal upwelling regime, Nature, 393(6685), 561–564, doi:10.1038/31203, 1998.

Hutchins, D. A., DiTullio, G. R., Zhang, Y. and Bruland, K. W.: An iron limitation mosaic in the California upwelling regime, Limnol. Oceanogr., 43(6), 1037–1054, doi:https://doi.org/10.4319/lo.1998.43.6.1037, 1998.

Hutchins, D. A., Hare, C. E., Weaver, R. S., Zhang, Y., Firme, G. F., DiTullio, G. R., Alm, M. B., Riseman, S. F., Maucher, J. M., Geesey, M. E., Trick, C. G., Smith, G. J., Rue, E. L., Conn, J. and Bruland, K. W.: Phytoplankton iron limitation in the Humboldt Current and Peru Upwelling, Limnol. Oceanogr., 47(4), 997–1011, doi:https://doi.org/10.4319/lo.2002.47.4.0997, 2002.

Johnson, K. S., Chavez, F. P. and Friederich, G. E.: Continental-shelf sediment as a primary source of iron for coastal phytoplankton, Nature, 398(6729), 697–700, doi:10.1038/19511, 1999.

Kelly, T. B., Goericke, R., Kahru, M., Song, H. and Stukel, M. R.: CCE II: Spatial and interannual variability in export efficiency and the biological pump in an eastern boundary current upwelling system with substantial lateral advection, Deep Sea Res. Part I Oceanogr. Res. Pap., 140, 14–25, doi:https://doi.org/10.1016/j.dsr.2018.08.007, 2018.

Kim, S. Y., Terrill, E. J., Cornuelle, B. D., Jones, B., Washburn, L., Moline, M. A., Paduan, J. D., Garfield, N., Largier, J. L., Crawford, G. and Kosro, P. M.: Mapping the U.S. West Coast surface circulation: A multiyear analysis of high-frequency radar observations, J. Geophys. Res. Ocean., 116(C3), doi:https://doi.org/10.1029/2010JC006669, 2011.

King, A. L.: Evidence for phytoplankton iron limitation in the southern California Current System , Mar. Ecol. Prog. Ser., 342, 91–103 [online] Available from: https://www.int-res.com/abstracts/meps/v342/p91-103/, 2007.

King, A. L. and Barbeau, K. A.: Dissolved iron and macronutrient distributions in the southern California Current System, J. Geophys. Res. Ocean., 116(C3), doi:10.1029/2010JC006324, 2011.

Knauer, G. A., Martin, J. H. and Bruland, K. W.: Fluxes of particulate carbon, nitrogen, and phosphorus in the upper water column of the northeast Pacific, Deep Sea Res. Part A. Oceanogr. Res. Pap., 26(1), 97–108, doi:https://doi.org/10.1016/0198-0149(79)90089-X, 1979.

Krause, J. W., Brzezinski, M. A., Goericke, R., Landry, M. R., Ohman, M. D., Stukel, M. R. and Taylor, A. G.: Variability in diatom contributions to biomass, organic matter production and export across a frontal gradient in the California Current Ecosystem, J. Geophys. Res. Ocean., 120(2), 1032–1047, doi:https://doi.org/10.1002/2014JC010472, 2015.

Kurczyn, J. A., Pérez-Brunius, P., López, M., Candela, J., Delgadillo-Hinojosa, F. and García-Mendoza, E.: Water Masses and Ocean Currents Over the Continental Slope off Northern Baja California, J. Geophys. Res. Ocean., 124(4), 2803–2823, doi:https://doi.org/10.1029/2018JC013962, 2019.

Lam, P. J., Lee, J.-M., Heller, M. I., Mehic, S., Xiang, Y. and Bates, N. R.: Size-fractionated distributions of suspended particle concentration and major phase composition from the U.S.

GEOTRACES Eastern Pacific Zonal Transect (GP16), Mar. Chem., 201, 90–107, doi:https://doi.org/10.1016/j.marchem.2017.08.013, 2018.

Landry, M. R., Ohman, M. D., Goericke, R., Stukel, M. R. and Tsyrklevich, K.: Lagrangian studies of phytoplankton growth and grazing relationships in a coastal upwelling ecosystem off Southern California, Prog. Oceanogr., 83(1), 208–216, doi:https://doi.org/10.1016/j.pocean.2009.07.026, 2009.

Lohan, M. C., Aguilar-Islas, A. M. and Bruland, K. W.: Direct determination of iron in acidified (pH 1.7) seawater samples by flow injection analysis with catalytic spectrophotometric detection: Application and intercomparison, Limnol. Oceanogr. Methods, 4(6), 164–171, doi:10.4319/lom.2006.4.164, 2006.

Longhurst, A. R. and Glen Harrison, W.: The biological pump: Profiles of plankton production and consumption in the upper ocean, Prog. Oceanogr., 22(1), 47–123, doi:https://doi.org/10.1016/0079-6611(89)90010-4, 1989.

Lukas, R. and Santiago-Mandujano, F.: Extreme water mass anomaly observed in the Hawaii ocean time-series, Geophys. Res. Lett., 28(15), 2931–2934, doi:https://doi.org/10.1029/2001GL013099, 2001.

M. Franck, V., Brzezinski, M. A., Coale, K. H. and Nelson, D. M.: Iron and silicic acid concentrations regulate Si uptake north and south of the Polar Frontal Zone in the Pacific Sector of the Southern Ocean, Deep Sea Res. Part II Top. Stud. Oceanogr., 47(15), 3315–3338, doi:https://doi.org/10.1016/S0967-0645(00)00070-9, 2000.

Marchetti, A. and Harrison, P. J.: Coupled changes in the cell morphology and elemental (C, N, and Si) composition of the pennate diatom Pseudo-nitzschia due to iron deficiency, Limnol. Oceanogr., 52(5), 2270–2284, doi:https://doi.org/10.4319/lo.2007.52.5.2270, 2007.

Marchetti, A., Maldonado, M. T., Lane, E. S. and Harrison, P. J.: Iron requirements of the pennate diatom Pseudo-nitzschia: Comparison of oceanic (high-nitrate, low-chlorophyll waters) and coastal species, Limnol. Oceanogr., 51(5), 2092–2101, doi:https://doi.org/10.4319/lo.2006.51.5.2092, 2006.

MARCHETTI, A. and CASSAR, N.: Diatom elemental and morphological changes in response to iron limitation: a brief review with potential paleoceanographic applications, Geobiology, 7(4), 419–431, doi:https://doi.org/10.1111/j.1472-4669.2009.00207.x, 2009.

Mohrholz, V., Eggert, A., Junker, T., Nausch, G., Ohde, T. and Schmidt, M.: Cross shelf hydrographic and hydrochemical conditions and their short term variability at the northern Benguela during a normal upwelling season, J. Mar. Syst., 140, 92–110, doi:https://doi.org/10.1016/j.jmarsys.2014.04.019, 2014.

MOREL, F. M. M.: The co-evolution of phytoplankton and trace element cycles in the oceans, Geobiology, 6(3), 318–324, doi:https://doi.org/10.1111/j.1472-4669.2008.00144.x, 2008.

Morrow, R. M., Ohman, M. D., Goericke, R., Kelly, T. B., Stephens, B. M. and Stukel, M. R.: CCE V: Primary production, mesozooplankton grazing, and the biological pump in the California Current Ecosystem: Variability and response to El Niño, Deep Sea Res. Part I Oceanogr. Res. Pap., 140, 52–62, doi:https://doi.org/10.1016/j.dsr.2018.07.012, 2018.

Muller, A. A., Mohrholz, V. and Schmidt, M.: The circulation dynamics associated with a northern Benguela upwelling filament during October 2010, Cont. Shelf Res., 63, 59–68, doi:https://doi.org/10.1016/j.csr.2013.04.037, 2013.

Nagai, T., Gruber, N., Frenzel, H., Lachkar, Z., McWilliams, J. C. and Plattner, G.-K.: Dominant role of eddies and filaments in the offshore transport of carbon and nutrients in the California Current System, J. Geophys. Res. Ocean., 120(8), 5318–5341, doi:https://doi.org/10.1002/2015JC010889, 2015.

Nelson, D. M., Tréguer, P., Brzezinski, M. A., Leynaert, A. and Quéguiner, B.: Production and dissolution of biogenic silica in the ocean: Revised global estimates, comparison with regional data and relationship to biogenic sedimentation, Global Biogeochem. Cycles, 9(3), 359–372, doi:https://doi.org/10.1029/95GB01070, 1995.

Ohman MD, Powell JR, Picheral M, Jensen DW. Mesozooplankton and particulate matter responses to a deep-water frontal system in the southern California Current System. J Plankton Res [Internet]. 2012 Sep 1;34(9):815–27. Available from: https://doi.org/10.1093/plankt/fbs028

Van Oostende, N., Dunne, J. P., Fawcett, S. E. and Ward, B. B.: Phytoplankton succession explains size-partitioning of new production following upwelling-induced blooms, J. Mar. Syst., 148, 14–25, doi:https://doi.org/10.1016/j.jmarsys.2015.01.009, 2015.

Plattner, G.-K., Gruber, N., Frenzel, H. and McWilliams, J. C.: Decoupling marine export production from new production, Geophys. Res. Lett., 32(11), doi:https://doi.org/10.1029/2005GL022660, 2005.

Price, N. M.: The elemental stoichiometry and composition of an iron-limited diatom, Limnol. Oceanogr., 50(4), 1159–1171, doi:https://doi.org/10.4319/lo.2005.50.4.1159, 2005.

Quéguiner, B.: Iron fertilization and the structure of planktonic communities in high nutrient regions of the Southern Ocean, Deep Sea Res. Part II Top. Stud. Oceanogr., 90, 43–54, doi:https://doi.org/10.1016/j.dsr2.2012.07.024, 2013.

Ren, A. S., Chai, F., Xue, H., Anderson, D. M. and Chavez, F. P.: A Sixteen-year Decline in Dissolved Oxygen in the Central California Current, Sci. Rep., 8(1), 7290, doi:10.1038/s41598-018-25341-8, 2018.

Rocha, C. L. D. La, Hutchins, D. A. and Brzezinski, M. A.: Effects of iron and zinc deficiency on elemental composition and silica production by diatoms , Mar. Ecol. Prog. Ser., 195, 71–79 [online] Available from: https://www.int-res.com/abstracts/meps/v195/p71-79/, 2000.

Rossi, V., Garçon, V., Tassel, J., Romagnan, J.-B., Stemmann, L., Jourdin, F., Morin, P. and Morel, Y.: Cross-shelf variability in the Iberian Peninsula Upwelling System: Impact of a mesoscale filament, Cont. Shelf Res., 59, 97–114, doi:https://doi.org/10.1016/j.csr.2013.04.008, 2013.

Rudnick, D. L., Zaba, K. D., Todd, R. E. and Davis, R. E.: A climatology of the California Current System from a network of underwater gliders, Prog. Oceanogr., 154, 64–106, doi:https://doi.org/10.1016/j.pocean.2017.03.002, 2017.

Sangrà, P., Troupin, C., Barreiro-González, B., Desmond Barton, E., Orbi, A. and Arístegui, J.: The Cape Ghir filament system in August 2009 (NW Africa), J. Geophys. Res. Ocean., 120(6), 4516–4533, doi:https://doi.org/10.1002/2014JC010514, 2015.

Schultes, S., Lambert, C., Pondaven, P., Corvaisier, R., Jansen, S. and Ragueneau, O.: Recycling and Uptake of Si(OH)4 when Protozoan Grazers Feed on Diatoms, Protist, 161(2), 288–303, doi:https://doi.org/10.1016/j.protis.2009.10.006, 2010.

Sedwick, P. N., DiTullio, G. R. and Mackey, D. J.: Iron and manganese in the Ross Sea, Antarctica: Seasonal iron limitation in Antarctic shelf waters, J. Geophys. Res. Ocean., 105(C5), 11321–11336, doi:https://doi.org/10.1029/2000JC000256, 2000.

Sherrell, R. M., Annett, A. L., Fitzsimmons, J. N., Roccanova, V. J. and Meredith, M. P.: A “shallow bathtub ring” of local sedimentary iron input maintains the Palmer Deep biological hotspot on the West Antarctic Peninsula shelf, Philos. Trans. R. Soc. A Math. Phys. Eng. Sci., doi:10.1098/rsta.2017.0171, 2018.

Smetacek, V.: Diatoms and the Ocean Carbon Cycle, Protist, 150(1), 25–32, doi:https://doi.org/10.1016/S1434-4610(99)70006-4, 1999.

Smith, S. R., Gillard, J. T. F., Kustka, A. B., McCrow, J. P., Badger, J. H., Zheng, H., New, A. M., Dupont, C. L., Obata, T., Fernie, A. R. and Allen, A. E.: Transcriptional Orchestration of the Global Cellular Response of a Model Pennate Diatom to Diel Light Cycling under Iron Limitation, PLOS Genet., 12(12), e1006490 [online] Available from: https://doi.org/10.1371/journal.pgen.1006490, 2016.

Strickland, J. D. H. and Parsons, T. R.: A practical handbook of seawater analysis, 1972.

Stukel, M. R. and Barbeau, K. A.: Investigating the Nutrient Landscape in a Coastal Upwelling Region and Its Relationship to the Biological Carbon Pump, Geophys. Res. Lett., 47(6), e2020GL087351, doi:https://doi.org/10.1029/2020GL087351, 2020.

Takeda, S.: Influence of iron availability on nutrient consumption ratio of diatoms in oceanic waters, Nature, 393(6687), 774–777, doi:10.1038/31674, 1998.

Till, C. P., Solomon, J. R., Cohen, N. R., Lampe, R. H., Marchetti, A., Coale, T. H. and Bruland, K. W.: The iron limitation mosaic in the California Current System: Factors governing Fe availability in the shelf/near-shelf region, Limnol. Oceanogr., 64(1), 109–123, doi:https://doi.org/10.1002/lno.11022, 2019.

Timmermans, K. R., van der Wagt, B. and de Baar, H. J. W.: Growth rates, half-saturation constants, and silicate, nitrate, and phosphate depletion in relation to iron availability of four large, open-ocean diatoms from the Southern Ocean, Limnol. Oceanogr., 49(6), 2141–2151, doi:https://doi.org/10.4319/lo.2004.49.6.2141, 2004.

Tréguer, P., Bowler, C., Moriceau, B., Dutkiewicz, S., Gehlen, M., Aumont, O., Bittner, L., Dugdale, R., Finkel, Z., Iudicone, D., Jahn, O., Guidi, L., Lasbleiz, M., Leblanc, K., Levy, M. and Pondaven, P.: Influence of diatom diversity on the ocean biological carbon pump, Nat. Geosci., 11(1), 27–37, doi:10.1038/s41561-017-0028-x, 2018.

Twining, B. S., Baines, S. B. and Fisher, N. S.: Element stoichiometries of individual plankton

cells collected during the Southern Ocean Iron Experiment (SOFeX), Limnol. Oceanogr., 49(6), 2115–2128, doi:10.4319/lo.2004.49.6.2115, 2004.

Twining, B. S., Antipova, O., Chappell, P. D., Cohen, N. R., Jacquot, J. E., Mann, E. L., Marchetti, A., Ohnemus, D. C., Rauschenberg, S. and Tagliabue, A.: Taxonomic and nutrient controls on phytoplankton iron quotas in the ocean, Limnol. Oceanogr. Lett., 6(2), 96–106, doi:https://doi.org/10.1002/lol2.10179, 2021.

Wilken, S., Hoffmann, B., Hersch, N., Kirchgessner, N., Dieluweit, S., Rubner, W., Hoffmann, L. J., Merkel, R. and Peeken, I.: Diatom frustules show increased mechanical strength and altered valve morphology under iron limitation, Limnol. Oceanogr., 56(4), 1399–1410, doi:https://doi.org/10.4319/lo.2011.56.4.1399, 2011.

Winant, C. D., Alden, D. J., Dever, E. P., Edwards, K. A. and Hendershott, M. C.: Near-surface trajectories off central and southern California, J. Geophys. Res. Ocean., 104(C7), 15713–15726, doi:https://doi.org/10.1029/1999JC900083, 1999.

Winant, C. D., Dever, E. P. and Hendershott, M. C.: Characteristic patterns of shelf circulation at the boundary between central and southern California, J. Geophys. Res. Ocean., 108(C2), doi:https://doi.org/10.1029/2001JC001302, 2003.

Zaba, K. D., Franks, P. J. S. and Ohman, M. D.: The California Undercurrent as a Source of Upwelled Waters in a Coastal Filament, J. Geophys. Res. Ocean., 126(2), e2020JC016602, doi:https://doi.org/10.1029/2020JC016602, 2021.

Zentara, S. J. and Kamykowski, D.: Latitudinal relationships among temperature and selected plant nutrients along the west coast of North and South America, J. mar. Res, 35(2), 321–337, 1977.

Zhang, S., Liu, H., Ke, Y. and Li, B.: Effect of the Silica Content of Diatoms on Protozoan Grazing , Front. Mar. Sci. , 4, 202 [online] Available from: https://www.frontiersin.org/article/10.3389/fmars.2017.00202, 2017.

Chapter 3 is being prepared for submission and the dissertation author was the primary investigator and first author of this chapter. Kayleen Fulton and Marley Weiss helped analyze bSi samples. We also thank Mike Stukel for contributing sediment trap data and Katherine Barbeau for supporting this work. The CCE LTER program supported these studies.

Chapter 4. Application of simultaneous processing of Multiple Analytical Window (MAW) electrochemical titration data to the study of iron-binding ligands

4.1. Abstract

Dissolved iron speciation was determined at select stations of research expeditions to the western Antarctic Peninsula and California Current, as well as in a microcosm experiment of a simulated phytoplankton bloom via a competitive ligand exchange electrochemical technique using multiple analytical windows (MAW), while employing a novel method for simultaneous processing of MAW voltammetric titration data. The method here improves upon existing iron speciation methodologies using a combination of publicly available metal speciation processing tools, KINETEQL and ProMCC, as well as a unified sensitivity for the processing of MAW data as a single data set. This advance eliminates the derivation of sensitivities from individual titrations. The processing method developed was also used to optimize the analytical windows for MAW analysis of iron speciation in seawater samples and incubation experiments, with an emphasis on resolving strong iron-binding organic ligands. Equilibration time as well as analytical windows were evaluated for how best to parameterize these analyses. The application of this method to cruises with the FjordEco and California Current Ecosystem Long Term Ecological Research (CCE LTER) programs revealed distinct iron-binding organic ligands detected throughout the oceanic water column in disparate geographic locations as well as during a simulated phytoplankton bloom in a microcosm remineralization experiment. These are some of the first open ocean and mechanistic experiment iron speciation data sets derived from simultaneous processing of MAW electrochemical titrations, providing a more accurate depiction of the natural ligand pool relative to multi-ligand data derived from the analysis of a single analytical window.

4.2. Introduction

Dissolved iron (dFe) concentrations in coastal and offshore oceanic waters are relatively low (generally <0.5 nM, Johnson et al. 1997; Biller et al. 2013). This is due to biological uptake (Johnson et al., 1997) and extreme insolubility of dFe in oxygenated seawater (Liu and Millero, 2002). The presence of organic dFe-binding ligands increases the solubility of Fe in seawater above its inorganic thermodynamic threshold (Rue and Bruland, 1995; Wu and Luther, 1995), but much work remains to elucidate sources and sinks (Gledhill and Buck, 2012). The quality of the organic ligand pool has been shown to differ across oceanic regions, from coastal to offshore and from surface and deep waters (Ardiningsih et al., 2020; Buck et al., 2015, 2018; Bundy et al., 2014, 2015; Forsch et al., 2021). Broad trends reveal ligands have regional inputs, seasonal trends, and patterns associated with biomass and nutrient limitation (reviewed in Hassler *et al.* 2017).

Strong dFe-binding ligands (L_1, $\log K_{FeL,Fe'cond} \geq 12.0$) measured in the surface ocean are thought to be biologically produced (Gledhill and Buck, 2012; Hunter and Boyd, 2007; Velasquez et al., 2016) and form a biologically available (bioavailable) pool of dFe. These L_1 ligands include siderophores, which are low-molecular weight compounds with high affinity and specificity for dFe. Weaker dFe-ligand complexes (L_2, $\log K_{FeL,Fe'cond} \leq 12.0$) might be also bioavailable (Hutchins and Bruland, 1994; Poorvin et al., 2011; Whitby et al., 2020). The sources for weak ligands (L_2) may include degraded products of strong ligands in the surface ocean (Barbeau 2006), microbial exudates (Boyd et al., 2010; Hassler et al., 2011; Hutchins and Bruland, 1994), humic-like substances (HS) (Laglera and van den Berg, 2009), diffusive fluxes from coastal sediment pore waters (Jones et al., 2011) and terrestrial inputs from rivers (Buck et al., 2007). A recent compilation revealed weak ligands are ubiquitous throughout the global ocean interior and that HS are important for maintaining baseline concentrations of dFe (Whitby et al., 2020), however, dFe complexation is thought to be governed by stronger ligands in surface waters, which are therefore more important in microbial Fe acquisition in the ocean.

Despite these advances in characterizing the external inputs and *in situ* sources, the role of organic dFe-binding ligands in productive planktonic systems, including how ligands remobilize less-bioavailable particulate Fe pools, remains undefined. Further, the co-existence of multiple dFe-binding ligands (L_1—L_4) means that competition exists between classes (e.g. siderophores and HS) altering the bioavailability of dFe (Hassler et al., 2017). The relative importance of the ligands constituting the 'ligand soup' clearly depends on location, season, and regional characteristics. As identified by Hassler *et al.* (2017), major hurdles remain in order to constrain the relative contribution of $L_{1\text{-}4}$ ligands in seawater: 1) spatial and seasonal resolution on the distribution of L_1 ligands in surface waters, 2) examination of production rates and residence times of different *in situ* ligands, and 3) analytical methods for simultaneous detection of multiple ligands to constrain the distribution, nature, and sources of strong and weak ligands.

Recent advances in the isolation and chemical separation of dissolved organic matter from seawater, combined with plasma-source mass spectrometry, has shown that hydroxamate siderophores are found to be present at picomolar concentrations in the surface ocean (Boiteau et al. 2016, 2018). The low picomolar concentrations determined by these methods also indicates potential bias with sampling and limited chemical characterization of the natural dFe-binding ligand pool, since many studies reveal nanomolar concentrations of L_1 ligands are present in seawater (Buck et al., 2015, 2018). This analytical discrepancy suggests a highly diverse pool of molecules controls dFe solubility in the ocean. Competitive ligand exchange-adsorptive cathodic stripping voltammetry (CLE-ACSV) is the electrochemical technique primarily used to measure the organic complexation of dFe, including organic dFe-binding ligand concentrations ($[L_i]$) and their associated conditional stability constants ($K_{FeLx,Fe'cond}$). The ambient dFe-binding ligands determined by this technique are typically described as ligand "classes," which are operationally defined by the associated conditional stability constant measured. Unlike methods which rely on searching databases which contain known molecules, this technique does not require *a priori* information about the possible chemical constituents present within the sample. Therefore,

electrochemical studies are our best approach to examine the ligand pool as a whole in order to accurately model the concentration and residence time of dFe in the ocean (Völker and Tagliabue, 2015).

To better constrain the seasonality and distribution of organic ligands, and to refine understanding of biological sources of organic ligands in productive planktonic systems, we use a MAW competitive ligand exchange-adsorptive cathodic stripping voltammetry (MAW-CLE-ACSV) approach (Figure 4.1). This method was employed for copper (Cu) speciation studies (Bruland et al. 2000) in estuarine (Buck and Bruland, 2005; Moffett et al., 1997) and coastal environments (Van Den Berg et al., 1990; Bundy et al., 2013), but less so for Fe speciation studies (Bundy et al., 2014, 2016). These previous studies report an overlapping range of conditional stability constants ($\log K_{FeLx,Fe'cond}$) of dFe-binding ligands detected by CLE-ACSV in the marine environment, which confounds the distinction between the stronger 'L_1' and progressively weaker '$L_{2\text{-}4}$' ligand classes. This precludes the interpretation of the sources and sinks of dFe-binding ligands, suggesting there are additional ligand classes in seawater to be resolved, with potentially distinct sources and reactivity. As pointed out by Ruacho *et al.* 2021 (*under review*), for MAW-CLE-ACSV Cu speciation data, advanced data processing is required to interpret overlapping ligand classes. Therefore, to obtain an accurate depiction of the dFe-binding ligand pool, we developed analysis parameterization and data processing methods for MAW-CLE-ACSV Fe speciation data. These methods were applied to the studies of dFe-binding ligands in seawater samples collected from seasonally productive planktonic systems: a glaciomarine fjord and an upwelling coastal filament. We also applied this method in the context of an incubation field study to better pinpoint the presence of the strongest (L_1) class of iron-binding ligands, ultimately with the goal of interpreting this chemical signature in the context of remineralization processes, microbial community composition, and the transcription of iron acquisition-related gene pathways. This methodology allows for the detection of a wider range of dFe-binding ligand classes than is determined in single window analyses.

4.3. Materials and Methods

4.3.1. A novel method for the processing of MAW electrochemical titration iron speciation data

The methods described herein were also developed for multiple analytical window (MAW) copper (Cu) speciation data (Ruacho et al., *under review*). The proposed methods use a combination of publicly available metal speciation processing tools, KINETEQL and ProMCC, as well as a unified sensitivity for the processing of MAW data as a single data set, eliminating the need to derive sensitivities from individual titrations. KINETEQL software can fit up to three ligand classes using an excel worksheet iterative solver (Hudson et al. 2003). ProMCC software employs mass balance equations, solving for MAW speciation parameters as a unified dataset (Omanović et al. 2015). In brief, the method uses KINETEQL to determine a unified sensitivity for the entire MAW dataset, and then uses this sensitivity to correct the raw MAW data prior to final processing using ProMCC. This method allows simultaneous processing of MAW electrochemical Fe speciation datasets for the first time.

An important step in the processing of these methods is identifying individual erroneous points in each titration. For the trained analyst, these points are easily identified, but standardization is needed. Therefore, prior to processing the MAW speciation data in KINETEQL, a statistical model is used to identify analytical errors in each titration. We used a cubic spline regression with 95% confidence intervals to identify data points subject to removal and reduce the overall uncertainties (Ruacho et al. *under review*). A final point removal was also carried out during data processing with ProMCC, where points that were visibly clear outliers on the ProMCC-generated plots for Scatchard and Langmuir fittings were removed. Titration data from each window was imported into KINETEQL and the solver was run. Following fitting, data points falling off the unified sensitivity line were subject to removal. The sensitivity determined in KINETEQL was used to correct raw peak heights prior to importing to ProMCC. Within ProMCC, outlier points

were removed, and the solver was run for final processing of the data, generating the final ligand data. In this step, the appropriate model (1, 2, or 3-ligand fitting) was applied to reduce the overall uncertainties computed by ProMCC.

4.3.2. Fe speciation analyses

All speciation samples were analyzed with MAWs with a single titration at each window. For the titrations, 10 mL aliquots of each dissolved Fe speciation sample were pipetted into 15 - 17 separate Teflon Savillex vials (17-mL flat bottom, with lid) that had been pre-conditioned with the added dFe concentrations used in this study. A 1.5 mol L^{-1} boric acid (> 99.99%, Alfa Aeasar) buffer was prepared in 0.4 mol L^{-1} NH_4OH (Optima, Fisher Scientific) and 50 µL was added to each vial (7.5 mmol L^{-1} final concentration, pH 8.2). Thirteen to eighteen aliquots (two vials remained as 'zero Fe' additions) were then spiked with Fe from a 100 nmol L^{-1}, 200 nmol L^{-1}, 1 µmol L^{-1}, 2 µmol L^{-1}, or 10 µmol L^{-1} secondary standard that had been diluted form an atomic absorption standard (CertiPrep) into pH 1.8 ultra clean water (MilliQ, >18.2 MΩ cm^{-1}, acidified with Optima grade HCl) to obtain a final concentration ranging from 0.25 – 35 nmol L^{-1}. The added Fe was left to equilibrate with the natural ligands for at least 2 hr. The appropriate concentration of the competing ligand was added following the 2 hr equilibration period with the added Fe, and left to equilibrate an additional 15 minutes (up to 2 hours). Each vial was then run separately using a controlled growth mercury electrode (CGME, BAS*i*) interfaced with an analyzer (E2, Epsilon) and a laptop computer using ACSV as described in detail elsewhere (Buck et al., 2007; Bundy et al., 2014; Rue and Bruland, 1995). A deposition time of 180 – 300 seconds was used in the analysis of these sample sets depending on if a sufficiently high signal was attained at the 25 nM dFe titration point. This was done when large changes in the dFe concentration was observed between seawater samples. For example, for the P1706 dataset, the BBL sample required short (180 s) deposition times compared to the extremely low concentration (<0.2 nM dFe) offshore stations (300 s). Importantly, we noted that once an appropriate deposition time was established for a

sample, the same deposition time was employed for each analytical window. The calibration of the side reaction coefficient was completed previously according to Rue and Bruland (1995) with corrections for salinity as described in Buck *et al.* (2007) and recalculated by Abualhaija and van den Berg (2014). An $\alpha_{Fe'}$ of 10^{10} (inorganic side reaction coefficient) was assumed in the Fe speciation calculations. Peaks generated from titrations were determined using the ECDSoft software package (Omanović et al., 2015).

4.3.3. Total dissolved iron analysis

Stored acidified filtered seawater samples were analyzed for Fe using flow injection with chemiluminescence methods described by Lohan *et al.* DFe in the resulting samples was oxidized to iron(III) for 1 h with 10 mM Q-H_2O_2, buffered in-line with ammonium acetate to pH ~3.5 and selectively pre-concentrated on a chelating column packed with a resin (Toyopearl® AF-Chelate-650M). DFe was eluted from the column using 0.14 M HCl (Optima grade, Fisher Scientific) and the chemiluminescence is recorded by a photomultiplier tube (PMT, Hamamatsu Photonics). The methods used were similarly described by King and Barbeau 2007, 2011, and a manifold adapted from Lohan et al. 2006. The standardization of Fe used was a matrix-matched standard curve (0, 0.4, 0.8, 3.2 nmol kg^{-1}) using low-Fe open ocean seawater. Standards were treated identically to samples. Accuracy was assessed by repeated measurements of GEOTRACES coastal and open Pacific Ocean reference seawater samples. Precision, determined by replicated analyses of an in-house large-volume reference seawater sample within each analytical session, was typically ±5% or better. For the duration of these analyses, the average limit of detection (LOD, defined as 3x the standard deviation of the blank) was 0.036 nM. For complete descriptions of analytical figures of merit, reference *Methods* sections in Forsch *et al.* (2021) and Chapter 3.

4.3.4. Field study locations

4.3.4.1. Antarctic glaciomarine fjord

In December 2015 and April 2016, we participated in two cruises of opportunity aboard the *ARSV Laurence M. Gould* and *RVIB Nathaniel B. Palmer* as part of the FjordEco project in Andvord Bay, an Antarctic fjord in the western Antarctic Peninsula (Figure 4.2, https://fjordeco.wordpress.com/). Electrochemical speciation measurements were carried out on both cruises. A recent paper includes dFe speciation data at a single analytical window ($\alpha_{Fe(SA)_x}$), where

$$\alpha_{Fe(SA)_x} = K^{cond}_{SA/Fe(III)} * [SA'] + \beta^{cond}_{2SA/Fe(III)} * [SA']^2 \quad (1)$$

Here, *SA*' is the concentration of the added ligand (salicylaldoxime), $K^{cond}_{SA/Fe(III)}$ is the formation constant of the Fe(SA) electroactive complex and $\beta^{cond}_{2SA/Fe(III)}$ the non-electroactive complex $Fe(SA)_2$, determined to be $10^{6.52}$ M^{-1} and $10^{10.72}$ M^{-2}, respectively (Abualhaija and van den Berg, 2014). In our study, we followed previous GEOTRACES publications (Buck et al., 2015, 2018) and used a moderately high analytical window ($\alpha_{Fe(SA)_x}$= 115) over the two cruises, highlighting seasonal differences in dFe speciation in a relatively unperturbed Antarctic fjord system (Forsch *et al.* 2021). Additional MAW analysis of speciation samples associated with the FjordEco project were carried out for this chapter.

4.3.4.2 'Morro Bay' coastal upwelling filament

The California Current System is a seasonally productive eastern boundary upwelling biome. During times of upwelling, cross-shore fluxes of water and particulate matter are found within filaments. Surface and benthic boundary layer (BBL) samples, including a single profile (to 300 m depth), were collected on the *R/V Roger Revelle* in July 2017 (summer) from within a coastal upwelling filament. In this study (termed the 'Morro Bay' filament), a cold, saline, and Chlorophyll-rich parcel of upwelled water was tracked in a Lagrangian fashion and sampled to

reveal changes in dFe speciation at multiple stages in the advection and age of the water parcel as it was displaced offshore. The shoreward filament source endmember was sampled in the Morro Bay benthic boundary layer (BBL). Hydrographic descriptions of the 'Morro Bay' filament are described in detail in Zaba *et al.* (2021).

4.3.5. Iron remineralization experiment

In April 2016, aboard the *R/V Sikuliaq*, seawater was collected in offshore stations to observe ecosystem responses to a persistent west coast warm anomaly in the California Current as part of the Long Term Ecological Research (LTER) program process cruise (Figure 4.2). This study (termed P1604) was initiated as a microbial community grow-out with a natural community present in offshore Pacific surface seawater (33 N 122.45 W) on the first day (t = 0). Water collected for the experiment was sampled from 22 m depth and placed in to 15x 2.7 L acid cleaned polycarbonate bottles (5 timepoints, 3 replicates). To each bottle, the following was added: 900 µL NO_3^- stock (to a concentration of 10 µM), 270 µL PO_4^{3-} stock (to a concentration of 1 µM), 5 mL $Si(OH)_4$ stock (to a concentration of ~9 µM), and 34 µL $FeCl_3$ stock (to a concentration of ~5 nM). Two hours following water collection, the 15 bottles were placed into an on-deck incubator screened to 30% surface irradiance. At each timepoint, including the initial surface water, DNA/RNA, Chlorophyll-a, dFe, dFe speciation, macronutrients, bacterial concentration, and total organic carbon (TOC) were sampled. Following 11 days of growth (indicated by Chlorophyll-a concentration as a proxy of biomass), the incubation was placed in the dark to observe remineralization processes for an additional 7 days. The microcosm experiment was performed in triplicate, indicated by letters A-C.

4.3.6. Sample collection

In the case of LMG1510 and NBP1603, samples were collected using acid-cleaned GO-Flo (General Oceanics) 12-L bottles attached to a metal-free hydroline (Amsteel) and triggered at depth using free-falling Teflon messengers. For P1604 and P1706, water column sample collection was accomplished by a deployment of a trace metal rosette on a non-conducting Kevlar-impregnated wire. The rosette contained up to 12 5-L X-Niskin bottles that were pre-cleaned before the cruise, as well as a sensor package equipped with a CTD (Sea-bird Scientific) and auto-fire module (AFM). Each collection of trace metal clean seawater was done immediately following a ship CTD cast in order to obtain synoptic hydrographic and biogeochemical profiles. Acute attention to cleanliness was applied in all cases. For dFe speciation samples, filtered seawater (<0.2 – 0.4 µm polycarbonate or supor filtered) was placed into acid-cleaned fluorinated polyethylene bottles (FLPE 500 mL, Nalgene) and frozen immediately at -20ºC until analysis. FLPE bottles prevent significant adsorptive loss to the bottle walls in unacidified seawater solutions, and also prevent leaching of dissolved organic carbon. Prior to analysis, each sample was allowed to thaw at room temperature overnight.

4.4. Results and Discussion

4.4.1. Equilibration time and analytical windows

A 2 hr equilibration between the natural ligands and Fe additions was optimal for these samples as it was found that a significant loss in sensitivity (defined as the voltammetric current per Fe added) resulted from overnight equilibration. We analyzed two seawater replicates (A and B) using three analytical windows, holding all other analytical parameters constant, to understand the effect of extended overnight equilibration on the internal sensitivity of each titration and found that the greatest loss in sensitivity (loss factor of 3.4-6.1 between short and overnight equilibration) was found at the highest SA concentration of 50 µM (Figure 4.3), whereas at other SA concentrations employed, a consistent factor of ~2.1-2.2 in sensitivity loss was found after

overnight equilibration. We suggest two possible explanations for the observed sensitivity decrease: 1) the high concentrations of salicylaldoxime (50 μM SA, the added competing ligand) used in these studies could adsorb on to the vial walls, resulting in a decrease in sensitivity as a function of time spent within the vials; 2) overnight equilibrations result in dimerization of the SA molecule, or the non-electroactive $FeSA_2$ complex is formed over extended equilibration periods at [SA] > 5 μM, which reduces the sensitivity as suggested in Abualhaija and van den Berg (2014). Therefore, we use a 2 hr equilibration time to achieve the highest sensitivity of this method.

Despite these anticipated sensitivity losses (see Fig. 2 in Abualhaija and van den Berg, 2014), the high SA concentrations (14.7 to 33.2 μM) employed here allow for the interrogation of the strongest binding ligands present in our samples, which contribute most to dFe speciation in the marine environment. This range of analytical windows was used in previous MAW studies of dFe speciation (Bundy et al., 2014, 2016; Fitzsimmons et al., 2015; Hogle et al., 2016). The analytical windows used, defined by the $\alpha_{Fe(SA)_x}$, were optimized for each dataset, thereby decreasing the number of analytical windows required and reducing the workload for the analyst. This was accomplished by identifying the combination of windows which reduces the overall uncertainty in ligand parameters determined by ProMCC. The analytical window is defined by the concentration of the added competing ligand, which is SA. By varying the analytical window, different ligands with varying affinity for Fe were measured, and a more accurate conditional stability constant was determined compared to single window titrations. Ligand classes are here defined by their $logK^{cond}_{FeL,Fe'}$ and classified as the following: L_1 ($logK_1 > 12$), L_2 ($11 < logK_2 < 12$), L_3 ($10 < logK_3 < 11$), L_4 ($logK_1 < 10$). Note here that all *K* values listed in this chapter are conditional stability constants even when the "K_{cond}" designation has been dropped for convenience.

4.4.2. *In situ* ligand pool characterization

4.4.2.1. Fe speciation in an Antarctic fjord

Single analytical window (SAW, $\alpha_{Fe(SA)_x}$= 115) methods were previously used to assess the seasonal quality of dFe-binding ligands in Andvord Bay, a heavily glaciated fjord located mid-latitude along the WAP (Forsch et al., 2021). Only a single ligand class was resolved in all samples. In order to resolve potentially more ligand classes present within the fjord, MAW methods described herein were used at two additional windows ($\alpha_{Fe(SA)_x}$= 60, 162). The results are presented in Table 4.1. These methods were able to further resolve additional ligand classes at select stations.

We find that MAW methods resolve multiple ligands more frequently than the SAW methods. Our data show that 6 samples analyzed by MAW were able to detect two ligand classes. In fact, the SAW analysis of the Andvord Bay data (Forsch *et al.* 2021) appears to reflect an average of the two ligands detected via MAW at these stations, indicated by bracketing of SAW results by MAW results (Table A1). These stations include those located within the inner basins close to glacier termini, and surface waters overlying a sill (Sill 3) located mid-fjord. Interestingly, these stations are locations where high rates of primary production were measured (Lindsey Ekern Thesis) and enhanced upwelling and mixing occurred (Forsch et al., 2021; Lundesgaard et al., 2020). These results indicate a potential contribution from multiple ligand sources, as strong (L_1) and weaker ligands (L_3), to an already strong ligand pool. As discussed in Forsch *et al.* (2021), ligand sources in the fjord include *in situ* sources from microbes during the vernal bloom, but also high concentrations of weak ligands produced during remineralization processes or from subsurface sources in the Fall. Once upwelled during episodic extreme wind events, these weak ligands could contribute to the surface ligand pool as shown at Sill 3 and Inner Basin stations (Table 4.1). These locations also exhibited the highest OTUs associated with archaea and

ammonium concentration at the surface (data not shown), again indicating these are locations for intensified entrainment of deeper microbial populations and ligand sources.

When we compare MAW and SAW methods for samples in which only one ligand class was detected, we find that on-average SAW underestimates the total ligand concentration by 16%. With samples where multiple ligand classes were detected by MAW, we find that SAW underestimates the total ligand concentration by 40±17% (*n* = 6). These results identify an important drawback of employing only a single analytical window: a significant fraction of the ligand pool is missed. Indeed, these large discrepancies are due to a significant contribution of very weak ligands ($L_{3\text{-}4}$) missed by SAW analysis. Despite the differences in these methods, both MAW and SAW determined similar free Fe concentrations (Table A1). The largest difference is where multiple ligands were detected by MAW and not SAW. We also found that a stronger correlation exists between the logα, or "binding capacity", defined by equation 2, and dFe concentrations when using MAW analysis (r^2 = 0.16 for SAW and r^2 = 0.52 for MAW).

$$\alpha = (1 + (excess\ L_{1,2} \times\ K_{1,2})) \qquad (2)$$

While logα is used to indicate the ability for the ligand pool to bind additional dFe, the stronger correlation with dFe concentrations might indicate that MAW more accurately captures the physicochemical process of solubilization and stabilization of dFe from particulate matter by the ligand pool, since a higher logα is both a result of excess ligand production and the binding strength of the strong ligands ($logK_{1,2}$).

By comparing MAW with SAW analyses on the same samples, we have found that the SAW method is likely missing additional ligand classes within samples when a large concentration of very weak ligands is present, or when dissolved organic carbon concentrations are elevated. We contend that SAW analysis sufficiently captures important changes in partitioning of

organically-bound Fe and 'free Fe' (Fe′), but it does not resolve ligand classes which originate from distinct sources. Further, SAW analyses have the potential to misinterpret the concentration of strong L_1 ligands when a large excess of very weak ligands exists, such as in productive surface waters and those influenced by sedimentary sources. This is a well-known issue for processing Cu speciation measurements, first identified by Voelker and Kogut (2011). They found weak organic ligands interfere in the determination of the titration sensitivity at a given analytical window. By using multiple analytical windows, we overcome this potential issue in our own Fe speciation data. The SAW results for the Inner Basin B station (Moser Glacier) in the late-Spring (LMG1510) revealed a L_2 ligand class of 6.22 ± 0.52 nM and $logK_2$ = 11.99 ± 0.14 in the surface. Using MAW analysis, we find the ligand pool is composed of a strong L_1 ligand class ([L_1] = 3.82 ± 0.42 nM, $logK_1$ = 13.10 ± 0.59) and a weaker ligand class ([L_3] = 6.83 ± 3.84 nM, $logK_3$ = 10.5 ± 0.34). By obtaining data from a high window where the weak ligands interfere little or not at all, we overcome poor calibration of the sensitivity. We note that when multiple ligands are resolved by ProMCC, the uncertainties are significantly greater with the weaker ligand classes (Gerringa et al., 2021; Pižeta et al., 2015).

4.4.2.2. Fe speciation in the 'Morro Bay' filament

The CCE-LTER process cruise tracked an upwelling filament from the nearshore Morro Bay region to offshore, revealing a gradient in iron stress as the water mass moved from Fe-replete conditions over the shelf, to Fe-limited offshore (Figure 4.4). We leveraged the Lagrangian cruise dataset to study changes in MAW Fe speciation ($\alpha_{Fe(SA)_x}$ = 60, 115, and 162) across gradients in Fe stress and as a function of distance from the Fe source. DFe speciation data is presented in Table 4.2. The shoreward filament source endmember was sampled in the Morro Bay benthic boundary layer (BBL). We found that the BBL was enriched in dFe (14.77 nM) and several classes of Fe-binding ligands (L_1, L_2 and L_3) were identified, notably a large excess of L_1

ligands (6.82 nM excess L_1 = [L_1] – [dFe]). Once upwelled, the total concentration of Fe-binding ligands decreased, but excess L_1 was maintained and increased to 10.11 nM once the water parcel had moved offshore. This large excess in L_1 also corresponded to the onset of Fe-limitation (indicated by negative Si_{ex} in Figure 4.4) and could indicate a strategy to access refractory forms of Fe (e.g. particulate matter) as dFe concentrations diminished. Interestingly, where we observe the greatest degree of Fe-limitation, was found to occur in the late stage of Cycle 2, where L_1 ligands were not detected. Further offshore, L_2 ligands became more dominant in the nearest surface waters, although patchy sub-surface distribution of L_1 ligands still had significant impacts on dFe binding capacity (Figure 4.5). Fe speciation in the offshore is controlled by a nearly constant surface pool of slightly weaker ligands (L_2). This is consistent with other published studies on the distributions of Fe-binding ligands in the CCS (Boiteau et al., 2019; Bundy et al., 2014, 2016).

The BBL was enriched in multiple ligand classes and had the overall highest logα, indicating that the sediments are a possible source of multiple ligands to the upwelling filament. This result is similar to the findings of Bundy *et al.* (2014) who found multiple ligands (L_1, L_2, and L_3) at similar concentrations in BBL samples collected during Spring and Summer cruises. However, in Bundy *et al.* (2014), each window was analyzed separately resulting in higher logα values (13.8 to 15.2, compared to 13.3 this study); likely a result of overcounting of overlapping ligands. In the surface, similar concentrations of L_1 were found in the 2014 study and were not detected >100 km from the coast. We too found that L_1 ligands were not detected in offshore cycles. Greater concentrations of L_2 were found within the filament (8.15 – 9.07 nM) when compared to Bundy *et al.* (2014) surface samples. This indicates that filaments are important sources of L_2 ligands to offshore surface waters. Interestingly, while we detected elevated concentrations of L_2 and L_3 ligands within the Morro Bay BBL, these ligand classes were absent in surface waters at Cycle 1 and the beginning of Cycle 2. This suggests distinct processes

influence their distributions within filaments. The MAW approach in this study helped to determine the full spectrum of ligands present in a coastal upwelling filament and their spatial relationship with the BBL source and nutrient limitation. In summary, we showed excess L_1 is maintained during upwelling and some advection before it is lost. A significant L_2 source is then produced >50 km away from the BBL and appears at the location of the highest degree of Fe-limitation in incubation studies (covered in Chapter 2). We also showed that the logα decreases with distance from shore, showing offshore surface waters are less able to buffer additional dFe sources. Phytoplankton may take advantage of higher logα and increased Fe solubilization and stabilization during bloom formation during the early stages of filament advection. This provides new information regarding the role of dFe-binding ligands in Fe supply to the CCS.

4.4.3. A comparison of ligands in fjords and upwelling filaments

We compare the dFe-binding ligand quality and quantity at these two productive sites. We detected a similar range of L_1 concentrations at both sites. The 'Morro Bay' filament contained a range of 4.46 to 10.3 nM L_1 (excluding the BBL station), while we observed water column concentrations of 2.82 to 10.50 nM L_1 within the fjord. The *excess* L_1 concentrations were noticeably different, with higher excess L_1 in the filament (8.46 to 10.11 nM at Cycle 1, Table 4.2) compared to the fjord (0.46 to 0.97 nM, Table 4.1). This is likely because the fjord was proximal to many dFe sources which led to overall higher dFe concentrations and saturation of the ligand pool. Within the surface waters of the filament, up to 6.82 nM *excess* L_1 came from the BBL, and the rest are likely produced during the bloom (Hogle et al., 2016). This large excess of L_1 in the filament surface layer led to higher logα values, compared to the fjord, but the means of both field studies are similar (filament: 12.62 ± 0.4, n = 5; fjord: 12.58 ± 0.2, n = 8). The highest binding capacity found in both datasets was in the BBL (13.3). These results show that the BBL and Fe-limited upwelling filaments are important sources of excess strong ligands, which facilitate dFe complexation during early stages of lateral advection, but a significant sink ensures no L_1 are

detected in the aged filament further offshore. No L_1 ligands were found within the fjord at the surface in the Fall, which again highlights that the presence of L_1 in surface waters is controlled by proximity to its source (BBL), the biogeochemical condition (Fe-limitation) and the age of the water mass (stage of the bloom and dominant sinks). Within the surface, one notable sink of L_1 ligands is thought to be degradation by sunlight, leading to the destruction of the ligand (Barbeau, 2006) or conversion to a weaker ligand class (Bundy et al., 2016). Therefore, it is critical to understand the residence time of excess L_1 with less bioavailable forms of Fe to understand how strong ligands form a bioavailable pool of dFe in the euphotic zone prior to degradation.

The global ocean is heavily under sampled for measurements of dFe-binding ligands. These studies contribute to our understanding of the spatial differences and seasonality of distinct productive regions. Based on our findings here, we suggest that productive eastern boundary currents contain a larger excess of ligands than polar fjords due to lower concentrations of dFe, despite phytoplankton biomass being comparable (fjord range: 2 – 8 µg Chlorophyll-a L^{-1} from Pan *et al.* 2020; filament range: 2.5 – 10 µg Chlorophyll-a L^{-1} from Chapter 2). However, it appears that strong ligands are produced at both sites during the formation of phytoplankton blooms. We next investigate the production of L_1 ligands in terms of phytoplankton bloom phenology.

4.4.4. Changing iron speciation during a simulated bloom

To capture ligand dynamics during the remineralization of particulate organic matter, Velasquez *et al.* (2016) used high-performance liquid chromatography (HPLC) coupled with mass spectrometry to measure the rates of ferrioxamine siderophore production. However, in that study, no L_1 ligands were detected electrochemically possibly because a relatively low analytical window was employed. The authors used the added ligand 2-(2-Thiazolylazo)-p-cresol (TAC) at a concentration of 3.5 µM, $\alpha_{Fe(TAC)_2}$= 30.625 (Croot and Johansson, 2000). This window is optimized for detecting weak, not strong ligands (Bundy et al., 2014). By tuning the concentration of the competing ligand, specific ligand classes of interest may be detected. The Fe speciation in

a simulated bloom experiment was determined using MAW electrochemical analysis ($\alpha_{Fe(SA)_x}$= 80, 160), in conjunction with metatranscriptomic sampling. These relatively high analytical windows allow us to detect ligands within two orders of magnitude of the $\alpha_{Fe(SA)_x}$. Complexometric titration results are presented in Table 4.3. The study was initiated as a microbial community grow-out with nutrient addition to a natural community present in offshore Pacific surface seawater. Following 11 days of growth and initial senescence (indicated by Chlorophyll-a concentration as a proxy of biomass), the incubation was placed in the dark to observe remineralization processes for an additional 7 days. The microcosm experiment was performed in triplicate (indicated by letters A, B, and C). Over the course of the experiment TOC concentrations peaked at the end of the light incubation period (day 10) and were drawn down to near pre-bloom levels during the remineralization phase (Figure 4.6 panel A). Bacterial carbon production (BCP) dramatically increased over the course of the incubation indicating active processing of organic matter by the bacterial population (Figure 4.6 panel B). 16S rDNA and metatranscroptomic results showed that the prokaryotic community shifted dramatically from one dominated by the oligotrophic groups SAR11 and *Prochlorococcus* to one dominated by the copiotrophic groups *Alteromonadales*, *Flavobacteriales*, and *Rhodobacterales* by the peak of the bloom (data not shown). There was also a concerted shift in Fe acquisition mechanisms over the course of the experiment. Initially, Fe transport genes consisted primarily of Fe(III) ABC transport systems from the SAR11 clade and alphaproteobacteria as determined by the detection of transcripts for the solute binding protein (SBP) component of these systems. As the relative abundance of Fe(III) ABCT systems decreased, the apparent utilization of complexed sources of Fe increased as evidenced by the expression of SBPs for dFe-ligand complexes (such as Fe-siderophore complexes or heme). These SBPs were not detected during the initial timepoints, but were expressed by *Alteromonadales*, *Flavobacteriales*, and the SAR92 clade during the peak bloom and remineralization stages. Interestingly, the MAW dFe speciation data (Figure 4.6 panel

C) indicates that the highest binding capacity of strong L_1 and L_2 ligands occurs during the peak phase of the bloom, rather than during the log-phase growth or the extended dark remineralization period.

The ability for the strong ligand pool to bind additional dFe, or "binding capacity", is summarized by the α value, defined in equation 2. This pattern in α is driven by a consistent peak in the binding constant of the strongest ligands detected right at the peak of the bloom, day 10, (Figure 4.6 panel D), which may be indicative of siderophore production at this stage. There is also a suggestion of a maximum in excess strong ligands in the immediate post peak/early senescence point on day 11. These results suggest that the extended remineralization period may not be as associated with the production of strong Fe-binding ligands as the bloom peak period. This supports earlier findings (Hogle et al., 2016), and, importantly, suggests that strong ligand production does not scale with bulk processes like TOC consumption or bacterial carbon production but may instead be synced to the phase of the phytoplankton bloom. The average L_1 ligand production and consumption rates determined between each experimental sampling day can be up to several nM d^{-1} in this experiment (Table 4.4). These results indicate that multiple processes must govern large quantities of L_1 ligands, since siderophore production rates are low (11.8 pM d^{-1}, Velasquez *et al.* 2016). While production and consumption rates are expected to be low for siderophore-dFe complexes, other processes such as photochemical or bacterial degradation could contribute to the observed trends. Additional compounds are likely to contribute substantially to this pool, such as exopolymeric substances produced during phytoplankton blooms, which are shown to be strong ligands (Hassler et al., 2011).

Further exploration of this data set will be accomplished by targeting specific Non-ribosomal Peptide Synthase (NRPS) biosynthetic pathways in the metatranscriptomes on days 10 and 11 as potential siderophore pathways. By correlating the presence of specific transcripts with the concentration and binding strength of strong ligands via network analysis we refine biological sources and turn-over rates of organic ligands involved in Fe acquisition in the ocean.

4.5. Conclusions

The MAW method described here improves the detection of multiple ligand classes within environmental samples and mechanistic incubation experiments. The determination of a unified sensitivity for the entire MAW speciation dataset prior to final processing in ProMCC is an improvement on MAW data processing. This step in KINETEQL eliminates the time-intensive step of determining individual window sensitivities and allows for processing all analytical window titration data simultaneously. Compared to SAW, MAW analysis can detect additional ligand classes, especially in instances when dissolved organic carbon concentrations are high (during blooms, close to sediments, remineralization). Therefore, for researchers interested in understanding the sources and sinks of particular ligand classes, MAW analysis is superior. MAW analysis allowed for multiple ligand classes of Fe-binding ligands to be observed, each with unique distributions with respect to depth and region. Whereas dCu speciation represents a continuum of incidental ligand binding, dFe speciation by strong ligands arises from purposeful complexation by discrete molecular families (i.e., siderophores) as a strategy to acquire Fe from less bioavailable forms when dFe concentrations become limiting (Butler, 1998). Therefore, MAW is well-suited to investigate the diversity of organic ligands that comprise the bulk ligand pool and possible controls on their occurrence in seawater. When strongly complexing ligands are the focus, as in the P1604 microcosm experiment, employing appropriately high analytical windows can provide critical information for querying large metatranscriptomic datasets, which can connect patterns in ligand production to microbial metabolic processes.

In a recent publication, Gerringa *et al.* (2021) discussed the drawbacks of using CLE-ACSV electrochemical methods. When a model ligand was analyzed with a single window titration, there was a tendency to overestimate the concentration of the ligand (Gerringa et al., 2021). Ligand concentrations determined from a single window analysis represent an average of

a consortium of natural ligands in environmental samples. Therefore, MAW analyses should be able to resolve better the concentrations of individual ligand classes. We found that MAW analysis results in lower uncertainties in open ocean samples, compared to enriched environmental settings, probably due to large effects associated with high DOC concentrations in coastal and productive regions and incubation studies. SAW likely underestimates the concentration of total ligands, but also could misinterpret the contribution of strong L_1 ligands to the ligand pool. Corollary: MAW can resolve strong ligand production when high concentrations of weak ligands are present.

In this chapter, through exploration of environmental and incubation samples, we arrived at a better understanding of 1) the spatial and seasonal distributions of L_1 ligands in surface waters of an Antarctic fjord and a California Current upwelling filament; 2) the residence times of different *in situ* ligands with respect to seasonality in a fjord and offshore advection by an upwelling filament, and also production/consumption rates of ligands in an incubation experiment; and 3) the distribution, nature, and sources of strong and weak ligands using an MAW approach with improved data analysis to simultaneously detect multiple ligand classes.

4.6. Acknowledgements

We would like to thank Randelle Bundy and Kristen Buck for their advice on parameterizing electrochemical analyses. We give special thanks to Angel Ruacho for his advice on the development of these MAW data processing techniques. The primary author greatly benefited from his knowledge of voltammetry and advancement of these techniques, with application to copper speciation. This chapter was support by the U.S. National Science Foundation (NSF grant no. PLR-1443705, OCE-1558841). K.F. was supported by an NSF GRF (NSF 15-597). This work was supported by grants to the *California Current Ecosystem* LTER site by NSF.

4.7. Figures and Tables

Table 4.1. MAW Fe speciation data from expeditions to Andvord Bay (LMG1510, NBP1603).

	Sample	Depth (m)	dFe (nM)	free Fe (pM)	L_1 (nM)	±	logK$_1$	±	L_2 (nM)	±	logK$_2$	±	L_3 (nM)	±	logK$_3$	±	L_4 (nM)	±	logK$_4$	±	L_5 (nM)	±	logK$_5$	±	L_6 (nM)	L_7:dFe	dL_7 (nM)	log(alpha)
LMG1510 (late-Spring)	Inner Basin A (Bagshawe Glacier)	6	1.85	0.42	2.82	0.92	12.40	0.43	3.17	1.94	11.60	0.52													5.99	3.24	0.97	12.57
	Inner Basin A (Bagshawe Glacier)	160	5.84	7.41					8.53	0.98	11.50	0.23													8.53	2.69	1.46	n.d.	12.43
	Inner Mid-Bay B (Moser Glacier)	6	3.36	0.45	3.82	0.46	13.10	0.59					6.83	3.84	10.50	0.34									10.65	7.29	3.17	0.46	12.78
	Sill 3 (Mid-Bay Sill)	11	3.41	0.48	4.20	0.25	12.80	0.23					4.51	1.30	10.80	0.22									8.71	5.30	2.55	0.79	12.72
	Outer Basin B	6	2.50	0.51					12.60	4.57	11.50	0.29													12.60	10.10	5.04	n.d.	12.60
NBP1603 (Fall)	Inner Basin A (Bagshawe Glacier)	25	7.80	1.70					19.80	2.97	11.60	0.26													19.80	12.00	2.54	n.d.	12.90
	Inner Basin A (Bagshawe Glacier)	110	6.72	7.64	10.50	0.10	12.20	0.28	9.60	1.18	11.40	0.23													20.10	13.38	2.99	3.78	12.92
	Inner Basin A (Bagshawe Glacier)	280	14.45	4.32					21.00	2.93	11.70	0.35													21.00	6.55	1.45	n.d.	13.02
	Inner "Mid-Bay" Basin A (Bagshawe Glacier)	80	8.51	3.95					22.80	4.91	11.20	0.25													22.80	14.29	2.68	n.d.	12.56
	Inner Mid-Bay B (Moser Glacier)	20	6.89	2.41					9.60	1.82	11.90	0.45	6.72	0.38	10.70	0.59									16.32	9.43	2.37	n.d.	12.88
	Inner Mid-Bay B (Moser Glacier)	75	5.94	2.30					9.11	1.96	11.80	0.38					28.80	15.80	9.97	0.37	37.91	31.97	6.38	n.d.	12.76
	Middle Basin	20																										
	Sill 3 (Mid-de Sill)	15	5.41	2.66					18.20	3.92	11.30	0.31													18.20	10.79	2.99	n.d.	12.51
	Sill 4	25	6.93	5.06					13.70	2.74	11.30	0.28													13.70	8.77	1.98		12.44
	Andvord Front	15	4.88	6.48					9.02	1.94	11.20	0.34													9.02	4.33	1.92	n.d.	12.16
	Andvord Front	120	5.37	3.73					10.30	1.44	11.50	0.26													10.30	4.93	1.92	nd	12.51
	Gerlache Slant	15	5.14	10.70					9.88	2.49	11.00	0.30													9.88	4.74	1.92	n.d.	11.99

Table 4.2. MAW Fe speciation data from the 'Morro Bay' filament cruise (P1706).

Cycle	Lat	Long	Depth (m)	dFe [nM]	± [nM]	free Fe [pM]	L_1 [nM]	± [nM]	$logK_1$	±	L_2 [nM]	± [nM]	$logK_2$	±	L_3 [nM]	± [nM]	$logK_3$	±	excess L_1 [nM]	log(alpha)
Morro Bay BBL			56	14.77	0.62	15.49	21.59	2.50	12.1	0.2	14.05	1.09	11.8	0.7	14.90	4.21	10.8	0.9	6.82	13.3
1			10	0.72	0.01	0.07	9.18	1.67	12.1	0.9									8.46	13.0
2			12	0.19	0.02	0.03	10.30	0.33	12.1	0.1									10.11	13.1
2			15	0.14	0.01	0.07					8.15	1.39	11.4	0.2					nd	12.3
2			10	0.14	0.004	0.08					9.07	5.44	11.3	0.4					nd	12.3
2			20	0.09	0.001	0.14									11.40	5.96	10.7	0.3	nd	11.8
2			40	0.15	0.01	0.02	4.46	1.73	12.2	0.4					12.50	12.20	10.1	10.6	4.31	12.8
2			60	0.40	0.003	0.34					5.18	4.53	11.1	11.3	20.60	18.80	10.3	10.5	nd	12.1
2			100	0.43	0.003	0.44					1.73	1.68	11.7	11.7	0.57	0.56	10.1	12.0	nd	11.9
2			300	0.82	0.02	0.44					6.13	2.91	11.4	0.5	37.20	23.20	10.1	0.5	nd	12.3
2			500	1.04	0.01	0.65	1.47	0.81	12.5	1.5									0.43	12.1
2			750	0.70	0.04	0.46	1.49	0.88	12.2	1.0									0.79	12.2
3			10	0.25	0.01	0.09					8.15	2.75	11.5	0.4					nd	12.4

Table 4.3. MAW Fe speciation data from the P1604 experiment. The average ± standard deviation of day 0 replicates is shown for the total ligand (L_t) and the free Fe concentrations. The strongest ligand class is presented in the table, while weaker ligands are not shown.

Experiment	time [days]	L_t [nM]	dFe [nM]	± [nM]	free Fe [pM]	L_1 [nM]	± [nM]	logK_1	±	excess L_1 [nM]	alpha
Pacific SW	0	9.88±0.30	0.15	0.01	0.037±0.036	5.02	0.94	12.4	0.3	4.86	1.3E+13
A	7	10.70	3.76	0.06	0.45	7.23	0.98	12.3	0.4	3.47	1.5E+13
A	10	14.47	4.05	0.12	0.68	4.61	0.48	13.0	0.9	0.56	4.2E+13
A	11	5.76	3.36	0.01	0.55	4.56	0.48	12.7	0.5	1.20	2.3E+13
A	14	9.18	2.40	0.04	0.38	5.79	1.61	12.3	0.5	3.39	1.1E+13
A	18	3.73	1.65	0.03	0.51	2.69	0.42	12.5	0.5	1.04	8.3E+12
B	7	21.70	8.36	0.11	1.12	11.30	0.80	12.6	0.3	2.94	4.9E+13
B	10	6.46	4.24	0.05	0.11	4.97	0.30	13.9	0.6	0.73	4.0E+14
B	11	9.18	1.04	0.01	0.06	3.37	1.60	12.7	0.8	2.33	2.1E+13
B	14	3.86	0.72	0.03	0.50	3.86	2.94	11.7	0.7	0.00	1.8E+12
B	18	0.00	1.03	0.03	0.00					0.00	1.0E+00
C	7	98.45	2.46	0.09	0.56	3.65	0.37	12.5	0.3	0.00	1.2E+13
C	10	63.77	1.11	0.00	0.03	1.87	0.21	13.7	1.2	0.76	1.0E+14
C	11	7.35	1.40	0.01	0.22	7.35	2.24	12.0	0.4	5.95	8.0E+12
C	14	4.20	1.21	0.00	0.90	4.20	2.47	11.8	0.5	0.00	2.5E+12
C	18	4.90	1.23	0.00	0.13	4.90	1.70	12.2	0.4	3.67	7.2E+12

Table 4.4. Ligand (L_1) production and consumption rates determined between each experimental sampling day. The units are in nM L_1 d^{-1} with average (Avg) and standard deviations (±) tabulated for the triplicate experiments.

Period	A	B	C	Avg	±
beginning-7	0.32	0.90	-0.20	0.34	0.55
7-10	-0.87	-2.11	-0.59	-1.19	0.81
10-11	-0.05	-1.60	5.48	1.28	3.72
11-14	0.41	0.16	-1.05	-0.16	0.78
14-end	-0.78	-0.97	0.18	-0.52	0.61

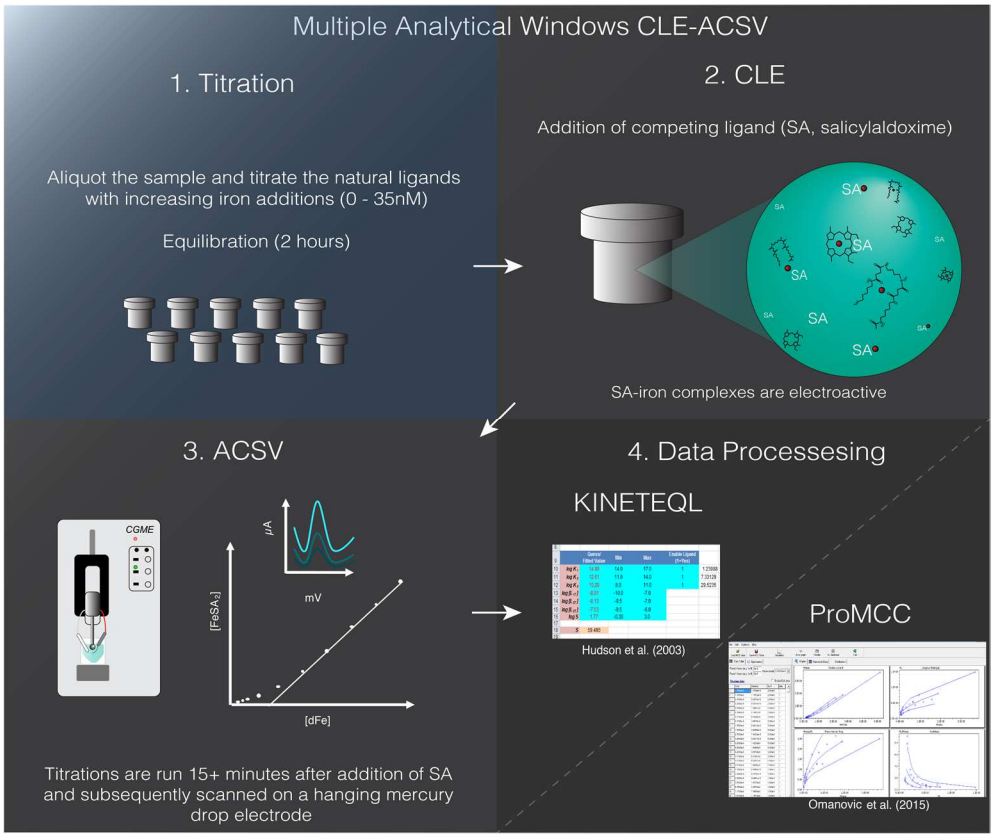

Figure 4.1. Method for dFe speciation measurements using CLE-ACSV with proposed developments for processing MAW Fe speciation titration data through a combination of KINETEQL (Hudson et al. 2003) and ProMCC (Omanovic et al. 2015) software.

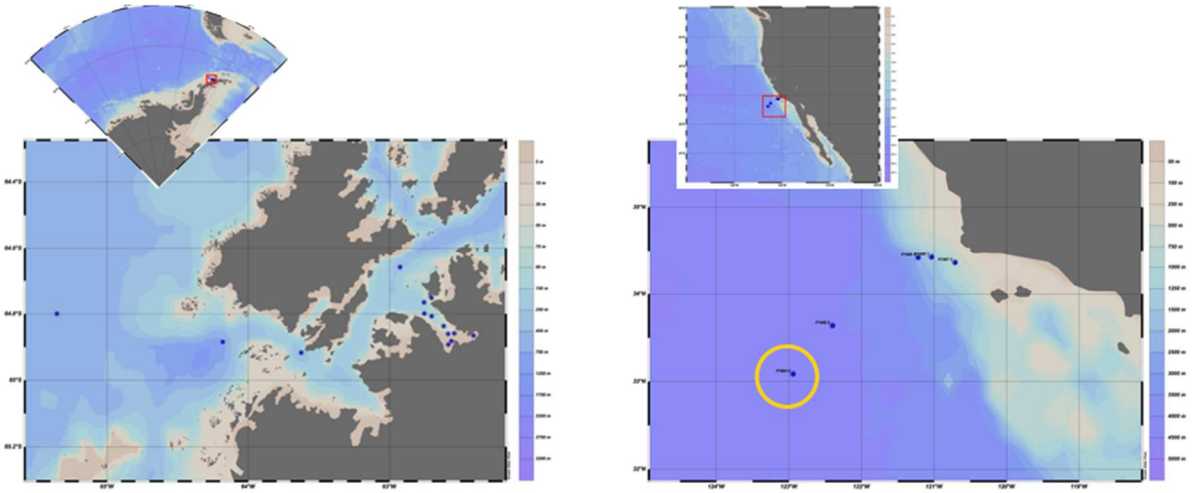

Figure 4.2. Geographically distinct regions of the ocean where studies of dFe-binding ligands were conducted. Andvord Bay (left map) and the California Current location of the P1604 microcosm experiment circled in yellow (right map).

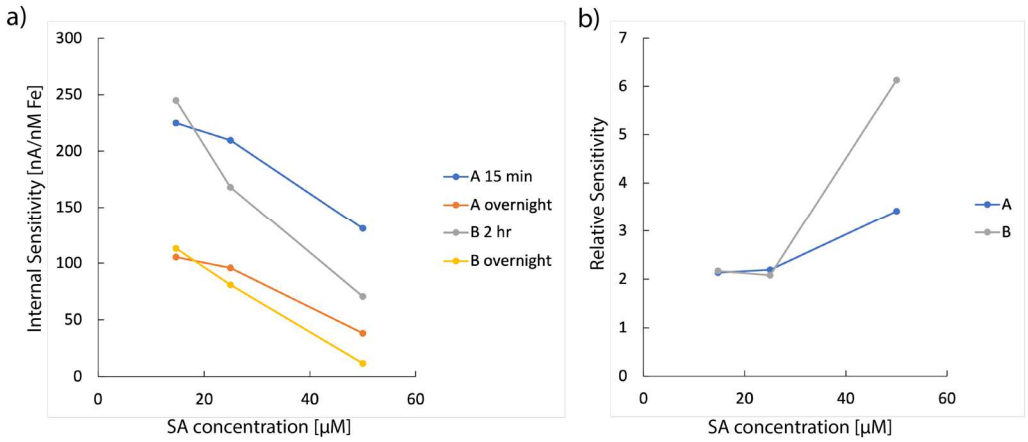

Figure 4.3. Analyses of Pacific ocean surface seawater replicates (A and B) to test equilibration time with added Fe. a) The internal sensitivity determined from the linear portion of each titration for each replicate at three SA concentrations (14.7, 25, 50 µM). b) The relative sensitivity between the short equilibration (15 min, 2 hr) and the overnight equilibrations for seawater replicates A and B. The largest relative change in sensitivity was for the highest SA concentrations (i.e., analytical window).

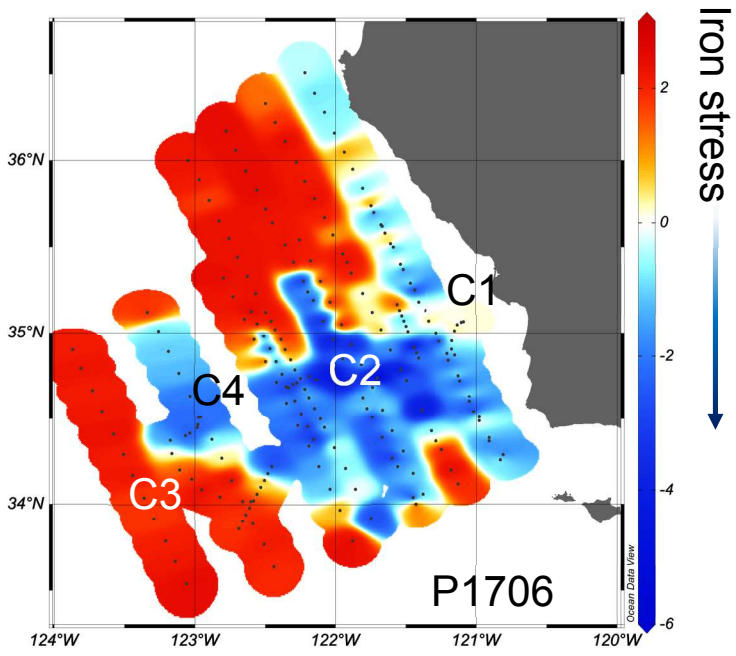

Figure 4.4. The concentration of Si_{ex} [μM] at the surface over the entire study region. More negative values of Si_{ex} indicate Fe stress conditions of diatoms in the southern California Current and is defined as, $Si_{ex} = [Si(OH)_4] - (R_{Si:NO_3} \times [NO_3^-])$, where $R_{Si:NO_3}$~1. The cruise track is roughly shown by the locations of Lagrangian 'Cycles', each cycle lasted 3-4 days. Cycle 1 (C1) is the initial location for the upwelled water parcel, and Cycle 2 and 4 (C2, C4) is the time-evolved filament, while Cycle 3 was no longer within the filament.

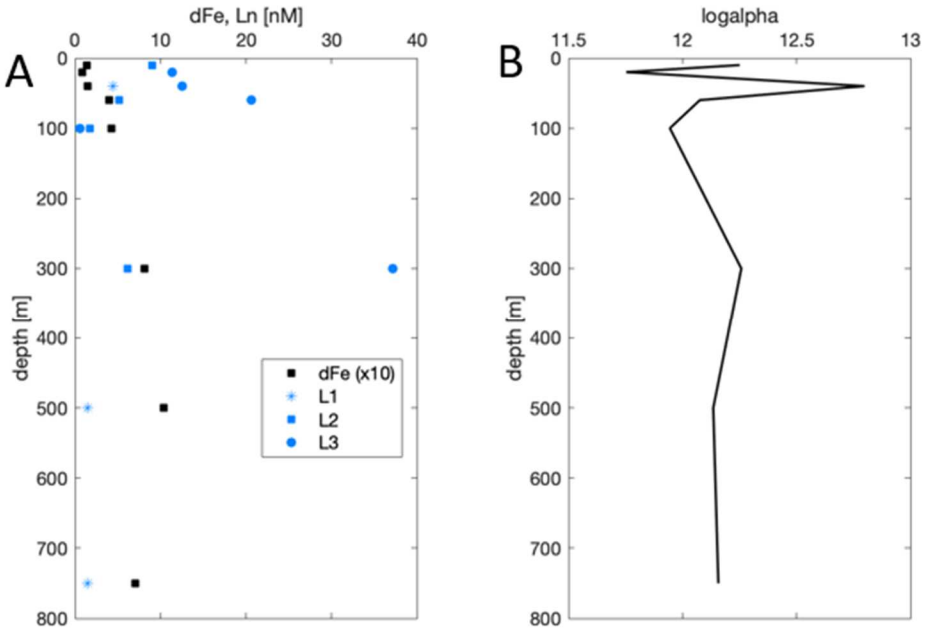

Figure 4.5. 'Morro Bay' filament (P1706) dFe speciation profile at Cycle 2 (see Fig. 3). A) Profiles of dFe and ligand concentrations for an off-shelf station within an upwelling filament. B) Iron "binding capacity" of the in situ strong ligand pool (logα), note maximum logα at 40 m depth, this was the base of the chlorophyll maximum layer and due to the presence of strong L_1 ligands.

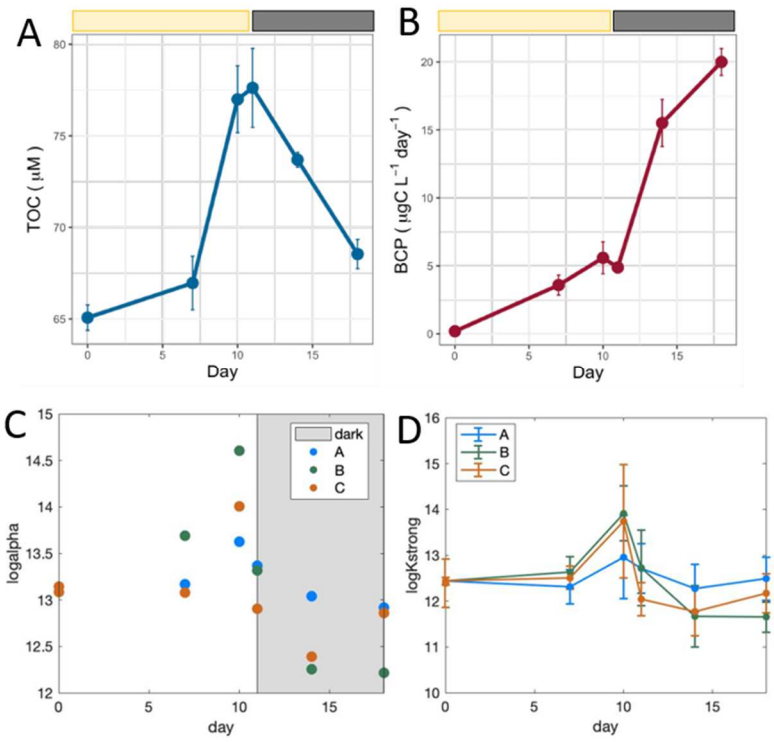

Figure 4.6. P1604 incubation experiment results. A) TOC concentrations peaked at the end of the light incubation period and were drawn down to near pre-bloom levels during the remineralization phase. B) BCP dramatically increased over the course of the incubation indicating active processing of organic matter by the bacterial population. C) Binding capacity of strong ligands peaked at 10 days, the peak of the bloom. D) Increased conditional stability constants for ligands at day 10 could be indicative of siderophore production at bloom peak/senescence.

4.8. Appendix

Table A1. Comparison of LMG1510 and NBP1603 dFe speciation data for select stations. Results are presented for both SAW (from Forsch *et al.* 2021) and MAW analyses (this chapter).

SAW or MAW?	Station	Depth [m]	L_1 [nM]	±	K_1	±	L_2 [nM]	±	K_2	±	L_3 [nM]	±	K_3	±	L_4 [nM]	±	K_4	±	Fe' [pM]	L_t [nM]	logalpha
SAW	IBA	6	4.06	1.74	12.13	0.69													0.62	4.06	12.5
MAW	IBA	6	2.82	0.92	12.4	0.43	3.17	1.94	11.6	0.52									0.42	5.99	12.6
SAW	IBB	6					6.22	0.52	11.99	0.14									1.19	6.22	12.4
MAW	IBB	6	3.82	0.46	13.1	0.59					6.83	3.84	10.5	0.34					0.45	10.65	12.8
SAW	S3	11	7.27	1.97	12.05	0.44													0.79	7.27	12.6
MAW	S3	11	4.2	0.25	12.8	0.23					4.51	1.3	10.8	0.22					0.48	8.71	12.7
SAW	IBA	110					8.54	0.88	11.69	0.35									7.18	8.54	12.0
MAW	IBA	110	10.5	0.1	12.2	0.28	9.6	1.18	11.4	0.23									7.64	20.1	12.9
SAW	IBB	20					11.18	1.39	11.58	0.26									4.16	11.18	12.2
MAW	IBB	20					9.6	1.82	11.9	0.45	6.72	0.38	10.7	0.59					2.41	16.32	12.9
SAW	IBB	75					14.03	1.57	11.3	0.13									3.64	14.03	12.2
MAW	IBB	75					9.11	1.96	11.8	0.38					28.8	15.8	9.97	0.37	2.3	37.91	12.8

4.9. References

Abualhaija, M. M. and van den Berg, C. M. G.: Chemical speciation of iron in seawater using catalytic cathodic stripping voltammetry with ligand competition against salicylaldoxime, Mar. Chem., 164, 60–74, doi:https://doi.org/10.1016/j.marchem.2014.06.005, 2014.

Alison, B.: Acquisition and Utilization of Transition Metal Ions by Marine Organisms, Science (80-.)., 281(5374), 207–209, doi:10.1126/science.281.5374.207, 1998.

Ardiningsih, I., Krisch, S., Lodeiro, P., Reichart, G.-J., Achterberg, E. P., Gledhill, M., Middag, R. and Gerringa, L. J. A.: Natural Fe-binding organic ligands in Fram Strait and over the northeast Greenland shelf, Mar. Chem., 224, 103815, doi:https://doi.org/10.1016/j.marchem.2020.103815, 2020.

Barbeau, K.: Photochemistry of Organic Iron(III) Complexing Ligands in Oceanic Systems, Photochem. Photobiol., 82(6), 1505–1516, doi:https://doi.org/10.1111/j.1751-1097.2006.tb09806.x, 2006.

Van Den Berg, C. M. G., Nimmo, M., Daly, P. and Turner, D. R.: Effects of the detection window on the determination of organic copper speciation in estuarine waters, Anal. Chim. Acta, 232, 149–159, doi:https://doi.org/10.1016/S0003-2670(00)81231-3, 1990.

Boiteau, R. M., Till, C. P., Coale, T. H., Fitzsimmons, J. N., Bruland, K. W. and Repeta, D. J.: Patterns of iron and siderophore distributions across the California Current System, Limnol. Oceanogr., 64(1), 376–389, doi:https://doi.org/10.1002/lno.11046, 2019.

Boyd, P. W., Ibisanmi, E., Sander, S. G., Hunter, K. A. and Jackson, G. A.: Remineralization of

upper ocean particles: Implications for iron biogeochemistry, Limnol. Oceanogr., 55(3), 1271–1288, doi:10.4319/lo.2010.55.3.1271, 2010.

Buck, K. N. and Bruland, K. W.: Copper speciation in San Francisco Bay: a novel approach using multiple analytical windows, Mar. Chem., 96(1–2), 185–198, 2005.

Buck, K. N., Lohan, M. C., Berger, C. J. M. and Bruland, K. W.: Dissolved iron speciation in two distinct river plumes and an estuary: Implications for riverine iron supply, Limnol. Oceanogr., 52(2), 843–855, doi:10.4319/lo.2007.52.2.0843, 2007.

Buck, K. N., Sohst, B. and Sedwick, P. N.: The organic complexation of dissolved iron along the U.S. GEOTRACES (GA03) North Atlantic Section, Deep Sea Res. Part II Top. Stud. Oceanogr., 116, 152–165, doi:https://doi.org/10.1016/j.dsr2.2014.11.016, 2015.

Buck, K. N., Sedwick, P. N., Sohst, B. and Carlson, C. A.: Organic complexation of iron in the eastern tropical South Pacific: Results from US GEOTRACES Eastern Pacific Zonal Transect (GEOTRACES cruise GP16), Mar. Chem., 201, 229–241, doi:https://doi.org/10.1016/j.marchem.2017.11.007, 2018.

Bundy, R. M., Barbeau, K. A. and Buck, K. N.: Sources of strong copper-binding ligands in Antarctic Peninsula surface waters, Deep Sea Res. Part II Top. Stud. Oceanogr., 90, 134–146, doi:https://doi.org/10.1016/j.dsr2.2012.07.023, 2013.

Bundy, R. M., Biller, D. V, Buck, K. N., Bruland, K. W. and Barbeau, K. A.: Distinct pools of dissolved iron-binding ligands in the surface and benthic boundary layer of the California Current, Limnol. Oceanogr., 59(3), 769–787, doi:10.4319/lo.2014.59.3.0769, 2014.

Bundy, R. M., Abdulla, H. A. N., Hatcher, P. G., Biller, D. V, Buck, K. N. and Barbeau, K. A.: Iron-binding ligands and humic substances in the San Francisco Bay estuary and estuarine-influenced shelf regions of coastal California, Mar. Chem., 173, 183–194, doi:https://doi.org/10.1016/j.marchem.2014.11.005, 2015.

Bundy, R. M., Jiang, M., Carter, M. and Barbeau, K. A.: Iron-Binding Ligands in the Southern California Current System: Mechanistic Studies , Front. Mar. Sci. , 3, 27 [online] Available from: https://www.frontiersin.org/article/10.3389/fmars.2016.00027, 2016.

Croot, P. L. and Johansson, M.: Determination of Iron Speciation by Cathodic Stripping Voltammetry in Seawater Using the Competing Ligand 2-(2-Thiazolylazo)-p-cresol (TAC), Electroanalysis, 12(8), 565–576, doi:https://doi.org/10.1002/(SICI)1521-4109(200005)12:8<565::AID-ELAN565>3.0.CO;2-L, 2000.

Fitzsimmons, J. N., Bundy, R. M., Al-Subiai, S. N., Barbeau, K. A. and Boyle, E. A.: The composition of dissolved iron in the dusty surface ocean: An exploration using size-fractionated iron-binding ligands, Mar. Chem., doi:10.1016/j.marchem.2014.09.002, 2015.

Forsch, K., Hahn-Woernle, L., Sherrell, R., Roccanova, J., Bu, K., Burdige, D., Vernet, M. and Barbeau, K. A.: Seasonal dispersal of fjord meltwaters as an important source of iron to coastal Antarctic phytoplankton, Biogeosciences Discuss., 2021, 1–49, doi:10.5194/bg-2021-79, 2021.

Gerringa, L. J. A., Gledhill, M., Ardiningsih, I., Muntjewerf, N. and Laglera, L. M.: Comparing CLE-AdCSV applications using SA and TAC to determine the Fe-binding characteristics of

model ligands in seawater, Biogeosciences, 18(19), 5265–5289, doi:10.5194/bg-18-5265-2021, 2021.

Gledhill, M. and Buck, K. N.: The organic complexation of iron in the marine environment: a review, Front. Microbiol., 3, 69, doi:10.3389/fmicb.2012.00069, 2012.

Hassler, C. S., Schoemann, V., Nichols, C. M., Butler, E. C. V and Boyd, P. W.: Saccharides enhance iron bioavailability to Southern Ocean phytoplankton, Proc. Natl. Acad. Sci., 108(3), 1076 LP – 1081, doi:10.1073/pnas.1010963108, 2011.

Hassler, C. S., van den Berg, C. M. G. and Boyd, P. W.: Toward a Regional Classification to Provide a More Inclusive Examination of the Ocean Biogeochemistry of Iron-Binding Ligands, Front. Mar. Sci., 4, 19, doi:10.3389/fmars.2017.00019, 2017.

Hogle, S. L., Bundy, R. M., Blanton, J. M., Allen, E. E. and Barbeau, K. A.: Copiotrophic marine bacteria are associated with strong iron-binding ligand production during phytoplankton blooms, Limnol. Oceanogr. Lett., 1(1), 36–43, doi:https://doi.org/10.1002/lol2.10026, 2016.

Hudson, R. J. M., Rue, E. L. and Bruland, K. W.: Modeling Complexometric Titrations of Natural Water Samples, Environ. Sci. Technol., 37(8), 1553–1562, doi:10.1021/es025751a, 2003.

Hunter, K. A. and Boyd, P. W.: Iron-binding ligands and their role in the ocean biogeochemistry of iron, Environ. Chem., 4(4), 221–232 [online] Available from: https://doi.org/10.1071/EN07012, 2007.

Hutchins, D. A. and Bruland, K. W.: Grazer-mediated regeneration and assimilation of Fe, Zn and Mn from planktonic prey, Mar. Ecol. Ser., 110, 259, 1994.

Johnson, K. S., Michael Gordon, R. and Coale, K. H.: What controls dissolved iron concentrations in the world ocean?, Mar. Chem., 57(3–4), 137–161, doi:10.1016/S0304-4203(97)00043-1, 1997.

Jones, M. E., Beckler, J. S. and Taillefert, M.: The flux of soluble organic-iron(III) complexes from sediments represents a source of stable iron(III) to estuarine waters and to the continental shelf, Limnol. Oceanogr., 56(5), 1811–1823, doi:10.4319/lo.2011.56.5.1811, 2011.

Laglera, L. M. and van den Berg, C. M. G.: Evidence for geochemical control of iron by humic substances in seawater, Limnol. Oceanogr., 54(2), 610–619, doi:10.4319/lo.2009.54.2.0610, 2009.

Liu, X. and Millero, F. J.: The solubility of iron in seawater, Mar. Chem., 77(1), 43–54, doi:https://doi.org/10.1016/S0304-4203(01)00074-3, 2002.

Lundesgaard, Ø., Winsor, P., Truffer, M., Merrifield, M., Powell, B., Statscewich, H., Eidam, E. and Smith, C. R.: Hydrography and energetics of a cold subpolar fjord: Andvord Bay, western Antarctic Peninsula, Prog. Oceanogr., doi:10.1016/j.pocean.2019.102224, 2020.

Moffett, J. W., Brand, L. E., Croot, P. L. and Barbeau, K. A.: Cu speciation and cyanobacterial distribution in harbors subject to anthropogenic Cu inputs, Limnol. Oceanogr., 42(5), 789–799, 1997.

Omanović, D., Garnier, C. and Pižeta, I.: ProMCC: An all-in-one tool for trace metal complexation studies, Mar. Chem., 173, 25–39, doi:https://doi.org/10.1016/j.marchem.2014.10.011, 2015.

Pižeta, I., Sander, S. G., Hudson, R. J. M., Omanović, D., Baars, O., Barbeau, K. A., Buck, K. N., Bundy, R. M., Carrasco, G., Croot, P. L., Garnier, C., Gerringa, L. J. A., Gledhill, M., Hirose, K., Kondo, Y., Laglera, L. M., Nuester, J., Rijkenberg, M. J. A., Takeda, S., Twining, B. S. and Wells, M.: Interpretation of complexometric titration data: An intercomparison of methods for estimating models of trace metal complexation by natural organic ligands, Mar. Chem., 173, 3–24, doi:https://doi.org/10.1016/j.marchem.2015.03.006, 2015.

Poorvin, L., Sander, S. G., Velasquez, I., Ibisanmi, E., LeCleir, G. R. and Wilhelm, S. W.: A comparison of Fe bioavailability and binding of a catecholate siderophore with virus-mediated lysates from the marine bacterium Vibrio alginolyticus PWH3a, J. Exp. Mar. Bio. Ecol., 399(1), 43–47, doi:https://doi.org/10.1016/j.jembe.2011.01.016, 2011.

Rue, E. L. and Bruland, K. W.: Complexation of iron(III) by natural organic ligands in the Central North Pacific as determined by a new competitive ligand equilibration/adsorptive cathodic stripping voltammetric method, Mar. Chem., 50(1–4), 117–138, doi:10.1016/0304-4203(95)00031-L, 1995.

Velasquez, I. B., Ibisanmi, E., Maas, E. W., Boyd, P. W., Nodder, S. and Sander, S. G.: Ferrioxamine Siderophores Detected amongst Iron Binding Ligands Produced during the Remineralization of Marine Particles , Front. Mar. Sci. , 3, 172 [online] Available from: https://www.frontiersin.org/article/10.3389/fmars.2016.00172, 2016.

Völker, C. and Tagliabue, A.: Modeling organic iron-binding ligands in a three-dimensional biogeochemical ocean model, Mar. Chem., 173, 67–77, doi:https://doi.org/10.1016/j.marchem.2014.11.008, 2015.

Whitby, H., Planquette, H., Cassar, N., Bucciarelli, E., Osburn, C. L., Janssen, D. J., Cullen, J. T., González, A. G., Völker, C. and Sarthou, G.: A call for refining the role of humic-like substances in the oceanic iron cycle, Sci. Rep., 10(1), 6144, doi:10.1038/s41598-020-62266-7, 2020.

Wu, J. and Luther, G. W.: Complexation of Fe(III) by natural organic ligands in the Northwest Atlantic Ocean by a competitive ligand equilibration method and a kinetic approach, Mar. Chem., 50(1–4), 159–177, doi:10.1016/0304-4203(95)00033-N, 1995.

Chapter 4 is being prepared for submission and the dissertation author was the primary investigator and first author of this chapter. Lauren Manck is a coauthor on incubation studies and provided syntheses of the transcriptomic data for this chapter. Katherine Barbeau supported this work as well as FjordEco and CCE LTER for the field studies.

Chapter 5. Conclusion

Aspects of the 'Iron Hypothesis' have been researched for decades, yet how inputs of new Fe contribute to primary production in the modern ocean remains a great unknown. This is partly due to poor coverage of the ocean, and poor constraints on fluxes of dust and other new Fe sources to Fe-limited and productive regions. Expanding coverage of the ocean, basin-wide surveys by the international program GEOTRACES (geotraces.org) have highlighted the need to consider multiple sources of Fe to the ocean interior. However, these studies alone cannot address the key underlying processes of ongoing Fe fertilization in the modern ocean. Knowledge of how phytoplankton meet their Fe needs, including what chemical species the Fe must be present in and how the formation of these species is regulated, is needed.

The research in this thesis attempts to understand Fe biogeochemistry in the context of multidisciplinary studies in non-High Nutrient Low Chlorophyll (HNLC) regions, and how Fe biogeochemistry couples to carbon and macronutrient cycles in productive coastal regions. The Antarctic and California Current coastal regions are far more productive than the open ocean, with seasonal phytoplankton blooms that support vibrant habitats for the world's largest fisheries and key biological "hotspots." The intensity in production is, in part, because these systems receive multiple inputs of weathered Fe-rich material, ultimately derived from the continental crust. These coastal regions are also important for sequestration of a fraction of carbon produced at the surface on the seafloor, which links processes occurring in the euphotic zone with the benthos. From this multidisciplinary approach, our understanding of the physics and biogeochemistry of these systems enabled the determination of the relative significance of different nearshore sources to coastal environments.

Work in this thesis attempted to understand how Fe contributed to the high levels of primary production in coastal regions by addressing the following questions. *What is the relative significance of different nearshore Fe sources to productive coastal environments?* To address

this problem, an understanding of how much Fe enters the ocean at ocean boundaries was needed. We identified important sources of Fe to two distinct regions: an Antarctic fjord and the California Current. In Chapter 2, cryospheric sources of Fe to the fjord euphotic zone included glacial meltwater and vertical entrainment of a subsurface subglacial plume via episodic katabatic wind events. Observations and dye experiments using a high-resolution physical circulation model informed us of how these multiple sources reach the euphotic zone. We determined that communication between the surface and deep waters enriched in sedimentary Fe was not significant. In Chapter 3, the benthic boundary layer and subsurface California Undercurrent provide coastal upwelling filaments with Fe likely coming from resuspended shelf sediments. *How bioavailable is Fe in coastal regions?* The complexity of Fe speciation in the ocean requires multiple analytical methods be employed. In Chapters 2 and 3, chemical characterization of Fe pools showed nearshore sources are rich in bioavailable Fe, with most Fe in the form of reactive Fe-minerals. In Chapter 4, the examination of Fe-binding ligands using electrochemical titrations with Multiple Analytical Windows (MAW) informed us of the spatial and temporal controls on Fe bioavailability in greater detail. A major contribution of this work was the development of novel methods for simultaneous processing of MAW electrochemical titration data. *What are the impacts of coastal Fe sources on phytoplankton populations?* In Chapter 2, we argued iron in meltwaters is supplied to the Southern Ocean from Antarctic fjords, and this is likely to become significant with regional climate change. In Chapter 3, the potential for Fe-stress was explored through *in situ* geochemical proxies and manipulation experiments in the field. This led to conceptualization of how Fe is linked to the biogeochemical cycles of the macronutrients in two coastal upwelling filaments in the California Current. We argued that coastal upwelling filaments are likely prone to Fe-limitation and that this is common to Eastern Boundary Upwelling Systems. Importantly, we found that Fe-stress affects the ability for diatoms to access nitrate, but not silicic acid, leading to a Si-ballasting effect of sinking particulate matter and contributing to efficient export of particulate organic carbon.

The cycling of Fe is intimately tied to the biogeochemistry of the macronutrients through biological assimilation by primary producers in coastal regions of the ocean. Minimizing the ambiguity of how fluxes of new Fe are regulated will ultimately result in a more comprehensive view of the Fe cycle and spatial and temporal gradients in oceanic primary production.

Fin